

Jacques Jestin
Laboratoire Léon Brillouin CEA/CNRS
CEA Saclay

**NANOSTRUCTURED PARTICLE-POLYMER COMPOSITES:
FILLER DISPERSION AND CHAIN CONFORMATION
FROM WELL-DEFINED MODEL TO “REAL” SYSTEMS,
CORRELATION WITH MECHANICAL PROPERTIES**

Accreditation to Supervise Research
Université Pierre et Marie Curie – Paris

Defended on November 14 2013 before the jury:

Dr. F. Boué	<i>CNRS/Laboratory Léon Brillouin, France</i>	Examiner
Prof. P. Cassagnau	<i>Claude Bernard University, France</i>	Referee
Dr. M. Couty	<i>Michelin Corporate, France</i>	Examiner
Dr. J. Daillant	<i>Synchrotron Soleil, France</i>	Examiner
Prof. S. K. Kumar	<i>Columbia University, USA</i>	Examiner
Dr. F. Lequeux	<i>CNRS/Pierre & Marie Curie University, France</i>	Referee
Prof. D. Richter	<i>Forschungszentrum Jülich, Germany</i>	Referee

PREAMBLE

My research activity is included in a general problematic of understanding the structure-properties correlations in complex multi-component systems. It is organized around two main axes. The **nanocomposites** for which we are looking for the correlations between the mechanical properties (reinforcement, flow, deformability...) and the nanometer scale organization of the particles inside the matrix and the polymer chain conformation. The **asphaltenes** (in collaboration with IFPEN, the French petroleum research institute located at Rueil-Malmaison near Paris), colloidal entities of crude oils whose volume and interface nanometric properties are driving the macroscopic behaviors of the fluids (viscosity, emulsion stability, flocculation etc...). This activity around the asphaltenes is the continuity of my post doc research realized in 2002-2003 at IFPEN with L. Barré. Many studies have been developed since 2007 on the stability of petroleum emulsions and the use of neutron contrast variation method to characterize the interfacial film structure^{1,2}, on adsorption of asphaltenes on surface of various morphologies using neutron reflectivity to identify the structure of the adsorbed layer (mono or multi layers)^{3,4} on rheo-reflectivity⁵ as well as the use of SANS to determine the asphaltenes adsorption in porous media^{6,7}. We recently continued the study of the nanometric structure of the asphaltenes aggregates by a combination of SAXS and SANS on diluted solutions on a broad Q range. We highlighted a refined internal structure of the aggregates, never observed before, constituted of poly-dispersed disks made of an aromatic core and an aliphatic shell⁸. We extended the characterization to see whether our model of nano-aggregate can be generalized to asphaltenes coming from different geographic and geologic origins⁹.

I have chosen to focus my accreditation on nanocomposites. Despite of a comparable experimental approach, I do not wish to merge both nanocomposite and asphaltenes thematic because they remain relatively far away in term of scientific expertise. The nanocomposite was the core of my research project presented to the CNRS when I was recruited as permanent scientist in 2004 for a position at the Laboratoire Léon Brillouin. My objective was to develop this thematic and more specifically to adapt the systems to neutron scattering techniques. In addition, I developed the subject through the management of students and PhD students in agreement with the principle of the accreditation to supervise research. Indeed, the work presented here is a compilation of three PhD already defended: Chloé Chevigny (defended on October 2009), Nicolas Jouault (defended on November 2009), Anne-Sophie Robbes (defended on October 2011) and two PhD currently in progress, Adrien Bouty (defense scheduled on December 2014) and Nicolas Genevaz (defense scheduled on October 2015).

¹ Jestin, J.; Simon, S.; Zupancic, L.; Barré, L. *Langmuir* **2007**, 23 (21), 10471-10478.

² Alvarez, G.; Jestin, J.; Argillier, J.-F.; Langevin, D. *Langmuir* **2009**, 25 (7), 3985-3990.

³ Simon, S.; Jestin, J.; Palermo, T.; Barré, L. *Energy & Fuels* **2009**, 23, 306-313.

⁴ Jouault, N.; Corvis, Y.; Cousin, F.; Jestin, J.; Barré, L. *Langmuir* **2009**, 25 (7), 3991-3998.

⁵ Corvis, Y.; Barré, L.; Jestin, J.; Gummel, J.; Cousin, F. *Eur. Phys. J. Special Topics* **2012**, 213 (1), 295-302.

⁶ Gummel, J.; Corvis, Y.; Jestin, J.; M'Hamdi, J.; Barré, L. *Eur. Phys. J. Special Topics* **2009**, 168, 171-176.

⁷ Barré, L.; Jestin, J.; Morisset, A.; Palermo, T.; Simon, S. *Oil & Gas Science and Technology* **2009**, 64 (5), 617-628.

⁸ Eyssautier, J.; Levitz, P.; Espinat, D.; Jestin, J.; Gummel, J.; Grillo, I.; Barré, L. *The Journal of Physical Chemistry* **2011**, 115 (21), 6827-6837.

⁹ Lysenko, A.; Jestin, J.; Barré, L. *to be submitted* **2013**.

ABSTRACT

Nanocomposite materials have raised a great interest over the last twenty years. This deep attractivity comes from the outstanding potentials of applications of these systems in a broad range of industrial fields. Putting together “soft” polymer chains and “hard” particles of similar nanometer size opens also the way to new questions of fundamental physics associated with polymer chains conformation and dynamic, dispersion mechanisms and confinement effects. However, the large variety of possible assemblies between different kind of polymers and particles makes difficult to dispose of a general trend to describe the correlations between the local structure of the materials and their macroscopic properties. Despite of unusual performances of mechanical reinforcement, adhesion or deformability, the general viscoelastic behaviors in nanocomposites remain still not fully described due to specific interactions, often difficult to identify and to complex organizations covering a large range of typical sizes from the nanometer to the micrometer.

The present work exposes the correlations that can be done between the particles dispersion, the polymer chain conformation with the viscoelastic behaviors of the materials at rest and under deformation across different examples of nanocomposites. The first chapter shows different strategies (chemical grafting, magnetic field, specific additives or controlled sample processing) to control the filler dispersion inside the polymer matrix with different particles (colloidal or industrial silica, magnetic nanoparticles) dispersed in polymers (polystyrene, polymethylmethacrylate) or elastomers (Styrene-Butadiene-Rubber). We go progressively from well defined model systems toward more complex “real” systems. We obtained a broad range of various morphologies from individual particles, to compact aggregates, oriented chains of particles to hierarchical networks described quantitatively by Small Angle X-ray Scattering (SAXS) and microscopy (TEM) at the different lengths scale (particle and aggregate shapes, sizes and inter-object correlations). With a combination of several methods, the viscoelastic behavior has been determined in the second chapter and analysed quantitatively with hydrodynamic and percolation models: the reinforcement is mostly driven by the aggregate morphologies and by the network strength (depending on inter-particle and inter-aggregate interactions) while the flow behavior is mostly driven by the polymer chain contribution whose physical origin appears to be related to specific polymer-particle interactions. This origin is discussed according to the different existing models. With a combination of SANS with different contrast variation methods, we demonstrated in the third chapter that the polymer chain conformation is not modified by the filler suggesting that the number of chains involved in the viscoelastic processes is low. By following the scattering of both filler and chain under deformation in the fourth chapter, we confirm that the non linear mechanical behaviors are mostly dominated by the filler reorganizations. The goal of the fifth chapter is then to define some strategies to progress in the understanding of the specific polymer-chain interactions with nanocomposites using grafted nanoparticles. We propose to focus on the chain dynamic with inelastic neutron scattering and some synthesis developments to manage the interface chain mobility or the polymer-chain interactions without changing the filler dispersion. In a more extended view, we discussed the necessity to go further in industrial systems with the development of new “real-time” experiments associated with the design of the future SANS spectrometers.

Keywords: Nanocomposites, filler dispersion, polymer chain conformation, Small Angle Neutron and X-ray Scattering, viscoelastic behavior, reinforcement, deformation.

CONTENTS

Preamble	3
Abstract	5
Introduction	9
1 Filler dispersion in nanocomposites: a broad range of morphologies	13
1.1 Synthesis and sample processing	14
1.1.1 Nanoparticles: the building block	14
1.1.2 Grafting: an incremental way of control	15
1.1.3 Nanocomposites processing by solvent casting	19
1.2 From individual dispersion to multiscale organization	20
1.2.1 The ideal case	21
1.2.2 Compacts aggregates	23
1.2.3 Aligned chain of particles: 1D filler network	26
1.2.4 3D connected filler network	27
1.2.5 Two levels of aggregation	29
1.2.5.1 Polymer matrix	29
1.2.5.2 Elastomer matrix	32
1.2.6 Multi-scale aggregation: toward the “real” systems	33
1.3 Conclusions	36
2 Mechanical and rheological behaviors	37
2.1 The effective volume contribution	38
2.2 Anisotropic reinforcement	40
2.3 Filler percolation	42
2.3.1 The local filler structure contribution	42
2.3.2 The flow behavior	48
2.4 Conclusions	51
3 Chain conformation in nanocomposites	53
3.1 The grafted brush conformation in nanocomposites	54
3.2 The bulk chain conformation in nanocomposites	57
3.2.1 The Zero Average Contrast ZAC Method	57
3.2.1.1 The Debye Approximation	57
3.2.1.2 The Random Phase Approximation RPA	59
3.2.2 The extrapolation method	61
3.3 Conclusions	63
4 Chain and filler structure under deformation	65
4.1 The grafted brush deformation in nanocomposites	66

4.2 The bulk chain deformation in nanocomposites	67
4.3 The filler network deformation	69
4.3.1 Oriented network	69
4.3.2 Effect of network constitution	70
4.4 Conclusions	72
5 Toward a better description: chain dynamic and interface setting	73
5.1 Chain dynamic	74
5.2 Interface setting	76
5.2.1 Di-block grafting	76
5.2.2 Photo-cleavable interface	77
5.3 Additional perspectives: chain distribution and particles dynamic	77
Conclusions and outlook	79
Bibliography	83
Curriculum Vitae	89
Publications and communications list	93
Publications list	93
Communications list	97
Selected papers	99
Anisotropic Reinforcement of Nanocomposites Tuned by Magnetic Orientation of the Filler Network <i>Advanced Materials</i> 2008 , 20 (13), 2533	101
Well-Dispersed Fractal Aggregates as Filler in Polymer-Silica Nanocomposites: Long-Range Effects in Rheology <i>Macromolecules</i> 2009 , 42 (6), 2031	109
Direct small-angle-neutron-scattering observation of stretched chain conformation in nanocomposites: More insight on polymer contributions in mechanical reinforcement <i>Physical Review E</i> 2010 , 82, 031801	119
Polymer-Grafted-Nanoparticles Nanocomposites: Dispersion, Grafted Chain Conformation, and Rheological Behavior <i>Macromolecules</i> 2011 , 44 (1), 122	123
Controlled grafted brushes of polystyrene on magnetic γ -Fe ₂ O ₃ nanoparticles via nitroxide-mediated polymerization <i>Soft Matter</i> 2012 , 8 (12), 3407	135

INTRODUCTION

Significantly increase the mechanical reinforcement of a material with only a few percent of « hard » filler constitutes a real gain from both industrial and economical point of view. These new performances are accessible with innovated materials called composites or nanocomposites. Indeed, including particles (filler) inside a polymer or an elastomer matrix enables for many situations to modify the intrinsic properties of the matrix like the mechanical reinforcement, the deformability, the rupture strength¹⁰ but also the optical properties (transparency, opacity), electrical (conducting, insulating) or the gas and fluid barrier properties (diffusion). These materials are used in many industrial fields like the tire industry, painting, cosmetics, food packaging and energy or petroleum industry. They have been studied intensively for twenty years for fundamental aspects but also to understand and provide the macroscopic properties knowing the intrinsic characteristic of the two main constituents, the polymer and the filler. For composite materials (made of micrometer size particles) the macroscopic behavior can usually be described with classical hydrodynamic models¹¹ when the mechanisms are mainly dominated by the inter-particle interactions. More recently, for cost reasons but also to improve the performances of the materials, we moved toward a decrease of the characteristic size of the particle to the nanometer range. The simple idea is to enhance the surface interaction between the filler and the polymer to raise the effects or to obtain similar results with fewer particles. At the nanometer scale, specific interactions between particles and between polymer and particles will drive the formation of new structures of particles inside the matrix¹². The particles can be organized according to multiscale processes from the individual dispersion to fractal aggregates more or less large or ramified that can be interpenetrated and/or percolated to form connected heterogeneous /complexes networks¹³. The filler is expected to alter the characteristic of the polymer chains whose conformation, typically Gaussian in bulk, can be affected by entropic constraints of excluded volume with interaction with the particle surfaces or directly by geometrical confinement. At the same time, the mobility of the chain should be also perturbed by the filler by modification of the dynamical relaxation modes¹⁴.

These modifications at the local nanometer scale will have strong consequences of the macroscopic behavior of the materials. Despite of an abundant literature on the subject for twenty years, the precise relationships between the local structure of the particle and of the polymer chains (and their modifications) with the mechanical behavior presents still unresolved questions. A complete state of the art review can be accessed within the following reference¹⁵. The classical hydrodynamical model failed to describe the experimental data because they do not consider aggregation or percolation effects. In addition, it is often difficult to dissociate experimentally the different contribution because they are intimately linked. The large diversity of nanocomposite components in term of chemical, physical and physical-chemistry properties and of shapes, size and composition, gives a large variety of results apparently dependent of the systems. It is thus currently difficult to provide a clear panel of the general tendencies to provide the filler dispersion inside the matrix and the macroscopic behavior as function of the microstructure. To face these difficulties, one strategy is to design model systems by combining under controlled conditions a polymer of known properties and a well-defined particle.

¹⁰ Leblanc, J. L. *Prog. Polym. Sci.* **2002**, 27, 627-687.

¹¹ Einstein, A. *Ann. Phys.* **1906**, 17, 549.

¹² Jing, X.; Zhao, W. ; Lan, L. *J. Mater. Sci. Lett.* **2000**, 19, 377-379.

¹³ Klüppel, M.; Heinrich, G. *Rubber Chem. Technol.* **1995**, 68, 623-651.

¹⁴ Berriot, J.; Montes, H.; Lequeux, F.; Long, D.; Sotta, P. *Macromolecules* **2002**, 35, 9756-9762.

¹⁵ Jancar, J.; Douglas, J. F.; Starr, F. W.; Kumar, S. K.; Cassagnau, P.; Lesser, A. J.; Sternstein, S. S; Buehler, M. J. *Polymer* **2010** 51, 3321-3343.

In this context, my research project when I arrived at the Laboratoire Léon Brillouin was to define and design model systems for which we would be able to dissociate the filler dispersion from the polymer chain organization contribution and identify the correlation with reinforcement and flow behavior. The use of neutron scattering techniques and specifically the Small Angle Neutron Scattering (SANS) associated with deuteration is determinant because it enables to probe directly the chain conformation (grafted or in bulk) inside the nanocomposite as function of the different dispersion states (individual dispersion, aggregates, 1D or 3D connected network) at rest and under deformation. We chose polymers, polystyrene (PS) and polymethylmetacrylate (PMMA), for which the deuterated forms are easily accessible using classical polymerization methods. The deuterated forms can be also directly bought for different molecular masses (M_w) and index of polymolecularity (I_p). The question of deuteration can become a critical issue when considering more complex systems as we will see for industrial systems made with Styrene-Butadiene-Rubber (SBR) matrices. The combination of SANS and SAXS is a refined way of optimizing the contrast on nanocomposites. Indeed, the fillers used (silica or maghemites particles) have a large electronic density and thus a strong sensibility to synchrotron radiation. We can then determine with SAXS the filler dispersion and with SANS the chain conformation on the *same samples*.

The synchrotron beam enables to get higher flux and resolution in comparison to neutron beams. The accessible Q range, similar for both radiations, covers typically 10^{-3} to 0.5 \AA^{-1} corresponding in the real space to distances from 1 to 100 nm. However synchrotron radiation allowed to probe smaller Q values, up to $2.10^{-4} \text{ \AA}^{-1}$, thanks to the Bonse-Hart geometry to characterize the particle organization around the micrometer size. Scattering patterns could be limited for many situations by the data interpretation when different analytical solutions can give identical scattering curves. It is then often suitable to complete the analysis with measurements in the real space using Transmission Electronic Microscopy (TEM) imaging to validate the hypothesis of scattering curves calculations but also to check whether the local structures are conserved or not at larger scale. The viscoelastic behaviors are determined by combination of uni-axial stretching, oscillatory shear and dynamical mechanical analysis (DMA) experiments that provide reinforcement and flow behaviors of the materials in the linear regime. Scattering can also be performed on stretched and frozen samples to check the evolution of structure under nonlinear deformation.

The initial idea was to define parameters as simple as possible to tune the filler dispersion in nanocomposites. In parallel, we developed an approach of increased complexity of the systems, from well-defined model toward more “real” or industrial example. The idea is to use the model to elaborate tools that can be later applied on more complex situations. Three main routes have been defined. The first one is the grafting which consists in functionalizing the surface of a particle with polymer chains before to mix them with free chains of the same polymer to make a film. The method has the advantage to promote the compatibility between the filler and the matrix with the grafted to free chain length ratio. However, it needs a critical pre-step of particle preparation to avoid aggregation while keeping efficient polymerization rates. The second route uses magnetic filler (maghemite oxide $\gamma\text{-Fe}_2\text{O}_3$) and applies an external magnetic field during the sample processing to orient the filler inside the polymer. The last route consists in mixing non functionalized particles with polymer chains in a common solvent and to evaporate the solvent under controlled conditions. The conditions of solvent casting, nature of the solvent, temperature and duration drive the final arrangement of the particles inside the polymer by controlling the attractive/repulsive balance. According to this route, we can verify the influence of the particle and of the polymer nature (size, polydispersity...). This last system which is close to the industrial situation leads to more realistic problematic by the substitution of the PS matrix by Styrene-Butadiene-Rubber (SBR) provided by Michelin. The control of the dispersion is realized with additives (mono or bi-functional silanes) that modulate the polymer-filler interactions. We also

investigate the influence of the sample processing by comparison between solvent casting methods with the manufacturing process which uses mechanical mixing.

The manuscript is composed of 5 parts. The first focuses on the analysis of the filler dispersion inside the matrix using a coupling of TEM/SAXS for different systems. We will see that simple functions enable to model the scattering and to characterize the shape of the aggregates as well as the interactions and the evolution when increasing the particle concentration for different arrangement of particles. In a second part, we will analyze the linear mechanical response of the materials (reinforcement and flow) while including in the model the parameter of the filler structure determined from the structural analysis. In a third part, we will focus on the contribution of the polymer chain conformation and its eventual modification induced by the particles inside the nanocomposites. By using SANS and deuteration, we will be able to discuss the chain conformation as function of the different filler network and about its contribution to rheological behaviors. We will then discuss in the fourth part the evolution of the filler and chain structure under deformation to probe the reinforcement mechanisms at large deformation in the nonlinear regime. The last section brings together the concepts detailed in the previous chapter to turn them into a research project, a program of my research activity for the years to come. It describes in particular a strategy to understand more deeply the polymer-chain interface influence.

CHAPTER 1

FILLER DISPERSION IN NANOCOMPOSITES: A BROAD RANGE OF MORPHOLOGIES

The knowledge and the control of the particle dispersion inside a polymer or an elastomer matrix is a key parameter with different levels of complexity. This is a multi-scale problem¹⁶ that needs to identify several sizes or distances on a characteristic range that can vary from the nanometer to the micrometer. Such a scale range is accessible by combination of electronic microscopy with scattering techniques. Imaging enables to probe the structure in the real space while scattering permits to get the mean information on a large number of atoms typically 10^{22} . This is also a multi-component problem in which the properties of the nanocomposites will depend on the intrinsic properties of the polymer and of the filler but also on the way to assemble them. Due to short range van der Waals interactions, the particles will spontaneously form aggregates inside the polymer matrix. We thus have to imagine processes to counter balance the attractive forces and limit the aggregation. The notion of model system means that we have to use well-defined particles and polymers but also a well-controlled sample processing. In laboratory, we will use the solvent casting way consisting in mixing the particle and the polymer in a common solvent and to evaporate the solvent under controlled conditions. For similar systems, we can obtain very different final filler dispersion according to the nature, the duration and the kinetic of the casting process¹⁷. The sample processing constitutes then an effective way of control of the filler dispersion inside the matrix. Other strategies exist. For systems driven by electrostatic, one can change the dispersion with the pH by modification of the particle interactions in solution before mixing with the polymer¹⁸. One can also play with the filler by changing the size or the nature of the nanoparticle but mostly the shape, from simple sphere¹⁹ to anisotropic objects like carbon nanowires²⁰, clays²¹, or natural filler like cellulose whiskers²² or by using fractal carbon black²³ or industrial silica²⁴ that will produce a broad area or various filler morphologies. Alternatively, the filler dispersion can also be tuned by an external trigger, an electrical or magnetic field²⁵ applied during the solvent casting to modulate the particle interactions or orient them in a specific direction. Finally, recent developments have been made by modifying the surface of the nanoparticles by adsorption or covalent grafting (silanes, surfactants, polymers...) to improve the compatibility with the polymer chains of the matrix.

¹⁶ Vilgis, T. A. *Polymer* **2005**, 46, 4223-4229.

¹⁷ Sen, S.; Xie, Y.; Bansal, A.; Yang, H.; Cho, K.; Schadler, L. S.; Kumar, S. K. *Eur. Phys. J. Spec. Top.* **2007**, 141, 161-165.

¹⁸ Oberdisse, J. *Macromolecules* **2002**, 35 (25), 9441-9450.

¹⁹ Botti, A.; Pyckout-Hintzen, W.; Richter, D.; Urban, V.; Straube, E. *J. Chem. Phys.* **2006**, 124, 174908.

²⁰ Dalmas, F.; Cavaillé, J.-Y.; Gauthier, C.; Chazeau, L.; Dendievel, R. *Compos. Sci. Technol.* **2007**, 67, 829-839.

²¹ Favier, V.; Chanzy, H.; Cavaillé, J.-Y. *Macromolecules* **1995**, 28, 6365-6367.

²² Wang, Y.-Z.; Zhang, L.-Q.; Tang, C.-H.; Yu, D.-S. *J. Appl. Polym. Sci.* **2000**, 78, 1879-1883.

²³ Heinrich, G.; Klüppel, M.; Vilgis, T.-A. *Curr. Opin. Solid State Mater. Sci.* **2002**, 6, 195-203.

²⁴ Baeza, G.; P.; Genix, A.-C.; Degrandcourt, C.; Petitjean, L.; Gummel, J.; Couty, M.; Oberdisse, J. *Macromolecules* **2013**, 46 (1), pp 317-329

²⁵ Fragouli, D.; Buonsanti, R.; Bertoni, G.; Sangregorio, C.; Innocenti, C.; Falqui, A.; Gatteschi, D.; Davide Cozzoli, P.; Athanassiou, A.; Cingolani, R. *ACS Nano* **2010**, 4 (4), 1873-1878.

1.1 Synthesis and sample processing

1.1.1 Nanoparticles: the building block

The starting point for modeling the filler dispersion in nanocomposites is the particles. Even restricted to spherical shape, a large range of size and size polydispersity can be found as a function of the particle nature and synthesis. These parameters can be easily accessible with SAXS experiments on diluted solutions or powders. For diluted systems, the interactions between the particles can be negligible and thus the scattering intensity is directly proportional to the form factor of the particles. The Figure 1.1 presents a series of SAXS curves obtained on different particles that we used as filler in model nanocomposites. These are commercial colloidal silica particles (a) Ludox dispersed in water and (b) Nissan dispersed in DMAc (Dimethylacetamide). The maghemite magnetic nanoparticles (c) have been chemically synthesized in water using a standard method²⁶ by co-precipitation in an aqueous ammonia solution of FeCl_2 and FeCl_3 salts. As a result, we obtained colloidal magnetite which is fully oxidized to maghemite by $\text{Fe}(\text{NO}_3)_3$ in acidic medium. A size-sorting process based on colloidal gas-liquid transitions allowed then to split up the population of nanoparticles according to their radius. The final example (d) concerns industrial silica powder (Zeosil 1165 MP) from Rhodia used as filler in rubber matrix.

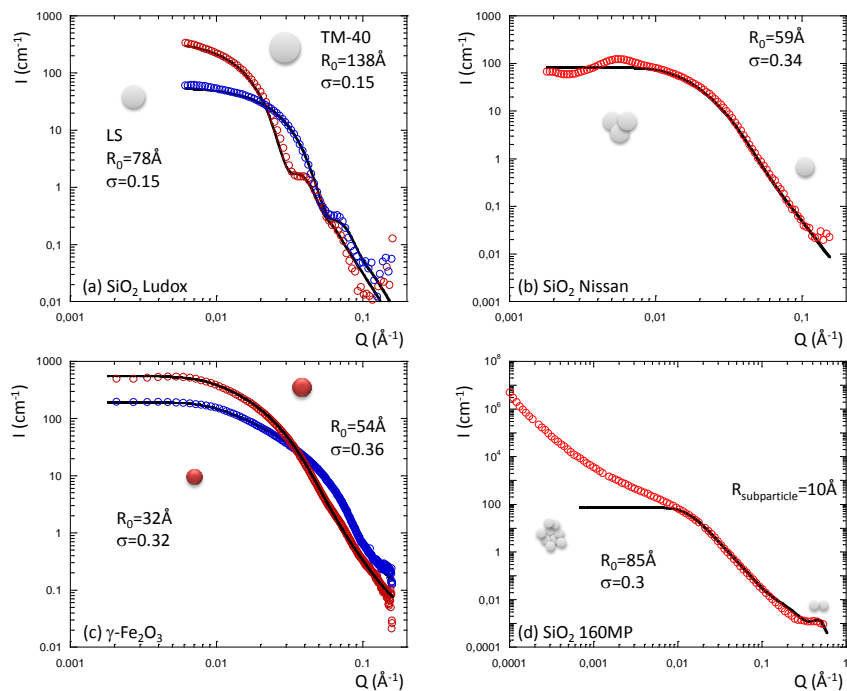


Figure 1.1: SAXS curves on different examples of nanoparticles used as fillers of nanocomposites and modeling using spherical form factor.

We model the scattering intensity with a form factor of a sphere convoluted with a log—normal function from which we can extract a mean particle radius and the polydispersity. We can observe various level of definition. The Ludox particles exhibit a low polydispersity level illustrated by the classical oscillation of the form factor in the intermediate Q range. This oscillation disappears when

²⁶ Massart, R. *IEEE Trans. Magn.* **1981**, 17, 1247

the polydispersity is increased as we can see for the Nissan and for the maghemite particles. For Nissan particles (b), we observe a maximum in the low Q domain indicating that even in diluted solution we can see some interactions due to low aggregation of the particles (2 or 3 particles per aggregates). The case of industrial powder is not so clear because the scattering pattern is rather unstructured indicating a multi-scale organization with large polydispersity. A mean polydisperse size ($R_0=85\text{\AA}$) can be extracted supposing the existence of a finite number of smaller sub-particles in close contact forming a compact primary particle. As illustrated here, the perfect knowledge of the form factor of the primary particles is of a critical importance as they will constitute the building blocks of the hierarchical structures that will appear in nanocomposites.

1.1.2 Grafting: an incremental way of control

The use of grafted nanoparticles as filler for further studies of nanocomposites can suffer from the necessity to have large amounts of particles. The critical point is thus to define reliable chemical synthesis route, with high conversion rates and good reproducibility to produce from an original sol grafted nano-beads quite well defined from the beginning to the final sol after grafting. Moreover, controlled polymerization is crucial to have a well-defined corona in term of architecture, composition and distribution (to study later its effect on the mechanical properties). Beyond the different polymerization techniques, we usually distinguish between the grafting “onto”²⁷ from the grafting “from” methods. The grafting “onto” will attach to the surface of the particle a polymer chain which has been already synthesized and characterized. This technique can be used for a large number of monomers but is limited in the range of grafting density and molecular masses. The grafting “from” technique makes the growth of the chain directly from the surface of the particles allowing grafting densities typically ten times larger. Various controlled radical polymerization methods²⁸ can be associated to grafting “from” like ATRP (atom transfer radical polymerization) developed by Matyjaszewski^{29,30}, NMP (nitroxide-mediated polymerization) by Hawker³¹ or RAFT³² (reversible addition fragmentation chain transfer). Keeping the control of the grafted particle suggests working on the colloidal suspension of the particles. The key point is then to be able to maintain the colloidal stability of the particles during the different steps of the synthesis despite of the surface modifications and of the addition of some additives that can modify the inter-particle interactions. A resulting issue is to try as best as possible to reduce the number of synthesis steps while limiting the number of synthesis components.

A first series of experiments was performed at the LLB using ATRP for grafting polystyrene chains at the surface of silica particles (PhD of A. El Harrak^{33,34,35,36}). It appeared that the use of a

²⁷ Wang, Y. P.; Shen, Y. Q.; Pei, X. W.; Zhang, S. C.; Liu, H. G.; Ren, J. M. *React. Funct. Polym.* **2008**, 68, 1225–1230.

²⁸ Prucker, O.; Ruhe, J. *Macromolecules* **1998**, 31 (3), 592-601.

²⁹ Pyun, J.; Jia, S. J.; Kowalewski, T.; Patterson G. D.; Matyjaszewski, K. *Macromolecules* **2003**, 36, 5094–5104.

³⁰ von Werne, T.; Patten, T. E. *J. Am. Chem. Soc.* **1999**, 121, 7409-7410.

³¹ Husseman, M.; Malmstrom, E. E.; McNamara, M.; Mate, M.; Mecerreyes, D.; Benoit, D. G.; Hedrick, J. L.; Minsky, P.; Huang, E.; Russell, T. P.; Hawker, C. J. *Macromolecules* **1999**, 32, 1424–1431.

³² Li, C. Z.; Benicewicz, B. C. *Macromolecules* **2005**, 38, 5929–5936.

³³ El Harrak, A.; Carrot, G.; Oberdisse, J.; Jestin, J.; Boué, F. *Polymer* **2005**, 46, 1095–1104.

³⁴ El Harrak, A.; Carrot, G.; Oberdisse, J.; Jestin, J.; Boué, F. *Macromolecular Symposia* **2005**, 226(1), 263–278.

³⁵ Oberdisse, J.; El Harrak, A.; Carrot, G.; Jestin, J.; Boué, F. *Polymer* **2005**, 46, 6695–6705, 2005.

³⁶ Carrot, G.; El Harrak, A.; Oberdisse, J.; Jestin, J.; Boué, F. *Soft Matter* **2006**, 2 (12), 1043-1047.

multiple-component initiating system, e.g. metal halide and ligand for ATRP, increased the source of possible aggregation phenomena by disturbing the particle interactions.

We chose to start from a colloidal suspension of well dispersed nanoparticles in an organic solvent and maintain the stability and the good dispersion in the sol during grafting. We must then optimize the process using a limited number of components for the synthesis while being straightforward to perform. We turned to NMP which is a mono-component system with additional advantages of versatility, robustness and simplicity. Our approach consists of covalently bind the alkoxyamine, which acts as initiator-controlling agent, in two steps onto the silica nanoparticles surface. After transfer of the particles from aqueous into an organic media, the first step is a reaction between the aminopropylsilane and the silica particles in order to functionalize the particle surface with amino group. In a second step the initiator-controlling alkoxyamine moiety is introduced via an over grafting reaction between the amino group and the N-hydroxysuccinimide-based MAMA-SG1 (MAMA-NHS) activated ester previously prepared in a straightforward manner from the commercially available MAMA-SG1 (BlocBuilder)³⁷. We have chosen the over grafting method because it has been already used for the functionalization of silica wafers or silica particles and was found to give better results in terms of control and degree of grafting than other methods. The general scheme of the grafting process is reported on Figure 1.2.

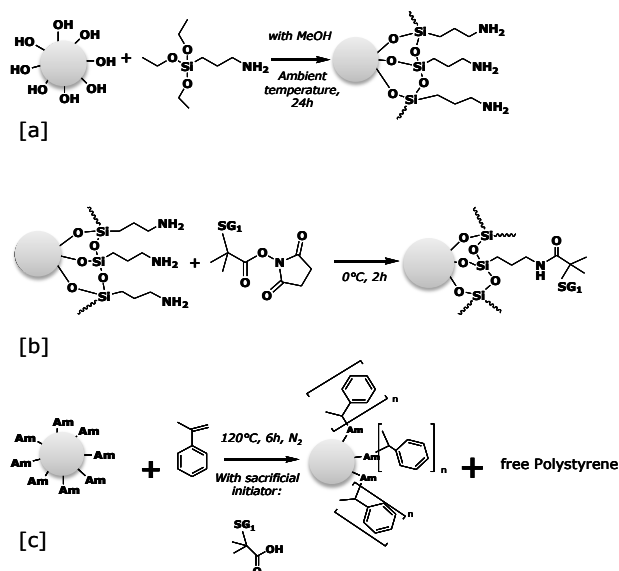


Figure 1.2: Scheme showing the three steps of grafting: [a] silanization, [b] over grafting of the initiator, and [c] the polymerization from the particle surface. Am = initiator.

The synthesis conditions are defined with model polymerization, without particles, to verify the control and estimate the conversion rates. Grafting process has been developed for many types of nanoparticles, mainly for silica but also for gold³⁸ or magnetic particles³⁹. We optimized the process on Ludox TM-40 silica nanoparticles⁴⁰ (Figure 1.1a) and adapted it in a second step to silica Nissan⁴¹ (Figure 1.1b) and to maghemites nanoparticles⁴² (Figure 1.1c). The first step is to

³⁷ Vinas, J. ; Chagneux, N. ; Gignes, D. ; Trimaille, T. ; Favier, A. ; Bertin, D. *Polymer* **2008**, 49, 3639–3647.

³⁸ Said-Mohamed, C. ; Niskanen, J. ; Karesoja, M. ; Pulkkinen, P. ; Tenhu, H. ; Daoud, M. ; Lee, L.-T. *Soft Matter* **2011**, 7, 7112-7122.

³⁹ Xu, C. ; Ohno, K. ; Ladmiral, V. ; Composto, R. J. *Polymer* **2008**, 49, 3568–3577.

⁴⁰ Chevigny, C. ; Gignes, D. ; Bertin, D. ; Jestin, J. ; Boué, F. *Soft Matter* **2009**, 5 (19), 3741-3753.

⁴¹ Chevigny, C. ; Jouault, N. ; Dalmas, F. ; Boué, F. ; Jestin, J. *Journal of Polymer Science Part B-Polymer Physics* **2011**, 49 (11), 781-791.

transfer the particle from water to the organic solvent (DMAc) used for the synthesis. This can be done simply by mixing and evaporation of the water as the DMAc presents a boiling point (~165°C) higher than 100°C. The colloidal stability of the nanoparticle is checked after each polymerization steps using scattering techniques. With particles, optimized conditions (30% v/v of monomer at 120°C) give a conversion rate of around 50%. For any polymerization ‘sacrificial’ free initiator is necessary to initiate the polymerization and to ensure good control of the chain growth; without the free initiator, the SG1 concentration would be too low to attain the persistent radical effect, thus allowing control. The consequence is the presence of free (non-grafted) polymer chains in the solvent at the end of the synthesis. The grafted nanoparticles can be separated from the free polymer chains by ultrafiltration.

Some results are presented on Figure 1.3 for polymerization performed with hydrogenated or deuterated monomers on silica and maghemite particles. The grafted nanoparticles were analyzed by TGA to evaluate the number of grafted chains per particle, typically 0.2 chain/nm², and the free polymer chains were analyzed by SEC to determine the M_w of the synthesized chains, typically of 25 000 g/mol with polydispersity index for the grafted masses (M_w/M_n below 1.3). Previous studies^{43,44} showed that the mass of the grafted chains are usually of the same order of magnitude that the non-grafted chains. By adding free controller SG1 instead of free initiator in solution, we could then polymerize from the nanoparticles in a controlled way, without creating the free chains and thus enable a tuning of the grafted chain mass from 5000 to 50 000 g/mol⁴⁵.

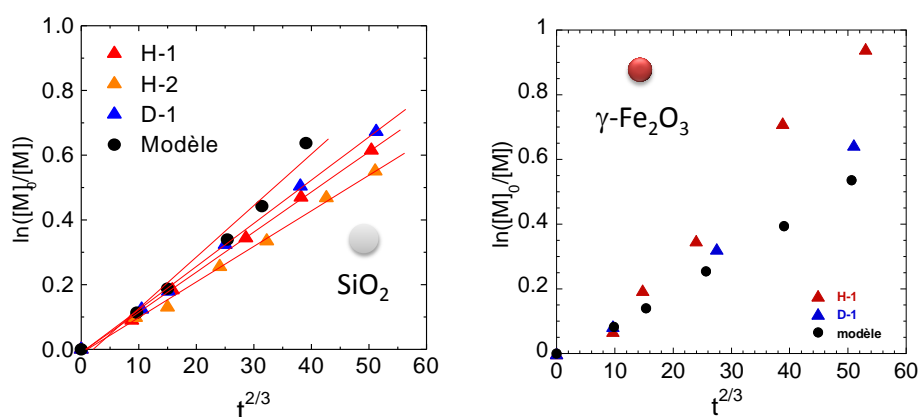


Figure 1.3: Semi-logarithmic evolution of the conversion as a function of $t^{2/3}$ illustrating the control of the reaction for model polymerizations and for polymerizations on silica particles (left) and maghemite particles (right) using hydrogenated and deuterated styrene.

⁴² Robbes, A.-S. ; Cousin, F. ; Meneau, F. ; Chevigny, C. ; Gigmes, D. ; Fresnais, J. ; Schweins, R. ; Jestin, J. *Soft Matter* **2012**, 8 (12), 3407-3418.

⁴³ Husseman, M.; Malmstrom, E. E.; McNamara, M.; Mate, M.; Mecerreyes, D.; Benoit, D. G.; Hedrick, J. L.; Mansky, P.; Huang, E.; Russell, T. P.; Hawker, C. J. *Macromolecules* **1999**, 32, 1424–1431.

⁴⁴ Flood, C.; Cosgrove, T.; Howell, I.; Revell, P. *Langmuir* **2006**, 22, 6923–6930.

⁴⁵ Chevigny, C.; Gigmes, D.; Bertin, D.; Schweins, R.; Jestin, J.; Boué, F. *Polymer Chemistry* **2011**, 2 (3), 567-571.

The strength of our approach is to associate a refined polymerization method with the grafted nanoparticle characterization using SANS and contrast variation. Using mixtures of deuterated and hydrogenated solvent, simplified SANS scattering patterns can be obtained by matching either the contribution of the grafted shell or the one of the particle core. This allows to check the degree of dispersion of the nanoparticles (individual or aggregated) and to probe precisely the composition of the grafted brushes (M_w , radius of gyration and grafting density) with appropriate models. Some examples of such characterizations are presented on Figure 1.4 for the polymer matching conditions for silica (a) and maghemite (c) and for the particle matching condition for silica (b) and for maghemite (d). We found individual particle for silica (modeled with a spherical shape) and small linear aggregates for maghemite as a result of attractive dipolar interactions adjusted with an ellipsoidal shape. From the form factor of the core, we can extract the structure factor of the center of masses of the grafted objects $S_{\text{core}} = I_{\text{match_pol}}/P_{\text{core}}$ that can be then used for the second contrast conditions (c) and (d) to extract the form factor of the grafted brushes $P_{\text{grafted}} = I_{\text{match_core}}/S_{\text{core}}$.

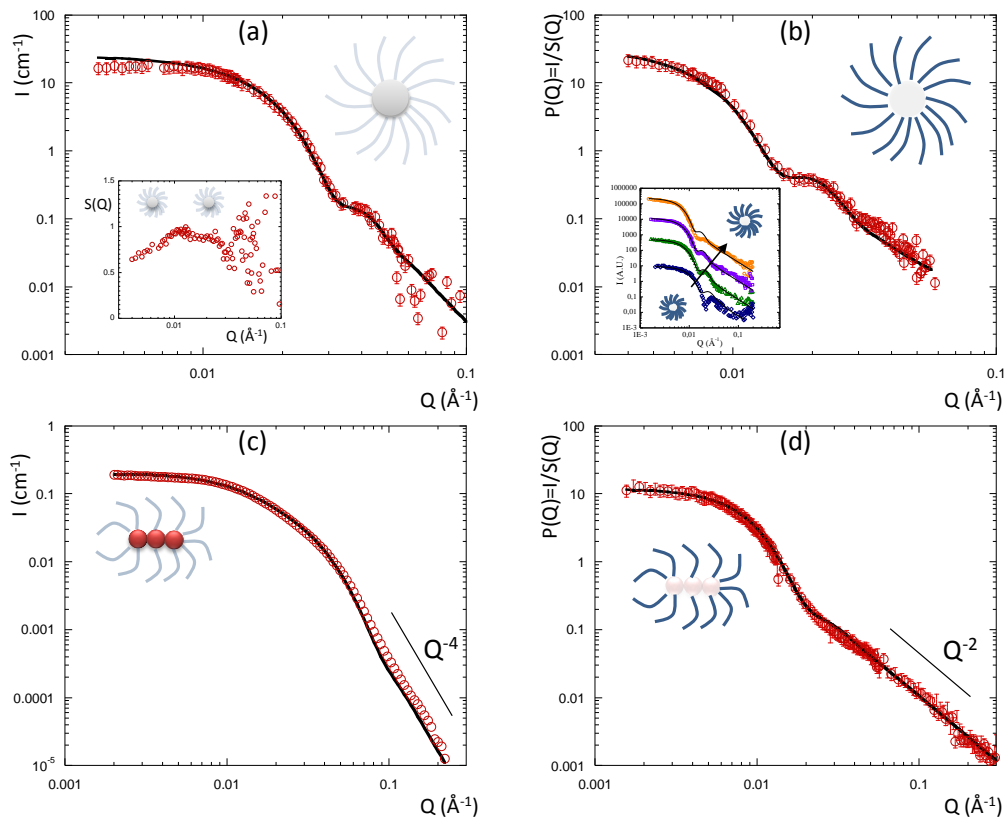


Figure 1.4: (a) PS-grafted-silica particles in polymer matching condition (match_pol), the full black line is the spherical form factor of the primary particle $P(Q)$, the inset is the structure factor of the particles deduced from the division of the intensity by $P(Q)$. (b) PS-grafted-silica particles in silica core matching condition (match_core), the full black line is the best fit result of the grafted brush form factor P_{grafted} using the Gaussian chain Pedersen model⁴⁰, the inset shows the evolution of the scattering when varying the mass of the grafted chain⁴⁵. (c) PS-grafted-maghemite particles in polymer matching condition (match_pol), the full black line is the form factor of the primary objects $P(Q)$ with an ellipsoid. (d) PS-grafted-maghemite particles in silica core matching condition (match_core), the full black line is the best fit result of the grafted brush form factor P_{grafted} using the Gaussian chain Pedersen model⁴².

The form factor of the grafted brushes can be well reproduced by an analytical function proposed by Pedersen⁴⁶ which is representative of non-interacting Gaussian chains attached onto an incompressible core. The Gaussian behavior of the grafted chain is highlighted by the Q^{-2} dependence of the scattering intensity in the high Q range nicely visible on Figure 1.4b and d.

The characteristics of the brush deduced from the fitting process with the Pedersen model are in very good agreement with the results deduced from standard chemical analysis. The grafted chain conformation is in accordance with scaling laws for brushes in solvent theta $h \sim N^{3/5} \sigma^{1/3} R_0^{3/5}$ for silica particles. For the maghemite particle, the extension corresponds to an intermediate geometry between a spherical and a planar surface according to the “quasi-linear” geometry of the core.

This refined combination between controlled polymerization and detailed characterization enables to dispose of well-defined grafted particles that we can use now to prepare nanocomposites using the sample processing described below.

1.1.3 Nanocomposites processing by solvent casting

As already mentioned, the preparation process of the nanocomposite is of a critical importance for the final organization state inside the matrix¹⁰. We have developed a new method of processing particle-polymer composites by solvent casting based on the use of a high boiling point solvent, in which the particles are well dispersed, and a long controlled evaporation procedure⁴⁷. The general scheme of the process, presented on Figure 1.5a, has been developed specifically for the silica-polystyrene system and adapted (temperature and evaporation duration) for the further additional couples particle/polymer used. For maghemites systems, we have added a specific device for applying a homogenous magnetic field during the solvent casting^{48,49}. To understand the process, we can follow the evolution of the inter-particle structure factor as function of the evaporation time as presented on Figure 1.5b. For both concentrations, we can see that the maximum of the $S(Q)$ moves first to the higher Q values illustrating a first step of the aggregation of the particles and then moves back to the lower Q values for higher evaporating times illustrating repulsion between aggregates due to polymer chains.

The final slope of the scattering curve shows a $Q^{-1.8}$ dependence of the intensity typical of DLCA (Diffusion Limited Clusters Aggregation)⁵⁰ process. The resulting well organized structure of the filler comes from a subtle balance between attractive van der Waals interactions and repulsive slowing down due to the increase of the viscosity of the medium induced by the solvent evaporation.

This question of the sample processing method, and the consequences on the filler dispersion, will be of a particular interest when addressing the industrial systems prepared by internal mixer inducing thermal and rheological history.

⁴⁶ Pedersen, J. S. ; Gerstenberg, M. C. ; *Macromolecules* **1996**, 29,1363.

⁴⁷ Jouault, N.; Vallat, P.; Dalmas, F.; Said, S.; Jestin, J.; Boué, F. *Macromolecules* **2009**, 42 (6), 2031-2040.

⁴⁸ Jestin, J.; Cousin, F.; Dubois, I.; Ménager, C.; Schweins, R.; Oberdisse, J.; Boué, F. *Advanced Materials* **2008**, 20 (13), 2533.

⁴⁹ Robbes, A.-S. ; Cousin, F. ; Meneau, F. ; Dalmas, F. ; Boué, F. ; Jestin, J. *Macromolecules* **2011**, 44 (22), 8858–8865.

⁵⁰ Stauer, D. *Introduction to Percolation Theory* **1985**, Taylor and Francis.

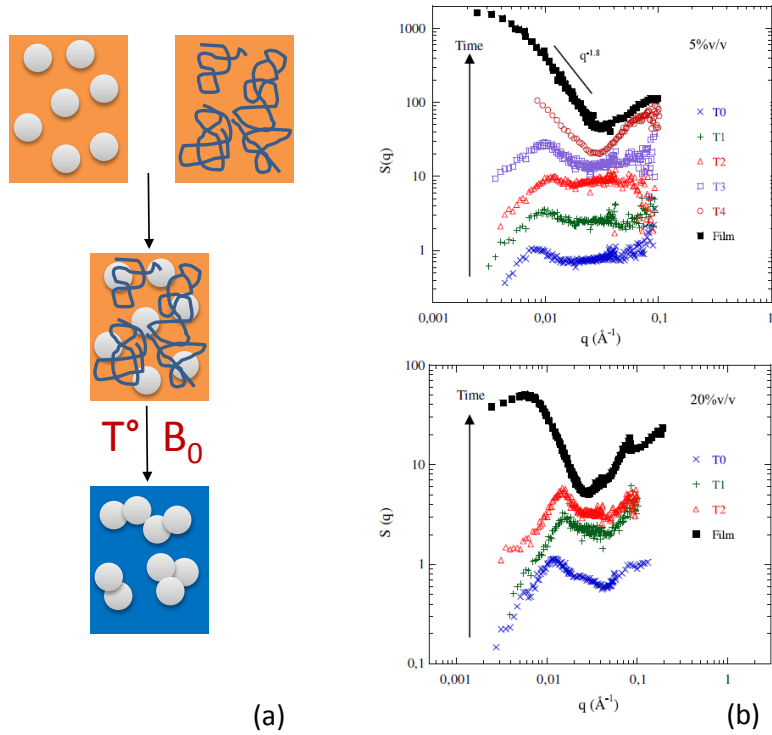


Figure 1.5: (a) general scheme of the sample processing by solvent casting, (b) evolution as function of the evaporating time of the inter-particle structure factor $S(Q)$ for the system silica Nissan/Polystyrene for a silica volume fraction of 5% v/v (top) and of 20% v/v (bottom).

1.2 From individual dispersion to multiscale aggregation

From the particles (grafted and non-grafted) and the sample processing described previously, we have studied a series of nanocomposites made with two kind of matrix: high T_g polymers, polystyrene PS and polymethylmethacrylate PMMA and low T_g elastomer, Styrene-Butadiene-Rubber SBR. The pertinent parameter is the particle volume fraction and we will describe different interesting morphologies as function of the specificity of the systems. The understanding of the local structure of the filler inside the matrix is crucial to move toward to the quantitative modeling of the mechanical properties and specially the identification of the pertinent length scale. One of the main issue is to separate the contribution of the structure factor between the objects (primary particles, primary or secondary aggregates) from the one of the form factor of the objects (aggregation number and fractal dimension). Both can be modified or not with the particle concentration. This point will be discussed using modeling function based on analytical considerations.

1.2.1 The ideal case

The first example of particle dispersion called “the ideal case”, corresponds to the individual dispersion of single particle inside the matrix without any aggregation. This can be obtained with grafted nanoparticles mixed with the homologous polymer for which the χ parameter is close to zero. The particle dispersion can be tuned with the grafted (of polymerization index N) to free chain (P) length ratio $R=N/P$. For either very low grafting density (σ) or very high σ , the particles are arranged as aggregates within the polymer matrix. The formation of aggregates is due to attractive interactions, either between particles at very low σ corresponding to allophobic wetting transitions⁵¹, or between grafted brushes at very high σ corresponding to autophobic wetting transitions. For intermediate σ , the dispersion state of the particles is mainly dependent on the interactions between the grafted and the free chains. It is then only tuned by R : when the free chains are smaller than the grafted ones, they can wet the grafted brushes owing to favorable mixing entropy. This induces repulsive interactions between the grafted objects inside the matrix leading to their perfect individual dispersion.

Two examples are given on Figure 1.6 for silica particles with a grafted to free chain length ratio $R=0.25$ ⁵² and for maghemite particles for $R=1$ ⁵³. The SAXS curves exhibit a nice repulsion peak, around 0.02 \AA^{-1} , corresponding to the interactions between the particles. The increase in the low Q domain is attributed to voids domains inside the materials due to the samples processing. The TEM image (Figure 1.7) confirms the nice individual repartition of the particles. The scattering intensities can be well reproduced as function of the contrast $\Delta\rho^2$, the particle volume V and the particle volume fraction ϕ by the product of the form factor of the particles with a structure factor of individual spheres:

$$I(Q) = \Delta\rho^2 V \phi P_{\text{part}}(Q) S_{\text{part}}(Q) \quad 1.1$$

The structure factor is defined here by a Percus-Yevick (PY) function⁵⁴. According to the characterization of the grafted objects in solution, the form factors of the cores are individual spheres for silica and small linear aggregates for maghemites. From the PY analysis, we can extract an inter-particle center to center distance from which we can deduce the extension of the grafted brushes inside the composite ($h \sim 6 \text{ nm}$) which is found to be reduced of a factor 2 in comparison with the extension in solution (Figures 1.4b, 1.4d). We can also extract an effective volume fraction of the particles, including the volume of the grafted brushes, which is found to be twice the initial particle volume fraction in agreement with the number of chain per particles.

⁵¹ Sunday, D.; Ilavsky, J.; Green, D.L. *Macromolecules* **2012**, 45 (9), 4007–4011.

⁵² Chevigny, C.; Dalmas, F.; Di Cola, E.; Gigmes, D.; Bertin, D.; Boué, F.; Jestin, J. *Macromolecules* **2011**, 44 (1), 122-133.

⁵³ Robbes, A.-S.; Cousin, F.; Meneau, F.; Dalmas, F.; Schweins, R.; Gigmes, D.; Jestin, J. *Macromolecules* **2012**, 45 (22), 9220–9231.

⁵⁴ Percus, J. K.; Yevick, G. J. *Phys. Rev. Second Ser.* **1958**, 110 (1), 1–13.

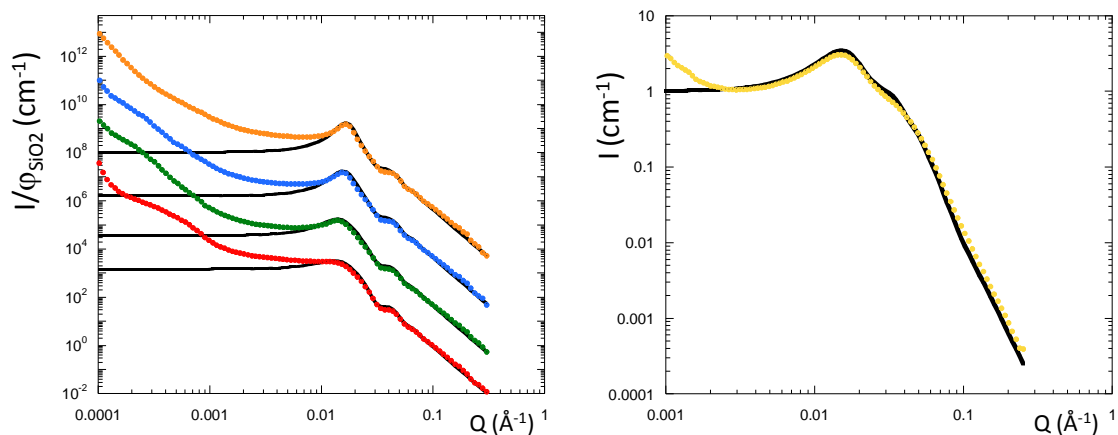


Figure 1.6: SAXS scattering curves of PS nanocomposites, *left*, (M_n matrix = 98 000 g/mol) filled with PS grafted silica nanoparticles (M_n grafted=24 400 g/mol) corresponding to a grafted-free chain length ratio $R=0.25$ as a function of the particles concentration (4 red, 9 green, 12 blue, and 15% v/v orange), *right*, (M_n matrix = 26 000 g/mol) filled with PS grafted maghemite particles (M_n grafted=26 000 g/mol) corresponding to a grafted-free chain length ratio $R=0.1$ for a particles concentration of 7% v/v yellow. The full black corresponds to the calculated scattering function (see text).

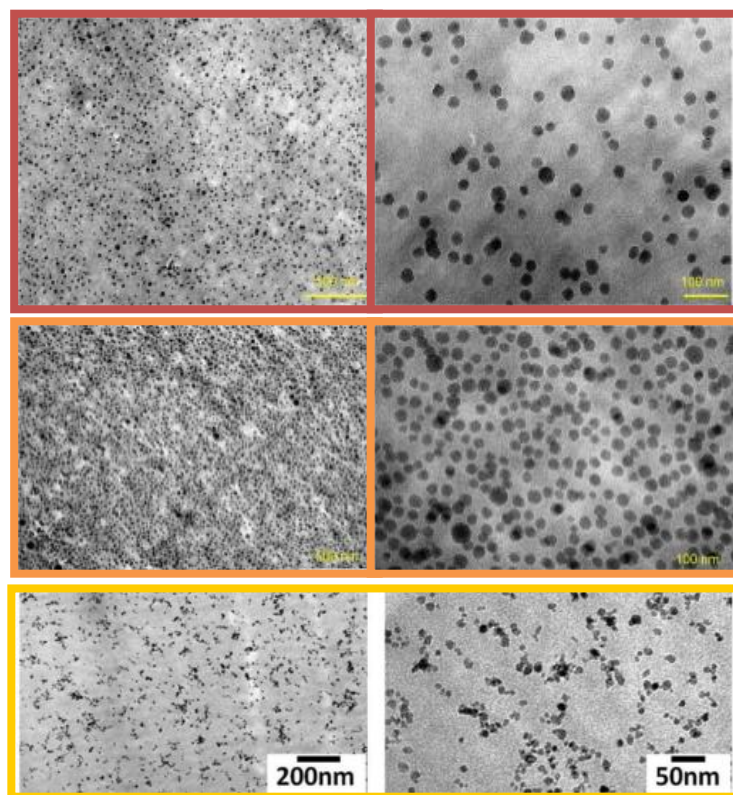


Figure 1.7: TEM pictures at large (left) and low (right) magnifications for PS silica grafted particles $R=0.25$ at 5 (red) and 15 (orange) % v/v and for PS maghemite grafted particles $R=0.1$ for a particles concentration of 7% v/v (yellow).

1.2.2 Compact aggregates

We consider now the reversed situation. When the free chains are larger than the grafted ones, the free chains are expelled from the grafted coronas because of the unfavorable mixing entropy, which results in attractive interactions between objects and ultimately to the formation of dense aggregates of particles inside the matrix. We can see on Figures 1.8 and 1.9 the characteristics SAXS/TEM corresponding to silica and maghemite grafted particles forming large compact aggregates inside the matrix for ratio $R=0.17$ and 0.26 . The scattering curves show a peak at low Q whose position moves to lower Q values when increasing the particle concentration illustrating the interactions between the aggregates. A second peak around 0.02\AA^{-1} , only visible for silica, illustrates the particles in contact inside the aggregates. This peak is not visible for maghemites due to the lower compactness of the aggregates. Indeed, the intermediate slope characteristic of the fractal dimension of the aggregates is close to 3 for silica (compact) and reduced to 2.6 for maghemites (less compact). To model the scattering curves (full black lines), we use a combination of analytical functions for structure and form factors. Starting from the spherical form factor of the particle, we can calculate the scattering of an aggregate composed of N native particles (N_{agg}) and described by a fractal dimension D_f . We add two PY functions, one to describe the interactions between the particles inside the aggregate S_{intra} , the other to describe the interactions between the aggregates S_{inter} :

$$I(Q) = \Delta\rho^2 V \phi P_{\text{agg}}(Q) S_{\text{inter}}(Q) S_{\text{intra}}(Q) \quad 1.2$$

where the form factor of the aggregates is defined according to:

$$P_{\text{agg}}(Q) = N_{\text{agg}} Q^{-D_f} \frac{\int_0^\infty P(Q, R) L(R, \sigma) R^3 dR}{\int_0^\infty R^3 L(R, \sigma) dR} \quad 1.3$$

It is important to notice that the PY function was first computed for mono-dispersed hard sphere particles. However, we can observe that it can also be used for long range interactions between aggregates even for poly-dispersed ramified entities. The modeling works indeed nicely for compact aggregates obtained with silica particles. From the calculations we can extract quantitative parameters about the morphology like the compactness of the aggregates (of the order of 40%) and the fractal dimension ($D_f=3$) as well as the distance in the real space between the objects of the order of the micrometer. The compactness of the aggregates is defined as:

$$\kappa = N_{\text{agg}} \left(\frac{R_{\text{agg}}}{R_{\text{part}}} \right)^3 \quad 1.4$$

With R_{agg} is defined as:

$$R_{\text{agg}} = R_{\text{part}} N_{\text{agg}}^{1/D_f} \quad 1.5$$

When the particle concentration increases, the aggregates become larger and move away from each other indicating that there is no direct connectivity or percolation between the objects. When the compactness of the aggregates decreases as for maghemite system, the S_{intra} do not presents a well-defined correlation peak. The feature is reduced to a smooth oscillation because the correlation ranges between the particles are reduced to limited directions.

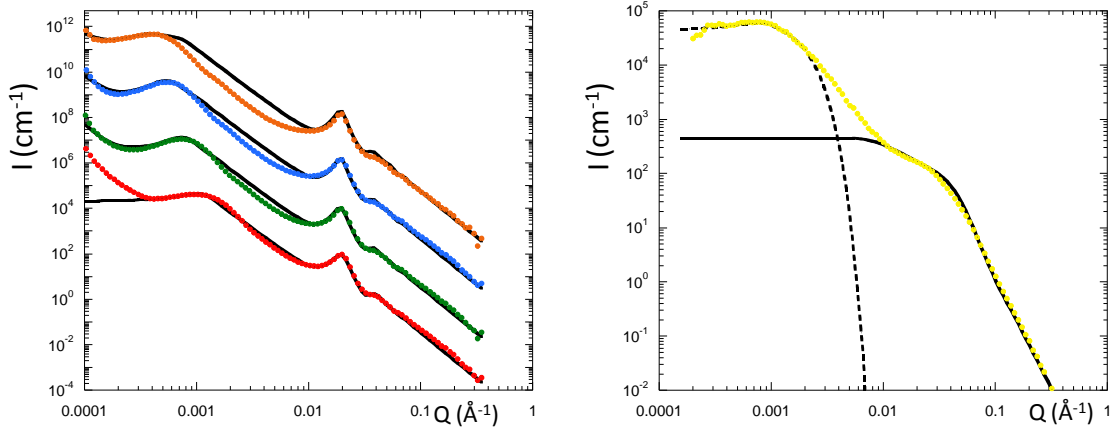


Figure 1.8: SAXS scattering curves of PS nanocomposites, *left*, (M_n matrix =140 000 g/mol) filled with PS grafted silica nanoparticles (M_n grafted=24 000 g/mol) corresponding to a grafted-free chain length ratio $R=0.17$ as a function of the particles concentration (4 red, 7 green, 9.5 blue, and 11% v/v orange), *right*, (M_n matrix = 65 000 g/mol) filled with PS grafted maghemite particles (M_n grafted=17 000 g/mol) corresponding to a grafted-free chain length ratio $R=0.26$ for a particles concentration of 0.5 %v/v yellow. The full black line corresponds to the calculated scattering function (see text).

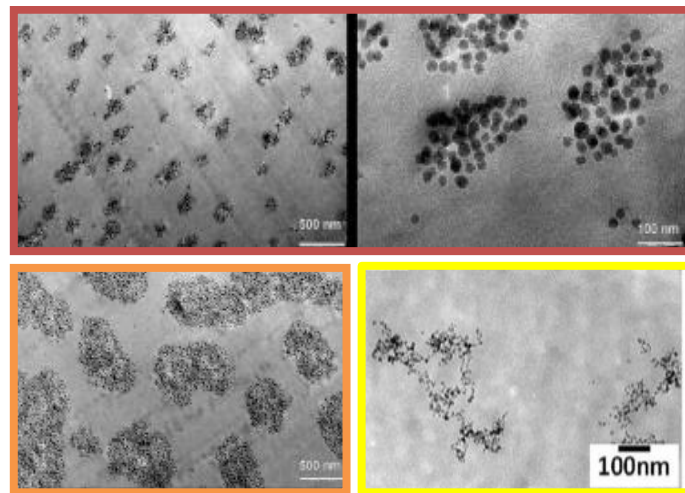


Figure 1.9: TEM pictures PS silica grafted particles $R=0.17$ at 5 (red) for two magnifications (500 and 100nm) and 15 (orange) % v/v and for PS maghemite grafted particles $R=0.26$ for a particles concentration of 0.5% v/v (yellow).

The transition between individual dispersion and aggregates formation as function of R , usually called the “wet-to-dry” transition is now a generalized result supported by many publications^{44,45,55,56,57}. This mechanism is accompanied by an elastic compression of the grafted chains for $P > N$ and with an extension for $P < N$ to minimize the free energy of the system. This point will be discussed in Chapter 3. Beyond this clear view of the general behavior of these systems, several points remain to be solved, as highlighted by recent simulations^{58,59}. It mainly concerns the threshold of the transition and the identification of the whole parameters that can influence it. According to the pioneer work of De Gennes⁶⁰ this transition is supposed to occur at $P = N$ in the case of planar surfaces but should be influenced by surface curvature effects when considering spherical particles, by the brush–brush and free chains–brush entanglement effects and by the sample processing conditions. By a direct comparison between silica, for which the transition is around $R=0.24$ (spheres), and maghemite for which the transition is above $R=0.4$ (linear aggregates), we can see the influence of the surface curvature of the grafted objects on the threshold of the transition: the modification of the particle surface curvature from sphere to linear aggregates shifts the transition threshold toward the expected value of $R = 1$ for planar surface.

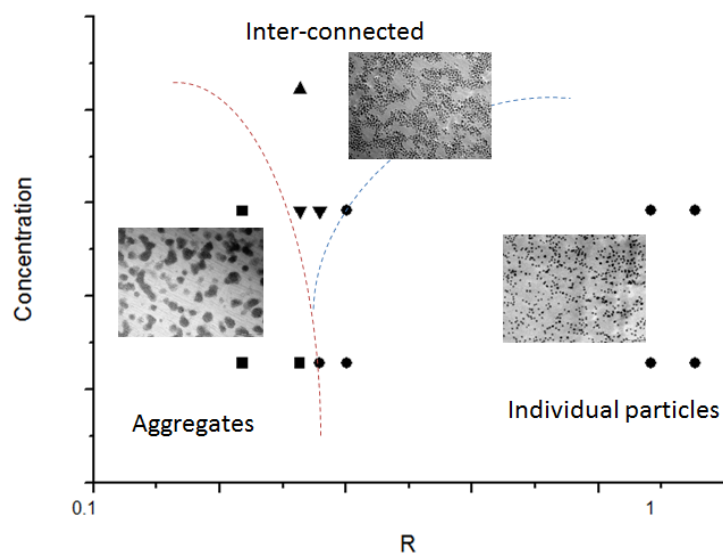


Figure 1.10: Phase diagram of particles dispersion as function of the particle concentration and of the grafted to free chain length ratio R .

We recently investigated more precisely the behavior around the transition $R=0.24$ reported on Figure 1.10. We obtained a new intermediate organization, an interconnected network, suggesting a metastable behavior around the transition.

⁵⁵ Wang, X.; Foltz, V. J.; Rackaitis, M.; Böhm, G. G. A. *Polymer* **2008**, 49, 5683–5691.

⁵⁶ Akcora, P.; Liu, H.; Kumar, S. K.; Moll, J.; Li, Y.; Benicewicz, B. C.; Schadler, L. S.;

Acehan, D.; Panagiotopoulos, A. Z.; Pryamitsyn, V.; Ganesan, V.; Ilavsky, J.; Thiyagarajan, P.; Colby, R. H.; Douglas, J. *Nat. Mater.* **2009**, 8, 354–359.

⁵⁷ Kumar, S.K.; Jouault, N.; Benicewicz, B.; Neely, T. *Macromolecules* **2013**, 46 (9), 3199–3214.

⁵⁸ Smith, G. D.; Bedrov, D. *Langmuir* **2009**, 25, 11239.

⁵⁹ Ghanbari, A.; Ndro, T. V. M.; Leroy, F.; Rahimi, M.; Böhm, M.C.; Müller-Plathe, F. *Macromolecules* **2012**, 45 (1), 572–584.

⁶⁰ de Gennes, P. G. *Macromolecules* **1980**, 13, 1069–1075

1.2.3 Aligned chains of particles: 1D filler network

Alternatively to grafting, a more promising flexible route to control the spatial repartition of nanoparticles inside a polymer matrix is the use of an external trigger which can be applied during the nanocomposite processing. This can be achieved using magnetic nanoparticles (maghemite) and an external homogenous magnetic field⁴⁸. The Figure 1.11a shows the 2D scattering patterns obtained with two magnetic field intensities (100 and 600 G) with increasing particles sizes. The TEM pictures show that the nanoparticles are organized as chains of particles oriented along the magnetic field direction (indicated by the red arrow). We can see nice anisotropic patterns whose anisotropy seems to increase both with the field intensity and the particles size. This indicates that the aggregation processes are dominated here by the dipolar interactions between the particles that are varying like the square of the particle volume ($\sim D_0^6$). This effect is thus even greater when the particles are larger. The 1D organization of the particles is confirmed by the scattering analysis by the radial averaging of the intensity parallel and perpendicular to the magnetic field direction. By dividing the scattering intensity by the well-known form factor of the particles, we can extract the structure factors of the particles in both directions. Looking at the evolution of the parallel $S(Q)$ with the particle concentration (Figure 1.11b), we can observed that we have alignments, not of single particles, but of finite size units of particles whose aggregation number is decreasing with the particle concentration (~ 10 at 1% and ~ 5 at 3%). The alignment illustrated by the slope of the power law decrease of the intensity is not perfect at 1% (slope ~ 1.3) certainly due to misalignments effects. It becomes nicely perfect at 3% (slope ~ 1) according to a rod-like scattering object⁴⁹.

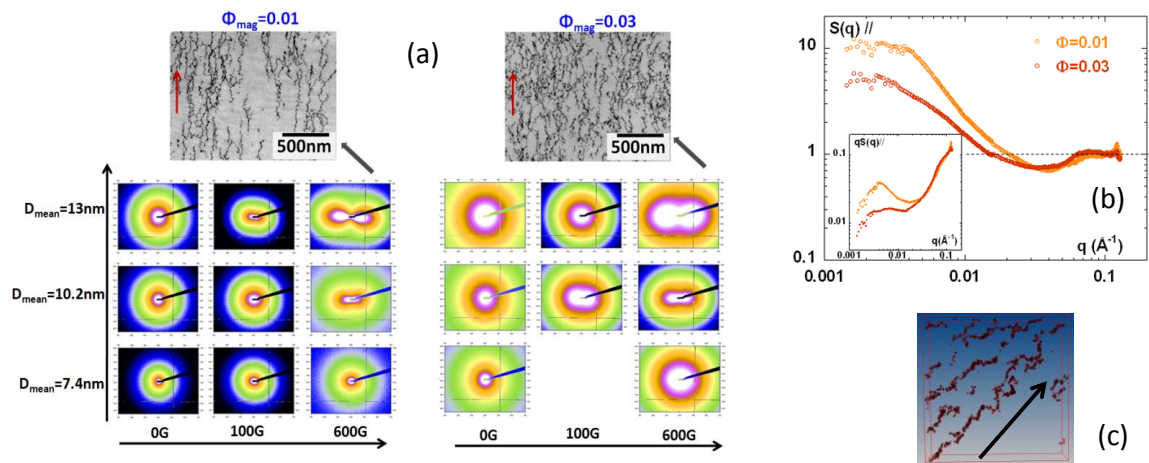


Figure 1.11: (a) Influence of the magnetic field on the nanoparticle dispersion in two concentrated regimes as a function of the nanoparticle size. 2-D SAXS images in reciprocal space of the nanostructure of the films at 1% v/v (left) and 3% v/v (right) for 3 nanoparticle sizes at 2 magnetic fields ($B = 100$ G, and $B = 600$ G) and corresponding TEM images. (b) Comparison of the magnetic field parallel structure factors $S(Q)$ for 2 particles concentrations 1 and 3% v/v. (c) Image reconstruction by 3 D tomography, the black arrow indicates the magnetic field direction.

1.2.4 3D connected filler network

We turn now to a more complex situation by studying non-functionalized silica (from Nissan described on Figure 1.1b) nanoparticles dispersed inside polymer matrix of PS and PMMA. Despite of different chemical compositions, both polymer matrixes have common points, equal molecular weights and molecular weights distribution (around 300 000g/mol, $I_p \sim 2$), same T_g (around 100°C) and comparable mechanical behaviors. We follow the evolution of the SAXS as function of the particles concentration over a range of concentration located between 5 and 35 % v/v for PS⁴⁷ (Figure 1.12c) and PMMA⁶¹ (Figure 1.12d). The analysis is completed with TEM pictures (Figure 1.13) at small (100nm) and large magnification (1µm). The SAXS curves exhibited two distinct behaviors as a function of the particle concentration: a plateau at low Q for low particles content indicating finite size objects (Figure 1.12a) and a nice peak appearing at larger concentration indicating repulsive interactions between the objects (Figure 1.12b). We fitted the scattering curves with the same analytical function used previously for grafted nanoparticles (Equation 1.2): the native silica particles are making fractal aggregates whose interaction between objects follows a PY potential. The main difference is that we suppressed the S_{intra} contribution that cannot be fitted with a monodisperse PY function. We think that it is related to the size of the aggregates, the number of particles in interaction, which is here too low ($N_{agg} \sim 10$) in comparison to the system with grafted particles ($N_{agg} \sim 100$) to give a significant contribution to the scattering signal. The repulsion peak disappears and is replaced by a smooth oscillation which is not reproduced by a PY function. This effect should be increased by the polydispersity of the particles that supposed to consider a more complex development than the simple product between the form and the structure factor. The analytical function is then reduced to:

$$I(Q) = \Delta\rho^2 V \phi P_{agg}(Q) S_{interagg}(Q) \quad 1.6$$

The scattering curves can be well described by Equation 1.6 from which we can extract the following description. Whatever the polymer, the particles are organized as fractal aggregates at low particle concentration: $N_{agg}=8$, $D_f=1.6$, $R_{agg}=216\text{\AA}$, $\kappa=0.16$ for PS and $N_{agg}=6$, $D_f=1.7$, $R_{agg}=172\text{\AA}$, $\kappa=0.25$ for PMMA. The primary aggregates are thus smaller and denser in the PMMA meaning the existence of specific polymer-particle interactions. When increasing the concentration, the aggregates size and density are progressively lowering to form a continuous 3D network characterized by a nice repulsion peak whose characteristic mesh size can be well reproduce by the PY prediction. The transition between isolated primary aggregates and a connected network is confirmed in the real space by TEM pictures for both polymers. We can also check that we do not observe any additional structure at larger scales up to the micron. From our quantitative analysis, we can follow the evolution of the effective volume fraction of the interacting objects (Figure 1.14a) which is increased typically from 2 to 20% v/v while the interacting distance d_0 is decreased from ~ 100 to ~ 50 nm. The corresponding Q^* (Figure 1.14b) scales as $\phi^{0.8}$ according to a percolation process⁴³. The transition between the two regimes, illustrated by the apparition of the interactions, for PS is found around a silica volume fraction of 8% v/v and slightly shifted to larger values for PMMA (10% v/v) in agreement with the smaller sizes of the primary aggregates.

⁶¹ Jouault, N.; Dalmas, F.; Boué, F.; Jestin, J. *Polymer* **2012**, 53 (3), 761-775.

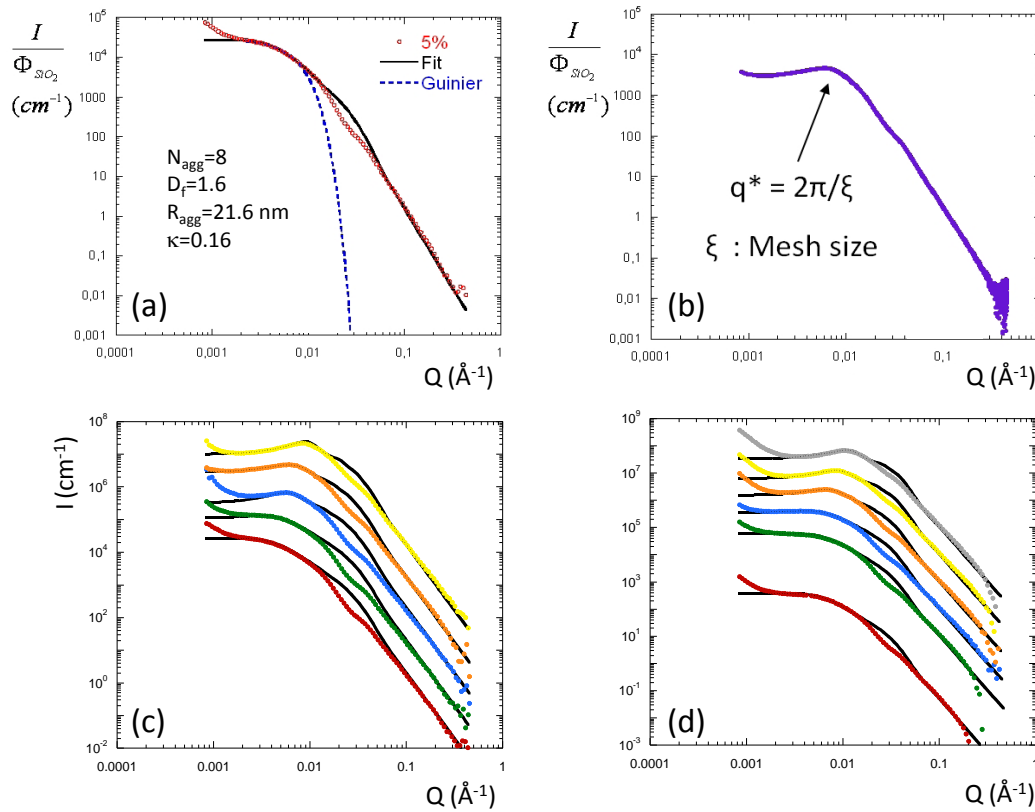


Figure 1.12: (a) SAXS curves of PS nanocomposite filled with 5% v/v of Nissan silica particle and modeling of the primary aggregate form factor. (b) SAXS curves of PS nanocomposite filled with 20% v/v of Nissan silica particle illustrating the network mesh size. (c) Evolution of the scattering curves of PS nanocomposites filled with silica Nissan particles at 5 (red), 10 (green), 15 (blue), 20 (orange) and 30 (yellow) % v/v. The curves have been shifted for clarity (d) Scattering curves of PMMA nanocomposites filled with silica Nissan particles at 5 (red), 10 (green), 15 (blue), 20 (orange), 30 (yellow), 35 (gray) % v/v. The curves have been shifted for clarity. The full black lines are the results of the fit using the analytical model described in the text.

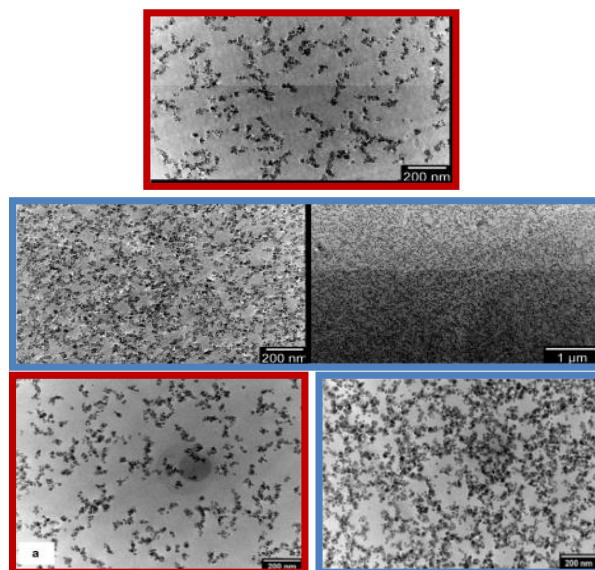


Figure 1.13: TEM pictures for 5 (red) and 15 (blue) % v/v for Nissan-PS (top) and for Nissan-PMMA (bottom) at low (200nm) and large magnification (1μm).

The mesh size of the connected network is always larger than the size of the primary aggregates suggesting an “opened” network. The same silica Nissan particle can be grafted with PS chains according to the grafting method described in section 1.1.2. The grafting modifies the morphology of the aggregates⁴¹ that become more ramified ($D_f=1.2$, $N_{agg}=7$, $\kappa=0.05$) but do not modified strongly the evolution of the particle dispersion with the particle concentration: we observed a similar transition between individual aggregates and a connected 3D network when increasing the particle concentration.

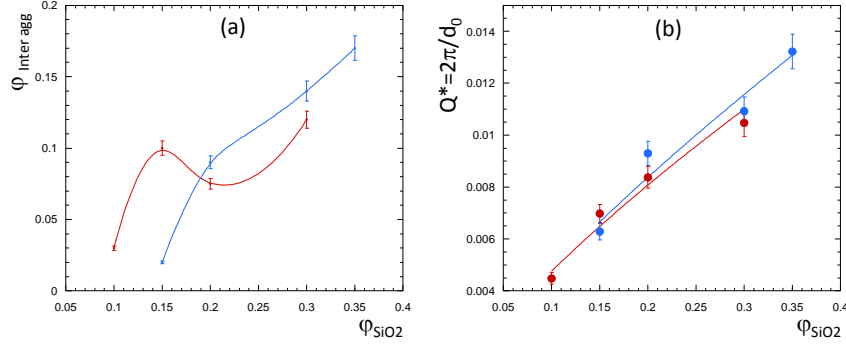


Figure 1.14: (a) Inter-aggregate effective volume fraction deduced from the PY calculation as a function of the silica volume fraction for the PS (red) and the PMMA (blue) system. (b) Power law variation of the Q^* as function of the particle volume fraction $Q^* \sim \varphi^{0.8}$.

1.2.5 Two levels of aggregation

1.2.5.1 Polymer matrix

We move to another kind of silica particles (SiO_2 Ludox LS and TM) and maghemite particles ($\gamma-Fe_2O_3$) to illustrate another example of filler dispersion in polymer matrix (PS and PMMA). Despite of the variety of the samples and of the specific interactions, one can find a unified description of the particle arrangements. The shapes of the scattering curves are different from the previous example as well as their evolution with the particle volume fraction. As shown on SAXS pattern on Figure 1.15a, the peak in the low Q domain, well visible on the previous example, is now matched by an additional low Q scattering intensity. The additional scattering intensity is characteristic of a second level of aggregation. To illustrate this level, we proceed by modeling first the form factor of the primary aggregates (Equation 1.3) that can be accessible on diluted samples as described on Figure 1.15a for the maghemite-PS system. As the form factor of the primary aggregates remains unchanged with the particle concentration, we can divide the total scattering intensity by this modeling to extract the product of the different structure factors:

$$S(Q)S_{inter\,agg}(Q)S_{intra\,agg}(Q) \approx \frac{I(Q)}{P_{agg}(Q)}. \quad 1.7$$

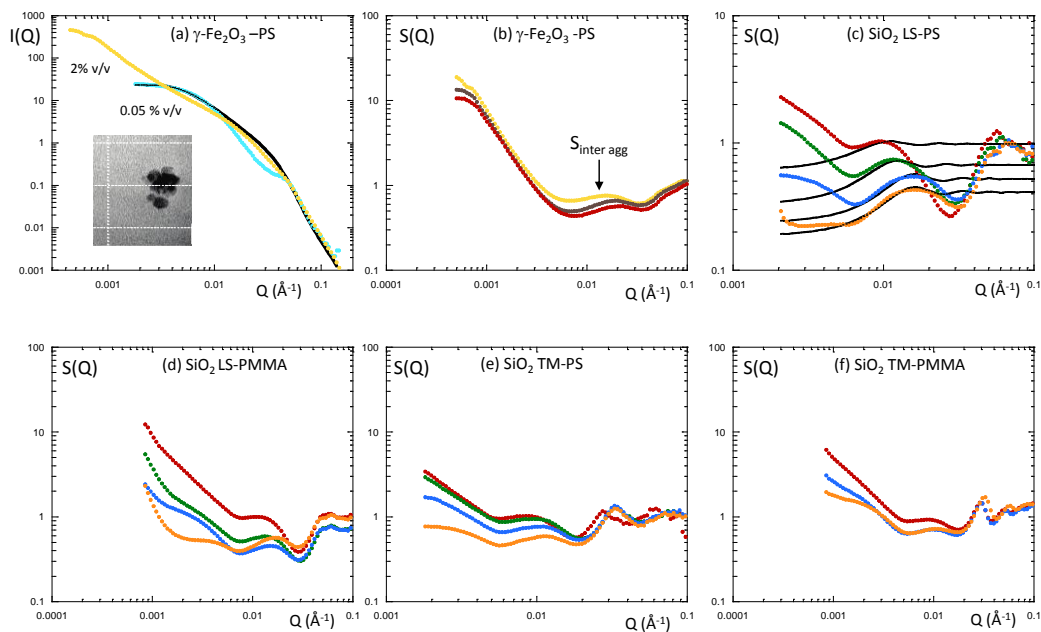


Figure 1.15: (a) SAXS intensity for nanocomposites maghemite particles in PS at a particle volume fraction of 0.05% (light blue) and 2% v/v (yellow). The full black line is the result of the calculation of the form factor of primary aggregates (illustrated by the TEM inset). $S(Q)$ resulting from the division of the scattering intensity by the calculated full line illustrating the secondary aggregation level for (b) maghemite-PS (2 yellow, 3 brown and 5 red % v/v), (c) Silica LS-PS, (d) Silica LS-PMMA, black lines are the PY prediction, (e) Silica TM-PS and (f) Silica TM-PMMA nanocomposites (5 red, 10 green, 15 blue and 20 orange % v/v). The intermediate oscillation visible in all cases is the inter-aggregate structure factor S_{inter} .

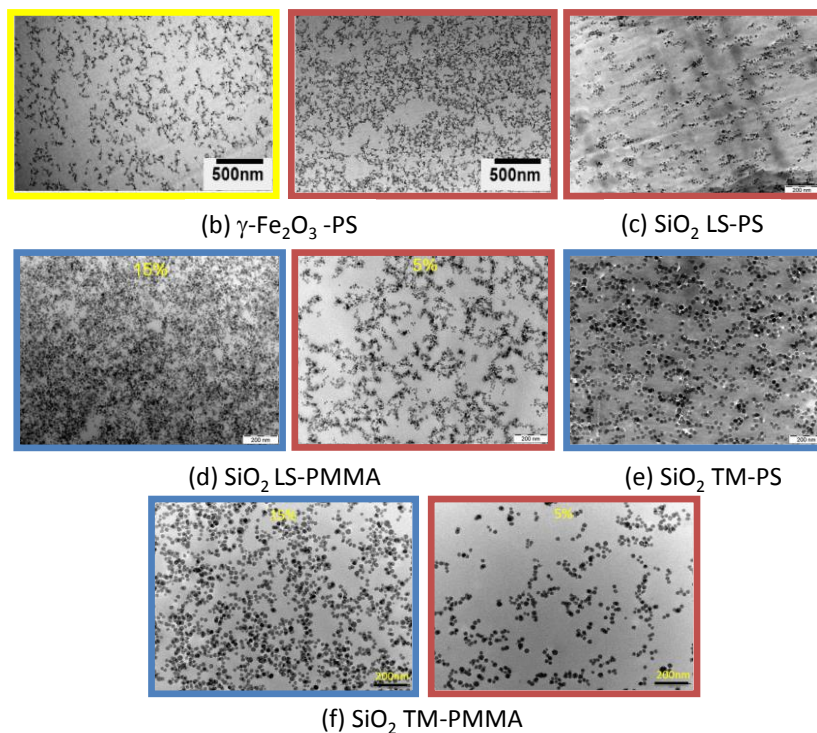


Figure 1.16: TEM picture for maghemite-PS at 2 and 5% v/v (b), LS-PS at 5% v/v (c), LS-PMMA at 15 and 5% v/v (d), TM-PS at 5% v/v, TM-PMMA at 15 and 5% v/v.

S_{inter} and S_{intra} are the already mentioned intra and inter-aggregate structure factors while $S(Q)$ represents the structure of the low Q secondary aggregation level.

The Figure 1.15 summarizes the evolution of the resulting structure factors as a function of the particle concentration determined for maghemite, Ludox LS and TM in PS and PMMA matrix⁶¹. The Figure 1.16 shows the corresponding TEM pictures. When primary aggregates are small, the interactions between the particles (S_{intra}) inside the aggregates are difficult to model with the aggregate form factor. This contribution induces a strong correlation hole in the $S(Q)$ around $3-4 \cdot 10^{-2} \text{ \AA}^{-1}$. More interesting is the possibility to highlight the inter-aggregate structure factor S_{inter} in the intermediate Q range, typically around 0.01 \AA^{-1} . The corresponding peak is indeed partially matched in the $I(Q)$ representation by the low Q scattering increased coming from the secondary structure. The S_{inter} aggregate behaves identically for all examples: it moves towards the high Q values when enhancing the concentration meaning that primary aggregates move gradually close to each other inside the secondary structure. A structural percolation occurs when the effective volume fraction of the primary aggregates inside the equivalent volume of the secondary aggregates is superior to 100%. For example, such a calculation gives a threshold around 2% v/v for the maghemite-PS system⁶². We give an example of the modeling of the S_{inter} using the PY function (Figure 1.15c) to extract the quantitative variation of the inter-aggregate distance d_0 . At the final state, the objects are more or less in close contact as function of the systems. This can be evaluated by comparing the aggregate size (R_{agg}) with the inter-aggregate distance (d_0). For the TM system, the ratio ($2 \cdot R_{\text{agg}}/d_0$) is always inferior to 1 (below the close contact) while for all other examples the ratio is superior to 1 (at or slightly above the close contact) suggesting the objects can be slightly interpenetrated. This result shows that the different primary networks can present various strengths depending directly of the inter-aggregates interactions.

The second interesting feature is the behavior of the low Q signal characteristic of the secondary aggregation level. It behaves identically for all cases: a signal close to a plateau at low concentration, an object of finite large size, whose intensity decreases when increasing the concentration meaning a reduction of the mean secondary aggregate size. The extrapolation of the structure factor when Q tends to zero is a direct determination of the secondary aggregation number (the number of primary aggregates inside the secondary structure) which is varying from 20 to 2-3. This value progressively tends to 1 suggesting that the secondary structure is progressively transformed to a continuous network. Such large structure is difficult to identify on the TEM pictures due to the close contact of the primary aggregates.

Contrary to Nissan silica particles, the primary aggregates are denser in PS than in PMMA meaning that the specific polymer particles interactions are also dependent of the nature of the silica. This might be also the case for the maghemite particle whose behavior is shifted to lower particles volume fractions.

⁶² Robbes, A.-S.; Jestin, J.; Meneau, F.; Dalmas, F.; Sandre, O.; Perez, J.; Boué, F.; Cousin, F. *Macromolecules* **2010**, 43 (13), 5785-5796.

1.2.5.2 Elastomer matrix

We have adapted the sample processing by solvent casting to an elastomer matrix, the styrene-butadiene-rubber (SBR) coming from Michelin. The idea is to compare this model system (model particles Ludox LS, controlled solvent casting process) with the “real” systems made with industrial silica and prepared according to the manufacturing process by mechanical mixing. One of the pertinent question is to elucidate the influence of additive agents (nature, quantity) on the final dispersion in the matrix. These additives are a covering agent octytriethoxysilane (Octeo) and a coupling agent TESPT (Si69) which are able to graft to the surface of the filler. In addition, the coupling agent is able to make covalent bonds between filler and SBR chains. As for the previous example, we observe two levels of particles aggregation inside the SBR matrix. We have treated the scattering curves according to the same process by modeling the primary aggregates form factor on the diluted sample and then extracted the inter-aggregate structure factor and the secondary aggregate scattering (Figures 1.17a, b for one quantity of Octeo O_1 and Si69 Si_1 and c for two quantities of Octeo O_2). The precise mechanisms of the additives regarding the filler dispersion as well as the density of adsorbed agent (bound rubber) and their conformation at the filler surface are generally quite difficult to access⁶³. However, one can identify here some characteristics. Contrary to previous published results that does not see any influence of the additive on the filler dispersion⁶⁴, we observe that the primary aggregates are smaller and denser with Si69 than with Octeo suggesting a well-defined dispersion with Si69. To explain this, we suggest a DLCA process as already mentioned for silica particle which is limited for Si69 by the covalent bounding with the chains of the matrix that reduces the diffusion coefficient and thus decreases the probability of particle-particle encounter.

As illustrated by the black arrow, the inter-aggregate interactions vary differently as function of the additive with the filler concentration. For O_1 , the objects remain below the close contact and seem to move away from each other for O_2 . Conversely, with Si_1 the aggregates move toward to each other to be finally at the close contact. This suggests that the covering agent promotes repulsions between aggregates while the coupling agent supports attractions. The secondary structure also varies differently. It decreases with the concentration the O_1 series and increases for the series Si_1 and O_2 . This means an increase of the secondary aggregate size Si_1 maybe due to bounding with matrix, and finite size objects for the series O_2 . The formation of secondary aggregate of finite size can be the result of the particle surface saturation by the Octeo agent that screens overlap between the objects.

⁶³ Cassagnau, P. *Polymer* **2008** 49, 2183-2196.

⁶⁴ Ramier, J.; Gauthier, C.; Chazeau, L.; Stelandre, L.; Guy, L. *J. Polym. Sci., Part B: Polym. Phys.* **2007**, 45 (3), 286–298.

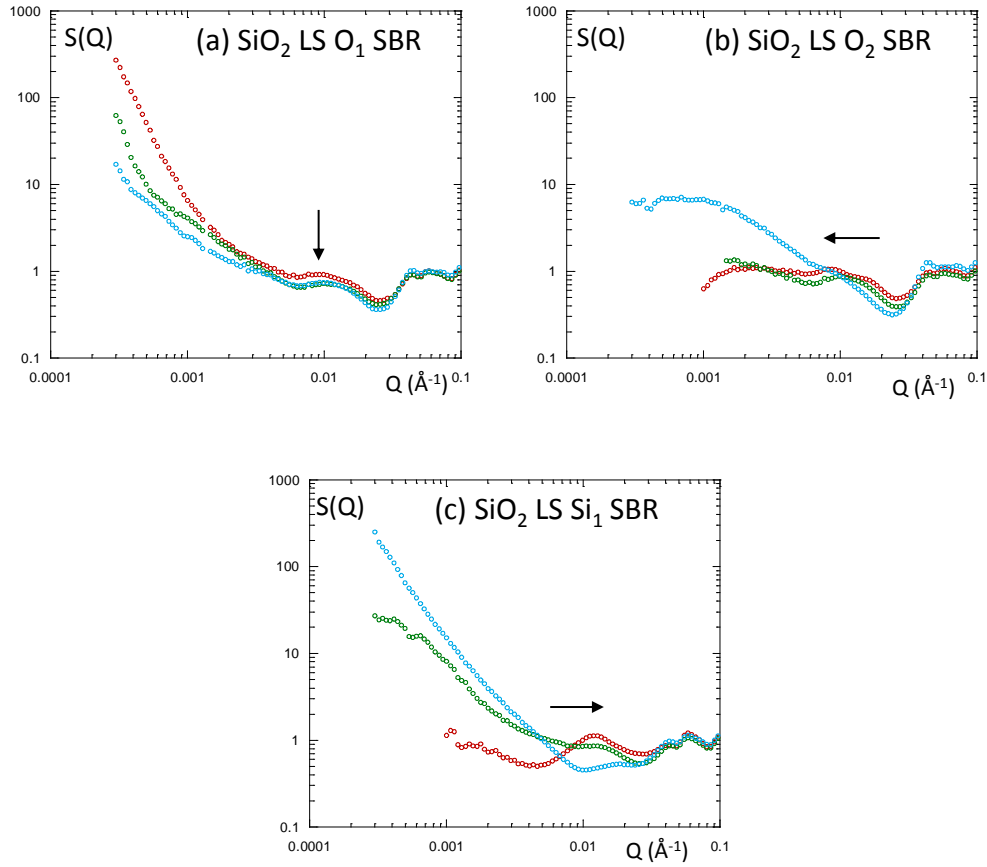


Figure 1.17: Structure factor illustrating the inter-aggregate interactions (pointed by the black arrow) and the secondary aggregates for (a) silica LS-O₁-SBR, (b) silica LS-O₂-SBR and (c) silica LS-Si₁-SBR for 4.7% (red), 9.1% (green) and 16.1% v/v (blue) of particles.

1.2.6 Multi-scale aggregation: toward the “real” system

To conclude the presentation of the different examples of filler dispersion, we move to more complex systems which are then closer to “real” industrial systems. Silica-SBR nanocomposites are formulated by stepwise introduction and mixing of SBR chains with silica powder 160 MP (figure 1d) in an internal mixer (Haake). Compared to the complex samples usually studied in the literature, the system is thus designed to be a simplified industrial nanocomposite, i.e., ingredients have been limited to the strict minimum, conserving namely aggregated multi-scale silica as filler particles, SBR-chains, and a mixing process, all related to tire applications. The hierarchical organization starts with the silica powder, not colloidal, that can be modeled with sub-unit particles of 1nm densely structured in close contact to form a “native-like” bead of radius 8.5 nm. In a second step, these beads can be organized themselves according to fractal primary aggregates defined as previously with an aggregation number and an apparent fractal dimension D_f . The interactions of the native-like beads inside the primary aggregates as well as the interactions between the primary aggregates can be described with PY functions as also recently discussed on similar systems¹⁷. The primary aggregates form an additional structure, large agglomerates or fractal networks that finalize the hierarchical organization up to the micrometer scale. The SAXS

scattering curves of such samples are reported on Figure 1.18a for systems with covering agents Octeo (O_1) and Figure 1.18b for systems with coupling agents Si69 (Si_1) as function of the filler content. Additional TEM pictures (Figure 1.19) are also reported at two magnifications, 100 nm to probe the local structure and $1\mu\text{m}$ to probe the larger structure of the samples. We use the analytical function described in equation 1.2 to model the scattering curves (black lines). Despite of the large level of polydispersity in the system, the modeling curves reproduce very nicely the experimental data, especially for the S_{intra} contribution that works here because aggregation number are larger enough (~ 100) as for the compact aggregates obtained with grafted particles. Contrary to previous examples, both structure factors (intra and inter aggregates) and form factor are evaluating with the filler volume fraction. Concerning the primary aggregates, we find in “real” systems the same tendency that the one observed in previous model systems: the aggregates are smaller and denser with the Si69 than with Octeo agent. This suggests that the additive act at the same length scale than for the colloidal particles, i.e. the size of the primary particle ($\sim 10\text{nm}$), independently of the sample processing and according to the same DLCA aggregation process.

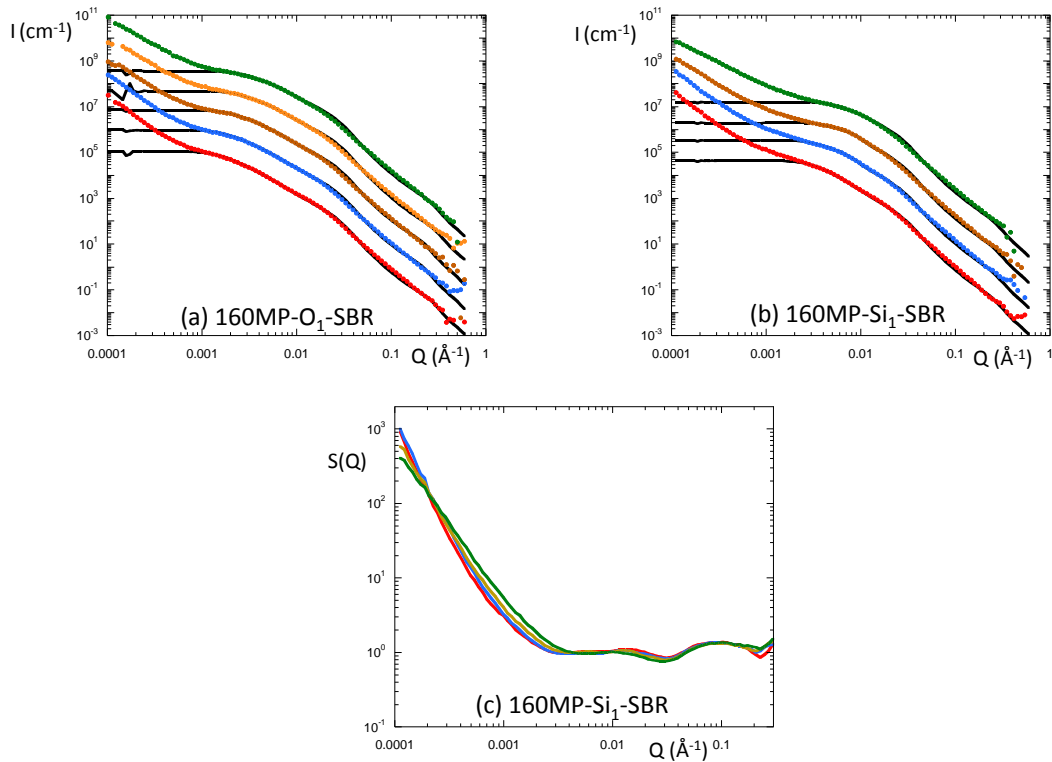


Figure 1.18: Evolution of the scattering curves of SBR nanocomposites filled with silica 160MP particles at 8.4 (red), 12 (blue), 15 (brown), 18 (orange) and 21 (green) % v/v for the series with (a) Octeo and (b) Si69 agent. The curves have been shifted for clarity. The black lines are adjustments with the analytical model described in the text. (c) Structure factor for the Si69 series obtained by the division of the total intensity with the analytical modeling curve.

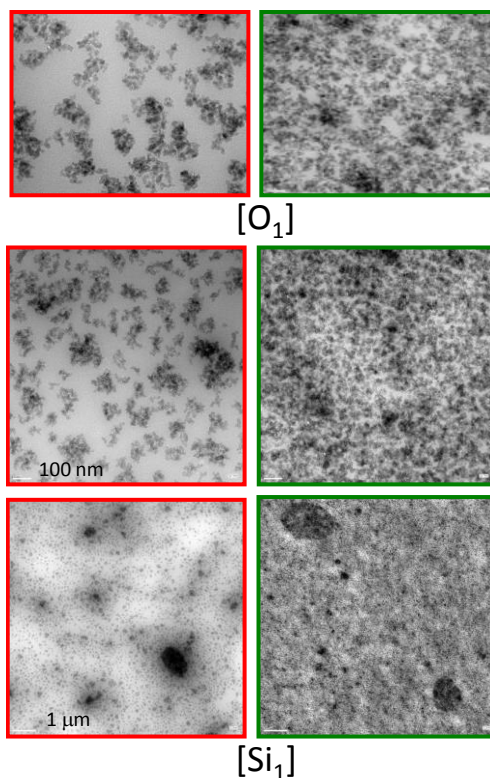


Figure 1.19: TEM picture for 8.4 (red) and 21 (green) % v/v at low magnification for the Octeo series (top) and for the Si69 series (bottom) at two magnifications (100 nm) and (1 μ m).

According to the scheme observed for model systems, the primary aggregates are in close contact with the coupling agent and well below the close contact with the covering one suggesting that the Octeo agent promotes repulsions between the objects. An interesting difference is that the mean radius of the aggregates is decreasing when increasing the particle content (aggregation number and apparent fractal dimension are reducing with a resulting constant compactness of the objects). However, this result already observed on similar systems⁶⁵ is rather not surprising regarding the way of sample preparation that applies strong rheological constraints depending on the filler volume fraction. On the Figure 1.15c, we can see the structure factor deduced from the scattering modeling (equation 1.7) as well as the TEM pictures at large magnification. This confirms the presence of a secondary aggregation level that could correspond here to large agglomerates whose structure seems to change when increasing the filler volume fraction. The low Q intensity is decreased as observed for model systems while the slope corresponding to the apparent fractal dimension of the objects also decreases suggesting that secondary objects become smaller and more ramified.

⁶⁵ Schneider, G. J.; Vollnhals, V.; Brandt, K.; S. V. Roth, S. V.; Göritz, D. *J. Chem. Phys.* **2010**, 133, 094902.

1.2 Conclusions

The filler organization of the particles inside the polymer matrix can be tuned by different triggers: grafting, external magnetic field, sample processing, additives, nature of particles and nature of the matrix, and gives a very broad and interesting range of various morphologies: individual objects, 1D aligned chains, 3D network, network of hierarchical aggregates. This panel leads to many situations from the well-defined model “fundamental” case to a multi-scale “real” example close to the industrial conception. With a combination of simple functions (finite size fractal aggregate of spherical beads and Percus-Yevick function), we can quantitatively model the evolution of the scattering with the particle concentration while dissociating the variations of the aggregates form factor induced by the modification of the morphologies (fractal dimension, aggregation number and compactness) to the ones of the aggregates structure factor coming from the interactions between the objects (number of objects in interactions and distance of correlations). If the two first situations (grafted particle and magnetic filler) can be described according to theoretical concepts (mixing entropy and dipolar interactions), the following examples reveal more complex results driven by diffusion limited aggregation processes which can be mediated either by the viscosity of the medium or by the covalent bound with the matrix. We can distinguish between 3D connected networks from network made of multi-scale objects (two or more) that can be organized at larger length scales according to secondary aggregates processes. We get networks of various apparent strengths whose structure is mainly driven by the inter-aggregate interactions, more or less in close contact. The contribution of the primary particle interactions is more difficult to evaluate because it clearly depends on the number of involved particles. This perfect knowledge of the aggregates morphologies and interactions constitutes a set of quantitative database that will be useful to interpret the viscoelastic behaviors of the materials.

CHAPTER 2

MECHANICAL AND RHEOLOGICAL BEHAVIORS OF NANOCOMPOSITES

The elastomeric or polymeric based materials present outstanding rheological and mechanical enhanced properties after addition of filler. This motivates to understand precisely the correlations between the filler structure and the macroscopic answer of the material. As we have seen on the previous chapter, as function of the filler/matrix specificities, the filler structure can present more or less complex hierarchical organizations covering a broad range of characteristic length scale from the size of the native particle filler to the one of large agglomerates or fractal networks. When the rheological and mechanical properties are experimentally investigated, the significant length scale of the system will depend on several factors like the rate of deformation, the frequency or the temperature. Most of the theoretical models that consider the reinforcement in filled nanocomposites calculate the dependence with the filler volume fraction. The effective values of filler volume fractions, and the typical associated length scales, are then difficult to estimate in presence of multi-scale aggregation and/or percolation processes. In addition, this effective value can also be influenced by the specific interactions between the filler components, primary particles, primary aggregates or secondary structures. As we will see in more details, the understanding of the correlations between reinforcement factors and filler structure is crucial to progress in the description of the whole processes involved, especially the role of the polymer chains.

We have investigated the viscoelastic properties of the different systems presented on chapter 1 by combination of different techniques: at low deformation by small amplitude (linear regime) oscillatory shear experiments and by dynamical mechanical analysis as a function of the temperature and at low and large deformation by uniaxial stretching methods. Nonlinear effects in nanocomposites (Payne⁶⁶ and Mullins⁶⁷ effects) have attracted considerable attention in the past. Here, we will focus on the linear regime considering only the Young modulus of the material given at low deformation and the reinforcement factor given by the ratio between filled and unfilled modulus. We have compared the evolution of the reinforcement factor with both hydrodynamical and percolation models in which the effective particle volume fraction is calculated knowing the aggregate morphology determined from our previous scattering analysis. We extract for each system a relative modulus of reinforcement which can be discussed as function of the relaxation terminal time (above and below τ_{ter}), of the aggregates morphologies and of the specific filler network organizations (individual dispersion, compacts aggregates, 1D and 3D and multi-level of aggregations) as well as possible “glassy layer” and “enhanced entanglement” effects.

⁶⁶ Payne, A. R.; Whitaker, R. E. *Rubber Chem. Technol.* **1971**, 44, 440–478.

⁶⁷ Bueche, F. *J. Appl. Polym. Sci.* **1960**, 4 (10), 107–114.

2.1 The effective volume contribution

We investigated first the mechanical response of the composites for both dispersion states described previously with grafted silica on section 1.2.1 and 1.2.2: individual particle dispersion, and large and compact aggregates. We used oscillatory shear measurements at small deformation (amplitude 0.5%) with a plate-plate rheometer ARES. The evolution of the elastic and loss moduli G' and G'' was determined as a function of the filler content (% v/v) at different temperatures (from 160°C to 120°C) and the Time-Temperature Superposition (TTS) is applied using WLF law at a reference temperature of 143°C with standard parameters. The results are reported on Figures 2.1a for the individual dispersion and 2.1b for the aggregates. The two matrices (98 000 and of 140 000 g/mol) used as references do not show significant differences as a function of the frequency, indicating that their contribution are similar for the two kinds of dispersion and will not influence the comparison of the nanocomposites.

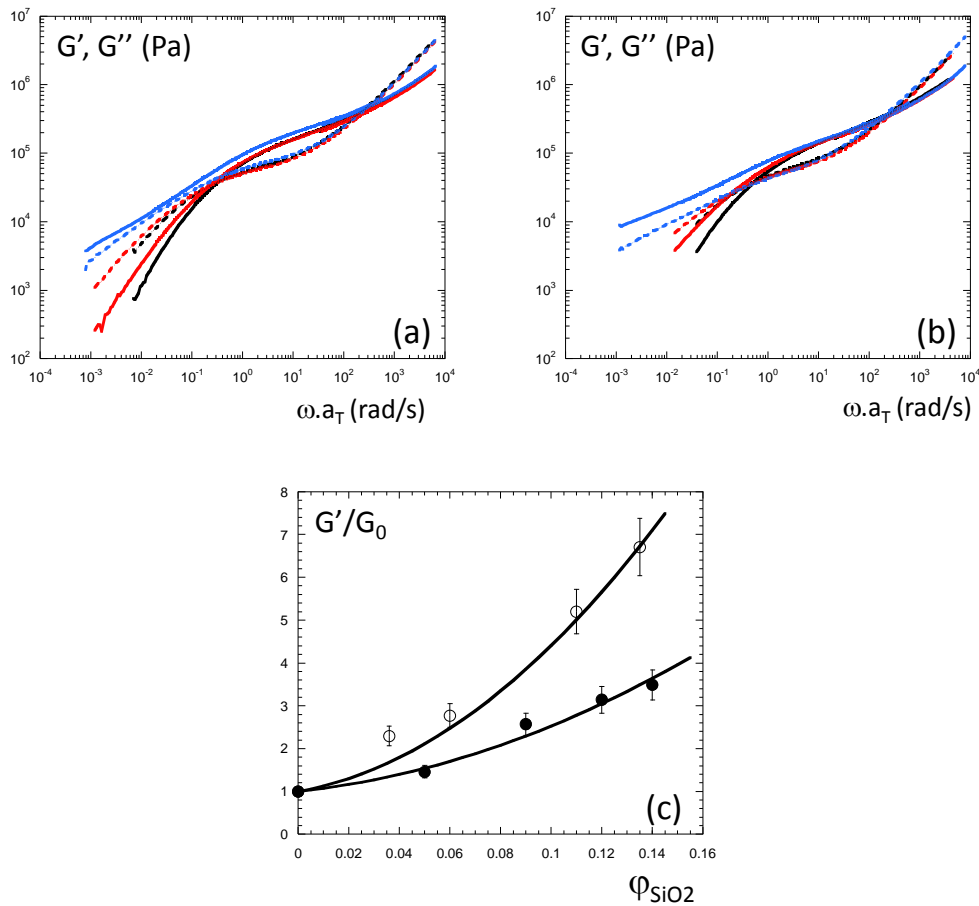


Figure 2.1: Elastic shear modulus as a function of pulsation for different volume fractions (% v/v) of grafted particles in the composite for two dispersion state of the particles inside the polymer matrix: (a) individual dispersion (b) aggregates. (c) Modulus ratio (at a pulsation 0.04 rad/s) as function of the silica volume fraction for individual particles (full circles) and aggregates (open circles). The full line is the modeling with equation 2.1.

Whatever the silica content and the dispersion state, the curves (G' and G'') superimpose perfectly in the whole high frequencies range (above 0.1 rad/s), namely the elastic domain, and show a typical variation as $\omega^{1/2}$. This means that the short characteristic times (the Rouse modes) of the polymer matrix are not affected by the fillers. We don't see any changes of the intermediate rubbery plateau level with introduction of filler meaning that the apparent entanglement mass M_e is here not influenced (for PS $M_e=18000$ g/mol corresponds to a plateau $G_N^0 \sim 1.5 \cdot 10^5$ Pa).

In the lower frequencies domain (between 10^{-3} and 0.1 rad/s), the flow domain, the pure matrix shows classical variation of $G' \sim \omega^2$ and $G'' \sim \omega^1$ while intersection between G' and G'' allows the determination of the relaxation terminal time of the polymer, here equal to $\tau_{ter}=18$ s for PS at 0.35 rad/s. With introduction of filler we observe especially on the G' an increase of the modulus for times superior to τ_{ter} with a significant reduction of the exponent of the power law dependence of the modulus with the frequency $G' \sim \omega^{1/3}$. This can be associated with the apparition of a longer time in the relaxation modes of the polymer chains, becoming longer with increased filler content. Such a long-time effect at low frequencies can be seen as a process analogous to a liquid-solid transition inside the materials, whose origin can be interpreted in different ways. To illustrate the difference between the two dispersions, we reported the modulus ratio $G'_{(filled)}/G'_{0 (unfilled)}$ as function of the particle volume fraction for a frequency below the terminal time (~ 0.04 rad/s) on Figure 2.1c. The difference between the two dispersions appears here clearly with larger amplitude for the aggregate case than for the dispersed one. Thanks to the previous filler structure analysis, we know that we have no direct filler percolation in both systems. We thus can compare the modulus ratio evolution with classical hydrodynamical models like the Guth and Gold prediction⁶⁸ available for high particle content:

$$G = G_0(1 + 2.5\phi + 14\phi^2) \quad 2.1$$

With the introduction of the *effective* filler volume fraction:

$$\phi = \phi_{eff} = \frac{\alpha \cdot \phi_{part}}{\kappa} \quad 2.2$$

ϕ_{part} is the experimental particle volume fraction and κ is the compactness of the considered objects deduced from the scattering model: $\kappa=1$ for individual particles and $\kappa=0.4$ for the compact aggregates. The single fitting parameter is the pre-factor α which can be related to the effective size of the particle including the layer of the grafted brushes according to:

$$\alpha = \frac{(R_{part} + e_{eff})^3}{R_{part}^3} \quad 2.3$$

where e_{eff} is the effective layer thickness. This approach gives a good agreement between the fitting function and the experimental data as illustrated by the full black line on Figure 2.1c. We find respectively effective thickness layers $e_{eff}=5$ nm and 2.5 nm for the individual and for the aggregates cases. These values are very consistent with the real thickness grafted layer determined by SANS and SAXS on the same systems which are respectively $e=6$ nm and 3nm for dispersed and for aggregated case (see chapter 3 for details) supporting strongly the contribution of an additional

⁶⁸ Guth, O.; Gold, E. *Phys. Rev.* **1938**, 53:322.

fraction of polymer of modified mobility to reinforcement according to a long range effect. The physical state of the chain inside this effective layer is still under debate: one idea is to consider the chain in a “glassy-like” state^{69,70}. However, the extension of the effective layer is depending of the frequency and becomes larger than the real layer thickness when looking at smaller frequency values ($e_{eff}=11$ nm at 10^{-3} rad/s). This increased extension when decreasing frequency and thus increasing the temperature is rather contradictory with the glassy model that predicts a decrease of the thickness when going far away from T_g . This thus suggests an additional contribution. The formation of indirect filler network through the grafted layers has been also proposed to contribute to reinforcement⁷¹. However, this idea is not in agreement with the fact that the inter-aggregate distances increase when the particle concentration increases. Alternatively, we can suggest that this effect is related to the local inter-particle interactions, more effective for compact aggregates than for individual dispersion. This is then still difficult to conclude but our approach and especially the perfect knowledge of the aggregate morphology shows here the importance of the filler structure to compare and understand the rheological behavior of various dispersion states.

2.2 Anisotropic reinforcement

We analyze the mechanical behavior of nanocomposites for which the filler, magnetic nanoparticles, can be oriented inside the matrix by applying an external magnetic field during the solvent casting as described in section 1.2.3. Mechanical tests were performed with a homemade uniaxial-elongation machine. They were stretched up in a controlled constant rate deformation ($\dot{\gamma}=0.005$ s⁻¹) at a temperature $T_{str} = T_g + 15^\circ\text{C}$, where T_g is the glass transition temperature of a given sample. The tuning of the anisotropy of the filler structure provides a spectacular effect on mechanical behaviors. Figure 2.2a and b presents the reinforcement factor σ/σ_{matrix} deduced from the strain stress isotherms of the nanocomposite films as a function of the particle content, stretched in the direction either parallel to the applied magnetic field or perpendicular to it. It is compared to the isotropic case and to the pure PS matrix. The reinforcement is important and strongly anisotropic. In the isotropic case, σ/σ_{matrix} shows a clear maximum around $\lambda = 1.2$ that becomes very marked at low λ when stretched along the parallel direction. The system behaves as a connected network in the direction of the alignment of the nanoparticle chains. This situation stands for the formation of a 1-D connected network, where the rupture points are reduced compared to the classical 3-D filler network.

⁶⁹ Tsagaropoulos, G.; Eisenberg, A. *Macromolecules* **1995**, 18, 60676077.

⁷⁰ Berriot, J.; Montes, H.; Lequeux, F.; Long, D.; Sotta, P. *Europhys.Lett.* **2003**, 64 (1), 50–56.

⁷¹ Akcora, P. ; Kumar, S. K. ; Moll, J. ; Lewis, S. ; Schadler, L. S. ; Li, Y. ; Benicewicz, B. C. ; Sandy, A. ; Narayanan, S. ; Ilavsky, J. ; Thiyagarajan, P. ; Colby, R. H. ; Douglas, J.F. *Macromolecules* **2010**, 43, 1003–1010.

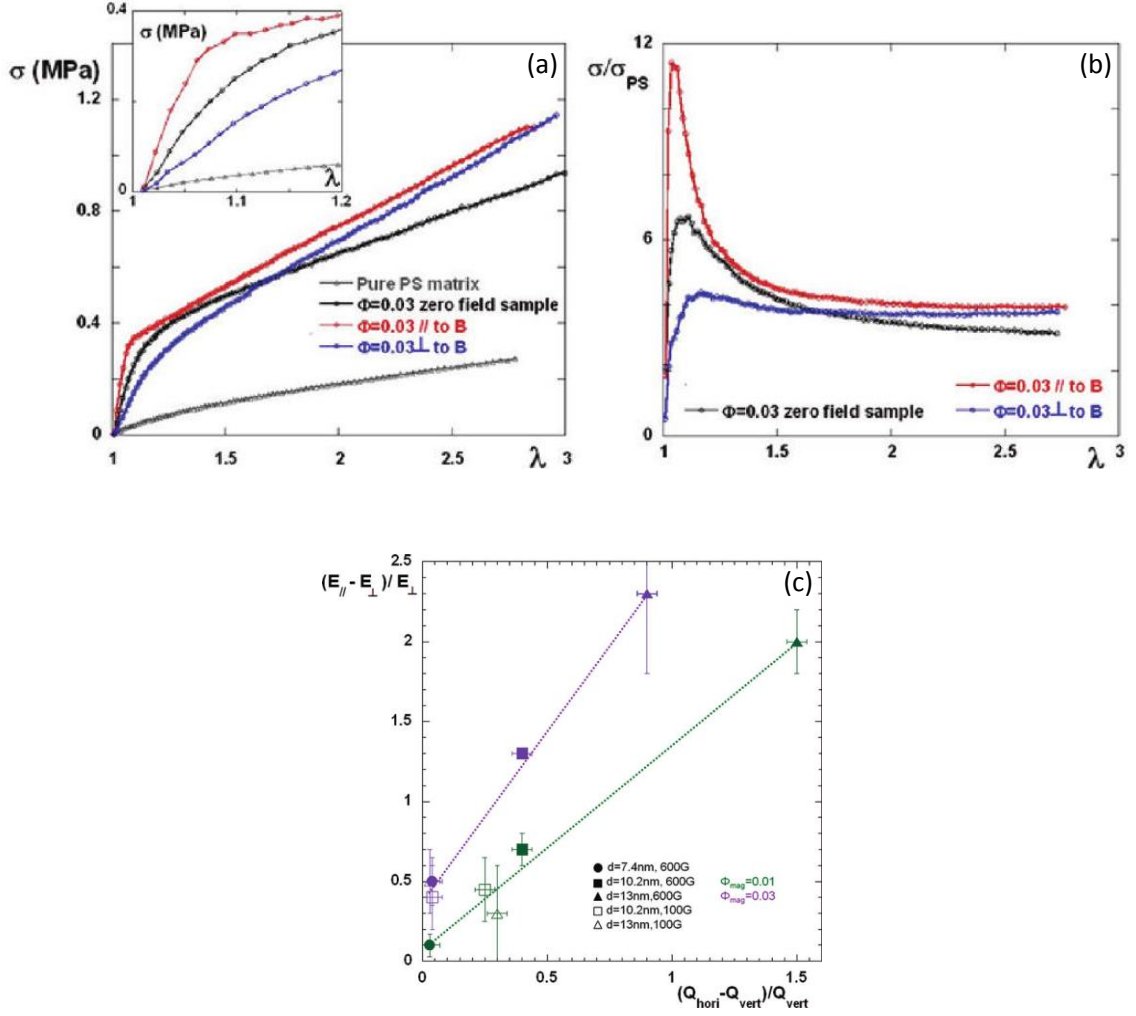


Figure 2.2: Real stress (a) and reinforcement factor $\sigma/\sigma_{\text{matrix}}$ (b) as a function of the elongation λ of nanocomposite films, synthesized with maghemite nanoparticles with and without an applied magnetic field of 600 G at a particle volume fraction of 3%. Black curves: nanocomposites synthesized without a magnetic field. Red curves: nanocomposites stretched parallel to the applied magnetic field. Blue curves: nanocomposites stretched in the direction perpendicular to the magnetic field. Gray curves: pure PS matrix. Inset: zoom on the linear part of the real stress as a function of the elongation ratio λ , for a better insight. The experiments have been performed at $T_g + 15^\circ\text{C}$. (c) Quantitative correlation of the anisotropy of the macroscopic mechanical properties with the anisotropy of the local structure of the fillers for all samples at particle volume fraction of 1 and 3% casted under a magnetic field.

We correlate in Figure 2.2c the anisotropy of the macroscopic mechanical properties with the anisotropy of the local structure of the fillers (Figure 1.9), for all of the samples synthesized under a magnetic field. To quantify the anisotropy of the mechanical properties of a given sample, we extract the Young modulus in the parallel direction and in the perpendicular direction from the linear regime of the strain stress isotherms to calculate $(E_{//} - E_{\perp})/E_{\perp}$. A value equals to zero corresponds to isotropic mechanical properties. The determination of the structural anisotropy is more difficult because the anisotropy of the scattering curves is Q -dependent. We thus considered $Q = \int I(Q) Q^2 dQ = 2\pi^2 \phi(1-\phi) \Delta \rho^2$ which is the pendent along one direction of the scattering invariant usually averaged over three dimensions. The overall anisotropy of the structure can thus be estimated through $(Q_{\text{horiz}} - Q_{\text{vert}})/(Q_{\text{vert}})$ and can be related to the effective volume fractions, i.e., to volume fractions of orientated aggregates, in both directions as $\sim (\phi_{\text{mag} //} - \phi_{\text{mag} \perp}) / (\phi_{\text{mag} \perp})$. $(Q_{\text{horiz}} - Q_{\text{vert}})/(Q_{\text{vert}})$ increases either with the nanoparticles size or with the applied magnetic field. It

illustrates the fact that the structural anisotropy is mainly governed by the dipolar interactions between the nanoparticles. Remarkably, for a given particle volume fraction, all the data from the different samples superimpose onto the same straight curve. As the Young modulus varies, to a first order, proportionally with the volume fraction, the tuning of the structural local anisotropy is directly converted into a macroscopic anisotropy of the mechanical properties. The slope of the curve increases with an increase of the particle volume fraction. This arises from the fact that transverse correlations between aligned chains of particles, which increase with the particle volume fraction, systematically correlate with stronger anisotropic reinforcement.

2.3 Filler percolation

2.3.1 The local filler structure contribution

We investigate now the situations for which the particles form a connected filler network according to a percolation process. Two main kinds of dispersions have been characterized previously: a 3D filler network made of small finite size primary aggregates and a connected network made of aggregates of different sizes (primary, secondary...). For the first network, the rheological and mechanical behaviors have been determined with a combination of oscillatory shear measurements (ARES), Dynamical Mechanical Analysis (DMA) as function of the temperature and uniaxial stretching experiments.

The shear oscillatory measurements results, reported on Figure 2.2a for the Nissan-PS system, present the same characteristics than for the grafted systems described previously with the appearance of a long time at low frequency when the filler content increased. We can notice a significant difference here which is related to a significant increase of the rubbery plateau level with the filler concentration related to elastic reinforcement. For high concentrations, we turned to DMA experiments performed at fixed frequency (5 Hz), with an amplitude deformation ratio of 0.1%. Using TTS, measurements between 143 and 200 °C correspond to a time range at 143 °C between 0.2 and 60 s. In Figure 2.2b, we show the evolution of the storage modulus E' for different volume fraction of Nissan silica in PS (from 0 to 20% v/v), as a function of temperature. For pure PS (without silica), at low temperature, i.e., for $T < T_{\alpha}$, the curve is typical of amorphous polymer with a high elastic modulus plateau of about 2.5 GPa. When T increases above T_{α} , a steep decrease of E' is observed, followed by a shoulder corresponding to the entanglement rubbery plateau, very narrow before to be cut at slightly larger temperature by a strong decrease corresponding to the terminal relaxation.

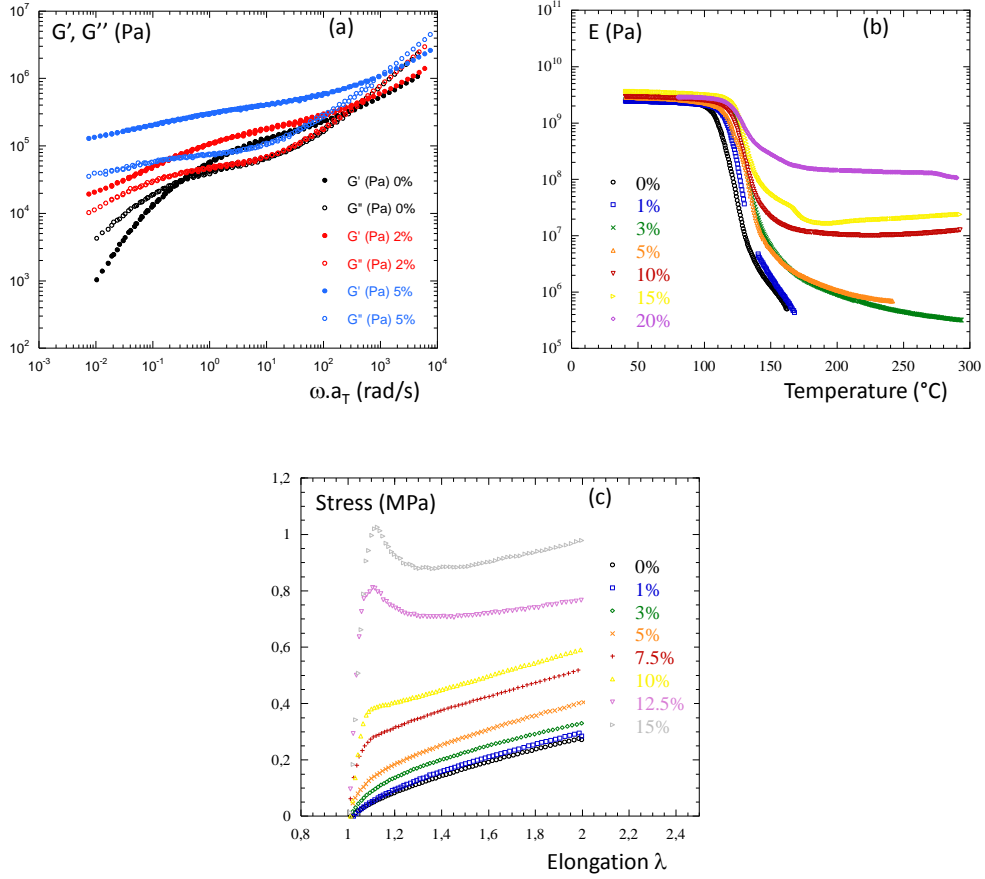


Figure 2.3: (a) Elastic shear modulus G' and G'' as a function of pulsation ω for different volume fractions of silica in the composite (0, 2, and 5% v/v). (b) DMA measurements of elastic modulus E' as a function of temperature for different volume fraction of silica (from 0 to 20% v/v). (c) Real stress as a function of elongation ratio for different silica volume fractions. The experiments have been performed at $T_g + 20$ $^{\circ}\text{C}$.

Note the amplitude of the inflection point is of the same order of magnitude as the modulus obtained on the oscillatory shear plate-plate ARES rheometer (i.e., of the order of 0.15 MPa; $E' = 3G$ in linear deformation range). In the presence of silica, the most important fact is that at high temperatures ($T \sim 150^{\circ}\text{C}$) the characteristic creep zone of pure PS disappears completely: the curvature is reversed, so that E' decreases slowly and tends toward a plateau, clearly visible for high silica concentrations. The set of data is completed with uni-axial stretching experiments (Figure 2.3c). Samples are stretched up to a predefined deformation value in a controlled constant-rate deformation ($d\lambda/dt = 0.005 \text{ s}^{-1}$, λ being the elongation ratio $L(t)/L(t=0)$), at temperature $T = 120$ $^{\circ}\text{C}$, i.e., ~ 20 $^{\circ}\text{C}$ above the glass transition temperature of the polymer matrix ($T_g = 98$ $^{\circ}\text{C}$ for pure PS). This corresponds to a typical time $(d\lambda/dt)^{-1} = 200$ s, which after applying the time-temperature superposition factor (0.0087 from 120 to 143°C) corresponds at 143 $^{\circ}\text{C}$ to 1.8 s. The set of stretching curves can be summarized by the progressive increase with ϕ_{SiO_2} of an initial stress jump at the beginning of the elongation, while the shape at large λ is similar, except for the shift due to the initial jump. This initial stress jump can be expressed in terms of an initial slope of stress vs deformation $\varepsilon = \lambda - 1$ in a low elongation ratio ($\lambda < 1.1$) regime, giving an effective Young modulus $E_{\text{nanocomposite}}$ in this range of deformation. For very high silica concentration ($\phi_{\text{SiO}_2} > 10\%$ v/v), a maximum is observed in the stress-strain curves, more and more pronounced when ϕ_{SiO_2} increases.

Most of the time, this peak appears simultaneously with local necking while we can notice a constant remaining stress at large deformation illustrating that the modulus of the filled samples don't go back to the one of the pure matrix even at very large deformation. Whatever the considered technique, we can investigate the reinforcement by the determination of the ratio of the filled sample modulus by the one of the pure matrix G'/G_0 . In addition, by applying the TTS principle at the reference temperature, we can compare directly the different reinforcement ratios for an equivalent time range (or frequency). This can be done in the elastic regime for times lower than the terminal time of the polymer τ_{ter} , with superposition of stretching at low deformation (1.8s at 143°C) with DMA at $T/T_\alpha=1.1$ corresponding to typical time of 0.2s at 143°C and with ARES at high frequency (100 rad/s) which gives a typical time of 0.0628s at the reference temperature. Such superposition is presented on Figure 2.3a and 2.3b for Nissan-PS and Nissan-PMMA systems. We can observe a very nice overlap of the data for the different techniques for the considered typical time range (0.1 to 1s). This means that at lower typical sizes, i.e., when considering mostly the local structure of the fillers, the system behaves identically whatever the geometry of deformation.

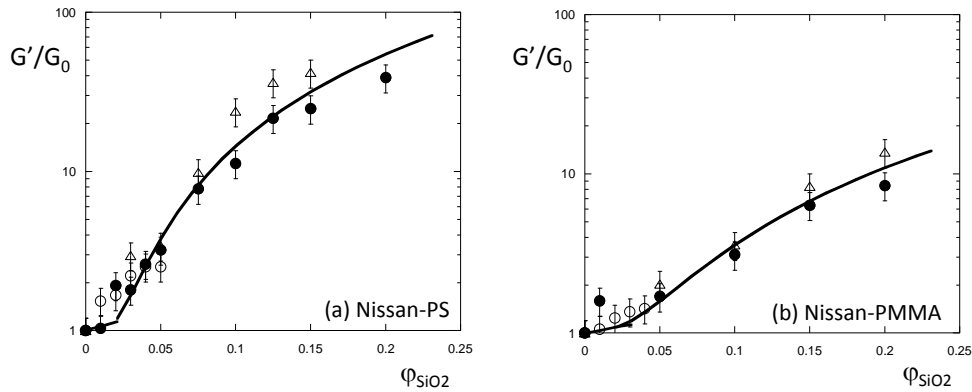


Figure 2.3: Reinforcement factor as function of the particle volume fraction determined for equivalent times using TTS principle for ARES data (open circles), DMA (open triangles) and uni-axial stretching data (full circles) for 3D connected network systems (a) Nissan-PS and (b) Nissan-PMMA. The full black is the best fitted result using the percolation model described in the text.

The evolution of the reinforcement factor with the particle concentration can be quantitatively described with a theoretical model. We choose an approach, called the mechanical percolation model, which consists in a series-parallel model extended by Ouali et al.^{72,73} and then by Kolarik and Favier et al.⁷⁴ with a percolation concept. In this model, the composite is described by a parallel mechanical coupling of a rigid phase, made of a theoretical volume fraction of filler network, and a soft one, made of the matrix reinforced with the fillers out of the network (i.e. dead branches and isolated aggregates). The network volume fraction is calculated from the percolation theory⁷⁵. In the case of randomly distributed objects, the volume fraction Φ of percolated structure depends on the total volume fraction of objects, Φ_{eff} , and is given by:

⁷² Ouali, N.; Cavaillé J.Y.; Perez J. *Plastics and Rubber Processing and Applications* **1991**, 16, 55-60.

⁷³ Kolarik J. *European Polymer Journal* **1997**, 34 (5/6), 5, 85-90.

⁷⁴ Favier V. ; Canova G. ; Shrivastava S. ; Cavaillé J.Y. *Polymer Engineering and Science* **1997**, 37 (10), 1732-9.

⁷⁵ Gouyet J.F. *Physique et structures fractales* Paris: Masson, **1992**, p. 234.

$$\Phi(\varphi_{\text{eff}}) = 0 \quad \text{for } \varphi_{\text{eff}} < \varphi_c$$

$$\Phi(\varphi_{\text{eff}}) = \left(\frac{\varphi_{\text{eff}} - \varphi_c}{1 - \varphi_c} \right)^\beta \quad \text{for } \varphi_{\text{eff}} > \varphi_c \quad 2.4$$

with φ_c , the percolation threshold and β , the critical exponent. As assumed by De Gennes⁷⁶, the dead branches do not participate actively in stress transmission and taking account only of the structure backbone requires a value of β close to 1.8. The Young's modulus, G , of the composite is then given by:

$$G = \frac{(1 - 2\Phi(\varphi_{\text{eff}}) + \Phi(\varphi_{\text{eff}})\varphi_{\text{eff}})G_m G_n + (1 - \varphi_{\text{eff}})\Phi(\varphi_{\text{eff}})G_n^2}{(1 - \varphi_{\text{eff}})G_n + (\varphi_{\text{eff}} - \Phi(\varphi_{\text{eff}}))G_m} \quad 2.5$$

G_m is the modulus of the pure matrix and G_n is the one of the filler percolating network. The calculation have been done using the primary aggregates compactness κ deduced from the scattering curves modeling to estimate φ_{eff} as function of the particle filler volume fraction φ_{SiO_2} ($\varphi_{\text{eff}} = \varphi_{\text{SiO}_2} / \kappa$). The percolation thresholds have been determined from the scattering calculation and/or from the TEM analysis and fixed at $\varphi_{\text{SiO}_2} = 8\%$ and 10% for both systems N-PS and N-PMMA. Finally, the single fitted parameter is the modulus of the percolating network G_n . The result of the calculation is the full black line reported on the Figures 2.3a and 2.3b enables to see the good agreement between the model and the experimental data.

⁷⁶ De Gennes P.G. *Journal de Physique Lettres* **1976**, 37, L1-2.

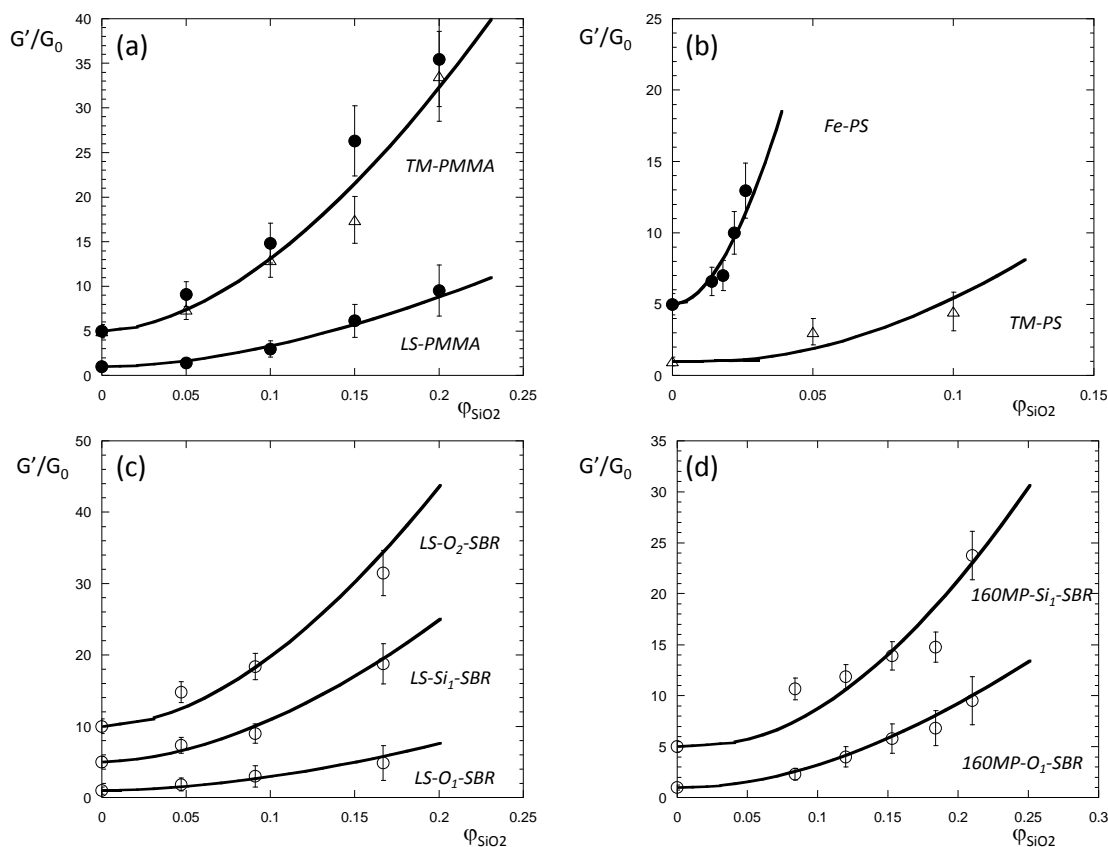


Figure 2.4: Reinforcement factor in the elastic regime as function of the particle volume fraction determined for equivalent times ARES data (open circles), DMA (open triangles) and uni-axial stretching data (full circles) for multi-level aggregated network systems (a) Ludox TM-PMMA and Ludox LS-PMMA, (b) maghemite-PS and Ludox TM-PS, (c) Ludox LS-O₁, LS-O₂ and LS-Si₁-SBR and (d) 160MP-Si₁ and 106MP-O₁-SBR. The full black is the best fitted result using the percolation model described in the text (equation 2.5). The curves have been shifted for clarity.

We applied the same analysis to all other studied systems, especially the one presenting a filler dispersion of multi-level (both or more) of aggregated network described in section 1.25 and 1.26 and present the results of the calculation on Figure 2.4. We obtained a good agreement between the model and the experimental data for all kind of particle/matrix couples for compactness ranging from 15 and 40% and percolation threshold of around 10% v/v for silica (and around 2% for maghemite system). We can notice that we never observed a decrease of the viscosity, which behaves as the reinforcement for low filler content as already reported in nanocomposites^{77,78}. Our purpose here is not to test the validity of the model or to compare between different theoretical functions. We are mostly looking for a tool, as simple as possible, from which we can extract a representative parameter of the reinforcement efficiency and discuss the efficiency as function of the filler structures, i.e., the aggregate morphologies as well as the inter-aggregates and inter-

⁷⁷ Nusser, K.; Schneider, G. J.; Pyckhout-Hintzen, W.; Richter, D. *Macromolecules* **2011**, 44 (19), 7820–7830.

⁷⁸ Wang, M.; Hill, R. J. *Soft Matter* **2009**, 5, 3940.

particles interactions. For comparison, the different values of the relative network modulus G_n deduced from the mechanical analysis are reported on Figure 2.5.

The resulting figure shows different aspects that must be discussed in details. The first obvious conclusion is that the reinforcement can be reproduced considering the percolation of primary aggregates made of primary particles. The morphology of the objects (compactness) is a driving parameter.

The second point is to see whether we can find a correlation between the reinforcement efficiency and the apparent network strengths and at which relevant length scale. At first sight, the variation looks randomly distributed. We propose an explanation based on the particle surface modifications. For systems in which the particle surface have been not modified (Silica Nissan, TM, LS and maghemite), the variation of reinforcement values is not correlate with the inter aggregates interactions: for example for TM, the primary aggregates are below the close contact and give a more reinforced network than for LS or maghemite systems for which the aggregates are slightly interpenetrated. This suggests that here the apparent strength of the network is mostly governed by the primary inter-particles interactions, dominant because not mediated by a surface agent. This is supported with the result obtained with grafted Nissan particles in PS⁴¹ showing a very low reinforcement value compared to the non-grafted one suggesting that reducing the inter-particle interaction with grafted chain reduces reinforcement. Grafted chains can deform and then induce the diminution of the network rigidity. By modifying the particle surface with an additive, the primary inter-particle interaction becomes less important and then the apparent strength of the network is governed at larger length scale by the inter-aggregate interactions. This is nicely highlighted with the elastomer series for which the covering agent Octeo gives more repulsive inter-aggregates interaction that decreases the reinforcement while the coupling agent Si69 gives more interpenetrated aggregates that increases the reinforcement. This tendency is observed for both model and industrial elastomer systems⁷⁹. This idea is also supported by the fact that the direct influence of the different additives on the inter-particle interaction is difficult to evaluate.

The final observation, the most spectacular, is the effect of the matrix across the difference observed for PMMA and elastomer SBR with PS that exhibits larger values. Beyond the effect of the morphology of the aggregates, this means that there is an additional contribution, depending on the specific PS-silica interactions, that increases the effective volume fraction of the objects induced by the polymer chain contribution. This can be the result of a fraction of chain acting as a hard fraction due to a modification of mobility close to the surface as already observed for the grafted silica particles. If we compare the reinforcement between N-PS and N-PMMA, we found a factor 2.8 that gives an effective layer thickness equal to 2.5 nm. This value is in agreement with the NMR prediction⁶⁹ of the “glassy layer” model at $T_g+20^\circ\text{C}$. However, it is always difficult to confirm such hypothesis with macroscopic evidences of immobilized polymer for example with calorimetric measurements. An alternative explanation⁸⁰ suggests that the reduced mobility of the chain comes from a slowing down of the reptation mode due to adsorption at the surface of the particles. The adsorbed amount of chain has been estimated in both N-PS and N-PMMA systems and respective values of 0.28 and 0.11 mg/mg whose ratio (~ 2.5) corresponds also to the observed reinforcement ratio. Chains contribution is also expected for SBR systems which are supposed to present different quantities of “bound rubber” depending of the additive: the quantity of occluded polymer has been found to be larger with coupling agent than with the covering one⁶³ while reinforcement is lower. However, bound rubber effect doesn't seem to be significant for reinforcement of elastomers here.

⁷⁹ Bouty, A. ; Petitjean, L. ; Degrandourt, C.; Gummel, J.; Kwasniewski, P.; Boué, F.; Couty, M.; Jestin, J. *Macromolecules* **2013**, to be submitted.

⁸⁰ Robertson, C. G.; Rackaitis, M. *Macromolecules* **2011**, 44, 11771181.

We observe a mean general tendency showing that the reinforcement follows percolation of primary aggregates whose morphologies drive reinforcement efficiency. The apparent strength of the different network seems to be correlated to the inter-particle interactions (for non-modified surface particles) and to the inter-aggregate interactions when additives are used. Some variations from this general tendency impose to include additional contribution depending of the polymer-particle interaction: an effective “glassy” or adsorbed layer of chain of reduced mobility that gives rise to enhanced reinforcement.

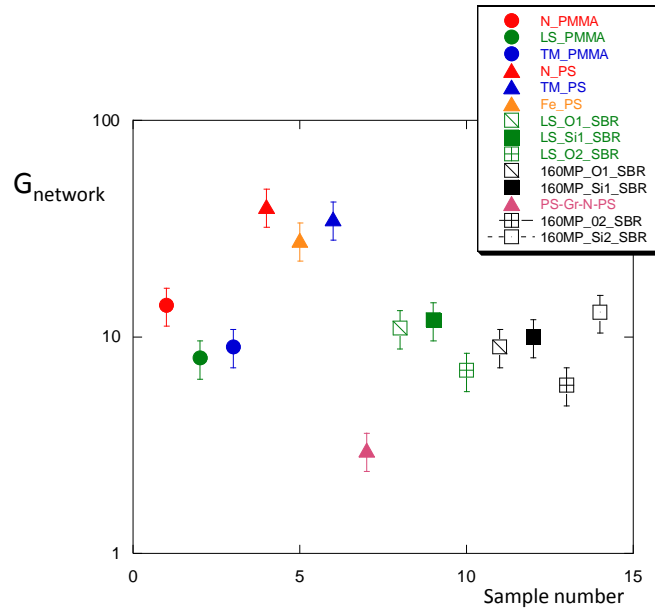


Figure 2.5: Summary of the relative reinforced network values deduced from the percolation function modeling for the different systems.

2.3.2 The flow behavior

As we have seen in the previous part, the aggregate morphologies and interactions drive the reinforcement efficiency in the elastic regime. We turn now to the flow behavior in a range of long typical relaxation times (for $\tau \gg \tau_{ter}$). As already mentioned, the characteristic of this regime is the appearance of a long time at low frequency accompanied with a drastic change of the modulus frequency power law dependence $G' \sim \omega^\alpha$ (α can varied typically from 2 to 1/3 with the filler concentration). This illustrates a specific flow behavior, usually called anomalous flow behavior and interpreted as a liquid-solid transition. To overcome from the specific behavior of the different matrixes used and compare the different systems, one practical way is to report the modulus ratio that we call “Flow Modulus Ratio (FMR)”, at a given frequency (here at $\omega \sim 0.06$ rad/s) corresponding to typical time (~ 100 s) larger than the polymer terminal time τ_{ter} , presented on Figure 2.6. The primary observation is that the FMR is typically larger by a factor 5 to 10 than for shorter times (excepted for the Nissan-PMMA for which the effect is lower). This means that this behavior cannot be simply related to the filler percolation as frequently suggested. The correlation with the large scale filler structure, the secondary aggregation level can be then investigated.

However, such correlation is not clear: for model LS-SBR systems, similar FMR corresponds to different secondary aggregation (Figure 1.14a and b) while for industrial SBR system, different FMR are correlated with similar secondary filler organization (Figure 1.15).

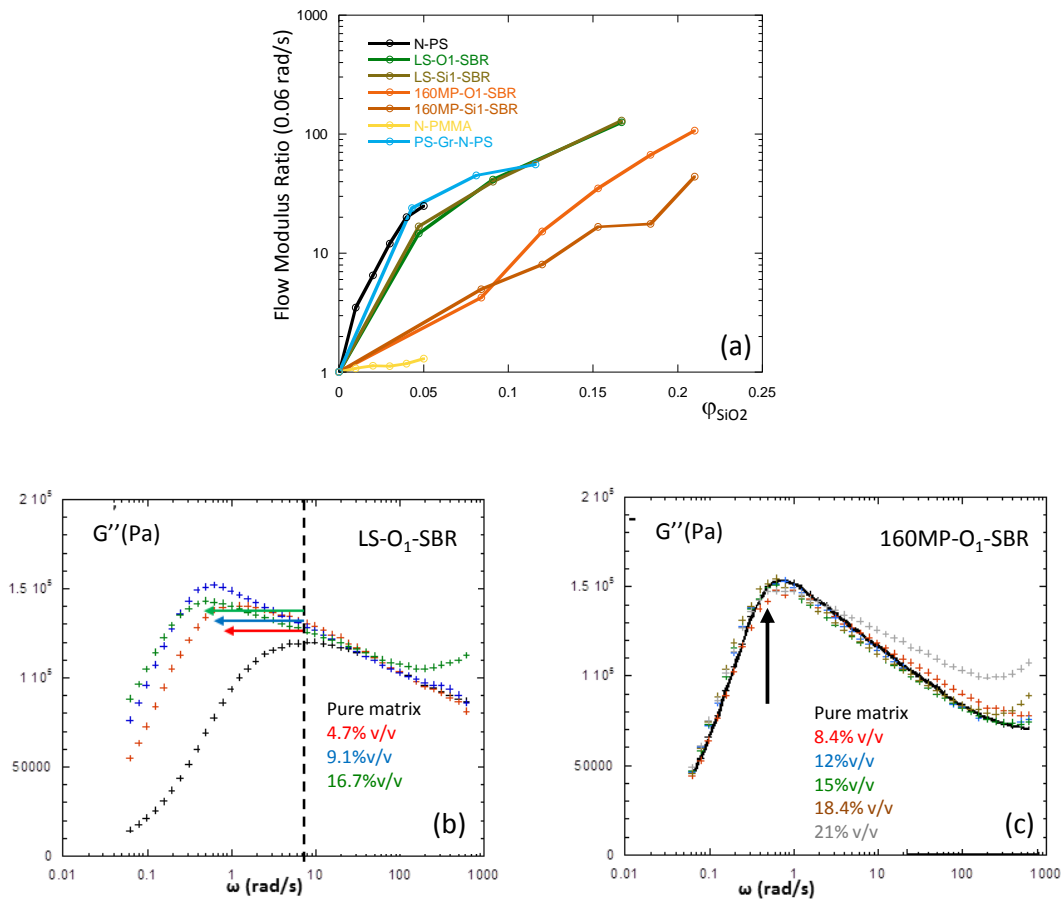


Figure 2.6: (a) some examples of Flow Modulus Ratio (FMR) variations with the particle content at a pulsation of 0.06 rad/s. (b) Illustration of the shift of the G'' toward the lower frequencies with the particle volume fraction for the LS-O₁-SBR nanocomposites. (c) Illustration of the absence of shift of G'' with the particle volume fraction for the industrial 160MP-O₁-SBR nanocomposites.

This is also supported by the Nissan-PS system behavior which presents below the percolation threshold a dispersion of individual aggregates separated by a rim to rim distance of the order of 50 nm while showing larger FMR amplitude. In addition, the Nissan-PMMA system who presents filler dispersion quasi-similar to the one of the Nissan-PS system shows very low FMR amplitude. In addition, identity between grafted and non-grafted Nissan-PS and between LS-O₁ and LS-Si₁-SBR suggests an independence with the polymer-filler interface.

That suggests that in the range of long relaxation times, the flow behavior is mostly dominated by the polymer chain contribution than by the large scale organization of the filler. The application of the percolation model gives unphysical compactness values compared to the morphology of the secondary aggregation level. At the same time, reproducing the data using the model imposes us to include an additional effective layer which is significantly higher than for the elastic regime suggesting a long range effect. For example, for the Nissan-PS system, it corresponds to an increase of the layer's thickness of the factor 3. A possible origin of the increase of the flow deformation modulus according to a long range effect is to consider chain bridging⁸¹ between aggregates. This assumption implies in our case that the radius of gyration of the chains involved would be increased, since they would have to join two aggregates separated in average by distances substantially larger than the R_g at rest.

An alternative idea is to suggest that anomalous flow behavior is driven by longer disentanglements. Longer disentanglements, i.e. longer reptation time, can be due to an increased density of entanglements that reducing the reptation tube diameter. This has been recently determined by neutron spin echo⁸² and rheological experiments⁸³ for high concentrated filler systems (up to 60% v/v) and by simulations⁸⁴. The reduction of the reptation tube diameter is illustrated by a shift of the G'' toward the low frequencies. This is indeed what we observed on some systems as illustrated on Figure 2.6b for the Ludox LS-O₁-SBR. However, this shift is not observed systematically for every systems like the example of the Figure 2.6c (160MP-O₁-SBR) showing the constant position of the G'' even at large filler content (~20%). The idea is that this effect is a result of a geometrical confinement due to filler structure suggesting a different filler organization between model and industrial SBR systems. However, we have seen that for a given additive the organization of the primary aggregates is similar, meaning that the G'' behavior is not related to the filler structure. Beyond the fact that it could be a solvent effect due to the sample processing, we also suggest that geometrical confinement can be related to the ratio between the size of polymer chain and the size of the aggregates. Indeed, in model systems both sizes are comparable ($R_g \sim R_{agg}$) and induced confinement while in industrial systems $R_g \ll R_{agg}$ do not give rise to an effective confinement and thus do not modify the G'' .

⁸¹ Sarvestani, A.S.; Picu, C. R. *Polymer* **2004**, 45, 7779-90.

⁸² Nusser, K.; Schneider, G. J.; Richter, D. *Soft Matter* **2011**, 7, 7988.

⁸³ Nusser, K.; Schneider, G. J.; Richter, D. *Macromolecules* **2013**, 46 (15), 6263–6272.

⁸⁴ Masnada, E.; Merabia, S.; Couty, M.; Barrat, J.-L. *Soft Matter* **2013**, DOI: 10.1039/c3sm51207j.

2.4 Conclusion

We highlighted through the different examples some evidences between the local structure of the filler dispersion and the viscoelastic behavior for non-percolating, oriented and percolating filler structures. The classical hydrodynamical or percolation models can reproduce quantitatively the reinforcement behaviors, considering the aggregate morphologies as a key parameter. The apparent strength of the network and the corresponding reinforcement efficiency are driven by the inter-aggregate interactions, more or less attractive, as well as by the inter-particle interactions mediated by the attached ligands. However, some variations to these tendencies induce to include in some cases an additional effective layer involving the polymer chains in reinforcement mechanisms. The anomalous flow behavior, observed for all the systems, appears to be a complex process, more than a simple result of filler percolation that do not present obvious correlations with the large scale structure of the network or with the polymer-filler interfaces. The flow behavior is clearly related to the polymer chain contribution according to mechanisms supported by several hypothesis. For systems that are able to induce a geometrical confinement of the polymer chain, the chain mobility can be affected by an increase of the entanglement density producing a reduction of the reptation tube and slowing down the reptation mode of the chains. For non-confined systems, the anomalous flow can be illustrated by an additional effective layer of chains of modified state corresponding to a long range effect. The physical state of the polymer chains inside the effective layer observed in both reinforcement and flow regimes can be related to the chain dynamic or mobility (glassy model, entanglement density model) and/or to the chain conformation (bridging effects, adsorption). These different statements are currently strongly debated in the literature. Whatever the origin of the effect (dynamical or conformational), it appears to be larger enough to affect significantly the mean shape of the polymer chains. One way to progress in the understanding of these mechanisms is thus to determine the polymer chain conformation in nanocomposites in presence of filler. This is the scoop of the next chapter.

CHAPTER 3

POLYMER CHAIN CONFORMATION IN NANOCOMPOSITES

Knowing both the filler dispersion and the mechanical behavior of the different systems, we can investigate now the polymer chain conformation inside the nanocomposites to complete the description of the processes. We consider here two main situations, the grafted chain conformation and the bulk chain conformation, to probe the influence of the surface vicinity. The case of the grafted chain conformation and the interaction with free chains has been extensively studied in the case of planar surfaces (see for example the reference⁸⁵) but much less in the case of nanocomposites for obvious reasons of geometry. Thanks to a refined combination of SANS with specific deuteration, we have been able to determine directly the grafted brush conformation inside the composite as a function of the particle dispersion, individual case or compact aggregates. On the contrary, the question of the bulk matrix chain conformation and its modification due to the presence of the fillers has been addressed several times with different approaches. However, a clear conclusion is still currently under debate. This point has been studied also by simulations^{86,87,88,89,90,91,92} considering the polymer radius of gyration $R_{g\text{ pol}}$ and the particles radius R_{part} ratio ($R_{g\text{ pol}}/R_{\text{part}}$) and leads to contrary conclusions, either swelling or decrease of the $R_{g\text{ pol}}$ as a function of the particle filler volume fraction, mostly when the polymer radius of gyration $R_{g\text{ pol}}$ is equal or superior to the particle radius R_{part} . For example, Termonia et al. and Sung et al.^{72,73} reported a significant swelling of the chain for $R_{g\text{ pol}}/R_{\text{part}} > 1$ while Vacatello et al.^{74,75} reported a decrease of the chain. Sharaf et al.⁷⁶ have reported a swelling of the chain but for $R_{g\text{ pol}}/R_{\text{part}} < 1$.

The situation has been also probed from an experimental view^{93,94,95,96,97,98,99} using SANS and specific deuteration of the polymer chains. These studies also provide controversy behaviors whose origins can be discussed according to different issues. A first possible origin is the difficulty to extract the experimental chain signal without ambiguous matching or undefined extra scattering.

⁸⁵ Maas, J. H.; Fleer, G. J.; Leermakers, F. A. M.; Stuart, M. A. C. *Langmuir* **2002**, 18(23), 8871–8880

⁸⁶ Termonia, Y. *Polymer* **2009**, 50, 1062–1066.

⁸⁷ Sung, B. J.; Chang, R.; Yethiraj, A. *J. Chem. Phys.* **2009**, 130, 124908.

⁸⁸ Vacatello, M. *Macromol. Theory Simul.* **2002**, 11, 757–765.

⁸⁹ Vacatello, M. *Macromolecules* **2002**, 35, 8191–8193.

⁹⁰ Sharaf, M. A.; Kloczkowski, A.; Sen, T. Z.; Jacob, K. I.; Mark, J. E. *Eur. Polym. J.* **2006**, 42, 796–806.

⁹¹ Picu, R. C.; Ozmusul, M. S. *J. Chem. Phys.* **2003**, 118, 11239–11248.

⁹² Ozmusul, M. S.; Picu, C. R.; Sternstein, S. S.; Kumar, S. K. *Macromolecules* **2005**, 38, 4495.

⁹³ Nakatani, A. I.; Chen, W.; Schmidt, R. G.; Gordon, R. V.; Han, G. C. *Polymer* **2001**, 42, 3713–3722.

⁹⁴ Mackay, M. E.; Tuteja, A.; Duxbury, P. M.; Hawker, C. J.; Van Horn, B.; Guan, Z.; Chen, G.;

Krishnan, R. S. *Science* **2006**, 311, 1740–1743.

⁹⁵ Botti, A.; Pyckhout-Hintzen, W.; Richter, D.; Urban, V.; Straube, E.; Kohlbrecher, J. *Polymer* **2003**, 44, 7505–7512.

⁹⁶ Sen, S.; Xie, Y.; Kumar, S. K.; Yang, H.; Bansal, A.; Ho, D. L.; Hall, L.; Hooper, J. B.; Schweizer, K. S. *Phys. Rev. Lett.* **2007**, 98, 128302.

⁹⁷ Nusser, K.; Neueder, S.; Schneider, G. J.; Meyer, M.; Pyckhout-Hintzen, W.; Willner, L.; Radulescu, A.; Richter, D. *Macromolecules* **2010**, 43, 98379847.

⁹⁸ Genix, A.-C.; Tatou, M.; Imaz, A.; Forcada, J.; Schweins, R.; Grillo, I.; Oberdisse, J. *Macromolecules* **2012**, 45 (3), 1663–1675.

⁹⁹ Tuteja, A.; Duxbury, P. M.; Mackay, M. E. *Phys. Rev. Lett.* **2008**, 100, 077801.

Nakatani et al.⁷⁹, Mackay et al.⁸⁰ (for the C60/PS system) and also Botti et al.⁸¹ extracted the conformation of the polymer chain from a complex scattering signal in which the interactions between labeled and non-labeled chains have to be taken into account for. Sen et al.⁸², Nusser et al.⁸³ and Genix et al.⁸⁴ (on latex/silica systems) used the zero average contrast (ZAC) method, which cancels inter and intra-chains correlations, but in unperfected matching conditions^{82,83} or in presence of extra scattering signal coming from chain diffusion⁸⁴. An unambiguous contrast matched method used is the one of Mackay et al.⁸⁵ with cross-linked PS particles as fillers but concerns a very specific case of nanocomposites filled with soft fillers. Another contribution comes from the role played by the particles dispersion inside the polymer matrix. Despite of the general prediction proposed by Mackay et al.⁸⁰ that suggested that the particle dispersion is only governed by the $R_{g\text{ pol}}/R_{\text{part}}$ ratio, it has been also demonstrated that the particle dispersion strongly depend on the processing conditions^{10,40}. Indeed, some of the previous studies suffer from a clear particle dispersion characterization that can render a confusing reading of the results. Anyway, when reducing the discussion to the specific case for which the polymer radius of gyration is of the same order of size that the particle radius ($R_{g\text{ pol}} \approx R_{\text{part}}$), the situation can be summarized as follow: most of the experiments have concluded that the chain conformation seems to be unaffected by the presence of the fillers^{80,81,82,84,85} excepted for Nakatani et al.⁷⁹ and Nusser et al.⁸³ that have shown a decrease of the polymer radius of the gyration $R_{g\text{ pol}}$ due to the presence of the fillers.

Beyond the fundamental interest of the previous studies mainly performed on model systems, the question of the chain conformation inside a composite is also a main preoccupation of industrial actors. In the present context of petroleum resources depletion, a new challenge of the tire industry is to develop new materials that can reduce the cars oil consummation and CO₂ emissions while offering improved mechanical performances (reinforcement, adhesion, tensile strength...). Consequently, the question of the matrix chain conformation modification and it correlation with the mechanical performances of the material becomes a central point also from an industrial point of view.

After the presentation of the chain conformation measurements in the specific case of grafted brushes, we will describe different methods to determine the bulk chain conformation in nanocomposite using a combination of SANS/SAXS with mixtures of deuterated and hydrogenated polymers.

3.1 The grafted brush conformation in nanocomposites

After the determination of the grafted brush conformation for particles in solution, an existing challenging step was to see whether it is possible to measure this conformation when particles are mixed with free chains to form a nanocomposite. In particular, the relation between the elastic/stretched conformation and the particles dispersion as predicted by the theoretical description remains a question of interest.

To succeed in such determination we have developed a refined chemistry to build controlled grafted silica particles with deuterated polystyrene (PS) chains (as described in Chapter 1) and synthesized a statistical hydrogenated-deuterated polystyrene matrix that matches the particles scattering in SANS experiments: the silica becomes invisible to neutrons in the matrix, and only the deuterated corona contributes to the signal. The polymer chains for the matrix, called “grey matrix” were synthesized by conventional radical polymerization (6 h at 80°C) by mixing normal and deuterated styrene to form a statistical H/D PS chain at the final state of the polymerization

process. The styrene H/D ratio was varied (from 35 to 100% v/v of H-monomer) and the neutron scattering length density (SLD) of the resulting chain measured with SANS (Figure 3.1a) to find the SLD value as close as possible of the one of the silica ($3.40 \cdot 10^{-6} \text{ \AA}^{-2}$). Then deuterated PS grafted particles were dispersed in the “grey matrix” and measured by SANS¹⁰⁰.

The scattered intensity is thus only due to the grafted deuterated chains around the silica particles as the silica signal contribution is suppressed by the matrix one and can be expressed in this case as $I_{\text{SANS}}(\mathbf{Q}) \sim S_{\text{gp}}(\mathbf{Q}) \cdot P_{\text{gp}}(\mathbf{Q})$, where the index “gp” represents the grafted particles. For a correct modeling of the grafted brush ($P_{\text{gp}}(\mathbf{Q})$), it is needed to suppress the contribution of the inter-particles structure factor ($S_{\text{gp}}(\mathbf{Q})$) related to the arrangement of the grafted coronas between them inside the matrix. As this organization is built across the network center of masses of the scattered grafted objects, the inter-particles structure factor is independent of the nature of the probe, i.e., is the same for neutron and for X-rays, $S_{\text{p}}(\mathbf{Q}) = S_{\text{gp}}(\mathbf{Q})$. Thus, the grafted corona form factor can be extracted by dividing the SANS signal by the particles structure factor deduced from SAXS. The grafted corona form factor can be perfectly modeled (Figure 3.1b) with a Gaussian chain model from which we can extract the physical parameters describing the system: the number of grafted silica particles (5% v/v), the number of polymer chains per particle (~ 400), the mass ($M_n = 25\,000 \text{ g/mol}$), and the radius of gyration of grafted chains equal to 3.1 nm, corresponding to a corona thickness of 6.2 nm. The grafted brush thickness can also be determined indirectly with the analysis of the SAXS pattern with the analytical function described on the Chapter 1.

From this modeling, we can calculate the inter particle distance and knowing the particle radius, we can deduce the grafted brush thickness variations. For the grafted silica system, the direct determination method is only available for well individual dispersion of particles (because of the limited mass of the grey matrix) while indirect method works for both individual dispersion and aggregates.

¹⁰⁰ Chevigny, C.; Jestin, J.; Gigmes, D.; Schweins, R.; Di Cola, E.; Dalmás, F.; Bertin, D.; Boué, F. *Macromolecules* **2010**, *43* (11), 4833–4837.

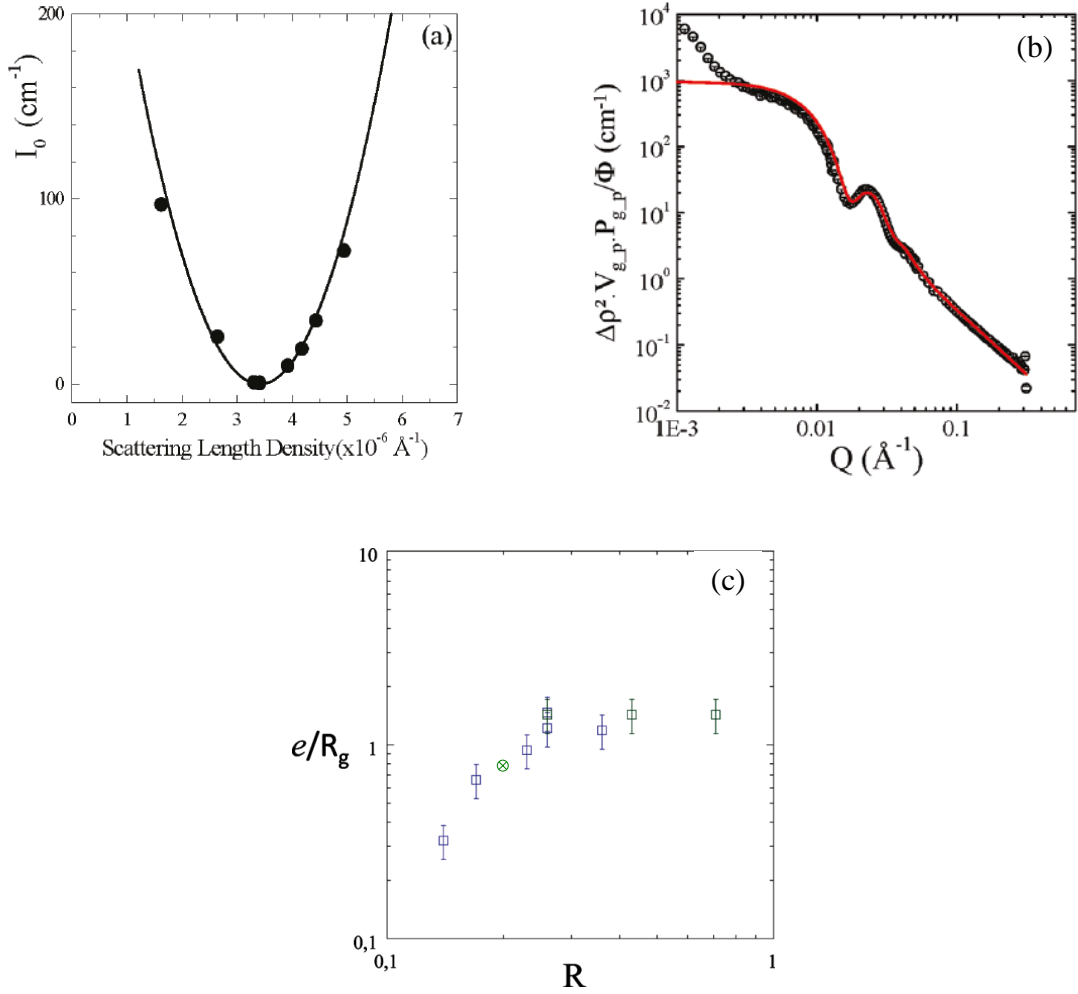


Figure 3.1: (a) Variation of the H/D styrene ratio for synthesis of a statistical H/D PS matrix of tunable scattering length densities (SLD): the minimum of the curve correspond to the SLD of the silica. (b) Modeling of the form factor of the deuterated PS grafted silica nanoparticles in a grey matrix with a Gaussian chain model⁹⁹. (c) Evolution of the thickness e of the spherical grafted polymer layer normalized by the Gaussian radius of gyration R_g as a function of the grafted/free chain length ratio R determined indirectly with the analysis of the inter-particle structure factor (blue symbol) and measured directly with SANS (green symbol).

We completed the direct determination method with the grafted maghemite system whose particles contrast can be simply matched with deuterated PS matrix and enables thus to measure the grafted brush thickness for the aggregate case. The results (direct and indirect) are reported as a function of R ⁴⁵ in Figure 3.1c. We see an excellent agreement between the two methods. Besides, we observe that the transition between complete dispersion and formation of aggregates is accompanied by a significant reduction of the normalized thickness of the grafted polymer layer: by about a factor of 2. These results show that the dispersion can be tuned by a refined control of the grafted/free chains wetting properties. These observations can be qualitatively described considering the total free energy as a combination of a mixing entropy term between the grafted and the free chain and an elastic term of compression or stretching of the grafted brushes. For $R < 0.24$ (the transition value), according to a depletion process, entropic expulsion of the free chains from the grafted corona is observed, and the corona eventually collapses. The resulting short-ranged inter-particle potential induces therefore aggregation. For $R > 0.24$, the free chains can

partly swell the grafted corona which is then more extended and creates repulsive long-ranged inter-particle potential, favoring the complete dispersion of the particles. We can note the interesting agreement between the grafted brushes thicknesses obtained here from scattering with the one of the effective layer thickness deduced from rheological modeling on chapter 2.

3.2 The bulk chain conformation in nanocomposites

3.2.1 The Zero Average Contrast ZAC method

The scattering intensity of a single chain in nanocomposite can be obtained directly by SANS using the zero average contrast (ZAC) method. This method was first used for a mix of normal, i.e., non-deuterated (H) and deuterated (D) chains in a solvent. The total scattering intensity $I(Q)$ can be expressed by the relation:

$$I(Q) = (\rho_D - \rho_H)^2 x(1-x)v\Phi NP(Q) + (x\rho_D + (1-x)\rho_H - \rho_0)^2 (v\Phi NP(Q) + V\Phi^2 S(Q)) \quad 3.1$$

where ρ_H , ρ_D , and ρ_0 are respectively the scattering length densities (SLD) of non-deuterated chains, deuterated chains, and solvent, x is the molar fraction of D-chains, v is the molar volume of D monomer, V is the global volume, Φ is the molar fraction of polymer, $P(Q)$ is the form factor of one chain, and $S(Q)$ is the inter-chain structure factor. When the average contrast between polymer mix and solvent is adjusted to zero, i.e.:

$$x\rho_D + (1-x)\rho_H - \rho_0 = 0 \quad 3.2$$

The scattering intensity is only related to the form factor of one chain:

$$I(Q) = (\rho_D - \rho_H)^2 x(1-x)v\Phi NP(Q) \quad 3.3$$

By this condition (eq 3.2), the intra and inter-chain correlations are matched and not observed. Equation 3.2 is possible when ρ_0 is comprised in between ρ_H and ρ_D ; to meet this condition, mixtures of normal and deuterated solvents are often used. In our case, the role of the solvent is played by silica.

3.2.1.1 The Debye Approximation

For athermal systems, when the Flory parameter is close to zero ($\chi_{HD} \sim 0$) (no interactions between monomers as for ideal mixtures) and for identical hydrogenated and normal chain lengths as for PS, the form factor of the chain is expressed by the Debye function:

$$P(Q) = \frac{2}{(Q^2 R_g^2)^2} (e^{-Q^2 R_g^2} - 1 + Q^2 R_g^2) \quad 3.4$$

depending only on the radius of gyration of the chain. We have applied the ZAC method to the silica Nissan-PS system to extract the single form factor as function of the filler dispersion and of the polymer chain length. To resolve the ambiguous problem of possible unperfected matching of the filler, we have compared two methods, the three components method (ZAC mixture of H and D PS chains with silica) and the four components method (ZAC mixture of H and D chains with silica in the “grey matrix”). The second approach enables the validation, without any doubt, of the perfect matching of the silica fillers. Moreover to progress in the extra scattering understanding, we have also investigated the chain SANS signal in a wide range of scattering vector Q significantly extended toward the low Q values region, corresponding to larger distances in the direct space. We have investigated two different mass of polymer (138 k and 430 k) and two filler concentrations 5 and 15% v/v corresponding to non-connected finite size aggregates (of radius of 20 nm) below the percolation threshold and to a connected 3D network above the percolation (see section 1.2.4).

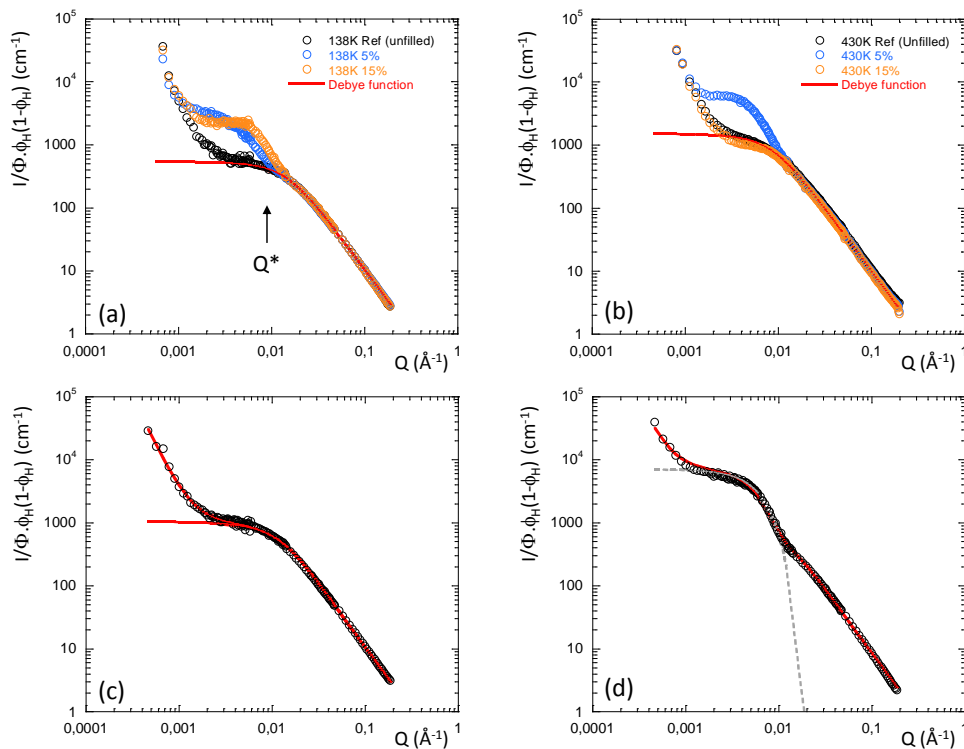


Figure 3.2: SANS curves in Zero Average Contrast (ZAC) conditions in Nissan-PS nanocomposites (pure matrix, 5 and 15% of particle volume fraction) for molecular mass $M_w=138k$ (a) and $M_w=430k$ (b). Extra scattering modeling by voids contribution for pure matrix (c) and by demixing H/D domains contribution (d).

The results are reported on Figure 3.2a for 138k and b for 430k and show the superposition between the unfilled and the filled samples. We found no difference between our two methods, three and four components, suggesting that complete matching of the particle is achieved¹⁰¹. The signal of the filled samples superimposed to the one of the unfilled whatever the polymer chain length and the filler content up to a critical Q^* value corresponding to the size of the polymer chain. Below this critical value, we see two kinds of extra scattering. The first one, mainly visible on the pure matrix, is a power law increase of the intensity which behaves as $\sim Q^{-3}$ as reported on

¹⁰¹ Jouault, N.; Dalmás, F.; Said, S.; Di-Cola, E.; Schweins, R.; Jestin, J.; Boué, F. *Macromolecules* **2010**, *43* (23), 9881-9891.

Figure 3.2c. We attribute this extra scattering to the presence of voids domains inside the sample, usually named crazes coming from the sample processing. The second extra scattering is a kind of shoulder whose amplitude seems to vary according to a non-systematic way mostly visible on the silica filled samples. We propose to analyze this extra scattering as demixing domains of H and D PS chains created by the interaction with the particles. We assumed that H and D domains have similar sizes and similar contrasts (H versus H/D mixture is very close to D versus H/D mixture). We modified the Debye function accordingly to extract the mean size and the volume fraction of the domains. The fitting curves reproduce nicely the experimental ones (Figure 3.2d) with large size domains of typically 300-400Å. A very low fraction of demixing domains (below 0.1% v/v) is enough to provoke strong extra low Q scattering. Otherwise, when taking into account for both extra scattering, the mean radius of gyration of the bulk chain is not modified by the presence of the particle whatever the filler dispersion or the polymer chain length as recently confirmed¹⁰². We can note that considering the radius of gyration ($R_{g\text{ pol}}$) and the radius of the aggregates (R_{agg}) and the network mesh size (ξ), we are still below the case of geometrical confinement of the chains.

3.2.1.2 The Random Phase Approximation RPA

We consider now the intermediate industrial system made of SBR matrix filled with colloidal Ludox particles and prepared by solvent casting (described in section 1.2.5.2). SBR is not ideal and one needs to introduce a monomeric interaction parameter (Flory-Huggins) χ_{HD} . Then, the polymer chain form factor is described by the Random Phase Approximation (RPA):

$$\frac{1}{I(Q)} = \frac{1}{\Delta\rho^2\Phi_{\text{H}}N_{\text{H}}v_{\text{H}}P_{\text{H}}(Q)} + \frac{1}{\Delta\rho^2\Phi_{\text{D}}N_{\text{D}}v_{\text{D}}P_{\text{D}}(Q)} - \frac{2\chi}{\Delta\rho^2V} \quad 3.5$$

Where $\Phi_{\text{D,H}}$, $N_{\text{D,H}}$, $v_{\text{D,H}}$, $P_{\text{D,H}}(Q)$ are the volume fraction, the number of monomeric unit per chain, the volume of monomeric unit and the form factor of the chains respectively for the hydrogenated and for the deuterated SBR polymers. V is the average monomer volume = $\Phi_{\text{H}}v_{\text{H}} + \Phi_{\text{D}}v_{\text{D}}$. The molecular weight determination with SEC experiments permits to extract the $N_{\text{D,H}}v_{\text{D,H}}$ product like $M_{\text{wD,H}} = dN_{\text{A}}N_{\text{D,H}}v_{\text{D,H}}$ where d is the density in g/cm^3 and N_{A} the Avogadro number. As the two monomers have the same structure, the numbers of parameters can be simplified according to $R_{\text{gD}} = R_{\text{gH}} (M_{\text{wD}}/M_{\text{wH}})^{1/2}$.

Here, deuterated polymer chains have been synthesized by Michelin for low molecular weights (~40k) to be far away from the critical demixing mass. Some tentatives made with M_{w} of 140k (used for filler dispersion), have revealed some synthesis limitations. Chemists from Michelin finally succeed in synthesize 140k chains but preliminary tests show strong phase separation between H and D chains.

¹⁰² Crawford, M. K.; Smalley, R. J.; Cohen, G.; Hogan, B.; Wood, B.; Kumar, S. K.; Melnichenko, Y. B.; He, L.; Guise, W.; Hammouda, B. *Phys. Rev. Lett.* **2013**, 110, 196001.

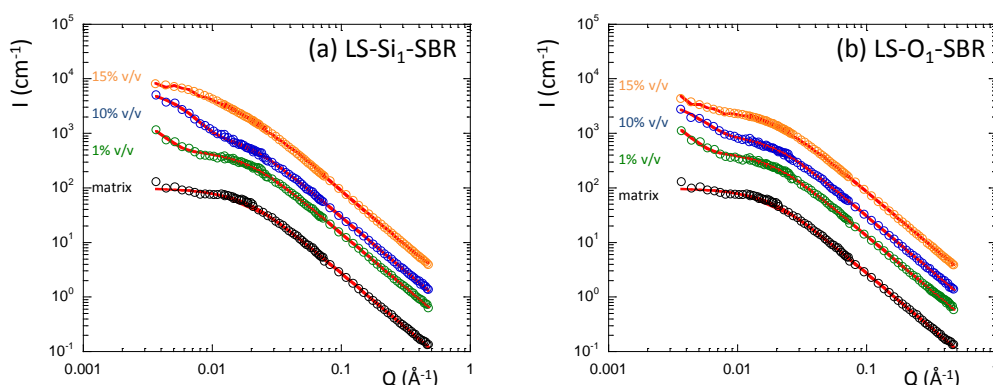


Figure 3.3: SANS curves in Zero Average Contrast (ZAC) conditions for silica Ludox-SBR nanocomposites with the coupling agent Si69 (a) and with the covering agent Octeo (b). The full red line is the modeling with the RPA function corrected with the demixing H/D domains contribution.

As for the filler dispersion study on section 1.2.5.2, we analyzed the chain scattering as function of the silica filler concentration and of the additive, the covering agent Si₁ (Figure 3.3a) and the coupling agent O₁ (Figure 3.3b). The pure matrix scattering is well modeled with the RPA function from which we can extract the radius of gyration of the H, D chains ($R_{gH}=69.5\text{\AA}$, $R_{gD}=82.8\text{\AA}$) as well as the χ parameter ($\chi=5.5 \cdot 10^{-4}$). Contrary to the previous case with PS, we don't see any extra scattering due to voids domains with the SBR matrix. However, when consider the silica filled samples, we can observe the appearance of extra low Q scattering, similar to the one already observed with PS and interpreted as H/D demixing domains induced by the filler. The scattering are again well reproduced by the corrected RPA function including the H/D demixing domain contribution. When tacking into account for a very low volume fraction (0.01%) of these large demixing domains (400\AA), we concluded that the parameters of the chains (R_{gH} , R_{gD} , χ) are not modified by the presence of the filler¹⁰³. This result can appear to be surprising regarding the two level filler dispersion described on section 1.2.5.2 in which the primary aggregates are very close to each other and thus suppose to create a geometrical confinement of the chain. This is also supported by the shift of G'' observed in chapter 2 which can be directly correlated to geometrical confinement. However, the filler dispersion is strongly dependent on the M_w of the polymer chain and the change of the M_w from 140k to 40k induces the disappearance of the two level aggregation processes which is reduced to a single one with formation of very large aggregates unable to create chain confinement. This is illustrated with TEM images on Figure 4.3.

¹⁰³ Bouty, A. ; Petitjean, L. ; Degrandourt, C.; Meneau, F.; Schweins, R.; Boué, F.; Couty, M.; Jestin, J. *Macromolecules* **2013**, to be submitted.

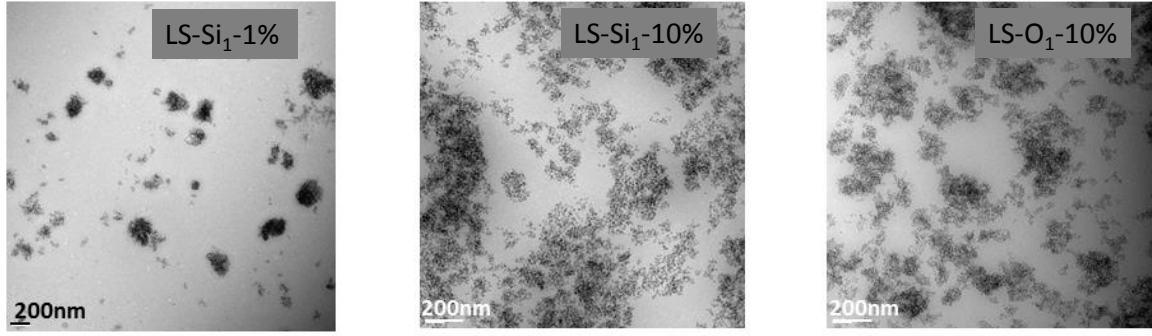


Figure 3.4: TEM images on nanocomposites prepared with SBR matrix of 40k to illustrate the formation of large aggregates.

3.2.2 The Extrapolation method

Here we investigated an alternative method to ZAC described previously to probe the polymer chain conformation using maghemite particles. As the scattering length density of the particles is the same than the one the deuterated PS chain, we can apply the extrapolation to zero concentration which consists in measuring different samples of various H and D PS chains ratio. The total scattering intensity can be written as:

$$I(Q) = k_H^2 S_{HH}(Q) + k_D^2 S_{DD}(Q) + 2k_H k_D S_{HD}(Q) \quad 3.6$$

where k is the contrast between the chains and the melt. When considering a melt of 100% of D chain, the terms involving the D chain becomes equal to zero and the equation simplifies as:

$$I(Q) = k_H^2 S_{HH}(Q) = \phi S_{1H}(Q) + \phi^2 S_{2HH}(Q) \quad 3.7$$

Where S_1 and S_2 are respectively the intra chain contribution related to the form factor $P(Q)$ of the chain and the inter-chain contribution related to the structure factor $S(Q)$. Finally, we can write:

$$\frac{I(Q)}{\phi_{PS-H}} = P(Q) + \phi_{PS-H} S(Q) \quad 3.8$$

illustrating that the extrapolation of the scattering to the limit of zero volume fraction of H chain enables to determine for each Q values the form factor $P(Q)$ of the chain. This is possible for pure melts of H and D chains but also for melts in presence of particles whose scattering length density is equal to the melt of PS D chains. The figure 3.5a summarizes the different measurements made from 0 to 100% of H chains dispersed inside a D melt with maghemite particles as well as the extrapolated form factor signal on Figure 3.5b. The strong interest of this system is that we can tune the chain confinement when applying a magnetic field to orient the particles inside the matrix as described on section 1.2.3. We can then compare the extrapolated form factor of the chain inside the non-oriented with the oriented one parallel or perpendicular to the magnetic field. We can also

graft “invisible” D chain at the surface of the particles as described in section 1.1.2 to probe the influence of grafting when applying or not a magnetic field.

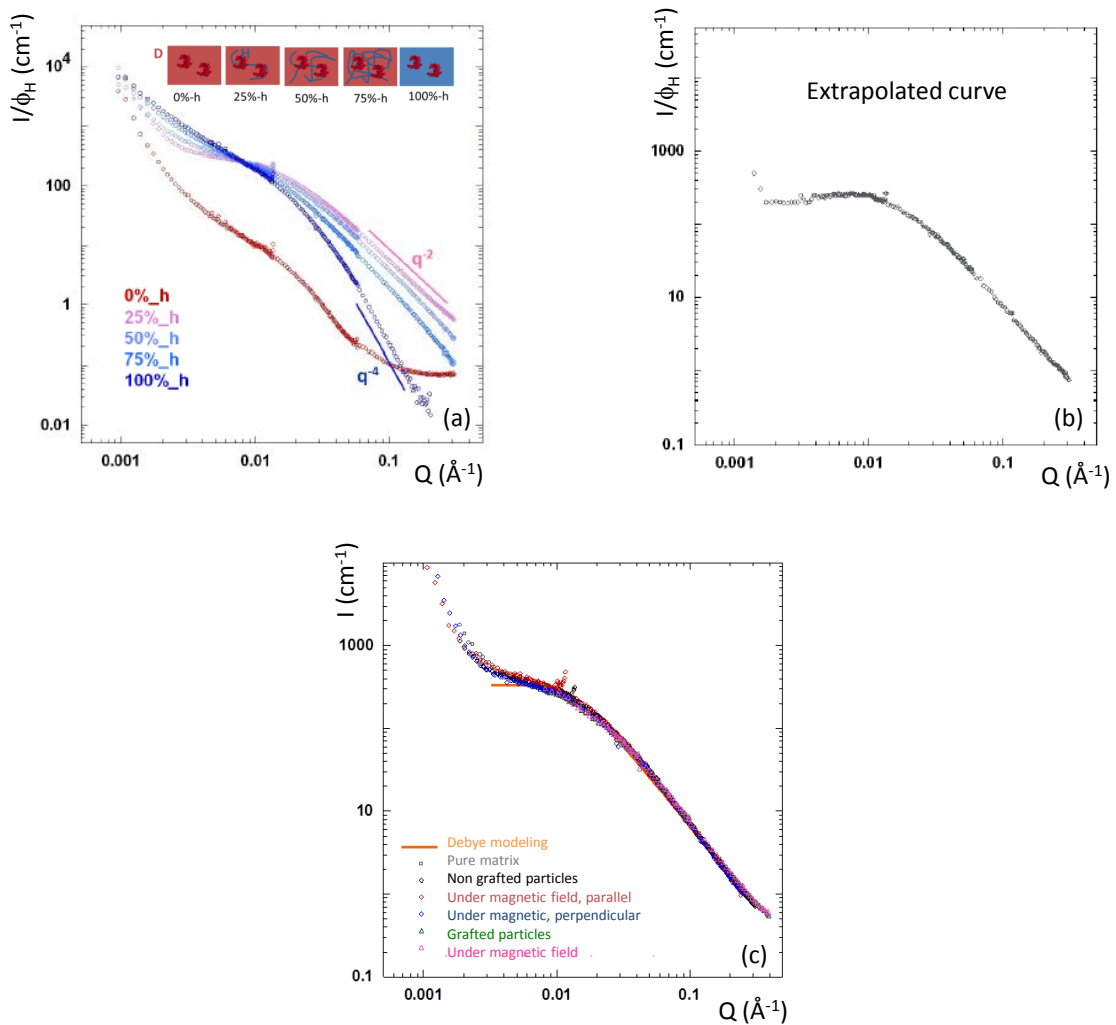


Figure 3.5: (a) SANS scattering curves of increasing volume fraction of H chain inside a D melt mixed with maghemite particles, from zero (crazes) scattering (red) to reveal progressively the filler structure (blue), (b) the chain form factor deduced from the extrapolation at zero concentration for each Q values and each concentration, (c) extrapolated signal for every situation: pure matrix, non-grafted particles, non-grafted particles oriented (parallel), non-grafted particles oriented (perpendicular), grafted particles, grafted particles oriented (parallel).

All situations have been determined experimentally and showed the same scattering signal reported on Figure 3.5c meaning that whatever the situation, the mean form factor of the chain is not influenced directly by the particles. Again for this system, the close proximity of the aggregates described in section 1.2.5.1 is expected to create chain confinement. This seems to be indeed not realized due to the reduction of the polymer chain length to avoid H/D chain phase separation that modified the filler dispersion to simple aggregates which are then too large to induced chain confinement.

3.3 conclusions

We saw that the application of different methods for the determination of polymer chain conformation in nanocomposites enables to clarify ambiguous results related to particle matching or additional low Q scattering. The ZAC method with or without the “grey matrix” as well as the extrapolation method unambiguously confirms the filler matching condition. The additional scattering contribution has been identified as demixing H/D domains induced by the presence of particles that can contribute strongly to the scattering curves even for very low quantities of domains. Including these contributions in the form factor model of the polymer chain conformation leads to a unified conclusion: the polymer chain conformation is not affected (pre-constrained or stretched) by the presence of the filler whatever the system, the filler content and the polymer molecular M_w investigated. However, to reduce the risk of H/D phase separation, we have worked with lower molecular M_w than the one used for filler dispersion. The Change of the M_w of the matrix changes the dispersion and as a consequence, we are never in the case of geometrical confinement for the polymer chains even when close proximity between aggregates was expected. We are thus not able to confirm an effect on the polymer chain conformation induced by larger entanglement density as suggest by mechanical results. The filler has thus no indirect influence on chain conformation. This can be surprising when considering the mechanical conclusions that always find a “long range effective layer” in both elastic and flow regimes. This means that the different origins of this layer (glassy layer or glassy paths, adsorbed layer, bridging) are possible but reduced to a low fraction of chains. An alternative proposition could be that this effect is related to the molecular weight distribution ($I_p = M_w/M_n$) of the polymer chains. All the studied systems used polymers (grafted or not) and elastomers of large I_p , typically around 2. From an empirical point of view, we can thus schematize the nanocomposite matrix as a heterogeneous distribution of long chains (for example 10%), medium chain lengths corresponding to the mean value (80%) and very small chains (10%). We can then consider that all macroscopics or mean chain contributions (chain conformation, filler dispersion, T_g ...) are driven by the 80% of the medium size chains while the mechanical reinforcement and the flow behavior are mostly driven by the 10% of longer chains that could bridge the filler or being confined even for long range inter-filler distances. Of course, such empirical hypothesis remains to be supported by experimental evidences and could be an interesting route of investigation.

CHAPTER 4

FILLER AND CHAIN STRUCTURE UNDER DEFORMATION

The mechanical behavior in the nonlinear regime at large deformation (above >5%) leads to many unsolved questions; for instance, for filled elastomer a decrease of the oscillatory storage modulus is commonly observed when the amplitude of the imposed oscillation is increased (the so-called Payne effect⁶⁴) and mechanical hysteresis is observed during load-unload cycles, with an appreciable change in mechanical properties after pre-straining (the Mullins effect⁶⁵). Many explanations have been proposed to explain the deformation dependence of the storage modulus involving either the polymer chains or the filler structure. Different changes in the dynamics under strain have been proposed. It could be related to desorption of chains immobilized at the filler surface¹⁰⁴, to slippage of entanglements (slip-links) of higher density at the surface or to release of occluded polymer trapped in filler agglomerates. An alternative suggestion is that these effects come from dynamical reorganization of glassy regions (glassy bridges), which can be broken during stretching and slowly rebuild after relaxation through an aging process¹⁰⁵. In addition, models implying structural filler rearrangements (non-affine reorganizations, cyclic filler network breakdown with rupture/re-agglomeration process)¹⁰⁶ have been proposed. SAS measurements on stretched filled-polymer systems can provide useful information among the different solutions. The anisotropy is observed through the 2D patterns of the scattering from either labeled chains (using SANS), or filler embedded in the deformed matrix (SAXS). These patterns display different shapes: ellipse, eight shaped butterflies or double wings depending of many processes inducing variation of interacting distances between the objects (structure), modification of the shape (form factor) or even breaking and rebirth of new entities. One of the challenges to progress in the interpretation of these complex patterns is to be able to dissociate between the different processes.

¹⁰⁴ Chen, J.; Zhang, L. X.; Cheng, J. *J. Chem. Phys.* **2004**, 121, 11481-11488.

¹⁰⁵ Papon, A.; Saalwachter, K.; Schaler, K.; Guy, L.; Lequeux, F.; Montes, H. *Macromolecules* **2011**, 44, 913-922.

¹⁰⁶ Heinrich, G.; Klüppel, M. *Ad. In Pol. Sci.* **2002**, 160, 1-44.

4.1 The grafted brush deformation in nanocomposites

The grafted brush conformation inside nanocomposite whose determination has been described in section 3.1.2 can be analyzed under deformation for different stretching rates. The samples has been stretched at $T_g+20^\circ\text{C}$ and then rapidly quenched at ambient temperature before measurements by SANS. We presented an example for individual grafted particle (10% v/v) on Figure 4.1. The scattering intensity is radially averaged in the parallel direction to the plane of the 2D pattern (a) and in the perpendicular one (b) for elongation rates of $\lambda=1$ and $\lambda=4$. The scattering signal depends only on the form factor of the grafted brushes around the particles. To model the scattering curves, we have modified the isotropic function of Pedersen⁹⁶ by including a radius of the brush depending on the direction (R_{para} and R_{perp}) in addition to the local radius of gyration of the chain R_g . We also included a function (a PY function⁵³) to take into account the inter-particle interactions coming from displacements of the particles under deformation.

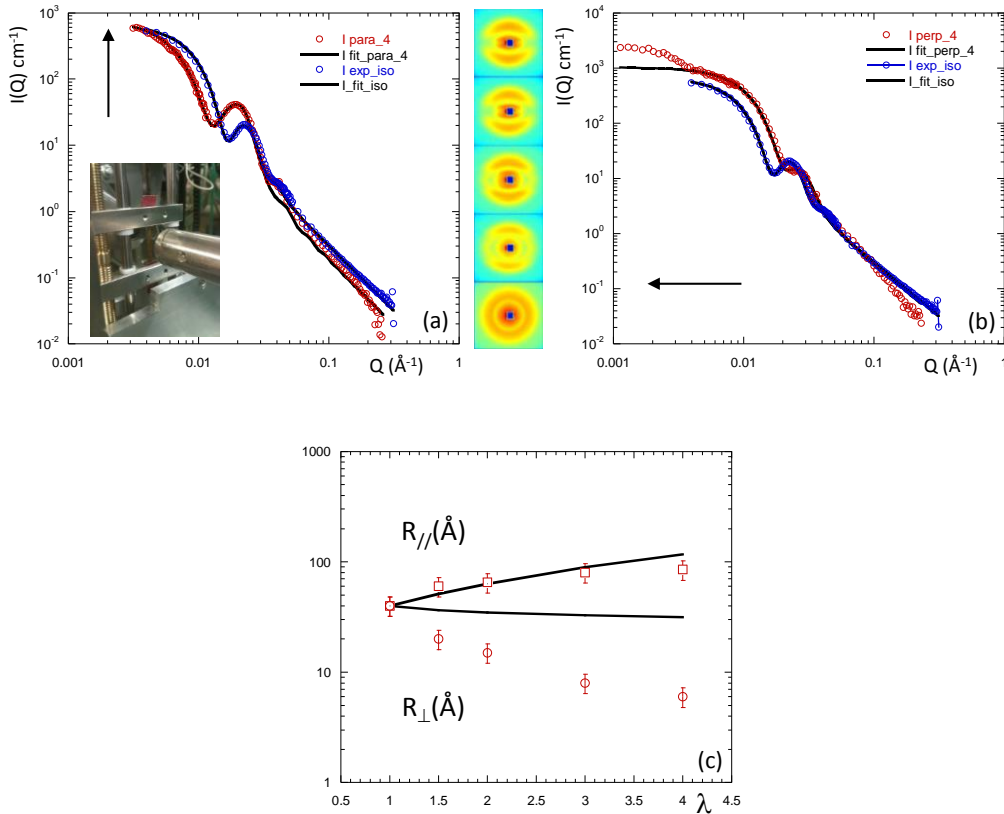


Figure 4.1: 2D SANS patterns and radial averaging along the parallel direction (a) and along the perpendicular one (b) for un-stretched grafted brush signal (blue symbols) and for stretched grafted brush at an elongation ratio of $\lambda=4$ (red symbols), the full black line are the result of the modeling described in the text. Inset: a picture of the setup, (c) radius of the grafted brushes deduced from the modeling as function of the elongation rate and comparison with the affine prediction (full line).

We obtained a good agreement between the model and the experimental curves from which we can extract the variation of the radius of the brush under stretching in both directions. We report these variations as function of the elongation ratio and compare with the expected one for an affine deformation of the chains which is, at a first order, the basic deformation mode for bulk polymer chains. We observe that the parallel deformation of the grafted brush follows nicely the affine estimation. The brush is more deformed in the perpendicular direction in agreement with the reduction of the inter-particle distance d_0 in this direction according to the PY function (d_0 increases in parallel direction). We can then consider that in the perpendicular direction the chain are compressed directly by the particles in close contact. However, when the grafted chain are not directly compressed by the particles (parallel direction), the grafted chains are apparently deformed as in pure melt without being influenced by the surface vicinity. This result is interesting regarding the “effective layer” of chains of modified mobility around the particle that we highlighted on section 2.1 as responsible for reinforcement efficiency. This means that at the typical time probed for chain deformation, we do not see a significant influence of the chain mobility or dynamic on the deformation suggesting that the number of effective chains contributing to reinforcement is limited.

4.2 The bulk chain deformation in nanocomposites

As described in section 3.2, the bulk chain conformation in presence of filler can be accessible using ZAC method. Such determination can be transfer to stretched samples and the evolution of the chain conformation can be followed as function of the elongation ratio. We made these experiments with SANS on the Nissan-PS system for different situations by varying the filler content (from 5 to 15% v/v), the polymer chain length (from 138k to 1777k) and the elongation rates from $\lambda=1$ to $\lambda=6$ ¹⁰⁷. Figure 4.2a shows the SANS results for $M_w=315$ k in directions parallel and perpendicular to the stretching for direct comparison of unfilled and filled polymer matrix at 5% silica, in log-log representation for $\lambda=6$. Intensity maps of the two-dimensional (2D) detector (inset) show strong anisotropy, evidencing the deformation of the chains.

At first sight, particularly striking is the unanimous identity of chain conformation with and without fillers, in both directions, for each elongation ratio. This is true at 5% silica from $\lambda=2$ to $\lambda=6$. It is also true for 15% silica: the samples were much more difficult to stretch, reaching only an elongation ratio $\lambda=1.28$ (not reported here). The chain deformation is unperturbed by the presence of silica contrary to previous study¹⁰⁸, with different characteristic sizes and filler structures in a cross linked matrix. It is not sensitive to any confinement due to filler reorganizations resulting from the deformation either for low filler content (below the percolation threshold) or for large filler content (above the percolation threshold). This effect is also confirmed when increasing the M_w of the polymer.

¹⁰⁷ Jouault, N.; Dalmas, F.; Said, S.; Di Cola, E.; Schweins, R.; Jestin, J.; Boué, F. *Physical Review E* **2010**, 82 (3), 031801.

¹⁰⁸ Westermann, S.; Kreitschmann, M.; Pyckhout-Hintzen, W.; Richter, D.; Straube, E.; Farago, B.; Goerigk, G. *Macromolecules* **1999**, 32, 5793.

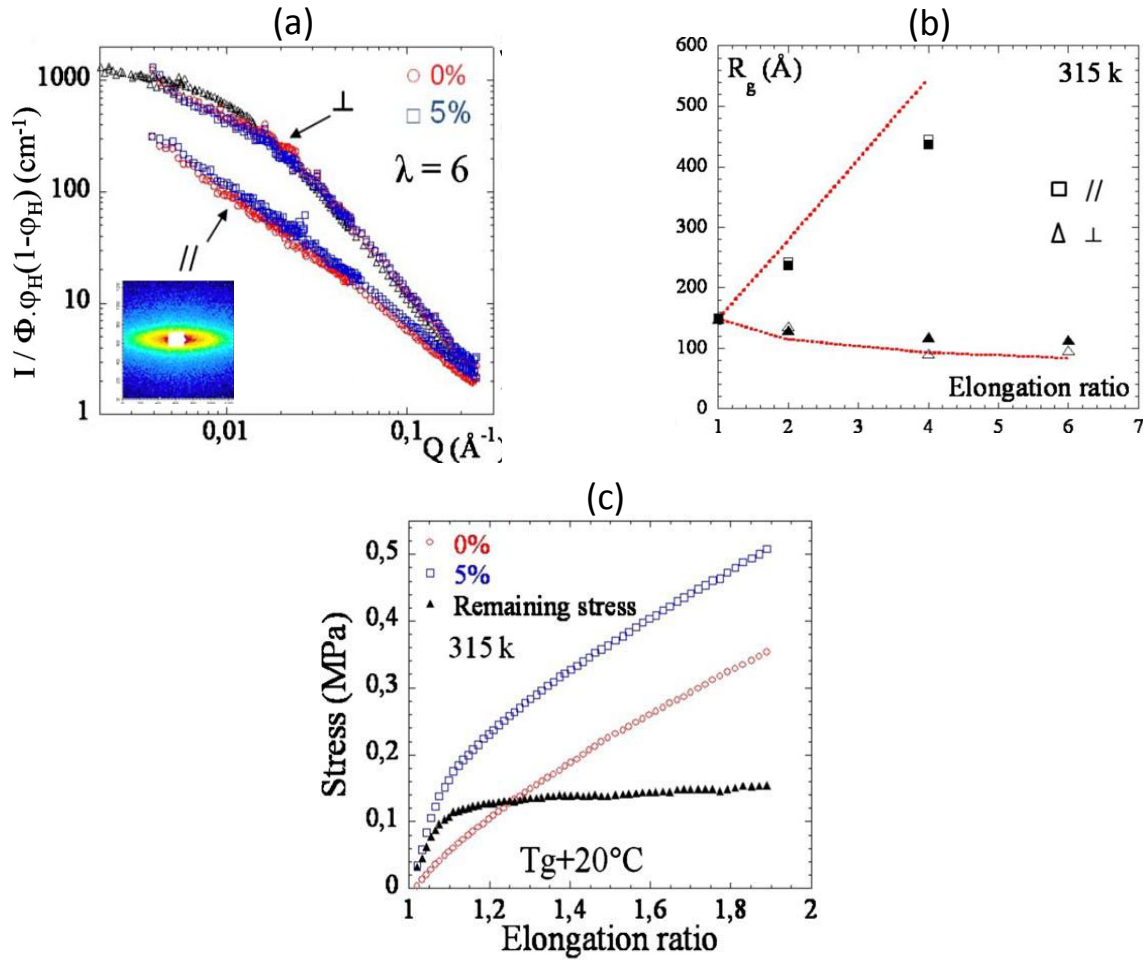


Figure 4.2: (a) SANS results (absolute intensity) from chains in stretched unfilled polymer (red circle symbols) and nanocomposites filled with 5% v/v of silica particles (blue square symbols) for a molecular weight of 315 k in directions parallel (lower symbols) and perpendicular (upper symbols) to the stretching, and for elongation ratio $\lambda=6$. Inset: intensity maps of the 2D detector. Black triangle symbols: isotropic scattering (identical in filled and unfilled un-stretched samples), (b) Radius of gyration of chains of molecular weight 315 k in direction parallel (squares) and perpendicular (triangles) to stretching: experimental result using Debye function for filled 5% v/v full symbols) and (unfilled 0% v/v empty symbols) polymers, and phantom network predictions (dashed red line) assuming one slip link, each with 180 segments, (c) Stress-strain for unfilled polymer (red circles) and 5% filled nanocomposite (blue squares) for $M_w=315$ k.

For the pure PS matrix, the curve is classical for stretched chains, and it has been well described in the literature. At low Q (Guinier regime), the radius of gyration R_g of the deformed chain is determined using the classical Debye function in parallel and perpendicular directions. Its experimental variation is compared in Figure 4.2b with predictions for a chain inside a tube extending the phantom network model by replacing cross links with entanglements slip links. It is known that this can be accounted by implying relaxation between the slip links, i.e., inside the tube, followed by reptation out of the tube. The presence of the filler is expected to modify this behavior for all chains or at least a fraction of them, by creating specific polymer/filler interaction which could apply at short or long range, as a function of the filler structure. This should affect the relaxation processes including reptation of the chains under stretching, but such modification is clearly not observed here. The same result has been obtained with maghemite-PS and Ludox-SBR system under deformation. The second important result concerns the mechanical response: at variance with chain conformation, the mechanical response of the nanocomposites is very different in the pure matrix and in the reinforced polymer. For the samples observed here, the difference in

stress survives at high elongation ratio as highlighted in Figure 4.2c. At this stage, it is worth noting that the curves look as shifted, with respect to the pure polymer curve, by a constant value, increasing with silica fraction. This has two important consequences with respect to the different reinforcement models. Models implying that some chains would connect elastically the fillers predict a stronger deformation of these chains: the absence of such effects suggests a very small fraction of them. In a simplistic picture, glassy chains then would not be largely deformed, with the other chains undergoing most of the deformation: this should also result in a difference in average chain deformation. However, we do not see any temperature dependence when reducing the ΔT_g suggesting again that these processes are possible but concern only a small fraction of chains. As a result, the constant value of the remaining modulus when increasing deformation could be attributed mostly to the contribution of the filler structure.

4.3 The filler network deformation

4.3.1 Oriented network

We investigate the evolution of the filler structure under deformation using SAXS and TEM. We start with a first example which corresponds in principle to the simplest situation, namely the 1D network constituted with aligned chains of particles (described in section 1.2.3) that we stretched in the direction of the particle alignment.

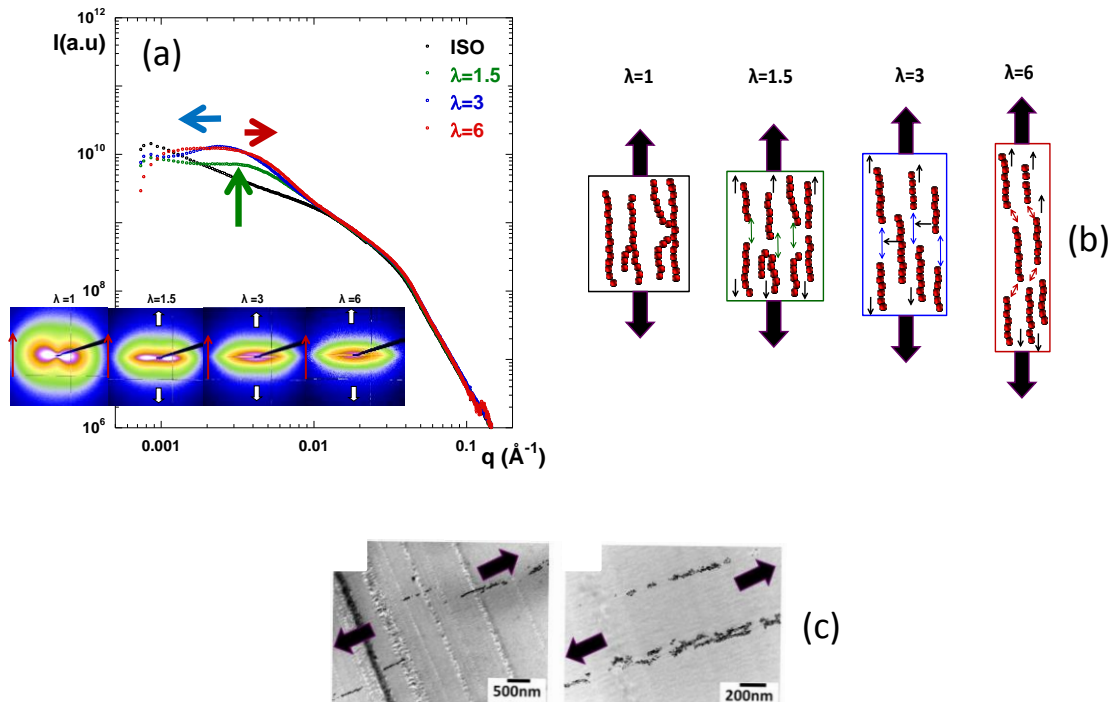


Figure 4.3: (a) 2D SAXS patterns and radial averaging along the parallel direction for the aligned chains of maghemite particle in PS matrix for different elongation rates, (b) sketch of the filler reorganization under deformation in the real space, (c) TEM imaging of the stretched sample at $\lambda=1.5$.

As we have seen in section 2.2, this sample presents a strong anisotropic reinforcement characterized by a larger modulus along the direction of alignment of the filler. At large deformation, we observed a residual stress as in the previous example which is expected to depend mostly on the filler reorganization than on the polymer chain deformation. But the precise mechanism of such reorganization remains to be described.

On Figure 4.3a are reported the SAXS patterns (2D and radial averaging along the parallel direction) on aligned chains of maghemite particles in PS matrix for different elongation ratios. A sketch (b) proposes a possible evolution of the filler structure under deformation⁴⁶ which can be summarized as follows: for the first stretching ratio $\lambda=1.5$, we observe the appearance of a peak (green curve) suggesting a break of the particles chain in sub-unit entities; the peak represents the correlation between these sub-units along the parallel direction. The rupture of the particles chain in sub-unit is visible in the real space on the TEM image (Figure 4.3c). When increasing the elongation to $\lambda=3$ (blue curve), the peak moves toward the small Q values suggesting an enhancement of the distance between the sub-units in the stretching direction. For larger elongation $\lambda=6$, the peak moves back to higher Q values illustrating a new correlation coming from the transverse intercalation of a neighboring sub-entity between two others of the same line. This new correlation appearing at large elongation can lead to offset the loss of modulus due to the move apart of the filler along the stretching direction and thus keeps a mean modulus larger than the one of the pure matrix even at very large deformation.

4.3.1 Effect of network constitution

We complete our investigation of the filler structure under deformation by a direct comparison between two different structures of filler network highlighted on chapter 1: the 3D connected network described on section 1.2.4 for the Nissan-PMMA system and the aggregated network for the Ludox-PMMA system described on section 1.2.5.1. As seen on chapter 2, the morphologies of the primary aggregates as well as the structure of the network are the driving parameters of the elastic reinforcement in the linear regime. Otherwise, these two examples present different structures of primary aggregates: a mesh size larger than the aggregate size for the Nissan and a slight interpenetration of the objects for Ludox. Let's check now the evolution of both types of networks with deformation and correlate it with the mechanical behavior at large deformation. The Figure 4.4 presents the evolution of the network structure under deformation for Nissan, Figure 4.4a and Ludox, Figure 4.4b. From a qualitative point of view, we can see different variations of the scattering curves with the elongation: for Nissan we see mainly a shift of the maximum representing the mesh size of the network toward the low Q value meaning while the scattering behavior is not affected in the intermediate Q range. This means a homogeneous deformation of the network whose typical size is enhanced with deformation without break or change of the primary aggregates. The variation of the peak position follows indeed the prediction for affine deformation.

Conversely, for the Ludox, the low Q maximum is not affected by the deformation while the intermediate Q range is strongly modified suggesting a heterogeneous deformation of the network with a strong modification of the shape of the primary aggregates, clearly visible with the decrease of the slope related to the fractal dimension of the aggregates.

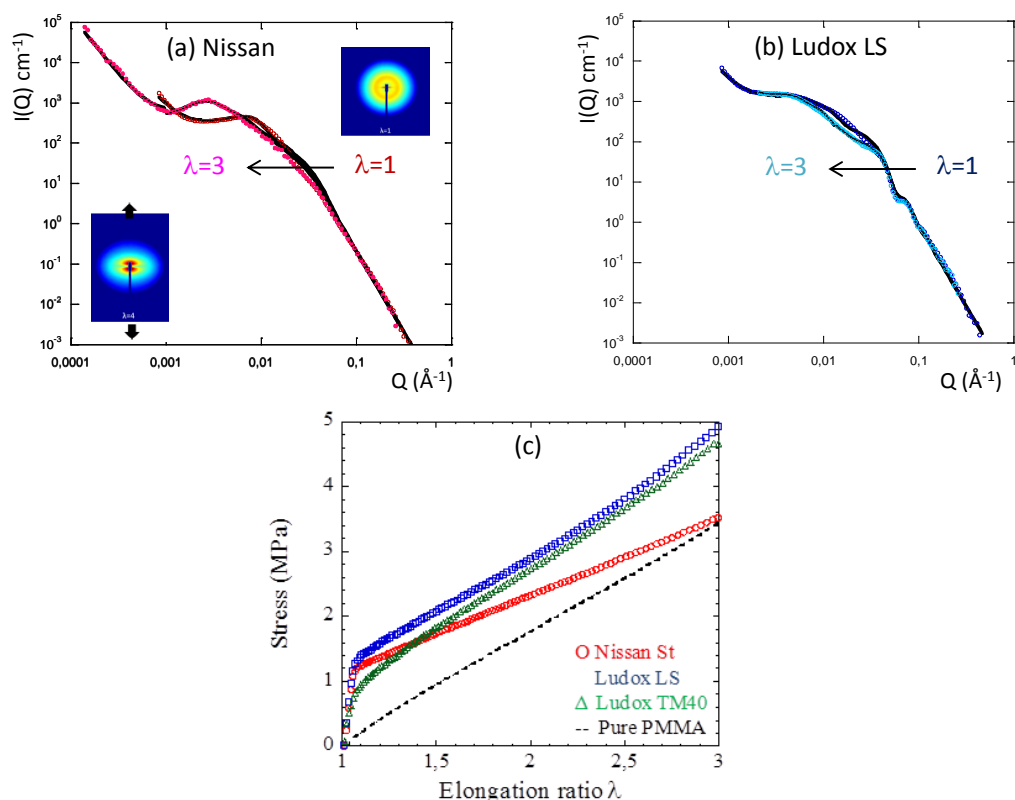


Figure 4.4: (a) SAXS 2D patterns and radial averaging along the parallel direction for the Nissan-PMMA network at 20% v/v of particles for un-stretched ($\lambda=1$, red symbols) and stretched ($\lambda=3$, pink symbols), (b) radial averaging SAXS along the parallel direction for the Ludox-PMMA network at 20% v/v of particles for un-stretched ($\lambda=1$, blue symbols) and stretched ($\lambda=3$, light blue symbols), (c) real stress as function the elongation rate for pure matrix (black line), Nissan (red), Ludox (LS blue and TM green) in PMMA at 20% v/v of filler volume fraction.

The peak maximum do not follows in this case the affine deformation. This qualitative description can be nicely confirmed with modeling starting from the function used on chapter 1 and changing either the form factor or the structure factor between the aggregates to reproduce the scattering curves (full black lines). The real stress behavior reported on Figure 4.4c shows that Nissan network recovers the modulus of the pure matrix at large deformation while a residual stress is maintained even at large deformation for Ludox network. As a consequence, homogenous (affine) deformation gives lower reinforcement while heterogeneous deformation (aggregates form factor modification) leads to an additional stress. We suggest that non-affine deformations are related to the slight overlapping between the primary aggregates¹⁰⁹.

¹⁰⁹ Jouault, N. ; Dalmas, F. ; Boué, F.; Jestin, J. *Macromolecules* **2013**, to be submitted.

4.4 Conclusions

We saw in this last chapter how to determine the polymer chain and the filler structure under deformation in nanocomposite and the correlation with the mechanical behavior in the nonlinear regime. Whatever the situation (grafted or non-grafted) the polymer chain deforms with filler the same way as in the pure polymer. This follows the conclusion of the previous chapter. The mean chain conformation is never constrained or stretched at rest. This means that the effective fraction of chains useful to explain reinforcement and flow behaviors and discussed in the literature according to different models can exist but must concern a reduced fraction of chains. Otherwise, the situation for the filler structure under deformation is clearer. Thanks to a refined knowledge of the different network structure, we are able to describe precisely the evolution of the scattering curves under deformation and to dissociate the effects of form factor variations from the ones of the structure factor. We can then identify that the break of the primary structure network and reorganization lead to additional residual stress at large elongation while homogenous deformation without breaking recovers the stress of the pure matrix.

CHAPTER 5

TOWARD A BETTER DESCRIPTION: CHAIN DYNAMIC AND INTERFACE SETTING

The four preceding chapter have summarized with different examples the correlations between the filler dispersion and the polymer chains conformation with the mechanical and rheological behaviors at rest and under deformation. If some evidences have been clearly identified mainly about the filler network contribution, some unclear points continue to resist to our understanding specifically related to the polymer chain contribution. The physical state of the chains involved in the mechanical processes must be clarified as well as the range of length scale on which this contribution is effective. We think that the most efficient way to answer these questions is to go further on the particle-chain interface.

In this last part, we propose some orientations that we think to be relevant in the description of nanostructured polymer-particle composites. This section is actually a research program that I plan to focus-on in the years to come.

5.1 Chain dynamic

The polymer chain dynamic, i.e., its modification in the presence of particles, is a key point in the field of nanocomposites that opens the discussions on mainly two questions. We have firstly to find the pertinent time scale for which the chain dynamic will influence significantly the rheological properties of the materials. Several time/scale domains have to be considered, short times at the local scale (segmental relaxation) and longer times at larger scales corresponding to the whole chain length (Rouse/reptation modes). Secondly, we have to identify the range of this influence; more or less close to the surface of the particle and possibly extended to longer distances.

We thus would like to develop this topic on the PS grafted silica particles dispersed in a PS matrix. This system presents many advantages. Firstly, we have a perfect knowledge of the synthesis conditions, reproducible enough to give a large amount of well-defined grafted nanoparticles to prepare nanocomposites. Secondly, as also reported in this manuscript, we have a perfect knowledge of the dispersion state of the particles inside the matrix as well as the corresponding effect of the grafted brush conformation. The rheological behavior as a function of the different dispersion states has been already determined. We can thus plan a complete study of the dynamic of the grafted chains and of the free chains by associating different inelastic neutron scattering techniques (INS) benefiting from the opportunity of labeling with deuteration of the grafted brushes or of the matrix chains and thus optimizing the coherent over incoherent ratio. Preliminary experiments have already been performed on different spectrometers.

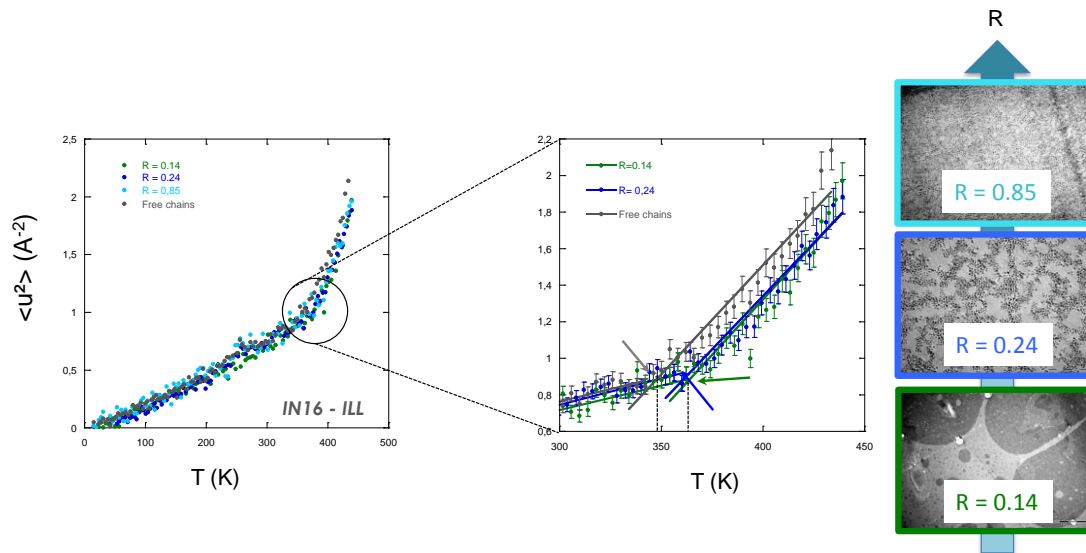


Figure 5.1: Mean Square Displacements MSD as function of the temperature for different grafted to free chain length ratios R for the whole temperature (left), with a focus on the transition (right). TEM picture illustrating the different particle repartitions inside the PS matrix.

We have performed a first experiment on the backscattering spectrometer IN16 at ILL (Grenoble) by comparing the temperature dependence of the Mean Square Displacement (MSD) of low M_w H free chains alone ($M_n=26.4k$) and of the same chains grafted on silica nanoparticles and dispersed in D matrix of various M_w ($M_n=169, 111.3$ and $31k$ giving grafted to free chains ratios $R=0.14, 0.24$ and 0.85). We can observe a significant difference of the MSD temperature dependence between free and grafted chains (Figure 5.1).

The transition between harmonic and an-harmonic behavior can be assimilated to the glass temperature transition T_g of the grafted chains. We can see a positive shift of around 5-10K between the free and the grafted chains illustrating the influence of the grafting on the local chain dynamic. However, no significant effect seems to be correlated with the dispersion state of the particles and as a consequence with the grafted brush conformation that is more collapsed when decreasing R .

This first set of results was completed with Neutron Spin Echo (NSE) measurements that enable to probe the chain dynamic at larger scale and longer times. The first experiments were made on the IN11C spectrometer at ILL. As the M_w of the grafted chain is close to the entanglement M_w for PS ($M_e=18k$), we expect to directly describe the experimental data with the Rouse model and to follow the Rouse parameters at fixed temperature well above (450K) the glass temperature transition. We thus compared the intermediate scattering function $I(Q,t)$ of the free polymer chains (D) with the intermediate scattering function of the same chains grafted on silica particles and dispersed in hydrogenated matrix for two states of particles dispersion (individual and aggregated). The Figure 5.2 reported the results for two typical Q values (0.073 and 0.46 \AA^{-1}) for free chains (Figure 5.2a), grafted chains individually dispersed in the matrix (Figure 5.2b) and aggregated in the matrix (Figure 5.2c). The intermediate scattering function has been normalized by measurement at low temperature. At a first order, these results show that we don't see a significant influence of the particles on the Rouse mode of the chains at this time scale window (up to a few ns). One of the main issues is to see whether the complete chain relaxation is affected by the filler. We thus have to probe the longer relaxation times in the reptation regime at lower Q values while having the possibility to look for the single chain scattering signal using the "grey matrix" to match the contribution of the silica particles. Such experiment is possible on IN15 at ILL. Some preliminary tests have been performed recently. We can investigate a low Q domain (from 0.03 to 0.08 \AA^{-1}) and have access to typical times up to 300 ns.

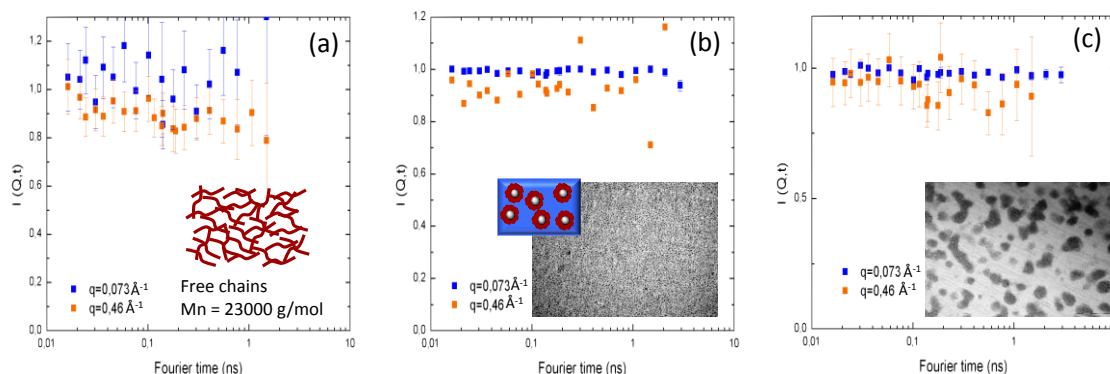


Figure 5.2: Normalized NSE (IN11) intermediate scattering function at $T=450K$ for (a) free deuterated chains, (b) grafted deuterated chains dispersed individually inside the hydrogenated matrix, (c) grafted deuterated chains dispersed as compact aggregates inside the hydrogenated matrix.

We compared the intermediate scattering function of the single chains (D) with the scattering of the same chains grafted around the particles dispersed in the "grey matrix" enabling to see mainly

the grafted chains contribution. The results presented on Figure 5.3 show that even at very long time, we do not see a significant influence of the filler on the chain dynamic.

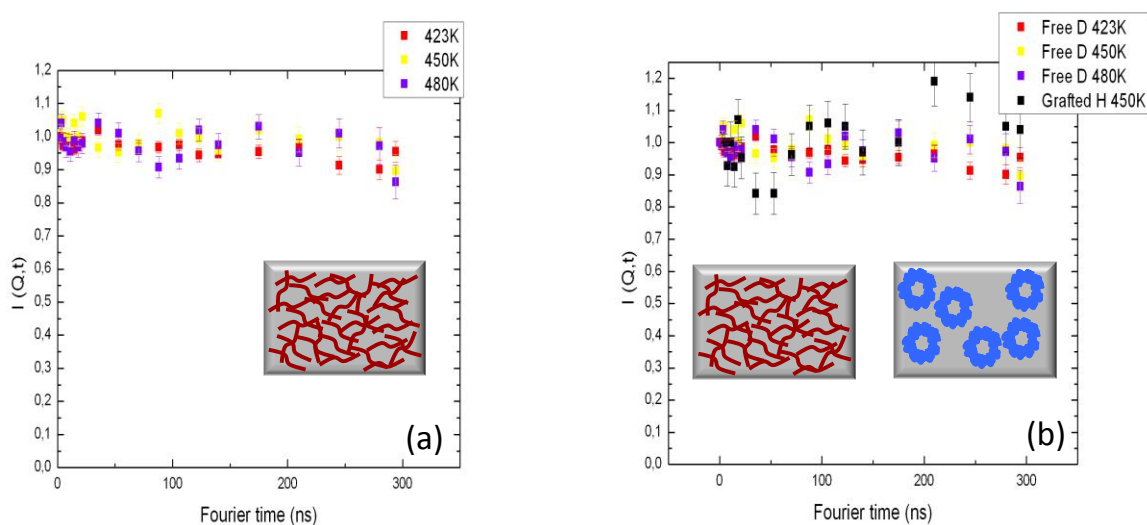


Figure 5.3: Normalized NSE (IN15) intermediate scattering function at $Q=0.07 \text{ \AA}^{-1}$ for (a) free deuterated chains inside the “grey matrix” for different temperatures and (b) comparison with the same hydrogenated grafted at the surface of the silica particles individually dispersed in the “grey matrix” at $Q=0.036 \text{ \AA}^{-1}$.

These results must be considered carefully because they deserve further analysis and must be confirmed with additional experiments. However, they appear to be rather not obvious and unexpected regarding the viscoelastic behaviors of the materials discussed previously. This thus motivates the necessity to address completely this question. This work is currently under progress with the PhD thesis of Nicolas Genevaz.

5.2 Interface setting

5.2.1 Di-block grafting

The polymer-filler interface is of a significant importance for many mechanisms in nanocomposites. One strategy to progress in the understanding consists in setting systematic variations of the polymer-filler interface to evaluate the consequences on the viscoelastic properties of the materials. Such approach has been tested several times in the past and recently¹¹⁰ using filler surface modifications by the way of grafting or additives or other types of compatibilizer molecules. It could be however sometimes difficult to conclude for two main reasons. First the characterization of the molecules at the interface could be difficult (grafting density, conformation...). Secondly, most of the time, the modification of the interface leads inevitably to change the filler dispersion. It becomes then delicate to dissociate the contribution coming from the interface modification from the one coming from the filler dispersion modification.

¹¹⁰ Le Strat, D.; Dalmás, F.; Randriamahefa, S.; Jestin, J.; Wintgens, V. *Polymer* **2013**, 54 (5), 1466-1479.

In this context, we suggest an alternative strategy based on developing processes enabling to modify the polymer-filler interface while keeping the filler dispersion unmodified. The idea is to set the interface mobility by adapting our grafting synthesis to a di-block copolymer presenting two blocks with different T_g , one low T_g block and one high T_g block. The first part of the di-block copolymer grafted at the surface of the particles can be the poly-(ter-butylacrylate-*b*-styrene ($T_g=30^\circ\text{C}$). Then keeping the living character of the radical polymerization enables to change the monomer and to restart the polymerization with the second monomer, the polystyrene PS ($T_g=100^\circ\text{C}$) for the high T_g part. Using PS as the second part of the di-block yields the control of the particle dispersion as for the previous case of the full PS grafted chain by the way of the free to grafted chain ratio R . This would be an encouraging way to compare directly for similar particles dispersion, either individual particles or aggregates, the consequences of the interface mobility related to a gradient of T_g on the viscoelastic behaviors of the nanocomposites.

5.2.1 Photo-cleavable interface

To be able to tune directly the polymer-filler interface with an external trigger, without to input chemical modifications inside the nanocomposites should certainly allow great progress. That could be in principle possible using an additional linker between the particle and the grafted polymer chains that could be cleaved under external UV radiations. The addition of such a linker could be done by adapting our synthesis of PS grafting on silica nanoparticles. Again, we should be able to keep the control of the particle dispersion with the grafted to free chains ratio R . That should opens the way to new experiments of rheological (oscillatory shear) or mechanical (uni-axial stretching) tests under UV radiation to measure directly the consequences of the in-situ chain cleaving on viscoelastic behaviors. The grafted to cleaved chains ratio, that could be controlled and adjusted with the radiation duration or intensity, will enable a direct tuning of the polymer-chain interactions.

5.3 Additional perspectives: chain distribution and particles dynamic

To complete this project, we propose two additional approaches. The first one already mentioned in the manuscript consists in identifying the effects of the molecular chain distribution of the polymer chains on the properties of the nanocomposites, the filler dispersion and rheological behavior. We indeed suggest that anomalous viscoelastic behaviors highlighted in this study could be explained by the contribution of a few fraction of long chains inevitably presented in a polymer melt of large broad weights distribution (typically $M_w/M_n\sim 2$). At the same time, this fraction is too low to be modified and have an influence on the mean chain characteristics (chain conformation) or on the macroscopic thermal behaviors of the material (T_g etc...). Up to day, only a very few experimental works exist on the molecular M_w distribution effects in nanocomposites¹¹¹. This can be extended to systematic studies by probing the viscoelastic properties (mainly in the flow regimes) of nanocomposites at fix filler volume fraction by varying the molecular distribution of the polymer matrix (from $M_w/M_n\sim 1$ to 3). One can suppose that the molecular M_w distribution has a limited influence on the filler structure whose range remains also to be checked.

¹¹¹ Triebel, C.; Kunzelmann, P.; Blankenburg, M.; Münstedt, H. *Polymer* **2011**, 52, 3621-3626.

The network relaxation or a long time relaxation of the component of the filler network (aggregates or agglomerates) are sometimes mentioned in some published papers to contribute to the rheological behavior at low frequency. The filler relaxation in nanocomposites can be studied with X-rays Photon Correlation Spectroscopy (XPCS) for example on grafted nanoparticles¹¹² or on elastomer filled with silica or carbon black on stretched samples¹¹³. It should be interesting to have access to such (longer) time range scale and push the X-rays/neutrons complementarity even for dynamic studies by associating the polymer chain dynamic by NSE with XPCS on similar filled samples.

¹¹² Ackora, P. ; Kumar, S. K. ; Moll, J.; Lewis, S.; Schadler, L. S.; Li, Y.; Benicewicz, B. C.; Sandy, A.; Narayanan, S.; Ilavsky, J.; Thiyagarajan, P. *Macromolecules* **2010**, 43, 1003–1010.

¹¹³ Ehrburger-Dolle, F.; Morfin, I.; Bley, F.; Livet, F.; Heinrich, G.; Richter, S.; Piché, L.; Sutton, M. *Macromolecules* **2012**, 45 (21), 8691-8701.

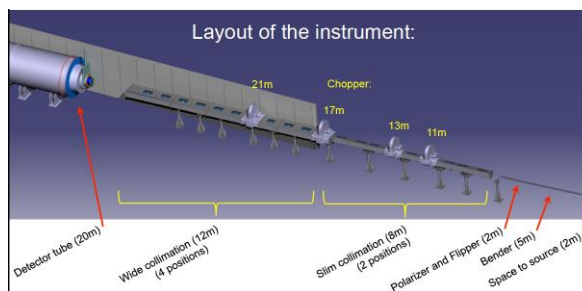
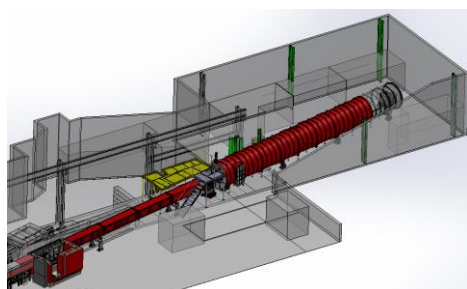
CONCLUSIONS AND OUTLOOK

Nano-structured polymer-particles are attractive systems presenting many stimulating challenges for industrial applications and fundamental researches in polymer physics. Due to the large variety of the possible assemblies, a significant effort remains to be done to give the general scheme that drives the nano-structures of the systems and their macroscopic properties to improve the performances and be able to predict the behaviors as function of a dedicated application. Separating the contributions of the particles from the one of the polymers to the viscoelastic properties is a strong issue to identify the mechanisms.

Using different systems, colloidal/industrial silica, and magnetic nano-particles dispersed in polymer and elastomer matrix, we developed several strategies to control first the particles dispersion inside the matrix described in chapter 1. We used an incremental approach which consists in starting with model systems, defined as well as possible, to go progressively to more complex ones and closer to “real” industrial mixtures. Thanks to chemical grafting, magnetic fields, additives or controlled sample processing, we can tune the filler dispersion along a broad range of particles arrangements from individual particles, compact aggregates, or oriented chains to networks of various constitutions (continuously connected or made of multi-size objects). Some mechanisms driving the final dispersion have been clearly identified: mixing entropy for grafted particles, dipolar interaction for magnetic particles as well as diffusion limited aggregation mediated by viscosity or covalent bond for silica particles. Imaging methods like TEM are very powerful and essential to characterize the structure especially at the micrometer length scale. In complement, scattering techniques like SAXS can provide a quantitative description of the particle multi-step organization from the primary particle size (~ 1 nm) to large structures (a few hundred of nm). Simple analytical functions enable to describe quantitatively the whole lengths scale of the systems; the morphologies of the primary particles, the primary aggregates (shape, size, and compactness) as well as the interactions between the different entities. One has some limitations to describe the very large structure (secondary aggregates) and the interactions between the primary particles inside one aggregate that works only for large and compact objects. We can finally classify the different networks, more or less connected and compacted and then confront this classification to the viscoelastic behaviors. These behaviors can be described in chapter 2 with hydrodynamical or percolating models showing that mechanical reinforcement is driven by the aggregate morphologies as well as by the inter-particles and inter-aggregates interactions. Some variations to this general trend suggest a contribution of the polymer chain on reinforcement, of conformational or dynamical origin that appears to be even more significant in the flow regime for which no direct correlation with the filler organization can be establish. This contribution can be either a long range effect or related to a geometrical confinement whose physical origin (glassy-like chains, entanglement density, bridging effects...) is currently actively debated in the literature. We demonstrate in chapter 3 with SANS and different contrast variations methods that the mean polymer chain conformation (and the chain deformation in chapter 4) is not directly modified by the filler. This suggests that the quantity of polymer chains involved in viscoelastic processes is reduced to a low volume fraction. We propose an influence of the polymer matrix M_w distribution that could be the scope of further experiments. Otherwise, nonlinear mechanical behaviors can be directly related to filler reorganization (aggregate form factor break and rebuild) as showed in the chapter 4.

We saw across this work that some clear general trends can be exposed even on variable complex systems while specific or anomalous behaviors are still visible due to unresolved mechanisms. We propose some scientific outlooks that should allow significant progress in the understanding described in chapter 5. One essential point is to identify the physical state of the polymer chains involved in the mechanical process. This could be a difficult task if the number of involved chain is supposed to be low. To do that, we propose to focus on the polymer-interface by first looking at the chain dynamic effects using inelastic neutron scattering techniques, neutron spin echo and backscattering spectrometer associated with a large choice of hydrogenated/deuterated combinations offered by our PS-grafted-silica-PS system. In a second step, we propose to develop some chemical processes to modify in-situ either the interface dynamic by grafting a di-block copolymer presenting two different T_g s (a high T_g block and a low T_g block) or the polymer-particle interactions by grafting a photo sensible linker between the chain and the particles that could be cleaved using UV radiations.

In a more extended view, we think that the scale-up to “real” industrial systems will be an essential issue in the next few years. Improving the materials performances needs a better knowledge of the local nanoscale structure of the systems. Across our collaboration with Michelin, we developed experimental methods and analytical tools allowing the extraction of some general behaviors even for complex multi-component systems. In a longer term outlook, such close collaborations with industrial partners can also drive and support new instrumentals developments of SANS spectrometers (but also on Synchrotron SAXS machines). For example, great benefits could be obtained from specific new sample environments to measure directly in the neutron beam the “real-time” viscoelastic properties of the reinforced elastomers (under stretching or shear) or the “real-time” dispersion processes with a mixing machine designed specifically for the SANS spectrometer. Such time-resolved performances will be accessible on the new SANS “PA20” spectrometer currently under development at the LLB and will be operating next year at the end of 2014 (Figure below on the left).



Left: Future layout of the Small Angle Neutron Scattering spectrometer at LLB, PA20 in the Orphée Guide Hall. From left to right, the heavy concrete casemate housing the monochromator, the polarizer and the spin flipper located at the end of the G5 guide, the 16m long collimator, the sample area with an upper platform, and the 20m long cylindrical tank housing the detectors. **Right:** Layout of SKADI SANS proposal for ESS. All lengths and positions (yellow) are given in m. The drawing is to scale, but the full length of the detector tube is hidden.

This new spectrometer will present a longer sample to detector distance (20m) enabling to operate at short wavelength (6Å, the maximum of the neutron flux) while benefiting from a multi-detector design (one for the small Q range and another one for the high Q range) and of the time of flight mode to cover a large Q range in a single shot. This is expected to be a competitive spectrometer whose performances and add-on devices would be benefit for nanocomposite researches.

Neutron science is progressing with the neutron sources and one exiting perspective is the new European Spallation Source (ESS) that will be built in Lund in Sweden around 2020. Most important is the development of the new generation of the SANS machines with dedicated sample environments and strongly supported with ambitious science cases including major societal impacts. Accordingly, we are actively implicated in the SKADI SANS project (Figure above on right part), a German-French consortium between JCNS (Jülich Center for Neutron Science) and the LLB to propose (October 2013) to ESS to build a multi-purposed SANS instrument with focusing VSANS and polarized neutrons. This machine, whose performances are expected to be around 40 times better than D22 at ILL (currently the best SANS machine in the world), will open the way to significant breakthroughs in the field of nanocomposites as well as in a broad range of scientific domains in soft matter, biology, materials and magnetism.

BIBLIOGRAPHY

- [1] Jestin, J.; Simon, S.; Zupancic, L.; Barré, L. *Langmuir* **2007**, 23 (21), 10471-10478.
- [2] Alvarez, G.; Jestin, J.; Argillier, J.-F.; Langevin, D. *Langmuir* **2009**, 25 (7), 3985-3990.
- [3] Simon, S.; Jestin, J.; Palermo, T.; Barré, L. *Energy & Fuels* **2009**, 23, 306–313.
- [4] Jouault, N.; Corvis, Y.; Cousin, F.; Jestin, J.; Barré, L. *Langmuir* **2009**, 25 (7), 3991-3998.
- [5] Corvis, Y.; Barré, L.; Jestin, J.; Gummel, J.; Cousin, F. *Eur. Phys. J. Special Topics* **2012**, 213 (1), 295-302.
- [6] Gummel, J.; Corvis, Y.; Jestin, J.; M'Hamdi, J.; Barré, L. *Eur. Phys. J. Special Topics* **2009**, 168, 171-176.
- [7] Barré, L.; Jestin, J.; Morisset, A.; Palermo, T.; Simon, S. *Oil & Gas Science and Technology* **2009**, 64 (5), 617-628.
- [8] Eyssautier, J.; Levitz, P.; Espinat, D.; Jestin, J.; Gummel, J.; Grillo, I.; Barré, L. *The Journal of Physical Chemistry* **2011**, 115 (21), 6827-6837.
- [9] Lysenko, A.; Jestin, J. ; Barré, L. *to be submitted* **2013**.
- [10] Leblanc, J. L. *Prog. Polym. Sci.* **2002**, 27, 627-687.
- [11] Einstein, A. *Ann. Phys.* **1906**, 17, 549.
- [12] Jing, X.; Zhao, W. ; Lan, L. *J. Mater. Sci. Lett.* **2000**, 19, 377-379.
- [13] Klüppel, M.; Heinrich, G. *Rubber Chem. Technol.* **1995**, 68, 623-651.
- [14] Berriot, J.; Montes, H.; Lequeux, F.; Long, D.; Sotta, P. *Macromolecules* **2002**, 35, 9756–9762.
- [15] Jancar, J.; Douglas, J. F.; Starr, F. W.; Kumar, S. K.; Cassagnau, P.; Lesser, A. J.; Sternstein, S. S; Buehler, M. J. *Polymer* **2010** 51, 3321-3343.
- [16] Vilgis, T. A. *Polymer* **2005**, 46, 4223-4229.
- [17] Sen, S.; Xie, Y.; Bansal, A.; Yang, H.; Cho, K.; Schadler, L. S.; Kumar, S. K. *Eur. Phys. J. Spec. Top.* **2007**, 141, 161–165.
- [18] Oberdisse, J. *Macromolecules* **2002**, 35 (25), 9441–9450.
- [19] Botti, A.; Pyckout-Hintzen, W.; Richter, D.; Urban, V.; Straube, E. *J. Chem. Phys.* **2006**, 124, 174908.
- [20] Dalmas, F.; Cavaillé, J.-Y.; Gauthier, C.; Chazeau, L.; Dendievel, R. *Compos. Sci. Technol.* **2007**, 67, 829–839.
- [21] Favier, V.; Chanzy, H.; Cavaillé, J.-Y. *Macromolecules* **1995**, 28, 6365–6367.
- [22] Wang, Y.-Z.; Zhang, L.-Q.; Tang, C.-H.; Yu, D.-S. *J. Appl. Polym. Sci.* **2000**, 78, 1879–1883.
- [23] Heinrich, G.; Klüppel, M.; Vilgis, T.-A. *Curr. Opin. Solid State Mater. Sci.* **2002**, 6, 195–203.

- [24] Baeza, G. ; P.; Genix, A.-C.; Degrandcourt, C.; Petitjean, L.; Gummel, J.; Couty, M.; Oberdisse, J. *Macromolecules* **2013**, 46 (1), pp 317–329
- [25] Fragouli, D.; Buonsanti, R.; Bertoni, G.; Sangregorio, C.; Innocenti, C.; Falqui, A.; Gatteschi, D.; Davide Cozzoli, P.; Athanassiou, A.; Cingolani, R. *ACS Nano* **2010**, 4 (4), 1873–1878.
- [26] Massart, R. *IEEE Trans. Magn.* **1981**, 17, 1247
- [27] Wang, Y. P.; Shen, Y. Q.; Pei, X. W.; Zhang, S. C.; Liu, H. G. ; Ren, J. M. *React. Funct. Polym.* **2008**, 68, 1225–1230.
- [28] Prucker, O.; Ruhe, J. *Macromolecules* **1998**, 31 (3), 592-601.
- [29] Pyun, J.; Jia, S. J.; Kowalewski, T.; Patterson G. D.; Matyjaszewski, K. *Macromolecules* **2003**, 36, 5094–5104.
- [30] von Werne, T.; Patten, T. E. *J. Am. Chem. Soc.* **1999**, 121, 7409-7410.
- [31] Husseman, M.; Malmstrom, E. E.; McNamara, M.; Mate, M.; Mecerreyes, D.; Benoit, D. G.; Hedrick, J. L.; Mansky, P.; Huang, E.; Russell, T. P.; Hawker, C. J. *Macromolecules* **1999**, 32, 1424–1431.
- [32] Li, C. Z.; Benicewicz, B. C. *Macromolecules* **2005**, 38, 5929–5936.
- [33] El Harrak, A.; Carrot, G.; Oberdisse, J.; Jestin, J.; Boué, F. *Polymer* **2005**, 46, 1095–1104.
- [34] El Harrak, A.; Carrot, G.; Oberdisse, J.; Jestin, J.; Boué, F. *Macromolecular Symposia* **2005**, 226(1), 263-278.
- [35] Oberdisse, J.; El Harrak, A.; Carrot, G.; Jestin, J.; Boué, F. *Polymer* **2005**, 46, 6695–6705, 2005.
- [36] Carrot, G.; El Harrak, A.; Oberdisse, J.; Jestin, J.; Boué, F. *Soft Matter* **2006**, 2 (12), 1043-1047.
- [37] Vinas, J. ; Chagneux, N. ; Gigmès, D. ; Trimaille, T.; Favier, A.; Bertin, D. *Polymer* **2008**, 49, 3639–3647.
- [38] Said-Mohamed, C. ; Niskanen, J. ; Karesoja, M. ; Pulkkinen, P. ; Tenhu, H. ; Daoud, M. ; Lee, L.-T. *Soft Matter* **2011**, 7, 7112-7122.
- [39] Xu, C. ; Ohno, K. ; Ladmiral, V. ; Composto, R. J. *Polymer* **2008**, 49, 3568–3577.
- [40] Chevigny, C. ; Gigmès, D. ; Bertin, D. ; Jestin, J. ; Boué, F. *Soft Matter* **2009**, 5 (19), 3741-3753.
- [41] Chevigny, C. ; Jouault, N. ; Dalmas, F. ; Boué, F. ; Jestin, J. *Journal of Polymer Science Part B-Polymer Physics* **2011**, 49 (11), 781-791.
- [42] Robbes, A.-S. ; Cousin, F. ; Meneau, F. ; Chevigny, C. ; Gigmès, D. ; Fresnais, J. ; Schweins, R. ; Jestin, J. *Soft Matter* **2012**, 8 (12), 3407-3418.
- [43] Husseman, M.; Malmstrom, E. E.; McNamara, M.; Mate, M.; Mecerreyes, D.; Benoit, D. G.; Hedrick, J. L.; Mansky, P.; Huang, E.; Russell, T. P.; Hawker, C. J. *Macromolecules* **1999**, 32, 1424–1431.
- [44] Flood, C.; Cosgrove, T.; Howell, I.; Revell, P. *Langmuir* **2006**, 22, 6923–6930.

- [45] Chevigny, C.; Gigmes, D.; Bertin, D.; Schweins, R.; Jestin, J.; Boué, F. *Polymer Chemistry* **2011**, 2 (3), 567-571.
- [46] Pedersen, J. S. ; Gerstenberg, M. C. ; *Macromolecules* **1996**, 29,1363.
- [47] Jouault, N.; Vallat, P.; Dalmas, F.; Said, S.; Jestin, J.; Boué, F. *Macromolecules* **2009**, 42 (6), 2031-2040.
- [48] Jestin, J.; Cousin, F.; Dubois, I.; Ménager, C.; Schweins, R.; Oberdisse, J.; Boué, F. *Advanced Materials* **2008**, 20 (13), 2533.
- [49] Robbes, A.-S. ; Cousin, F. ; Meneau, F. ; Dalmas, F. ; Boué, F. ; Jestin, J. *Macromolecules* **2011**, 44 (22), 8858–8865.
- [50] Stauer, D. *Introduction to Percolation Theory* **1985**, Taylor and Francis.
- [51] Sunday, D.; Ilavsky, J.; Green, D.L. *Macromolecules* **2012**, 45 (9), 4007–4011.
- [52] Chevigny, C.; Dalmas, F.; Di Cola, E.; Gigmes, D.; Bertin, D.; Boué, F.; Jestin, J. *Macromolecules* **2011**, 44 (1), 122-133.
- [53] Robbes, A.-S.; Cousin, F.; Meneau, F.; Dalmas, F.; Schweins, R.; Gigmes, D.; Jestin, J. *Macromolecules* **2012**, 45 (22), 9220–9231.
- [54] Percus, J. K.; Yevick, G. J. *Phys. Rev. Second Ser.* **1958**, 110 (1), 1–13.
- [55] Wang, X.; Foltz, V. J.; Rackaitis, M.; Böhm, G. G. A. *Polymer* **2008**, 49, 5683–5691.
- [56] Akcora, P.; Liu, H.; Kumar, S. K.; Moll, J.; Li, Y.; Benicewicz, B. C.; Schadler, L. S.; Acehan, D.; Panagiotopoulos, A. Z.; Pryamitsyn, V.; Ganesan, V.; Ilavsky, J.; Thiyagarajan, P.; Colby, R. H.; Douglas, J. *Nat. Mater.* **2009**, 8,354–359.
- [57] Kumar, S.K.; Jouault, N.; Benicewicz, B.; Neely, T. *Macromolecules* **2013**, 46 (9), 3199–3214.
- [58] Smith, G. D.; Bedrov, D. *Langmuir* **2009**, 25, 11239.
- [59] Ghanbari, A.; Nodoro, T. V. M; Leroy, F.; Rahimi, M.; Böhm, M.C.; Müller-Plathe, F. *Macromolecules* **2012**, 45 (1), 572–584.
- [60] de Gennes, P. G. *Macromolecules* **1980**, 13, 1069–1075
- [61] Jouault, N.; Dalmas, F.; Boué, F.; Jestin, J. *Polymer* **2012**, 53 (3), 761-775.
- [62] Robbes, A.-S.; Jestin, J.; Meneau, F.; Dalmas, F.; Sandre, O.; Perez, J.; Boué, F.; Cousin, F. *Macromolecules* **2010**, 43 (13), 5785-5796.
- [63] Cassagnau, P. *Polymer* **2008** 49, 2183-2196.
- [64] Ramier, J.; Gauthier, C.; Chazeau, L.; Stelandre, L.; Guy, L. *J. Polym. Sci., Part B: Polym. Phys.* **2007**, 45 (3), 286–298.
- [65] Schneider, G. J.; Vollnhals, V.; Brandt, K.; S. V. Roth, S. V.; Göritz, D. *J. Chem. Phys.* **2010**, 133, 094902.
- [66] Payne, A. R.; Whitaker, R. E. *Rubber Chem. Technol.* **1971**, 44, 440–478.
- [67] Bueche, F. *J. Appl. Polym. Sci.* **1960**, 4 (10), 107–114.
- [68] Guth, O.; Gold, E. *Phys. Rev.* **1938**, 53:322.

- [69] Tsagaropoulos, G.; Eisenberg, A. *Macromolecules* **1995**, 18, 60676077.
- [70] Berriot, J.; Montes, H.; Lequeux, F.; Long, D.; Sotta, P. *Europhys.Lett.* **2003**, 64 (1), 50–56.
- [71] Akcora, P. ; Kumar, S. K. ; Moll, J. ; Lewis, S. ; Schadler, L. S. ; Li, Y. ; Benicewicz, B. C. ; Sandy, A. ; Narayanan, S. ; Ilavsky, J. ; Thiyagarajan, P. ; Colby, R. H. ; Douglas, J.F. *Macromolecules* **2010**, 43, 1003–1010.
- [72] Ouali, N.; Cavailé J.Y.; Perez J. *Plastics and Rubber Processing and Applications* **1991**, 16, 55-60.
- [73] Kolarik J. *European Polymer Journal* **1997**, 34 (5/6), 5, 85-90.
- [74] Favier V. ; Canova G. ; Shrivastava S. ; Cavailé J.Y. *Polymer Engineering and Science* **1997**, 37 (10), 1732-9.
- [75] Gouyet J.F. *Physique et structures fractales* Paris: Masson, **1992**, p. 234.
- [76] De Gennes P.G. *Journal de Physique Lettres* **1976**, 37, L1-2.
- [77] Nusser, K.; Schneider, G. J.; Pyckhout-Hintzen, W.; Richter, D. *Macromolecules* **2011**, 44 (19), 7820–7830.
- [78] Wang, M.; Hill, R. J. *Soft Matter* **2009**, 5, 3940.
- [79] Bouty, A. ; Petitjean, L. ; Degrandourt, C.; Gummel, J.; Kwasniewski, P.; Boué, F.; Couty, M.; Jestin, J. *Macromolecules* **2013**, to be submitted.
- [80] Robertson, C. G.; Rackaitis, M. *Macromolecules* **2011**, 44, 11771181.
- [81] Sarvestani, A.S.; Picu, C. R. *Polymer* **2004**, 45, 7779-90.
- [82] Nusser, K.; Schneider, G. J.; Richter, D. *Soft Matter* **2011**, 7, 7988.
- [83] Nusser, K.; Schneider, G. J.; Richter, D. *Macromolecules* **2013**, 46 (15), 6263–6272.
- [84] Masnada, E.; Merabia, S.; Couty, M.; Barrat, J.-L. *Soft Matter* **2013**, DOI: 10.1039/c3sm51207j.
- [85] Maas, J. H.; Fler, G. J.; Leermakers, F. A. M.; Stuart, M. A. C. *Langmuir* **2002**, 18(23), 8871–8880
- [86] Termonia, Y. *Polymer* **2009**, 50, 1062–1066.
- [87] Sung, B. J.; Chang, R.; Yethiraj, A. *J. Chem. Phys.* **2009**, 130, 124908.
- [88] Vacatello, M. *Macromol. Theory Simul.* **2002**, 11, 757–765.
- [89] Vacatello, M. *Macromolecules* **2002**, 35, 8191–8193.
- [90] Sharaf, M. A.; Kloczkowski, A.; Sen, T. Z.; Jacob, K. I.; Mark, J. E. *Eur. Polym. J.* **2006**, 42, 796–806.
- [91] Picu, R. C.; Ozmusul, M. S. *J. Chem. Phys.* **2003**, 118, 11239–11248.
- [92] Ozmusul, M. S.; Picu, C. R.; Sternstein, S. S.; Kumar, S. K. *Macromolecules* **2005**, 38, 4495.
- [93] Nakatani, A. I.; Chen, W.; Schmidt, R. G.; Gordon, R. V.; Han, G. C. *Polymer* **2001**, 42, 3713–3722.
- [94] Mackay, M. E.; Tuteja, A.; Duxbury, P. M.; Hawker, C. J.; Van Horn, B.; Guan, Z.; Chen, G.; Krishnan, R. S. *Science* **2006**, 311,1740–1743.

- [95] Botti, A.; Pyckhout-Hintzen, W.; Richter, D.; Urban, V.; Straube, E.; Kohlbrecher, J. *Polymer* **2003**, *44*, 7505–7512.
- [96] Sen, S.; Xie, Y.; Kumar, S. K.; Yang, H.; Bansal, A.; Ho, D. L.; Hall, L.; Hooper, J. B.; Schweizer, K. S. *Phys. Rev. Lett.* **2007**, *98*, 128302.
- [97] Nusser, K.; Neueder, S.; Schneider, G. J.; Meyer, M.; Pyckhout-Hintzen, W.; Willner, L.; Radulescu, A.; Richter, D. *Macromolecules* **2010**, *43*, 98379847.
- [98] Genix, A.-C.; Tatou, M.; Imaz, A.; Forcada, J.; Schweins, R.; Grillo, I.; Oberdisse, J. *Macromolecules* **2012**, *45* (3), 1663–1675.
- [99] Tuteja, A.; Duxbury, P. M.; Mackay, M. E. *Phys. Rev. Lett.* **2008**, *100*, 077801.
- [100] Chevigny, C.; Jestin, J.; Gigmes, D.; Schweins, R.; Di Cola, E.; Dalmas, F.; Bertin, D.; Boué, F. *Macromolecules* **2010**, *43* (11), 4833–4837.
- [101] Jouault, N.; Dalmas, F.; Said, S.; Di-Cola, E.; Schweins, R.; Jestin, J.; Boué, F. *Macromolecules* **2010**, *43* (23), 9881–9891.
- [102] Crawford, M. K.; Smalley, R. J.; Cohen, G.; Hogan, B.; Wood, B.; Kumar, S. K.; Melnichenko, Y. B.; He, L.; Guise, W.; Hammouda, B. *Phys. Rev. Lett.* **2013**, *110*, 196001.
- [103] Bouty, A.; Petitjean, L.; Degrandourt, C.; Meneau, F.; Schweins, R.; Boué, F.; Couty, M.; Jestin, J. *Macromolecules* **2013**, to be submitted.
- [104] Chen, J.; Zhang, L. X.; Cheng, J. *J. Chem. Phys.* **2004**, *121*, 11481–11488.
- [105] Papon, A.; Saalwachter, K.; Schaler, K.; Guy, L.; Lequeux, F.; Montes, H. *Macromolecules* **2011**, *44*, 913–922.
- [106] Heinrich, G.; Klüppel, M. *Ad. In Pol. Sci.* **2002**, *160*, 1–44.
- [107] Jouault, N.; Dalmas, F.; Said, S.; Di Cola, E.; Schweins, R.; Jestin, J.; Boué, F. *Physical Review E* **2010**, *82* (3), 031801.
- [108] Westermann, S.; Kreitschmann, M.; Pyckhout-Hintzen, W.; Richter, D.; Straube, E.; Farago, B.; Goerigk, G. *Macromolecules* **1999**, *32*, 5793.
- [109] Jouault, N.; Dalmas, F.; Jestin, J. *Macromolecules* **2013**, to be submitted.
- [110] Le Strat, D.; Dalmas, F.; Randriamahefa, S.; Jestin, J.; Wintgens, V. *Polymer* **2013**, *54* (5), 1466–1479.
- [111] Triebel, C.; Kunzelmann, P.; Blankenburg, M.; Münstedt, H. *Polymer* **2011**, *52*, 3621–3626.
- [112] Ackora, P.; Kumar, S. K.; Moll, J.; Lewis, S.; Schadler, L. S.; Li, Y.; Benicewicz, B. C.; Sandy, A.; Narayanan, S.; Ilavsky, J.; Thiyagarajan, P. *Macromolecules* **2010**, *43*, 1003–1010.
- [113] Ehrburger-Dolle, F.; Morfin, I.; Bley, F.; Livet, F.; Heinrich, G.; Richter, S.; Piché, L.; Sutton, M. *Macromolecules* **2012**, *45* (21), 8691–8701.

CURRICULUM VITAE

JACQUES JESTIN

Born April 25 1973 (age 40)
47 publications, H index=14
Research scientist CNRS
French

Laboratory Léon Brillouin
French Neutron Facility
CEA/CNRS UMR 12
CEA Saclay
91191 Gif/Yvette France
Tel. +33 1.69.08.52.61
Fax. +33 1.69.08.82.61
jacques.jestin@cea.fr

Academic Qualifications and Scientific Experience

2009-2013 Instrument Scientist Small Angle Neutrons Scattering SANS
2008-2013 Research Scientist 1^{ère} class CR₁
2004-2008 Research Scientist 2^{ème} class CR₂ at Laboratory Léon Brillouin CEA-Saclay
2003-2004 Post-doc position at Laboratory Léon Brillouin CEA-Saclay
2002-2003 Post-doc position at the French Petroleum Research Institute IFPEN Paris
1998-2001 PhD in Physical-chemistry University of Bretagne Occidentale and Soft Condensed Matter Physic Department (SPEC) of CEA-Saclay
1996-1997 DEA of Chemistry, University of Bretagne Occidentale (Brest)

Research Thematic

Nanocomposites, polymers/colloids, reinforced elastomers
Formulation/synthesis, grafting/Controlled Radical Polymerization
Dispersion/Particle aggregation, polymer chain conformation
Small Angle Scattering (X and Neutrons)
Mechanical and rheological properties
Petroleum system, asphaltenes, emulsions, interfacial behavior
Neutron reflectivity

Scientific Awards

PhD award of the French Neutron Society (SFN) 2001
Price of Scientific Excellence (PES) from CNRS 2012

Scientific Production

47 publications (H index=14)
17 oral communications, 4 invited (3 internationals and 1 national)
7 invited seminars

Collectives Responsibilities

- 2012-2013 Co-responsible of the instrumental group « Large Scale Structure » of LLB (8 neutron spectrometers, 20 permanent peoples, researchers and technicians)
- 2012-2013 Project Manager « Working Package VSANS for the long SANS SKADI spectrometer » for ESS (European Spallation Source, Lund, Sweden) in collaboration with JCNS (Forschungszentrum Jülich, Germany).
- 2011-2013 Chemical safety responsible
- 2006-2013 Responsible of the user chemistry lab

Scientific Expertise

- Since 2011 Secretary of the selection committee 1 (Physical-chemistry-biology) of LLB
- 2006-2013 Reviewer for different international journals: *Macromolecules*, *Langmuir* (ACS), *Soft Matter* (RSC), *Polymer* (Elsevier), *Journal of Polymer Science Part B : Polymer Physics* (Wiley), *Journal of Applied Crystallography*...
- 2011 SANS Expert for the instrumental review of the ILL (European Neutron facility) Grenoble France
- 2007-2011 Reviewer for the selection committee of LLB
- Since 2008 PhD jury (8) and recruitment commission (2)

Supervision of PhD

- 2006-2009 C. Chevigny « *Nanocomposites polymère/particules greffées : de la synthèse en solution colloïdale à l'étude des propriétés macroscopiques* » defended on October 10 2009, **6 publications**
PhD award of the French Neutron Society (*SFN*) 2010
- 2006-2009 N. Jouault « *Nanocomposites silice/polymère, structure des charges, renforcement mécanique, conformation des chaînes, évolution sous déformation* » defended on November 3 2009, **6 publications**
- 2008-2011 A.-S. Robbes (with Synchrotron SOLEIL) « *Nanocomposites à base de particules magnétiques: synthèse et contribution de la dispersion des charges et de la conformation des chaînes sur les propriétés de renforcement* » defended on October 14 2011, **4 publications**
- 2010-2013 A. Bouty (with Michelin) « *Structure des charges et conformation des chaînes dans des systèmes SBR/Silice* » in progress.
- 2011-2014 N. Genevaz (with Institute of Radical Chemistry of Marseille) « *Dynamique des chaînes dans les nanocomposites: contribution au renforcement mécanique* », in progress.

Supervision of Master II Student

2005	Sophie Lorrain (ENSCP, Bordeaux) master II, 6 months
2005	Antoine Millet (Ecole des mines, Nancy) master II, 6 months
2006	Gwenaël Bourget (ENSCP, Bordeaux) master II, 6 months
2006	Sébastien Charles (Université d'Evry) master II, 6 months
2008	Zineb Guennouni (INSA, Paris) master II, 6 months (supervised with F. Cousin, LLB).

Supervision of Post-Docs

2007-2008	P. Vallat « Rheology of Nanocomposites »
-----------	--

Teaching Activity

2012-2013	Lecture in Master II Polymer Materials of University of Marseille “Neutron Scattering: principles and applications for materials and complex systems”, 10h/year
2004-2013	SANS Practical: FAN of LLB, HERCULES school, Ecole Centrale of Paris, University Paris 13, 50h/year
2009	Lecture in French Neutron School « data treatment in SANS » JDN 17, School « Neutrons and Soft Matter », la Grande Motte France
2006	Lecture in French Neutron School « data treatment in SANS » JDN 14, School « Surface, Interfaces and Confined media by Neutron Scattering », Murol France

Organization of Meetings and Conferences

Conference	SXNS 10 - International Conference on Surface X-ray and Neutron Scattering, Saint Aubin (Fr.), 07/2008
Workshops	6 ^{ème} LLB/Soleil meeting “Soft Matter”, Saint Aubin (Fr.), 03/2008 (local organization committee) “The Science Case for High Intensity and Focusing SANS at ESS”, Bonn (All.), 05/2013 (local organization committee) in collaboration with JCNS (Forschungszentrum Jülich)
School	“Neutron and Soft Matter”, JDN 17, la Grande Motte (Fr.), 05/2009 (local organization committee)

Industrial Contracts

2005-2007	French Petroleum Research Institute IFPEN « Neutrons Scattering for crude oils characterizations » 15 000 euros (responsible)
2007-2008	ANR Géo-carbone « SANS for rock alteration and CO ₂ storage » 6 000 euros (responsible)
2010-2013	Michelin « Filler dispersion and Chain conformation in SBR/silica systems » 160 000 euros (co-responsible)
2013	French Petroleum Research Institute IFPEN « SANS Characterization of Petroleum Emulsions » for Saudi Aramco, 20 000 euros (responsible)

Local Contact activity

I am actively involved in the local contact activity of the LLB across the welcome of many research teams on the SANS and reflectivity spectrometers. This activity enabled me to have an extended scientific overview and to discover other thematic like glass corrosion [13], copolymer characterization [22, 27], micro-emulsions [26], polymer interdiffusion [35], bio-surfactants [40], micelles for liquid extraction [41], clay pickering [42] fuel cells membranes [44] and organic nanotubes [47].

PUBLICATIONS AND COMMUNICATIONS LIST

Publication list

- [1] **J. Jestin**, L.-T. Lee, M. Privat, G. Zalczer. Test of the universality of the critical adsorption profile by neutrons reflectivity. *Eur. Phys. J. B* 24, 541-547, **2001**.
- [2] A. Menelle, **J. Jestin**, F. Cousin. Liquid interfaces investigated by neutron reflectivity. *Neutrons News*, 14(3), 26-30, **2003**.
- [3] M. Sadiki, F. Quentel, C. Elléouet, J.-P. Huruguen, **J. Jestin**, D. Andrieux, R. Olier, M. Privat. Coadsorption at the air/water interface likely explains some pollutants transfer to the atmosphere: benzene and lead case. *Atmospheric Environment*, 37, 3551-3559, **2003**.
- [4] **J. Jestin**, L. Barré, Application of NMR solvent relaxation and SAXS to asphaltenes solution characterization. *Journal of Dispersion Science and Technology*, 25(3), 34-347, **2004**.
- [5] D. Andrieux, **J. Jestin**, N. Kervarec, R. Pichon, M. Privat, R. Olier, Adsorption mechanism of substituted pyridines on silica suspensions : an NMR study, *Langmuir*, 20, 10591-10598, **2004**.
- [6] A. El Harrak, G. Carrot, J. Oberdisse, **J. Jestin**, F. Boué, Atom Transfer Radical Polymerization from Silica Nanoparticles using the “Grafting From” Method and Structural Study via Small-Angle Neutron Scattering, *Polymer*, 46, 1095–1104, **2005**.
- [7] A. El Harrak, G. Carrot, J. Oberdisse, **J. Jestin**, F. Boué, Control of the colloidal stability of polymer-grafted-silica nanoparticles obtained by Atom Transfer Radical Polymerization, *Macromolecular Symposia* 226(1), 263-278, **2005**.
- [8] J. Oberdisse, A. El Harrak, G. Carrot, **J. Jestin**, F. Boué, Structure and rheological properties of soft-hard nanocomposites: Influence of aggregation and interfacial modification, *Polymer*, 46, 6695–6705, **2005**.
- [9] N. Díaz, F-X. Simon, M. Schmutz, M. Rawiso, G. Decher, **J. Jestin**, P. Mésini, Self-Assembled Diamide Nanotubes in Organic Solvents, *Angewandte Chemie*, 117(21), 3324–3328, **2005**.
- [10] G. Carrot, A. El Harrak, J. Oberdisse, **J. Jestin**, F. Boué, Polymer grafting from 10-nm individual particles: proving control by neutron scattering, *Soft Matter*, 2 (12), 1043-1047, **2006**.
- [11] **J. Jestin**, S. Simon, L. Zupancic, L. Barré, A small angle neutron scattering study of the adsorbed asphaltene layer in water-in-hydrocarbon emulsions: Structural description related to stability, *Langmuir*, 23 (21), 10471-10478, **2007**.
- [12] **J. Jestin**, F. Cousin, I. Dubois, C. Ménager, R. Schweins, J. Oberdisse, F. Boué, Anisotropic reinforcement of nanocomposites tuned by magnetic orientation of the filler network, *Advanced Materials*, 20 (13), 2533, **2008**.
- [13] C. Cailleateau, F. Angéli, F. Devreux, S. Gin, **J. Jestin**, P. Jollivet, O. Spalla, Insight into silicate glass corrosion mechanisms, *Nature Materials*, 7, 978-983, **2008**.

- [14] S. Simon, **J. Jestin**, T. Palermo, L. Barré, Relation between solution and interfacial properties of asphaltene aggregates, *Energy & Fuels*, 23, 306–313, **2009**.
- [15] N. Jouault, P. Vallat, F. Dalmas, S. Said, **J. Jestin**, F. Boué, Well dispersed fractal aggregates as filler in polymer-silica nanocomposites: long range effects in rheology, *Macromolecules*, 42 (6), 2031-2040, **2009**.
- [16] N. Jouault, Y. Corvis, F. Cousin, **J. Jestin**, L. Barré, Asphaltene adsorption mechanisms at the local scale probed by neutron reflectivity: transition from mono to multilayer growth above flocculation threshold, *Langmuir*, 25 (7), 3991-3998, **2009**.
- [17] G. Alvarez, **J. Jestin**, J.-F. Argillier, D. Langevin, A Small Angle Neutron Scattering study of crude oil emulsions. Structure of the oil-water interfaces, *Langmuir*, 25 (7), 3985-3990, **2009**.
- [18] J. Gummel, Y. Corvis, **J. Jestin**, J. M'Hamdi and L. Barré, Asphaltene multilayer growth in porous medium probed by SANS, *Eur. Phys. J. Special Topics*, 168, 171-176, **2009**.
- [19] F. Cousin, **J. Jestin**, G. Chaboussant, S. Gautrot, A. Menelle, F. Ott, GISANS: a scattering technique to measure simultaneously the structure of objects on the surface and in the bulk at a solid–liquid interface, *Eur. Phys. J. Special Topics*, 168, 177-183, **2009**.
- [20] L. Barré, **J. Jestin**, A. Morisset, T. Palermo, S. Simon, Relation between nanoscale structure of asphaltene aggregates and their macroscopic solution properties, *Oil & Gas Science and Technology*, 64 (5), 617-628, **2009**.
- [21] C. Chevigny, D. Gigmes, D. Bertin, **J. Jestin**, F. Boué, Polystyrene grafting from silica nanoparticles via nitroxide-mediated polymerization (NMP): synthesis and SANS analysis with the contrast variation method, *Soft Matter*, 5 (19), 3741-3753, **2009**.
- [22] E. Lejeune, C. Chassenieux, O. Colombani, M. Drechsler, **J. Jestin**, A. H. E. Müller, Amphiphilic diblock copolymers with a tempered hydrophobic block: the key towards dynamic micelles, *Macromolecules*, 43 (6), 2667–2671, **2010**.
- [23] C. Chevigny, **J. Jestin**, D. Gigmes, R. Schweins, E. Di Cola, F. Dalmas, D. Bertin F. Boué, “Wet-to-Dry” Conformational Transition of Polymer Layers Grafted to Nanoparticles in Nanocomposites, *Macromolecules*, 43 (11), 4833–4837, **2010**.
- [24] A.-S. Robbes, **J. Jestin**, F. Meneau, F. Dalmas, O. Sandre, J. Perez, F. Boué, F. Cousin, Homogeneous Dispersion of Magnetic Nanoparticles Aggregates in a PS Nanocomposite: Highly Reproducible Hierarchical Structure Tuned by the Nanoparticles’ Size, *Macromolecules*, 43 (13), 5785-5796, **2010**.
- [25] N. Jouault, F. Dalmas, S. Said, E. Di Cola, R. Schweins, **J. Jestin**, F. Boué, Direct SANS Observation of Stretched Chain Conformation in Nanocomposites: More Insight of Polymer Contributions in Mechanical Reinforcement, *Physical Review E*, 82 (3), 031801, **2010**.
- [26] N. Puesh, S. Mora, T. Phou, G. Porte, **J. Jestin**, J. Oberdisse, Microemulsion nanocomposites: phase diagram, rheology and structure using a combined small angle neutron scattering and reverse Monte Carlo approach, *Soft Matter*, 6 (21), 5605-5614, **2010**.
- [27] J. Causse, J. Oberdisse, **J. Jestin**, S. Lagerge, Small-Angle Neutron Scattering study of solubilization of tributyl phosphate in aqueous solutions of L64 Pluronic triblock copolymers, *Langmuir*, 26 (20), 15745-15753, **2010**.

- [28] N. Jouault, F. Dalmas, S. Said, E. Di-Cola, R. Schweins, **J. Jestin**, F. Boué, Direct Measurement of Polymer Chain Conformation in Well Controlled Model Nanocomposites by combining SANS and SAXS, *Macromolecules*, 43 (23), 9881-9891, **2010**.
- [29] F. Cousin, I. Grillo, **J. Jestin**, J. Oberdisse, *Une Brève Introduction à la Matière Molle*, DOI: 10.1051/sfn/201011001 "Neutrons et Matière Molle" Collection SFN 11 (**2010**) 1–6. Editeurs: F. Cousin, A.–C. Genix, I. Grillo, J. Jestin, J. Oberdisse
- [30] C. Chevigny, D. Gigmes, D. Bertin, R. Schweins, **J. Jestin**, F. Boué, Controlled grafting of polystyrene on silica nanoparticles using NMP: a new route without free initiator to tune the grafted chain length, *Polymer Chemistry*, 2 (3), 567-571, **2011**.
- [31] C. Chevigny, F. Dalmas, E. Di Cola, D. Gigmes, D. Bertin, F. Boué, **J. Jestin**, Polymer-Grafted-Nanoparticles Nanocomposites: Dispersion, Grafted Chain Conformation and Rheological Behavior, *Macromolecules*, 44 (1), 122-133, **2011**.
- [32] G. Bealle, **J. Jestin**, D. Carrière, Osmotically induced deformation of capsid-like icosahedral vesicles, *Soft Matter*, 7 (3), 1084-1089, **2011**
- [33] J. Eyssautier, P. Levitz, D. Espinat, **J. Jestin**, J. Gummel, I. Grillo, L. Barré, Insight into Asphaltene Nano-Aggregate Structure Inferred by Small Angle Neutron and X-Ray Scattering, *The Journal of Physical Chemistry*, 115 (21), 6827-6837, **2011**.
- [34] C. Chevigny, N. Jouault, F. Dalmas, F. Boué, **J. Jestin**, Tuning the Mechanical Properties in Model Nanocomposites: Influence of the Polymer-Filler Interfacial Interactions, *Journal of Polymer Science Part B-Polymer Physics*, 49 (11), 781-791, **2011**.
- [35] S. Coppée, S. Gabriele, A. M. Jonas, **J. Jestin**, P. Damman, Influence of Chain Interdiffusion Between Immiscible Polymers on Dewetting Dynamics, *Soft Matter*, 7 (21), 9951-9955, **2011**.
- [36] A.-S. Robbes, F. Cousin, F. Meneau, F. Dalmas, F. Boué, **J. Jestin**, Nanocomposite Materials with Controlled Anisotropic Reinforcement Triggered by Magnetic Self-Assembly, *Macromolecules*, 44 (22), 8858–8865, **2011**.
- [37] N. Jouault, F. Dalmas, F. Boué, **J. Jestin**, Multiscale Characterization of Filler Dispersion and Origins of Mechanical Reinforcement in Model Nanocomposites, *Polymer*, 53 (3), 761-775, **2012**.
- [38] A.-S. Robbes, F. Cousin, F. Meneau, C. Chevigny, D. Gigmes, J. Fresnais, R. Schweins, **J. Jestin**, Controlled Grafted Brushes of Polystyrene on Magnetic γ -Fe₂O₃ Nanoparticles via Nitroxide-Mediated Polymerization, *Soft Matter*, 8 (12), 3407-3418, **2012**.
- [39] G. Pabst, C. Loney, M. Vandenbranden, **J. Jestin**, A. Radulescu, J.-M. Ruyschaert, T. Gutberlet, Novel Fusion Mechanism for the Cationic Lipid Amidine, *Soft Matter*, 8 (27), 7243-7249, **2012**.
- [40] N. Baccile, F. Babonneau, G. Pehau-Arnaudet, **J. Jestin**, I. Van Bogaert, Unusual, pH-induced, Self-assembly of Sophorolipid Biosurfactants, *ACS Nano*, 6 (6), 4763, **2012**.
- [41] S. Dourdain, I. Hofmeister, O. Pecheur, J-F. Dufrêche, R. Turgis, A. Leydier, **J. Jestin**, F. Testard, S. Pellet-Rostaing, T. Zemb, Synergy by co-assembly at the origin of ion selectivity in liquid-liquid extraction, *Langmuir*, 28 (31), 11319-11328, **2012**.
- [42] F. Muller, A. Salonen, J. Degrouard, **J. Jestin**, A. Brûlet, How Clay Colloids Surround Internally Self-assembled Phytantriol Drops, *Soft Matter*, 8 (40), 10502-10510, **2012**.

- [43] Y. Corvis, L. Barré, **J. Jestin**, J. Gummel, F. Cousin, Asphaltene Adsorption Mechanism under Flow probed by *in situ* Neutron Rheo-reflectivity Measurements, *Eur. Phys. J. Special Topics*, 213 (1),295-302, **2012**.
- [44] R. Sood, C. Iojoiu, E. Espuche, F. Gouanvé, G. Gebel, H. Mendil-Jakani, S. Lyonnard, **J. Jestin**, Proton Conducting Ionic Liquid Doped Nafion Membranes: Nano-Structuration, Transport Properties and Water Sorption, *The Journal of Physical Chemistry C*, 116 (46), 24413-24423, **2012**.
- [45] A.-S. Robbes, F. Cousin, F. Meneau, F. Dalmas, R. Schweins, D. Gigmes, **J. Jestin**, Polymer-grafted magnetic nanoparticles in nanocomposites: Curvature effects, conformation of grafted chain, and bimodal nano-triggering of filler organization by combination of chain grafting and magnetic field, *Macromolecules*, 45 (22), 9220–9231, **2012**.
- [46] D. Le Strat, F. Dalmas, S. Randriamahefa , **J. Jestin**, V. Wintgens, Mechanical reinforcement in model elastomer nanocomposites with tuned microstructure and interactions, *Polymer*, 54 (5), 1466-1479, **2013**.
- [47] F.-X. Simon, T.T.T. Nguyen, N. Díaz, M. Schmutz, B. Demé, **J. Jestin**, J. Combet, P. J. Mésini, Self-assembling properties of a series of homologous ester-diamides – from ribbons to nanotubes, *Soft Matter*, 9, 8483-8493, **2013**.

Communications list

- [1] 19th Conference of the European Colloid and Interface Society (2005 September 18–23) Geilo (Norway) Nanofillers in polymer films, **J. Jestin**, A. El Harrak, G. Carrot, J. Oberdisse, F. Boué. *Oral Com.*
- [2] Molecular Structure of Heavy Oils (2007 April 12–13) Lyon (France) A SANS study of hydrocarbon emulsions, **J. Jestin**, S. Simon, T. Palermo, L. Barré. *Oral Com.*
- [3] Surfaces and Interfaces in Soft Matter and Biology (2008 May 21-23) Grenoble (France) Asphaltene Adsorption at the Local scale, **J. Jestin**, N. Jouault, Y. Corvis, F. Cousin, L. Barré. *Oral Com.*
- [4] EPS-CMD 22 (2008 August 25-29) Rome (Italy) Well defined nanofiller controlled structure in polymer, **J. Jestin**, C. Chevigny, N. Jouault, D. Gigmes, D. Bertin, F. Dalmas, S. Said, F. Boué. *Oral Com.*
- [5] Nanocomposites 2008 (2008 September 15-17) San Diego (U.S.) Anisotropic Reinforcement in Nanocomposites, **J. Jestin**, C. Chevigny, F. Cousin, F. Boué. *Oral Com.*
- [6] Analyse des polymères par rayonnement (2009 February 5-6) Nancy (France) Etude des nanocomposites par diffusion de rayonnement, **J. Jestin**. *Invited Conference.*
- [7] CONFIT 2010 Dynamics in confinement (2010 March 3-5) Grenoble (France) Polymer grafted silica nanocomposites, dispersion and dynamics, **J. Jestin**, C. Chevigny, N. Jouault, F. Boué. *Oral Com.*
- [8] MRS Spring meeting 2010 (2010 April 5-9) San Francisco (U.S.) Polymer-silica nanocomposites, dispersion, chains conformation and mechanical behavior, **J. Jestin**, C. Chevigny, N. Jouault, F. Boué. *Oral Com.*
- [9] The Power of Neutron Techniques in Nano and Biosciences (2010 July 12-16) Jaca (Spain) Complementarities between X-rays and neutron for nanosciences, **J. Jestin**. *Invited Conference.*
- [10] Evaluation AERES du LLB (2011 May 16), Saclay (France) Axe 3 Soft Matter, Nanomaterials: from local scale structure to macroscopic properties, **J. Jestin**, *Oral Com.*
- [11] IAEA Workshop, Concerted Actions in Research and Applications with Neutron Beams in Europe (2011 June 1-3) Budapest (Hungary) Research and Application using SANS, **J. Jestin**. *Invited Keynote lecture.*
- [12] The Future of Soft Matter SANS, ESS Science Symposia (2012 February 22-24) Lund (Sweden) Model nanocomposites to mechanical reinforcement, **J. Jestin**. *Oral Com.*
- [13] IKON 3 – Third In-Kind Contributions Meeting for Neutron Science for the ESS (2012 September 19-21) Lund (Sweden) Planned Activity Report from French Working Package Project "GISANS/VSANS", **J. Jestin**. *Invited Conference.*
- [14] JCNS Workshop 2012 Trends and Perspectives in Neutron Scattering for Soft Matter and Biophysics (2012 October 8-11) Tutzing (Germany) Neutron Scattering for Polymer Chains Conformation in Nano-composites, **J. Jestin**. *Oral Com.*

[15] User Meeting Synchrotron SOLEIL (2013 January 23-24) Saint Aubin (France) Polymer chains conformation and filler dispersion in nanocomposites: from model to industrial systems to progress in reinforcement, **J. Jestin**. *Oral Com.*

[16] The science case for the high intensity SANS and focusing SANS (2013 May 22-24) Bonn (Germany) VSANS multi-slit project for ESS, **J. Jestin**. *Oral Com.*

[17] LPBMS 2013 (2013 August 29-31) Tsukuba (Japan) Polymer-particles Nanocomposites for Reinforcement: From Model to Industrial Rubber Systems, **J. Jestin**. *Oral Com.*

SELECTED PUBLICATIONS

DOI: 10.1002/adma.200702758

Anisotropic Reinforcement of Nanocomposites Tuned by Magnetic Orientation of the Filler Network

By Jacques Jestin,* Fabrice Cousin, Isabelle Dubois, Christine Ménager, Ralf Schweins, Julian Oberdisse, and François Boué

In the past two decades, the extension of the range of fillers for polymer reinforcement to nanometer-sized filler materials has led to progress in both the design of innovative materials and understanding of their properties.^[1] Among the future challenges, the improvement and possibly tuning of a specific material property through a simple external trigger will be of particular importance. A promising pathway to achieve such a design is to introduce a new degree of freedom, i.e., by using magnetic instead of classical inorganic particles as filler. The design of a functional nanocomposite material with the possibility to orient the filler inside the matrix by using a simple external magnetic field should allow the tuning of macroscopic material properties, in particular the mechanical ones. In the past twenty years this concept has been explored by many research teams, most of whom have been studying the effect of micrometer-sized particles or fibres (needles).^[2–5] Two routes are possible when using magnetic filler particles: applying the field on the material after synthesis or applying it during the synthesis. In this study, we used the second approach for the nanoparticles; for this case, the consequences for the mechanical properties due to local anisotropy resulting from specific orientation of the nanofiller (i.e., particles with a size comparable to the polymer network mesh-size) still have to be researched.

Here, we present a new material based on the dispersion of magnetic nanoparticles in a polymer matrix. This was achieved in a controlled way by adapting the knowledge on systems in solution (“Ferroluids”)^[6] to our own method, where a “ferrolatex nanocomposite” was formed by dispersion of silica nanoparticles in a polymer matrix made of latex beads^[7–9] via

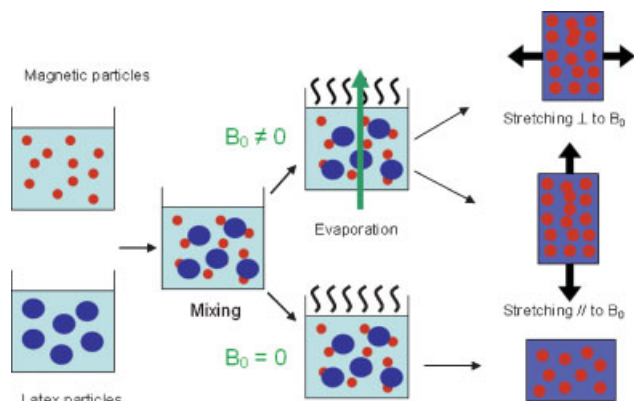
solvent (water) casting of a suspension of magnetic nanoparticles and polymer latex. In this article, we will show that these steps can be achieved by application of a weak magnetic field, which induces an orientation of the nanofillers that causes a strong anisotropic effect of the reinforcement. Moreover, the mechanical anisotropy in our system was studied by measuring the spatial arrangement and orientation of the isotropic particles in a range of 1–200 nm using small-angle neutron scattering (SANS).

The synthesis of a composite made of a latex film filled with magnetic particles required two main steps (Scheme 1). The first step was the synthesis of the magnetic particles according to a well-known process described in the Experimental section. Secondly, the particles, still in the same batch, were covered with a thin layer of silica. The silica shell made the particles pH-compatible with the latex beads, while retaining the initial size and magnetic properties of the core. Hence, we could use the developed technique for introducing silica particles in a latex film.^[7,9] The colloidal suspension of particles was mixed with a polymer-latex bead suspension ($R_{\text{bead}} \sim 200 \text{ \AA}$) at a fixed, high pH, followed by evaporation of the (aqueous) solvent, which made the latex nanospheres come in contact with each other. Above the film-formation temperature, capillary forces compressed them into adjacent polyhedrons separated by a membrane depending on the nature of the specific polymer shell of the latex beads. Above the glass-transition temperature (T_g), the matrix, which has a rubberlike elasticity similar to that of the membrane,^[7a] follows affinely (homothetically) at larger scale the macroscopic deformation down to the scale of one bead. At lower scales (not relevant here), relaxation of the chain occurs similarly to that of a polymer network. It is also known that diluted particles show an affine displacement in a similar nanolatex matrix as long as they do not have any interactions.^[7b]

The colloidal mixture, with a proportion of magnetic nanoparticles to the latex spheres of 5% by volume, was poured into rectangular moulds (1 cm × 6 cm × 0.1 cm) and dried at $T \sim 60 \text{ }^\circ\text{C}$, i.e., above the film-formation temperature, which was close to the glass-transition temperature of the latex ($T_g \sim 33 \text{ }^\circ\text{C}$).

A weak, constant field (150 Gauss (G); $1 \text{ G} = 10^{-4} \text{ T}$) was applied during evaporation in order to orient the magnetic filler. A similar sample was also evaporated in the same mould, but without the application of a magnetic field; this was labeled the “zero-field cast sample”.

[*] Dr. J. Jestin, Dr. F. Cousin, I. Dubois, Dr. F. Boué
Laboratoire Léon Brillouin (LLB)
CEA/CNRS, CEA Saclay
91191 Gif-sur-Yvette (France)
E-mail: jacques.jestin@cea.fr
Dr. C. Ménager
Laboratoire Liquides Ioniques et Interfaces Chargées (LI2C)
UMR 7612 CNRS/Université Paris 6
4, Place Jussieu - case 63 75252 Paris Cedex 05 (France)
Dr. R. Schweins
Institut Laue-Langevin, DS/LSS
6 rue Jules Horowitz, 38042 Grenoble Cedex 9 (France)
Dr. J. Oberdisse
Laboratoire des Colloïdes, Verres et Nanomatériaux (LCVN)
CC 26 UMR 5587 Université Montpellier II
34095 Montpellier Cedex 05 (France)



Scheme 1. Schematic representation of the synthesis route for incorporation of magnetic nanoparticle fillers in polymer films by latex-film formation and the orientation of the fillers with a constant field.

Mechanical tests were performed with a homemade uniaxial-elongation machine. Keeping in mind the direction of the magnetic field during casting, we studied two simple, but fundamental cases — stretching parallel or perpendicular to the field — using two rectangular films (1 mm × 6 mm × 40 mm) cut from the same sample. This allowed a direct comparison of the stress–strain isotherms in the two different directions. The samples were first immersed in a silicone oil bath at a temperature of $(T_g + 27)^\circ\text{C}$ and then elongated at a constant-velocity gradient. When the desired elongations were reached (i.e., $\lambda = 1.5, 2,$ and 3), the samples were immediately frozen by immersion into a carbonic ice bath. The reference for the mechanical tests was the stress–strain isotherm of the pure latex matrix. All stress–strain isotherms measured for the nanocomposites were normalized to this reference value; this gave us a reinforcement factor $R(\lambda)$ for each composite with respect to its own matrix. We manufactured a second series of films synthesized from a second batch of magnetic nanoparticles of similar size to check the reproducibility of the synthesis of the magnetic nanoparticles. Figure 1a shows the stretching curves (σ versus λ) of the two nanocomposites, the pure matrix, and the zero-field cast film. For all samples containing nanoparticles, the shape of the curves was similar: these showed a fast increase at the beginning of the elongation compared to that of the pure latex, while the curve shape at large λ tended to be similar to that of the pure latex sample. There was a very strong effect for the zero-field cast sample, whereas we observed that the σ values for the reinforcement samples after field-casting were lower by one order of magnitude.

But the most striking effect was the difference between the field-cast samples stretched parallel and those stretched perpendicular to the magnetic field. They showed very different behavior, especially at low deformation. Moreover, the mechanical tests for the two batches of magnetic nanoparticles showed excellent reproducibility for the two directions.

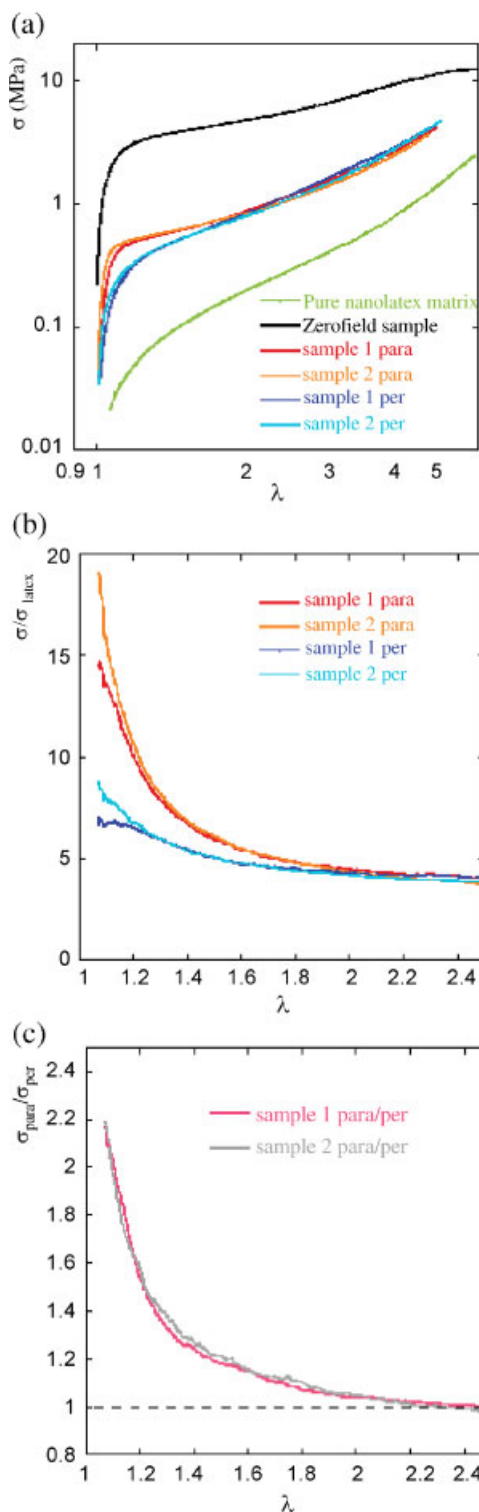


Figure 1. a) Stress-strain isotherm for: a pure latex matrix, a zero-field composite sample containing 5% (v/v) magnetic nanoparticles, and nanolatex films cast under a constant magnetic field; samples were stretched in directions parallel and perpendicular to the magnetic field. b) The reinforcement factor as function of the deformation for the field-cast samples under a constant magnetic field. c) Parallel-to-perpendicular field reinforcement ratio for the field-cast samples under a constant magnetic field.

Figure 1b shows the reinforcement factor $R(\lambda)$ as function of the deformation λ ; a strong reinforcement was observed for small deformation values, but a rapid decrease of $R(\lambda)$ was noticed with increasing deformation towards a lower, constant value for $R(\lambda)$. These results were the same as those previously described for nanolatex composites filled with silica nanoparticles.^[9] The curve aspect was similar in the two directions. The most important finding was that *the reinforcement factors obtained were much higher when the field was applied along the deformation direction than when the field was perpendicular to it*. The anisotropy of the mechanical properties of a given sample was quantified by calculating the ratio of the parallel reinforcement to the perpendicular reinforcement (Fig. 1c). It

was found to be more than a factor two at low deformation. It is important to note for the discussion below that such anisotropy in $R(\lambda)$ vanished for large elongations ($\lambda > 2$).

In summary, we were able to obtain a strong anisotropic effect for the mechanical properties by using nanocomposites under orientation of a magnetic field. Next, we tried to correlate the macroscopic effect with the local organization of the filler network in the matrix and its evolution under mechanical strain by using SANS measurements analysis.

SANS measurements were performed on the samples after each successive step of the synthesis. Here below, Figures 2–4 will be presented in the same way: the upper part of the figure shows 2D intensity patterns, in the middle section the radially

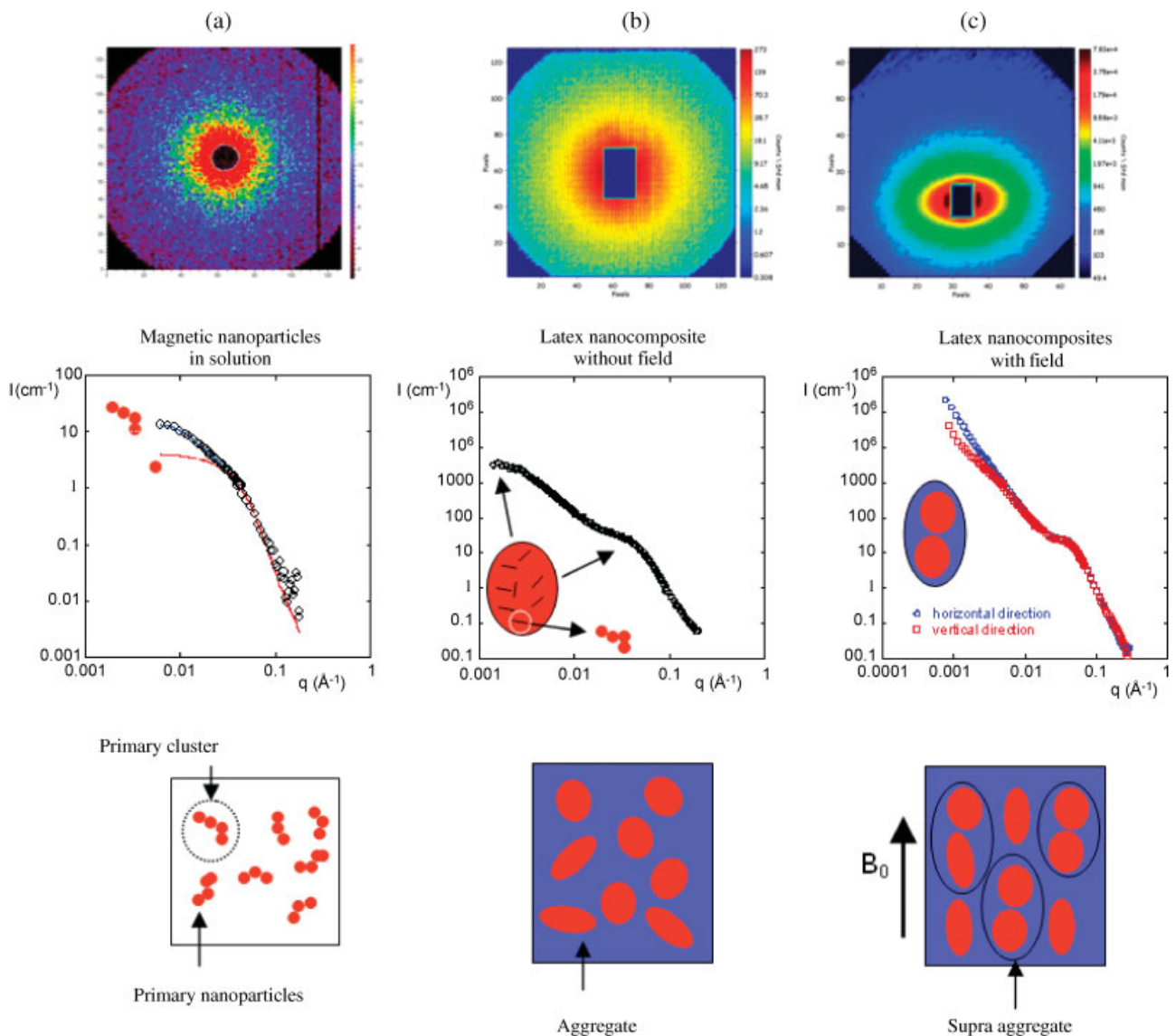


Figure 2. SANS scattering of the samples at rest. Upper part: 2D spectra probed at the lowest q -range in the experiment; middle part: 1D scattering intensity versus the scattering vector q ; lower part: the corresponding schematic representation of the structure. a) The initial magnetic-particle aggregates covered with a silica layer, the full blue line corresponds to the form of a cluster of 3–4 nanoparticles with $D_f = 1$ and the full red line to the form factor of an isolated nanoparticle. b) A zero-field nanolatex composite sample. c) A nanolatex composite film evaporated under a constant magnetic field.

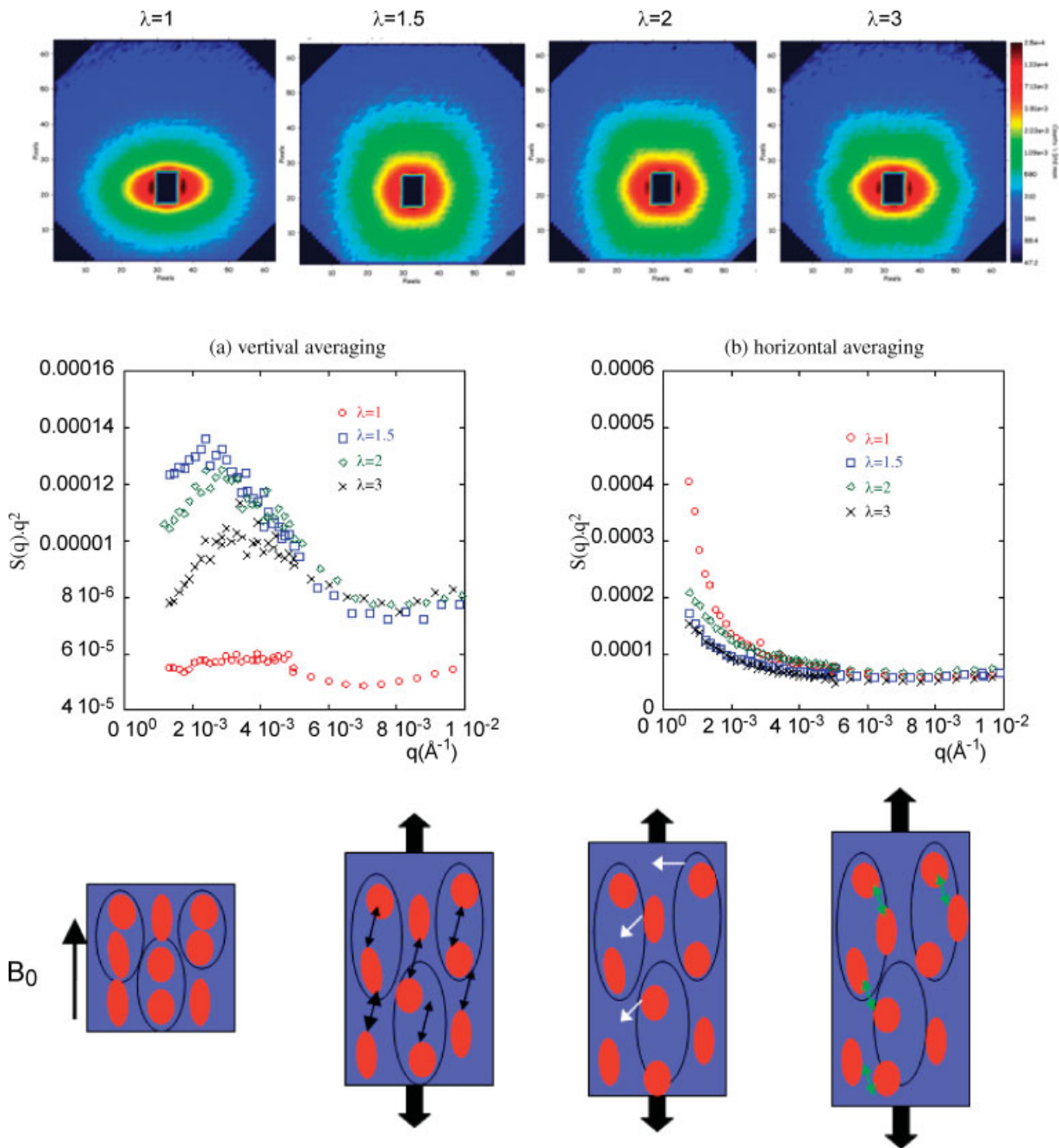


Figure 3. 2D scattering of the stretched nanolatex film when the oriented fillers are parallel to the elongation direction. The middle section shows the radial averaging of $S(q)q^2$ versus q along the vertical (a) and the horizontal (b) direction for each elongation value and the lower part shows a sketch of the structure in the real space. The hexagonal aspect of the 2D picture is due to the apparition of a correlation peak, which corresponds to a characteristic distance between the aggregates along the stretching direction (the black arrows for $\lambda = 1.5$). The green arrows for $\lambda = 3$ illustrate a smaller characteristic distance between the aggregates. This is the result of displacement of the objects under stretching (intercalation); the supra aggregates are brought closer to each other along the horizontal plane of the figure.

averaged intensities are shown as a function of the scattering vector, and at the bottom there is a sketch in real space illustrating the structure of the network of aggregates. First, Fig. 2a shows the results for magnetic particles in a dilute aqueous solution at a low volume fraction ($\Phi = 0.001$) before

and after the silica-covering process. The scattering is obviously isotropic and its radial average can be fitted with a polydisperse log-normal distribution for spherical primary particles with an average radius of 35 \AA and a variance of $\sigma = 0.3$. The low- q , rod-like scattering (q^{-Df} , fractal dimension

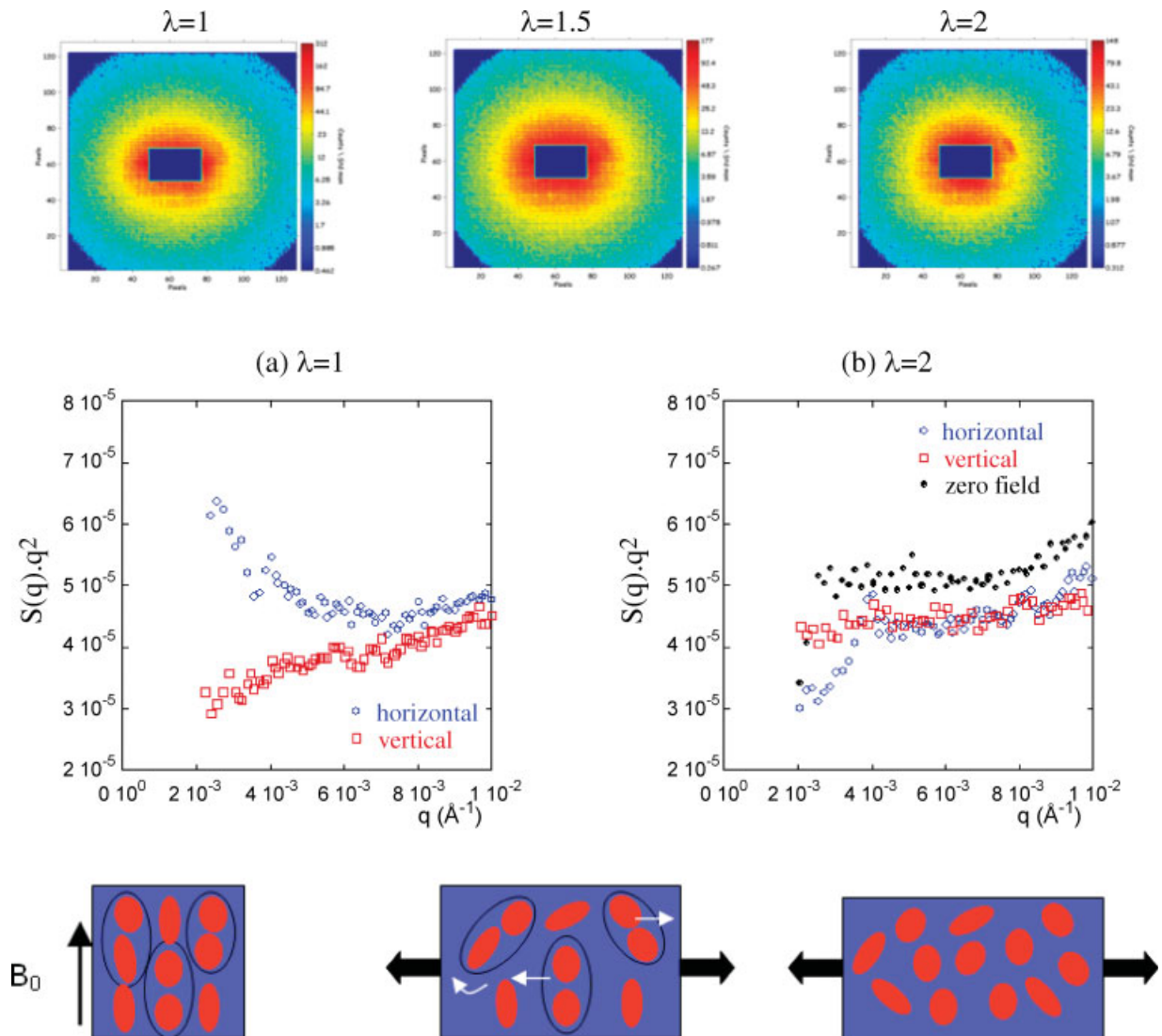


Figure 4. SANS scattering of the stretched nanolatex film when the oriented fillers are perpendicular to the elongation direction. Radial intensities averaged along the vertical and the horizontal direction of the 2D picture as a function of q for a non-stretched sample (a) and an elongated sample with $\lambda = 2$ (b). Comparison with the zero-field cast isotropic sample (black dots) is shown in (b).

$D_f=1$) suggested that the particles were organized in small “primary clusters”. The mean number of particles in a cluster, $N_{\text{prim.}}$, is of the order of three to four particles, as obtained from the fit for the scattering of a fractal aggregate with $D_f=1$ (cf. [10] for details). Second, patterns that occurred after casting and before stretching are presented in Figure 2b. As expected, the zero-field cast sample was isotropic. The radial average displays the characteristic signature of aggregate formation during film-drying. Fortunately, the size of such large objects was observable in our q -window, as illustrated by the plateau in the scattering curve at low q . This intensity limit corresponded to an aggregation number of around 10 primary clusters (~ 30 nanoparticles). At slightly larger q , where the internal structure of the aggregates was probed, we observed a q^{-2} behavior (i.e., a fractal dimension of $D_f \sim 2$), as typically

encountered for either diffusion-limited aggregation (DLA, $D_f=1.8$ in 3D)^[11] or reaction-limited aggregation (RLA, $D_f=2.1$ in 3D).^[12] For larger values of q (around $4 \cdot 10^{-2} \text{\AA}^{-1}$), an oscillation was observed in the scattering curve, which corresponded to the correlation (i.e., repulsive interactions) between primary clusters inside the aggregates. Figure 2c shows the results for the field-cast film, which displayed an evident anisotropic scattering pattern. The elliptic shape with a large horizontal axis (i.e., transverse to the field) is characteristic for objects elongated vertically: thus, there were aggregates aligned parallel to the field. To quantify this effect, we performed radial-averaging of the scattering inside an angular sector along one direction, either vertical or horizontal, with a width of 25° . For small q values, the intensity was smaller along the vertical than along the horizontal axis. The

aggregates were aligned on a larger scale along the field (vertical here) and we assumed that they formed “chains of aggregates” inside the matrix. The intensity along the horizontal axis showed a strong q^{-3} decrease. This power-law decrease with exponent three is mostly encountered for compact objects, composed here of chains of aggregates that we will define as “supra-aggregates”. The scattering was still increasing at the lowest q of the experimental window. This meant that the size of the supra-aggregates was too large to be probed here. The structural organization of the aggregates inside one supra-aggregate was also too large to be accessible within the experimental q -range. For high q values, the intensities along the vertical and horizontal axis were superimposed on the zero-field sample. This indicated that the local structure of the aggregates, composed of the primary clusters, was not affected by the application of the magnetic field. To summarize this section, we succeeded in orienting the filler as chains of aggregates, inside the nanolatex composite using a constant field.

Furthermore, we investigated the evolution of the structure of the filler network under stretching. We started with the case, where the oriented chains were parallel to the elongation (vertical). Figure 3 shows the 2D intensity map for each λ . When the elongation rate increases, the anisotropy is increasing towards a surprisingly clear-cut hexagonal form. This hexagonal form was related to the rise of a maximum occurring in the vertical direction. The maximum appears at a small q value for the first elongation ($\lambda = 1.5$) and its position moves to higher q values at higher elongations. This behavior is highlighted in the $S(q)q^2$ versus q representation of Figure 3a and b, which is convenient here since the scattering decays with q^{-2} at intermediate q . $S(q)$ was determined from dividing the scattering intensity $I(q)$ by the form factor $P(q)$ of the primary clusters. The data showed that elongation of the sample induced the organization of the aggregates with a characteristic distance between the aggregates in the vertical direction. Please note that the curve for the unstretched sample showed no maximum in the available q range. Since the correlation peak shifted towards higher q with increasing elongation, the characteristic distance decreased. Intuitively, one would expect the contrary, as the aggregates moved away from each other along the stretching direction. This implied that some aggregates coming from neighboring, chainlike supra-aggregates intercalated vertically between two aggregates under strong deformation. Such a mechanism results in an effective decrease of the vertical inter-aggregate distance, as illustrated in the real-space sketches of Figure 3. Along the horizontal direction, the intensity decreased compared to that of the isotropic signal: the supra-aggregates were brought closer due to lateral shrinking of the sample, which increased the effective compressibility between them.

In Figure 4, we present the second case where the stretching direction (here horizontal) is perpendicular to the chainlike supra-aggregates. In addition to the isotropic intensity map, two elongation ratios are presented, $\lambda = 1.5$ and $\lambda = 2$. The result of the deformation experiments is in this case completely

different from that of the previous experiments; the scattering pattern becomes *isotropic* as the elongation is increased. This becomes evident when $S(q)q^2$ is plotted as a function of q along both the vertical and horizontal directions of the 2D intensity map: the anisotropy effect was significant for the nonstretched sample (Fig. 4a), but became small for the elongated one (Fig. 4b). The orientation of the filler disappeared under mechanical constraint: the aggregates were reoriented isotropically. Moreover, the supra-aggregates were destroyed: the final scattering of the sample stretched to $\lambda = 2$ superimposes well on the scattering from the zero-field cast sample (black symbols).

A consistent picture emerges when confronting the structural organization of the filler network deduced from SANS to the reinforcement: under stretching, the parallel-oriented chains rearrange along the deformation direction due to a contraction of the interconnecting particle network. In contrast, the perpendicularly oriented network breaks under deformation. This leads to a higher reinforcement factor in the parallel direction. In the perpendicular direction, the final structure of the chains reverted to the organization of the zero-field cast sample (at least in the available q range), but the latter had a higher reinforcement factor. We attribute this difference to the existence of larger aggregates connected at larger scales.

To summarize, we designed an original nanometer-sized material, which displayed anisotropic and tunable mechanical properties. The samples were formulated rather easily by mixing aqueous suspensions of polymer and magnetic colloids, followed by casting. The prepared nanocomposites bore magnetic properties and therefore possessed the possibility of pre-orientation when cast under a magnetic field. Detailed insight on dispersion was obtained from SANS measurements, which showed that primary-particle aggregates were organized at the nanometer scale and aligned in the presence of a magnetic field. Such anisotropy had a clear effect on the mechanical reinforcement introduced by the fillers. The interesting novelty is the anisotropic reinforcement: it is larger by a factor of two at low deformation along the field than transverse to it. Microscopically, this can be understood with the SANS-data: while strain perpendicular to the chains destroys chain ordering, strain parallel to the field induces additional organization. Thus, anisotropic mechanical reinforcement is obtained through anisotropic interconnection of nanoparticles, which is a one-dimensional version of the filler-network effect.

In addition to the observed controlled anisotropy of our nanocomposites, we want to point out another contribution of this study, which concerns the conceptual side. Our system opens the way to discriminate between the two dominant contributions assigned to the filler in reinforcement mechanisms: on the one hand, the role of the particle interface and on the other hand, that of the filler network. The former contribution includes the interaction between the particles and polymer, and the consequences on the chain dynamics,^[13–17] the latter interconnected networks and/or aggregation.^[18]

It appears to be very difficult to separate the two effects experimentally, as one usually influences the other. The new system provides a simple alternative to act on the nanoparticle filler network without any important modifications of the interface. This can be achieved by a simple orientation of the filler network, which does not involve modification of the matrix chains themselves (at variance with, for example, strain exerted on the full sample).

Experimental

The nanoparticles were made of maghemite ($\gamma\text{-Fe}_2\text{O}_3$). They were chemically synthesized in water by co-precipitation of FeCl_2 and FeCl_3 in an alkaline solution [19]. A size-sorting procedure [20] performed at the end of the synthesis enabled a reduction of the polydispersity of the nanoparticles. The final particle size was determined with magnetization measurements and SANS experiments; both techniques produced the same results. The size distribution was described by a log-normal distribution with a mean radius (R_0) of 35 Å and a polydispersity index (σ) of 0.3. At the end of the synthesis procedure, the “naked” nanoparticles were stabilized at pH 12 with $\text{N}(\text{CH}_3)_4^+$ counterions. In order to increase their stability range (their PZC is 7.2 and they are only stable for $\text{pH} > 10$), their surface was coated with a thin shell of silica. The silica coating process was based on a two-step procedure described in [21] to obtain silica particles with a magnetic core; in this study, we only performed the first step of the procedure. A solution of $\text{SiO}_2/\text{Na}_2\text{O}$ was added to a suspension of naked nanoparticles at pH 12, which induced the formation of silica oligomers in the solution. The oligomers adsorbed on the nanoparticle surface. The concentration of the nanoparticles and silica corresponded to a molar ratio of $[\text{Fe}]/[\text{Si}] = 1$; a dilute solution of nanoparticles and silica was chosen to prevent the formation of silica bridges between the particles and thus irreversible aggregation. In order to eliminate the excess of silica oligomers, the suspension was dialyzed against a reservoir with a NaOH solution at pH 10. The nanoparticles had the same size before and after the silica-coating process (confirmed with SANS measurements) and were now stable from pH 4–12. A very thin layer of silica was thus coated on the nanoparticles; this modified their surface properties, but not their magnetic properties.

The nanolatex was kindly provided by Rhodia; it was a core-shell latex solution containing poly(methyl methacrylate) (PMMA) and poly(butylacrylate) (PBuA) as the core compounds and methacrylic acid forming the hydrophilic shell to ensure the colloidal stability in water. The approximate particle size given by Rhodia was $R \sim 200$ Å. Before mixing, the nanolatex solution was dialyzed against the same reservoir as used for the dialysis of the silica-coated magnetic nanoparticles, in order to obtain the same pH and ionic strength in both solutions. Both solutions were then mixed as $\Phi_{\text{nanoparticles}}/\Phi_{\text{nanolatex}} = 0.05$. The final mixture was degassed under primary vacuum conditions for about one day to avoid bubble formation. The solvent was then slowly evaporated for four days at $T = 60^\circ\text{C}$ under atmospheric pressure to get a homogeneous bubble-free film. During the drying step, a magnetic field of 150 Gauss was imposed to the sample along the plane of the final film.

The samples for determination of the stress-strain isotherms were polished with sandpaper to obtain a constant thickness. They were stretched up to rupture in a controlled constant-rate deformation ($\dot{\gamma} = 0.0016\text{ s}^{-1}$) at $T = 60^\circ\text{C}$ (i.e., well above the glass transition temperature of the matrix ($T_g = 33^\circ\text{C}$)). The force $F(\lambda)$, where $\lambda = L/L_0$ defines the elongation with respect to the initial length L_0 , was measured with a HBM Q11 force transducer and converted to (real) stress inside the material, σ . The deformation of the film was supposed to elapse homogeneous and incompressible. In our silica-latex system, the physico-chemical parameters that control the morphology of aggregates of silica nanoparticles are the silica concentration, the pH, and the salinity in solution before solvent evaporation. We have

previously shown that the rheological properties of the pure nanolatex matrix were pH-dependent [10]. Therefore, we analyzed our data in terms of the nanocomposite reinforcement factor $R(\lambda) = \sigma(\lambda)/\sigma_{\text{latex}}(\lambda)$, where the stress of the pure matrix $\sigma_{\text{latex}}(\lambda)$ was measured at the same pH.

Experiments were performed at Laboratoire Leon Brillouin (LLB, Saclay, France) on beam line SANS, at the Institut Laue-Langevin (ILL, Grenoble, France) on beam line D11 and at the Hahn-Meitner Institut (HMI, Berlin, Germany) on beam line V4. With regard to SANS, two sample-to-detector distances (1 and 5 m) at wavelength 6 Å gave us a q range from 8.10^{-3} to 0.3 \AA^{-1} . With respect to the D11 measurements, two wavelengths (6 and 12 Å) with four sample-to-detector distances (1, 5, 20, and 34 m) allowed us to have access to a q range between 8.10^{-4} and 0.3 \AA^{-1} . Regarding V4, three sample-to-detector distances (1, 4 and 12 m) and two wavelengths (6 and 12 Å) gave us a q range from 2.10^{-3} to 0.1 \AA^{-1} . Data treatment was performed following standard procedures, with H_2O as the calibration standard, to get absolute intensities. Incoherent scattering and background contributions of the nanolatex films were subtracted from the pure-latex matrix scattering (the incoherent scattering from maghemite nanoparticles is null). In the most simple case of centrosymmetrical monodisperse particles, the scattering intensity $I(q)$ can be written as function of the scattering vector q as follows: $I(q) = \Phi \Delta\rho^2 V P(q) S(q)$, where Φ is the volume fraction of the filler, $\Delta\rho^2$ the contrast term with respect to its environment (matrix, solvent, etc.), V the volume of the particle, $P(q)$ the form factor and $S(q)$ the structure factor. For dilute systems, the structure factor is close to 1 because interactions are negligible. For concentrated systems with repulsive interactions, $S(q)$ presents a correlation peak at $q^* = 2\pi/D$, where D is the average distance between the scattering mass centres. For attractive systems, aggregates of initial particles can be formed with different compactness. For open systems, one gets a fractal organization of particles with a fractal dimension D_f and the scattering spectra decay with q^{-D_f} , whereas for dense systems the compactness can be obtained from the close packing-volume fraction.

Received: November 6, 2007

Revised: February 26, 2008

Published online: June 5, 2008

- [1] S. C. Tjong, *Mater. Sci. Eng.* **2006**, *R53*, 73.
- [2] G. B. Sohoni, J. E. Mark, *J. Appl. Polym. Sci.* **1987**, *34*, 2853.
- [3] C. Bellan, G. Bossis, *Int. J. Mod. Phys. B* **2002**, *16*, 2447.
- [4] C. Coquelle, G. Bossis, *Int. J. Solids Struct.* **2006**, *43*, 7659.
- [5] Z. Varga, G. Filipcsei, M. Zrinyi, *Polymer* **2006**, *47*, 227.
- [6] R. E. Rosensweig, *Ferrohydrodynamics*, Cambridge University Press, Cambridge **1985**.
- [7] a) Y. Rharbi, F. Boué, M. Joanicot, B. Cabane, *Macromolecules* **1996**, *29*, 4346. b) Y. Rharbi, M. Joanicot, A. Vacher, B. Cabane, F. Boué, *Europhys. Lett.* **1999**, *46*, 472.
- [8] J. Oberdisse, B. Demé, *Macromolecules* **2002**, *35*, 4397.
- [9] J. Oberdisse, *Macromolecules* **2002**, *35*, 9441.
- [10] C. Rivière, F. Wilhelm, F. Cousin, V. Dupuis, F. Gazeau, R. Perzynski, *Eur. Phys. J. E* **2007**, *22*, 1.
- [11] M. Y. Lin, H. M. Lindsay, D. A. Weitz, R. C. Ball, R. Klein, P. Meakin, *Phys. Rev. A* **1990**, *41*, 2005.
- [12] M. Y. Lin, H. M. Lindsay, D. A. Weitz, R. C. Ball, R. Klein, P. Meakin, *J. Phys. Condens. Matter* **1990**, *2*, 3093.
- [13] D. Long, F. Lequeux, *Eur. Phys. J. E* **2001**, *4*, 371.
- [14] J. Berriot, H. Montes, F. Lequeux, D. Long, P. Sotta, *Macromolecules* **2002**, *35*, 9756.
- [15] H. Montes, F. Lequeux, J. Berriot, *Macromolecules* **2003**, *36*, 8107.
- [16] J. Berriot, H. Montes, F. Lequeux, D. Long, P. Sotta, *Europhys. Lett.* **2003**, *64*, 50.

- [17] A. Bansal, H. Yang, C. Li, K. Cho, B. C. Benicewicz, S. K. Kumar, L. S. Schadler, *Nat. Mater.* **2005**, *4*, 693.
- [18] J. Oberdisse, *Soft Matter* **2006**, *2*, 29.
- [19] R. Massart, *IEEE Trans. Magn.* **1981**, *17*, 1247.
- [20] R. Massart, E. Dubois, V. Cabuil, E. Hasmonay, *J. Magn. Mat.* **1995**, *149*, 1.
- [21] A. P. Philipse, M. P. B. Bruggen, C. Pathmamanoharan, *Langmuir* **1994**, *10*, 92.
-

Well-Dispersed Fractal Aggregates as Filler in Polymer–Silica Nanocomposites: Long-Range Effects in Rheology

Nicolas Jouault,[†] Perrine Vallat,[†] Florent Dalmas,[‡] Sylvère Said,[§] Jacques Jestin,^{*,†} and François Boué[†]

Laboratoire Léon Brillouin, CEA Saclay, 91191 Gif-sur-Yvette Cedex, France; Institut de Chimie et des Matériaux Paris-Est, CNRS UMR 7182, 2-8 rue Henri Dunant 94320 Thiais, France; and Laboratoire Polymères, Propriétés aux Interfaces et Composites, Université de Bretagne Sud, Centre de Recherche, Rue Saint Maudé, BP 92116, 56321 Lorient Cedex, France

Received August 22, 2008; Revised Manuscript Received January 16, 2009

ABSTRACT: We are presenting a new method of processing polystyrene–silica nanocomposites, which results in a very well-defined dispersion of small primary aggregates (assembly of 15 nanoparticles of 10 nm diameter) in the matrix. The process is based on the use of a high boiling point solvent, in which the nanoparticles are well dispersed, and a controlled evaporation procedure. The filler's fine network structure is determined over a wide range of sizes, using a combination of small-angle neutron scattering (SANS) and transmission electronic microscopy (TEM) experiments. The mechanical response of the nanocomposite material has been investigated for both small (ARES oscillatory shear and dynamical mechanical analysis) and large deformations (uniaxial traction) as a function of the concentration of the particles in the matrix. Our findings show that with a simple tuning parameter, the silica filler volume fraction, we can investigate in the same way the structure–property correlations related to the two main reinforcement effects: the filler network contribution and a filler–polymer matrix effect. Above a silica volume fraction threshold, we were able to highlight a divergence of the reinforcement factor, which is clearly correlated to the formation of a connected network built up from the finite-size primary aggregates and is thus a direct illustration of the filler network contribution. For a silica volume fraction lower than this percolation threshold, we obtain a new additional elastic contribution of the material, of longer terminal time than the matrix. This cannot be attributed to the filler network effect, as the filler is well dispersed, each element separated from the next by a mean distance of 60 nm. This new result, which implies the filler–matrix contribution of the reinforcement, must include interfacial contributions. Nevertheless, it cannot be described solely with the concept of glassy layer, i.e., only as a dynamic effect, because its typical length scale extension should be much shorter, of the order of 2 nm. This implies a need to reconsider the polymer–filler interaction potential and to take into account a possible additional polymer conformational contribution due to the existence of indirect long-range bridging of the filler by the chains.

I. Introduction

Reinforcement of polymers, and particularly of elastomers, using inorganic particles is still an open challenge, from both the industrial and fundamental points of view. According to the characteristics of the filler (nature, shape, matrix structure, concentration) and of the elastomer matrix (interaction potential with the filler), many systems with many associated mechanical properties can be found.¹ More recently, a specific interest has developed in the size effect due to a better availability of much smaller particles. The first, simple idea was that the enhancement of the composite properties could be induced by increasing the specific contact area between the filler and the matrix, i.e., by reducing the size of the particle filler. This reduction could be made by downscaling to the polymer network mesh size, allowing further interaction.^{2,3} The second idea was that using nanosized particles would produce a convenient extent of clustering. Controlled clustering could make it possible to control the hierarchical organization of the matrix's filler, resulting in specific filler–matrix interactions opening the way to new mechanical properties. These ideas, together with advances in characterization methods, lead to the creation of elaborate advanced composites with nanofillers, from classical carbon black,⁴ to silica,^{5–9} and up to carbon nanotubes.¹⁰ Most studies used rheological approaches of various mechanical

solicitations and showed various kinds of rheological transition related to reinforcement.

In this context, two main contributions to reinforcement stand out, borrowing both from earlier research and from more recent theory. The first contribution is linked to the filler network structure: beyond the classical hydrodynamic description of Einstein,¹¹ Guth and Smallwood,¹² and Batchelor,¹³ the idea is that in a further range of particle concentration the particles can form a connected network (as in the percolation model), whatever their shape: simple spheres, more anisotropic rods, platelets,^{9,10} or complex shapes like fractals.¹⁴ The second contribution is attributed to the interface between the matrix polymer chains and the particle filler. Beyond earlier ideas of adsorption–desorption and occluded rubber confinement, the idea that the chain dynamics could be modified in the area close to the filler object was reformulated in terms of a kind of “glassy layer” through earlier^{15–18} and more recent¹⁹ works, including NMR evidence on mobility and signature on the temperature dependence of mechanical response.

The experimental distinction between these two classes of contributions to the reinforcement mechanisms, filler network and interface, is difficult because they are often correlated:

- When starting from already complex fillers (such as carbon black or fumed silica), the structure of the filler affects the buildup, the geometry, the connectivity of the filler network, and the related interfacial interaction. The interaction potential between the chain and the filler is also associated with the filler's form factor. As discussed by Vilgis,²⁰ the problem is multilength

* Corresponding author. E-mail: Jacques.Jestin@cea.fr.

[†] CEA Saclay.

[‡] CNRS UMR 7182.

[§] Université de Bretagne Sud.

and multitime scale so that many characteristic lengths must be identified, from the nanometer range to the macroscopic one.

• When starting from individual nanoparticles, once again, an (often spontaneous) buildup of clusters brings the problem back to the former situation. However, particularly in industry, dispersion control implies a use of surfactants, grafted short linear molecules, and coupling agents, which greatly and simultaneously modify—and thus correlate—the filler structure and the local interface. Trying to reduce this correlation, this same idea of controlling the filler's local dispersion, in particular the nanofillers, has been used in academic research, through more or less sophisticated chemistries like *in situ* polymerization after dispersion of nanoparticles²¹ or grafting polymerization on individual nanoparticles.^{22,23} Other methods implied simple control of electrostatics repulsion,²⁴ or of magnetic attraction,²⁵ by mixing the particles with polymer beads (latex)—instead of polymer chains like in the great majority of tire processing (at least up to very recently).

In the present paper, we are presenting another strategy, which turns out to be very simple, based on a new method of nanocomposite processing, using a polystyrene matrix filled with silica nanoparticles. First, we will present the method, based on the use of a particular solvent, with a high boiling point, above the glass transition temperature T_g of the polymer, and a controlled-evaporation procedure which appears to limit the attractive van der Waals interactions effect and thus makes it possible to obtain a particularly well-defined dispersion of the silica particles in the matrix. Second, we will describe the fine characterization of the filler dispersion in the matrix on a very wide length range through a combination of small-angle neutron scattering (SANS) and transmission electronic microscopy (TEM). Third, we will report the mechanical response of the material at low (ARES oscillatory shear plate–plate rheometer and dynamical mechanical analysis, DMA) and large deformation (uniaxial stretching). Finally, we will discuss the link between the filler structure inside the matrix at the local scale, with the mechanical behavior of the nanocomposites at the macroscopic scale.

II. Materials and Methods

1. Sample Preparation. The colloidal solution of silica nanoparticles is a gift from NISSAN (DMAC-ST). In this solution, the native particles, of an average radius of 5.2 nm, are electrostatically dispersed in the dimethylacetamide (DMAc), a polar solvent which is also a good solvent for the polymer used as a matrix, polystyrene (PS, Aldrich, $M_w = 280\,000$ g/mol, $I_p = 2$, used as-received). The glass transition T_g of pure PS is around 100 °C. A concentrated solution of PS in DMAc (10% v/v) is mixed with a solution of silica in DMAc at various fractions, ranging from 0 to 30% v/v. The mixtures are stirred (using a magnetic rod) for 2 h. They are then poured into Teflon molds (5 cm × 5 cm × 2.5 cm) and let cast in an oven at constant temperature $T_{\text{cast}} = 130$ °C. This yields dry films of dimension of 5 cm × 5 cm × 0.1 cm (i.e., a volume of 2.5 cm³). The specific conditions of film formulations, solvent titration, etc., are discussed in the Results section. We cut some disks out of the films (diameter 1 cm, thickness 1 mm) for the plate–plate oscillatory shear cell, and 2 cm × 0.5 cm rectangular 1 mm thick films, for DMA as well as for uniaxial stretching.

2. SANS Experiments. Measurements were performed at the Laboratoire Léon Brillouin (LLB) on the SANS spectrometer called PACE. Three configurations were used: a first with wavelength 17 Å, sample-to-detector distance of 4.70 m, and a collimation distance of 5.00 m, a second with wavelength 6 Å, sample-to-detector distance of 3 m, and a collimation distance of 2.50 m, and a third with wavelength 6 Å, sample-to-detector distance of 1 m, and a collimation distance of 2.50 m corresponding to a total q range of 2×10^{-3} to 0.3 \AA^{-1} . Data processing was performed with a homemade program following standard procedures²⁶ with H₂O as calibration standard. Small deviations, found in the spectra at the

overlap of two configurations, are due to different resolution conditions and (slight) remaining contributions of inelastic, incoherent, and multiple scattering. To get the cross section per volume in absolute units (cm⁻¹), the incoherent scattering cross section of H₂O was used as a calibration. It was estimated from a measurement of the attenuator strength and of the direct beam with the same attenuator. The incoherent scattering background, due to protons of the matrix chains, was subtracted using a blank sample with zero silica fractions.

3. Transmission Electronic Microscopy. In order to complete on a larger scale the SANS analysis of the nanocomposite structure, conventional TEM observations were also performed on composite materials. The samples were cut at room temperature by ultramicrotomy using a Leica MZ6 Ultracup UCT microtome with a diamond knife. The cutting speed was set to 0.2 mm s⁻¹. The thin sections of about 40 nm thickness were floated on deionized water and collected on a 400 mesh copper grid. Transmission electron microscopy was performed on a Philips Tecnai F20 ST microscope (field-emission gun operated at 3.8 kV extraction voltage) operating at 200 kV. Precise scans of various regions of the sample were systematically done, starting at a small magnification which was then gradually increased. The slabs observed were stable under the electron beam. The sample aspect was the same in every area of every piece. Apart from a few cutting scratches, moderate buckling, very rare bubbles, and impurities, the pictures given below are completely representative of the single aspect of the sample, which thus appears homogeneous.

4. Oscillatory Shear Small Deformation Tests. Shear tests, corresponding to low deformation levels (0.5%), were carried out in the dynamic mode in strain-controlled conditions with a plate–plate cell of an ARES spectrometer (Rheometrics-TA) equipped with an air-pulsed oven. This thermal environment ensures a temperature control within 0.1 °C. The samples were placed between the two plate (diameter 1 mm) fixtures at high temperature (160 °C), far above the glass transition, put under slight normal stress (around 0.5 N), and temperature was decreased progressively, while gently reducing the gap to maintain a constant low normal stress under thermal retraction. The zero gap is set by contact, and the error on sample thicknesses is thus minimal—estimated at +0.010 mm with respect to the indicated value. Artifacts slipping are noticeably reduced by this procedure, as checked by its reproducibility, and also by a sweeping in amplitude, at constant pulsation, which also made it possible to determine the limit of the range of linear deformation. To stay below this limit, the shear amplitude was fixed to 0.5%. Samples are stabilized at the temperature for 30 min before starting measurements. The reproducibility was first tested on pure PS samples with an average of five repetition measurements, permitting an estimation of variations of the order of 10%. In dynamic mode, the frequency range was from 0.5 to 100 rad/s for different temperatures (from 160 to 120 °C), and time–temperature superposition was applied. The obtained multiplicative factor can be adjusted to WLF law²⁷ as follows

$$\log(a_T) = \frac{C_1(T_{\text{ref}} - T)}{C_2 + T - T_{\text{ref}}} \quad (1)$$

where a_T is the multiplicative factor, T_{ref} is the reference temperature of the master curve (in our case 143 °C), T is the temperature of the measurement, and C_1 and C_2 are the WLF parameters. We found $C_1 = 6.72$ and $C_2 = 98.03$ °C, which is commonly obtained for PS samples.²⁸ For this plate and plate technique, we only focused on the samples with low silica concentration (from 0 to 5% v/v) because for higher silica fractions (>5% v/v) the measurement reproducibility was not ensured (risk of slippage).

5. Dynamic Mechanical Analysis. Rectangular pieces of film 2 cm long × 0.5 cm wide were sanded down to a constant thickness of 0.8 mm. Dynamic mechanical analysis (DMA) measurements were performed on a TA DMA Q800 device in oscillatory tension mode, at fixed deformation rate (0.1%) and fixed frequency (5 Hz), at temperatures ranging from 40 to 300 °C with a heating rate of 10 K/min. Analysis of the oscillatory stress response is done by

the software provided by TA; a preloading of 0.04 N is applied to avoid buckling. Note that 5 Hz corresponds to a short time span, 0.2 s. However, a measurement at 200 °C, applying a time–temperature superposition factor of 296, corresponds when using eq 1 to 60 s at the reference temperature of 143 °C (equivalent to $2\pi/60 = 0.1$ rad/s). Two identical experiments (for pure PS samples) were performed to check the reproducibility of the measurements and correct obtained values. The storage (E') and the loss (E'') moduli of the complex Young modulus (E^*), and the loss factor $\tan \delta = (E''/E')$ at 5 Hz, are extracted from the measurements. The temperature at which $\tan \delta$ shows a maximum is noted T_α .

6. Stress–Strain Isotherms. Samples for stress–strain isotherms cut from films are carefully sanded down to a constant thickness ~ 1 mm within a few microns. A grid of lines is drawn on the sample with a felt pen. Samples are stretched up to a predefined deformation value in a controlled constant-rate deformation ($d\lambda/dt = 0.005$ s $^{-1}$, λ being the elongation ratio $L(t)/L(t=0)$), at temperature $T = 120$ °C, i.e., ~ 20 °C above the glass transition temperature of the polymer matrix ($T_g = 98$ °C for pure PS). This corresponds to a typical time $(d\lambda/dt)^{-1} = 200$ s, which after applying the time–temperature superposition factor (0.0087 from 120 to 143 °C) corresponds at 143 °C to 1.8 s. The tensile force $F(\lambda)$, where $\lambda = L/L_0$, defines the elongation ratio with respect to the initial length L_0 , measured with a HBM Q11 force transducer and converted to (real) stress inside the material σ by dividing the force by the assumed cross section during elongation. Indeed, the deformation of the film is assumed to be homogeneous and at constant volume; thus, the cross section decreases as $(1/\sqrt{\lambda})^2$. Apart from stress–strain curves, we analyze our data in terms of the nanocomposite reinforcement factor $R(\lambda) = \sigma(\lambda)/\sigma_{\text{matrix}}(\lambda)$, where $\sigma_{\text{matrix}}(\lambda)$ is the stress–strain curve for the polymer with a zero silica fraction.

7. Thermal Characterizations. Differential scanning calorimetry (DSC) measurements were performed on TA DSC Q100 under helium flow to characterize the T_g of the nanocomposites. 5–10 mg of samples was put into a hermetic aluminum pan. An empty cell was used as reference. Samples were heated from 25 to 140 °C at a heating rate of 10 °C/min and kept at this temperature for 15 min to erase the thermal history of the materials. Then they were cooled to 25 °C at the same speed. This cycle was repeated once; reported T_g was from the second heating, determined as the midpoint of the heat flow step. Thermal gravimetry analysis (TGA) measurements were performed on TA TGA Q50 under nitrogen flow to evaluate the quantity of residual solvent and check silica volume fraction. A mass of 15 mg of the sample was heated from 25 to 600 °C at a heating rate of 10 °C/min, and weight loss was measured. The weight fraction of residual solvent was found to be between 100 and 200 °C.

III. Results

1. Composite Films Formulation and Processing. As we said in the Introduction, we feel it is very important in nanocomposite science to obtain well-defined model systems, in which one knows how the filler is dispersed inside the matrix, to discriminate the polymer chain interfacial effects (including the dynamic ones) from effects of the network filler structure in the composites' mechanical properties. Nanocomposites of PS filled with silica nanoparticles have been extensively studied in the past decade.^{29,30} The results show the difficulty of obtaining a good dispersion of the silica particles at the nanometer scale, which formed in most cases large compact aggregates (of the order of a hundred nanometers or larger) in the PS matrix. One cause of this dispersion problem may be a difficulty in controlling, during the filmification process, the evaporation speed of the solvent used (toluene, THF, methyl ethyl ketone (MEK),²⁹ etc.) and the temperature with respect to boiling point and T_g . Indeed, various dispersions can be obtained with the same solvent.^{29,30} Anyway, in our case, dimethylacetamide (DMAc), the solvent in which silica particles are electrostatically stabilized (and which is also a good solvent

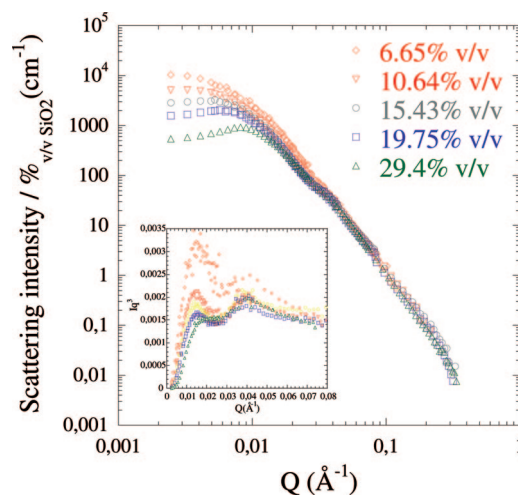


Figure 1. Scattering of the PS nanocomposite as a function of the filler concentration. The curves are normalized by the volume fraction of silica. In the inset, the IQ^3 vs Q representation for the same scattering curves. The oscillation, corresponding to initial spheres in contact, is highlighted around 4×10^{-2} Å $^{-1}$.

for the PS), has a high boiling point, 167 °C. The casting temperature could be fixed at 130 °C, which corresponds to a relatively controlled evaporation regime, while remaining above the T_g of the bulk polymer. The drying time has been determined, using the dry film reference (without silica particles), as the one for which DSC measurements showed a glass transition temperature stabilizing at $T_g = 98$ °C, i.e., very close to the one of native polymer powder ($T_g = 100$ °C). The residual quantity of solvent inside the composite film is found to plateau around 0.4 wt %, as determined by thermogravimetry.

2. Local Structure by SANS. The structure of the silica–PS composite films has been explored by SANS. The evolution of the SANS signal as a function of the silica volume fraction Φ_{SiO_2} in the films, respectively 6.6, 10.5, 15.7, 19.8, and 29.4% v/v, is presented in Figure 1. After the standard corrections and normalizations, the intensities ($(1/V)d\Sigma/d\Omega$, in cm $^{-1}$) are normalized by the volume fraction and corrected from the incoherent scattering of the nonfilled PS matrix as follows:

$$I(Q) = I_{\text{film}} - ((1 - \phi_{\text{SiO}_2})I_{\text{matrix}}) \quad (2)$$

Let us now discuss the aspect of the different spectra, which evidence different Q ranges:

(i) At high Q , all curves superimpose perfectly after dividing by the silica fraction, indicating a good normalization of the concentration and the thickness of the samples. The scattering intensity decreases like Q^{-4} , which is characteristic of the scattering of a sharp well-defined interface between the native silica particles ($R_0 = 5$ nm) and the polymer matrix. At the intermediate Q range, we note an oscillation, highlighted in a Q^3I vs Q representation (see inset in Figure 1) where it gives a maximum. Since the position of this maximum does not vary with the concentration, we can assume that it corresponds to a privileged distance inside every object, more precisely between initial spheres in contact inside the objects (in other words, an internal structure factor).

(ii) At low Q , the remarkable point of the whole set of data in Figure 1 is the absence of any upturn in intensity, for Q tending to 0. This indicates that if larger agglomerates existed, it would require lower Q s to detect them; in practice, TEM at low magnification (see below) shows, in the direct space, a complete absence of such agglomerates. For small concentrations (6.6 and 10.5% v/v), at low Q , the curves exhibit a plateau which is the signature of finite-size objects in the probed length

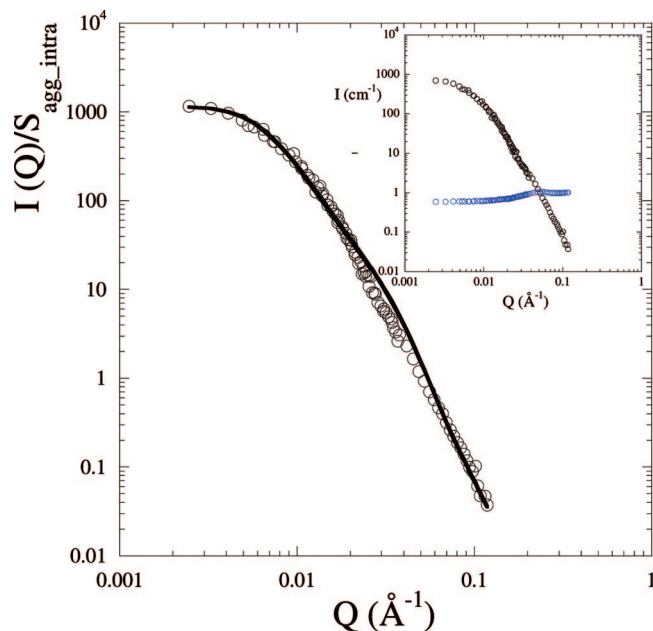


Figure 2. Form factor of the aggregates for the most diluted nano-composite (6.6% v/v). Black open circles are experimental data, and black full line is the calculation (see eq 2 and eq 3 for details of fit). In the inset, raw intensity (black open circles) and structure factor of the initial beads inside the aggregates (blue open circles).

scale. These objects, which we will now call “primary aggregates”, are the results of the aggregation of a finite number of the native silica beads. The form factor of the primary aggregate can be approached from the most diluted scattering curve (6.6% v/v, neglecting interaggregate correlations). We propose to model it by the form factor of fractal objects with the following equation:³¹

$$P_{\text{agg}}(Q) \approx N_{\text{agg}} Q^{-D_f} \frac{\int_0^\infty P_{\text{native beads}}(Q, R) L(R, \sigma) R^3 dR}{\int_0^\infty R^3 L(R, \sigma) dR} \quad (3)$$

where N_{agg} is the number of native beads inside the primary aggregate, D_f is the fractal dimension of the primary aggregates, $P_{\text{native beads}}(Q, R)$ is the form factor of a sphere, and $L(R, \sigma)$ is the log-normal distribution of the radius, with a variance σ . As we are dealing with the most diluted film, neglecting interaggregates correlations as explained above, we assume the structure factor between aggregates $S_{\text{agg inter}}$ to be close to 1. The total scattering intensity can thus be expressed as

$$I(Q) \approx \phi \Delta \rho^2 P_{\text{agg}}(Q) S_{\text{agg intra}}(Q) \quad (4)$$

where $\Delta \rho^2$ is the contrast difference between the silica and the PS matrix. The intra-aggregate structure factor, due to the repulsive interaction between initial silica beads in contact, can be expressed on the basis of the Percus–Yevick relation,³² which depends only on the radius and the concentration of the particles. We then use this structure factor $S_{\text{agg intra}}$ to divide the measured intensity of the film containing 6.6% v/v of silica particles; Figure 2 shows the result and its fit to eq 3 for $P_{\text{agg}}(Q)$. In the inset, one can see the superposition of the intensity and the calculated structure factor before division by $S_{\text{agg intra}}$.

In the calculation of eq 3, we use the radius and the log-normal polydispersity distribution (σ) of the native particles, determined from a SANS measurement of a diluted solution of particles (0.1% v/v) and fixed here to $R_0 = 5$ nm, $\sigma = 0.36$. The concentration is also fixed at the nominal value, so only the aggregation number and the fractal dimension are fitted. The result of the analysis, $N_{\text{agg}} = 15$, $D_f = 2.5$ (corresponding to

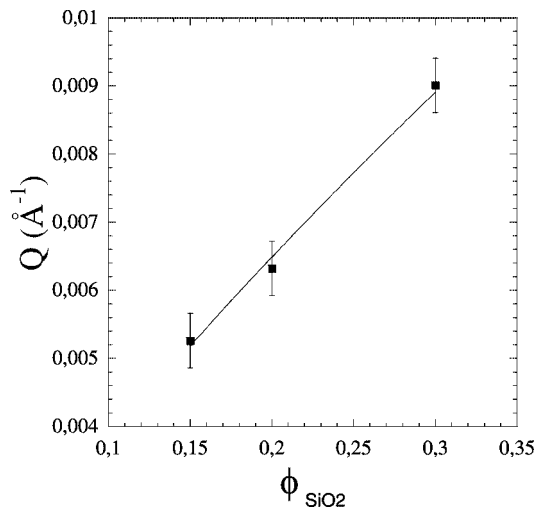


Figure 3. Variation of the filler nanocomposite concentration as a function of the scattering curve peak position (black open circle). The full line corresponds to a fit $q^* \sim \Phi_{\text{SiO}_2}^{0.87}$ with error ± 0.05 on the slope.

objects of a mean radius around 30 nm), agrees well with the experimental curve. The difference between the calculation and the experimental data around $4 \times 10^{-2} \text{ \AA}^{-1}$ comes mainly from the fact that we have not taken into account the polydispersity in the expression of the PY structure factor. The fractal dimension of the primary aggregates (2.5) extracted from the analysis should be also a little bit overestimated by the presence, but not clearly visible and accessible in the experimental Q range, of the interaggregates structure factor.

For larger silica fractions in the film, we see at low Q a second remarkable feature: a maximum appears. At first sight, the presence of this “peak” confirms the good dispersion of the particles in the polymer matrix: there is a privileged distance in the system. Let us now discuss its origin, using the evolution of the peak position as a function of the concentration (Figure 3).

Two situations can be considered. The first situation is described by the well-known hard-sphere model: the primary aggregates are distributed at random, on the condition that they cannot overlap; when increasing their concentration, they come closer to each other without being connected. This would lead to a liquidlike order showing repulsive interaction between the mass centers of the primary aggregates, and the variation of the peak position as the function of the concentration should be³³ $Q^* \sim \Phi^{1/3}$. The second situation is that the fractal primary aggregates connect with each other, which can be analogous to a percolation transition. In this case, Q^* should correspond to the characteristic size of the network mesh and display a $Q^* \sim \Phi^{0.88}$ scaling.³⁴ Plotting Q^* vs Φ (Figure 3), we obtain a slope of 0.87 ± 0.05 , suggesting that we are in this second situation for $\Phi_{\text{SiO}_2} > 10\%$ (below this value no maximum is seen in our Q range). Thus, SANS measurements give us a global but relevant view of both the form factor of the primary aggregates and the organization of the filler network in the polymer matrix.

However, to correlate the rheological macroscopic properties with the local filler structure, we need to make a final check and verify that there is no additional organization of the objects at a larger scale than the one probed with SANS. At the same time, it will also be interesting to confirm the local structure deduced from scattering, i.e., from correlations in reciprocal space, with a picture in real space. This is what we will show in the next section, using electronic transmission microscopy.

3. Structures on a Larger Scale by TEM. Two concentrations of silica particles, 6.6 and 15.7% v/v, have been investi-

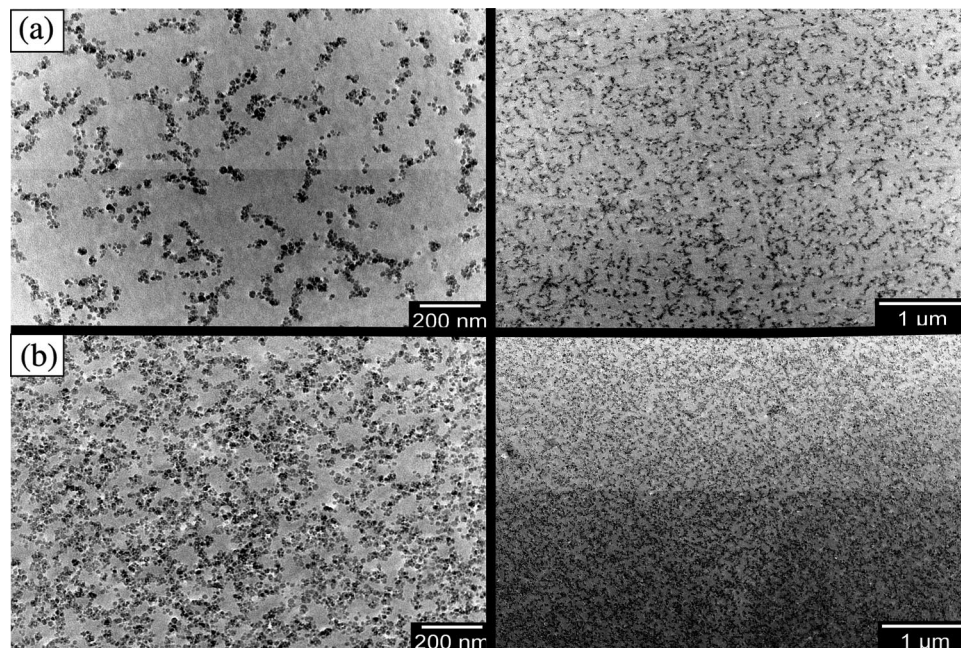


Figure 4. Transmission electronic microscopy on the nanocomposite filled with 6.6% v/v (a) and with 15.7% v/v (b) of silica particles. Observation at medium (left) and low (right) magnification are shown. The black zone corresponds to the silica and the gray to the polymer.

gated with TEM. Figure 4 presents the results obtained at two magnifications (see bars for 200 nm and 1 μm in the top and bottom figures, respectively). The most important result is that the homogeneity of the two samples is extremely good from the 50 nm scale to the macroscopic scale.

At $\Phi_{\text{SiO}_2} = 6.6\%$, the size distribution of the objects appears centered on a mean value which agrees well with the mean radius of primary aggregates deduced from the SANS analysis, i.e., 30 nm. The width of the distribution is enough to let objects of 200–300 nm at most appear. The origin of these objects is briefly discussed below. However, a further analysis of TEM would be out of this paper's scope, and we will keep using SANS results as a safe ensemble average of correlations. At $\Phi_{\text{SiO}_2} = 15\%$, the real-space picture confirms the model deduced from SANS. The structure keeps an “open” shape, i.e., does not show larger compact lumps: it shows a connected structure. We observe a characteristic net mesh size of the same order as $D = 2\pi/Q^* = 2\pi/5.3 \times 10^{-3} \text{ \AA}^{-1} \sim 120 \text{ nm}$, corresponding to the abscissa Q^* of the repulsion peak in the SANS spectrum for 15%. Thus, the important result here is that on a larger scale, up to macroscopic scale, the silica spatial distribution is homogeneous, with no connectivity signature at 5% and with connectivity at 15%.

Such changes from one picture to the next, at larger silica fractions, raise the question of the evolution of the structure with silica volume fractions. Is it related to an aggregation process specific to each concentration or to the progressive aggregation or percolation, according to the concentration, of initial building bricks which would be the primary aggregates, until one reaches a connected network? We will not attempt to answer this question here.

For $\Phi_{\text{SiO}_2} = 6.6\%$, to evaluate the mean rim-to-rim distance between two primary clusters, we have to return to SANS data. Because of the absence of a maximum in the available range $(2-3) \times 10^{-3} \text{ \AA}^{-1}$ in the SANS curve for the diluted regime, this cannot be calculated directly. We can make two different estimates. On the one hand, in the hypothesis of a progressive connection of primary aggregates, D is larger than the minimal distance D_{min} , at a larger concentration, extracted when a maximum is detectable: in Figure 2, the peak appears for $\Phi_{\text{SiO}_2} = 15\%$ and gives $D_{\text{min}} \sim 120 \text{ nm}$, as shown above. On the other

hand, ignoring this hypothesis, we can, on a general basis, use the absence of a visible maximum at $Q > 3 \times 10^{-3} \text{ \AA}^{-1}$. This suggests, in a less accurate way, that this distance is larger than $D = 2\pi/3 \times 10^{-3} \text{ \AA}^{-1} \sim 200 \text{ nm}$. Knowing the mean radius of the primary aggregates, 30 nm, we can deduce that the minimal distance between the rims of two primary aggregates, for the diluted regime ($\Phi_{\text{SiO}_2} = 6.6\%$), can be estimated around 60 nm in the first case and 100 nm in the second case. This order of magnitude is also confirmed by a careful examination of a large number of real-space picture (an example being Figure 4a). Since the thickness of the slab is of the order of 50 nm here, a value of 60 nm can safely be drawn for the 3d space.

4. Low Deformation Mechanical Measurements. Low deformation measurements are interesting because the microstructure of the films shows much less alteration. The first set was obtained using the shear plate–plate rheometer ARES (amplitude 0.5%). In Figure 5a the variation of the elastic modulus G' is presented for a fraction of silica increasing from 0 to 5% v/v, as a function of the product of the pulsation ω (rad/s), by the factor a_T of time–temperature superposition to a reference temperature 143 °C. For further discussion, we note that the lowest value of ωa_T , 10^{-2} rad/s , corresponds to a maximum accessible time $2\pi/10^{-2} \text{ rad/s} = 600 \text{ s}$ at 143 °C. For pure PS, the curve has the usual shape in a log–log plot. At a high frequency, it shows a slope of $-1/2$ associated with the Rouse modes of the chains. At an intermediate pulsation $\omega \sim 0.1 \text{ rad/s}$, a drop is observed which is characteristic of a terminal time (“creep zone”, around $2\pi/\omega \sim 60 \text{ s}$, at $T = 143 \text{ °C}$). At a lower pulsation, a decrease with $G'(\omega) \sim \omega^2$ can be, as usual, associated with a liquid state of the polymer. The terminal time measured is in agreement with the molecular weight used here for the matrix. The height of the plateau is of order of $1 \times 10^5 \text{ Pa}$, i.e., close to the value G_N^0 , well-known for the entangled rubbery plateau of PS ($2 \times 10^5 \text{ Pa}$). The behavior of $G''(\omega)$ is given in Figure 5b and is also characteristic of entangled polystyrene of this molecular weight.

When silica is introduced, both $G'(\omega)$ and $G''(\omega)$ show clearly that, at high pulsation $\omega a_T > 100 \text{ rad/s}$, whatever the silica volume fraction, the behavior of the nanocomposite is very close to the one of the PS matrix: the Rouse modes of the chains are

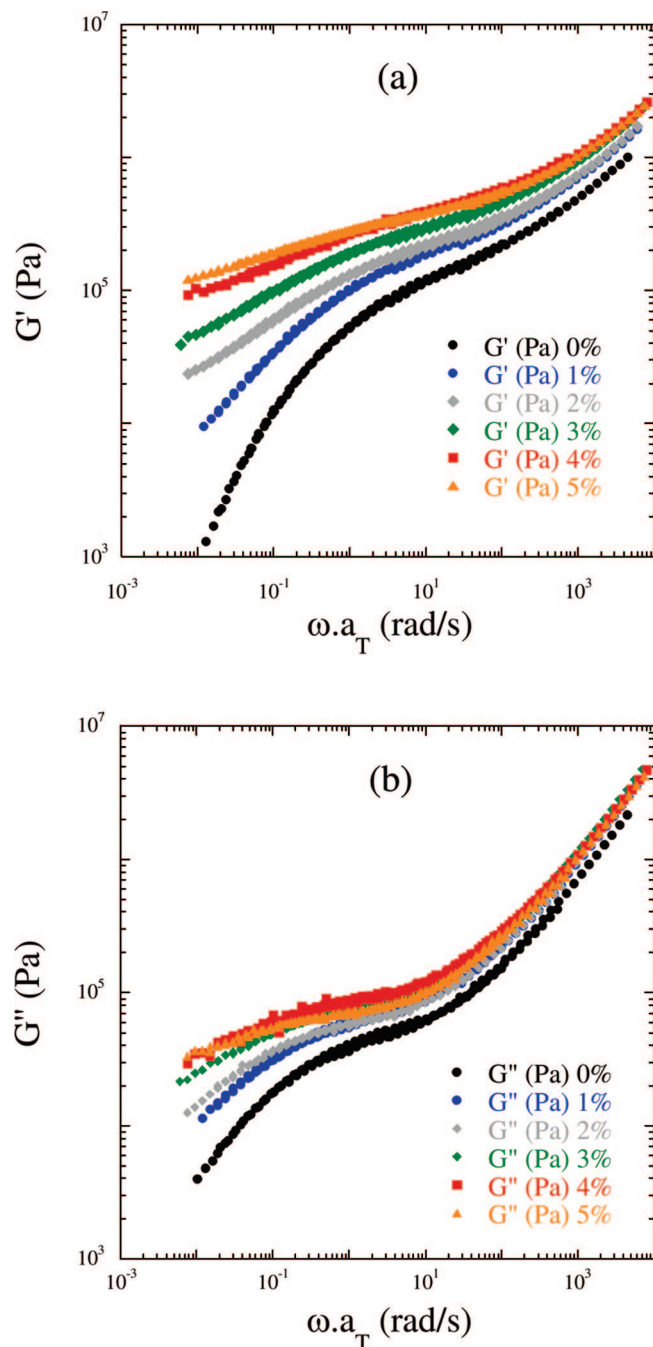


Figure 5. Elastic shear modulus G' (a) and G'' (b) as a function of pulsation ω , using time–temperature superposition ($T_0 = 143$ °C) coefficient a_T defined in the text, for different volume fractions of silica in the composite (0, 1, 2, 3, 4, and 5% v/v).

still observed. At intermediate and low frequencies, differences appear. At $\omega a_T > 10$ rad/s, this is limited to a progressive increase of G' with silica fractions, analogous to elastic reinforcement as expected. But in the lowest pulsation regime, $\omega a_T < 1$ rad/s, a much more differentiated behavior is observed: adding silica greatly increases the terminal times. For the lowest silica volume fraction, it is only slightly increased compared to the one for pure PS; the creep zone stays in the same pulsation range, but a more accurate value can be extracted from the ω abscissa of the crossing of G' and G'' . As soon as the silica fraction reaches 2% v/v, the terminal relaxation time become so long that the creep zone is no longer visible in the experimental window. The existence of a long elasticity time is accompanied, predictably, by a low dissipation, so that the G'' values become inferior to the G' values in the low frequency

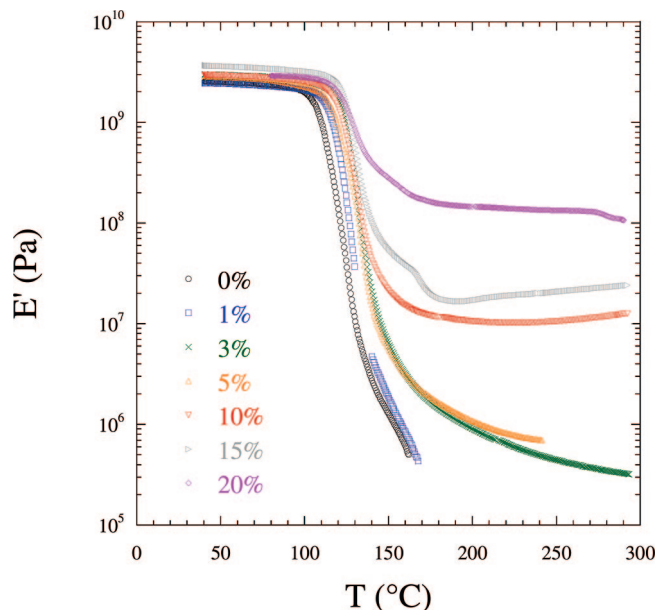


Figure 6. DMA measurements of elastic modulus E' as a function of temperature for different volume fraction of silica (from 0 to 20% v/v) (note for comparison with Figure 5 that $E' = 3$ G).

range. In such a low ω range, the slopes n of the G' and G'' curves in the log–log plot become parallel—in a rather narrow window in practice—and the ratio G'/G'' , written as $\tan \delta(\omega)$, is equal to $\tan(n\pi/2)$, as observed in a gelling process.⁸ For higher silica concentrations (from 3 to 5%), this additional (with respect to pure matrix) elastic behavior is even more marked in the same low ω range. It seems at $\Phi > 3\%$ that the curve decay for ω tending to 0 is slower. The trend of a plateau at lower ω is more and more apparent at $\Phi = 4\%$ and 5% . Comparison of parts a and b of Figure 5 enables us to see the parallel evolution of G' and G'' . We can note, on the curve corresponding to 4%, the same type of shoulder at the same abscissa as for pure PS, suggesting that we see a contribution from chain reptation before (i.e., at higher ω than) the final slow decay. The height at low ω of what we could call the “secondary plateau” is close to 1×10^5 Pa. Values at intermediate pulsations have also increased, becoming of the order of 5×10^5 up to 10^6 Pa. This makes measurements at higher Φ_{SiO_2} more delicate, due in particular to risks of slippage.

For high concentrations, we turned to DMA experiments performed at fixed frequency (5 Hz), with an amplitude deformation ratio of 0.1%. As detailed in section II, using time–temperature superposition, measurements between 143 and 200 °C correspond to a time range at 143 °C between 0.2 and 60 s. In Figure 6, we show the evolution of the storage modulus E' for different volume fraction of silica (from 0 to 20% v/v), as a function of temperature. For pure PS (without silica), at low temperature, i.e., for $T < T_\alpha$, the curve is typical of amorphous polymer with a high elastic modulus plateau of about 2.5 GPa. It corresponds to the glassy regime. The value obtained for T_α is the usual one retained for the glass temperature of PS.

When T increases above T_α , a steep decrease of E' is observed, followed by a shoulder corresponding to the entanglement rubbery plateau, very narrow before to be cut at slightly larger temperature by a strong decrease corresponding to the terminal relaxation. Measurements were stopped above the temperature at which the modulus becomes too weak because the samples were flowing over during the measurement time.

In the presence of silica, different behaviors appear successively as the volume fraction increases. First, the glassy plateau

keeps the same height over the whole range of Φ_{SiO_2} . Second, at high temperatures ($T > 130$ °C), three successive types of behavior can be distinguished: (i) For the lowest value of Φ_{SiO_2} (1% v/v), the behavior remains close to that of pure PS: the creep zone shoulder at higher temperatures keeps the same shape; it shifts slightly when passing from pure PS to 1% silica—by less than 10 °C—after which the sample flows. Note the height of the inflection point is of the same magnitude as the modulus obtained on the oscillatory shear plate–plate ARES rheometer (i.e., of the order of 0.1 MPa; we recall that $E = 3$ G in linear deformation range). (ii) For higher Φ_{SiO_2} range, 3 and 5% v/v, the most important fact is that at high T ($T \sim 150$ °C) the characteristic creep zone of pure PS disappears completely: the curvature is reversed, so that E' decreases slowly and seems to tend toward a plateau (~ 1 MPa) at high temperatures (which however it does not reach). (iii) For volume fractions of 10% v/v, this plateau becomes clearly visible, and much higher (10^7 Pa). For 10 and 15% v/v, definitely, high elastic plateaus are present, at the 5 Hz frequency (10 and 100 MPa). For 20% v/v, the plateau height has jumped to more than 10^8 Pa, only 1 decade below the glassy plateau height. The slight decrease visible at the highest temperature may be an artifact. We did not measure at larger temperatures than 300 °C because this would pass the limit of matrix's thermal stability. These results will be examined further in the Discussion section.

5. High Deformations: Stress–Strain Isotherms. Figure 7a shows the evolution of real stress σ as a function of the elongation ratio λ for $\Phi_{\text{SiO}_2} = 0, 1, 2, 3, 4, 5, 7.5, 10, 12.5,$ and 15% v/v. For higher concentrations ($> 15\%$ v/v), samples did not stretch homogeneously at high elongation ratios: the stress was extreme, and the samples escaped it by forming local shear bands in different zones along the sample, leading to a somehow disorganized deformation. We do not present those curves and only focus on homogeneous and well-stretched samples. In these elongation measurements, all shorter processes will not produce an elastic reversible contribution, though they will contribute to the effective viscosity, but this contribution is not dominant. The set of stretching curves can be summarized by the progressive increase with Φ_{SiO_2} of an initial stress jump at the beginning of the elongation, while the shape at large λ is similar, except for the shift due to the initial jump. This initial stress jump can be expressed in terms of an initial slope of stress vs deformation $\varepsilon = \lambda - 1$ in a low elongation ratio ($\lambda < 1.1$) regime, giving an effective Young modulus $E_{\text{nanocomposite}}$ in this range of deformation. We have to be aware of the limitations of this analysis: the deformation ε and the initial velocity gradient $d\varepsilon/dt$ at λ close to 1 are not accurately known, so that the sample may initially be subjected to a stronger and faster deformation than the nominal values. This may, in particular, alter the filler network. However, we will see in the Discussion that these values compare well with the DMA values at equivalent instrumental times.

For very high silica concentration ($\Phi_{\text{SiO}_2} > 10\%$ v/v), a maximum is observed in the stress–strain curves, more and more pronounced when Φ_{SiO_2} increases. Most of the time, this peak appears simultaneously with local necking, which is not discussed here. Actually, to compare with the pure matrix, a simplistic way to represent the reinforcement effect in nanocomposites is to plot the ratio of nanocomposite stress over the pure matrix stress versus λ . In Figure 7b this reinforcement factor $R(\lambda)$ increases notably with Φ_{SiO_2} for small λ (from 1 for 1% v/v to 100 for 15% v/v). At large λ , all curves show a rapid decrease toward what seems to be a constant value. This final “value” is a more slowly increasing function of Φ_{SiO_2} ; no strong divergence with Φ_{SiO_2} is seen here. Note however that the reinforcement factor remains 4 for 15%, at an elongation ratio of 2.

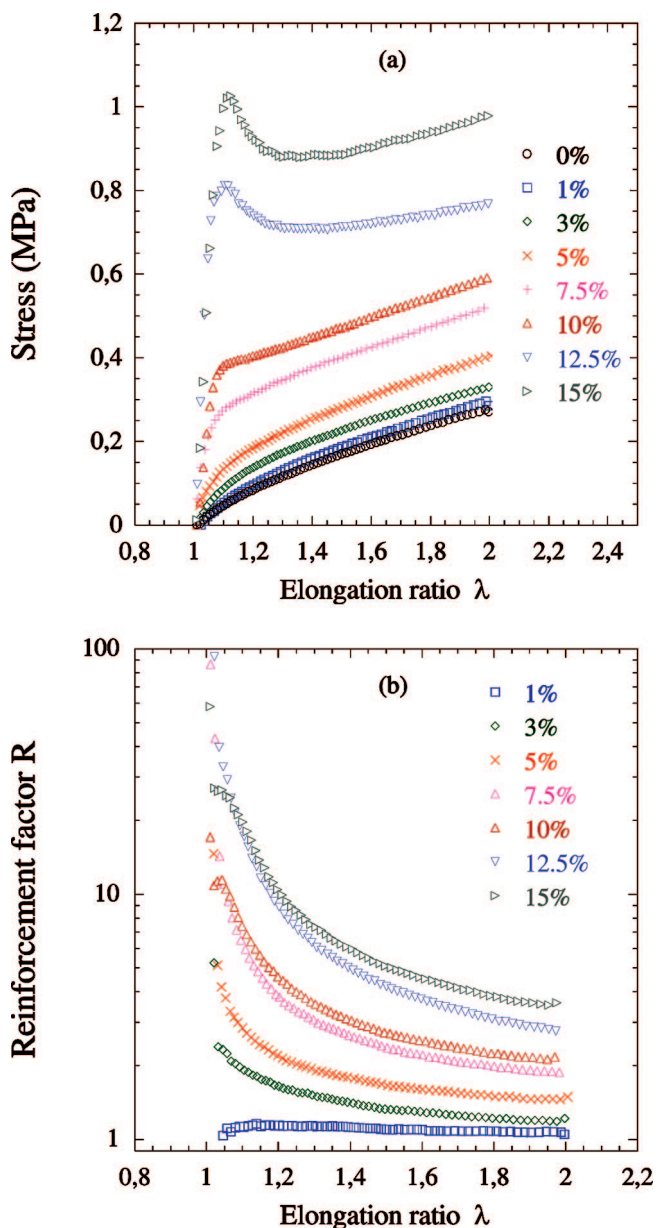


Figure 7. (a) Real stress as a function of elongation ratio for different silica volume fractions. (b) Reinforcement factor as a function of the elongation ratio. The experiments have been performed at $T_g + 20$ °C.

6. Differential Scanning Calorimetry. Figure 8a shows the differential scanning calorimetry thermograms for the pure polymer and the different nanocomposites (from 1% to 20% v/v). All curves exhibit similar behavior: a slow decrease of heat flow followed by a steeper descent, provoking a step and corresponding to the glass transition temperature (T_g). We did not observe change of step height, i.e., of specific heat capacity ΔC_p (normalized by weight fraction of polymer) at T_g which is constant as a function of silica content. The width ΔT is also constant with the increase of filler concentration. So magnitude and width of the step associated with the glass transition remain constant with the increase of silica fractions. In every case, we observe a single transition, in agreement with the spatial homogeneity of the sample.

Figure 8b shows the change in such measurement of T_g compared to that of pure PS for several nanocomposites (1, 3, 5, 10, 15, and 20% v/v). The T_g determined by DSC increases with the addition of silica. The positive shift is 6 °C for $\Phi_{\text{SiO}_2} = 20\%$. An opposite shift (negative) has been found for other

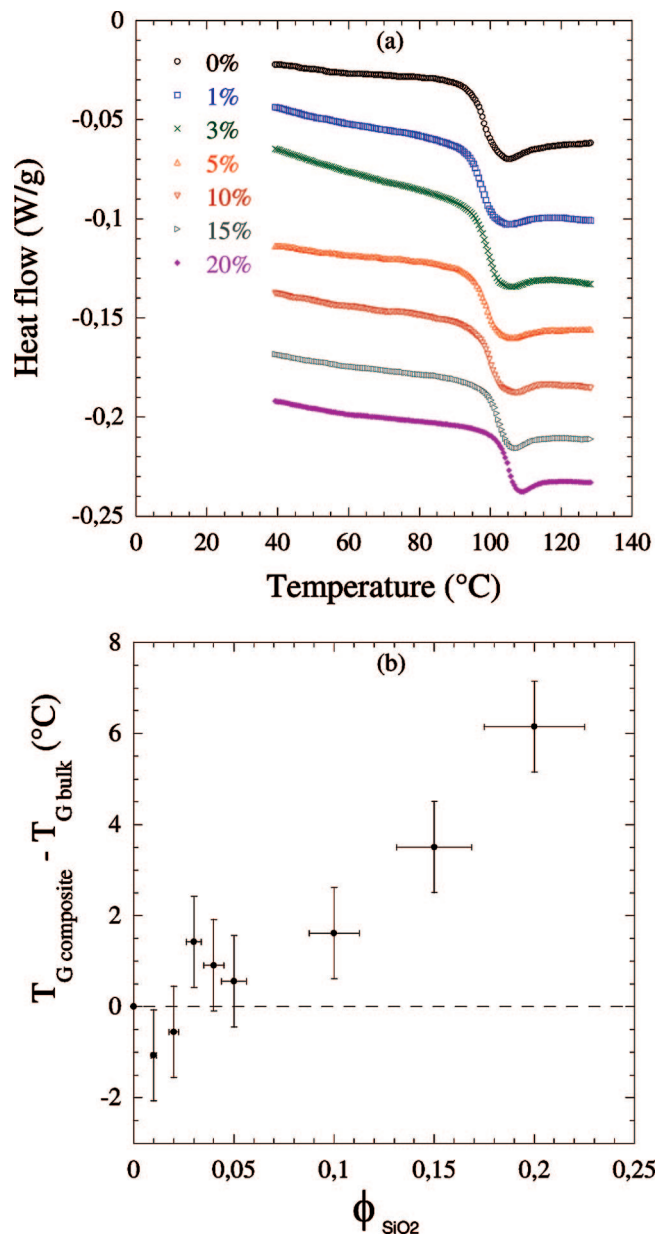


Figure 8. (a) Heat flow vs temperature for different silica content % v/v: 0, 1, 3, 5, 10, 15, and 20 (to clarify, all data have been shifted along the heat flow axis). (b) $T_{g, \text{composite}} - T_{g, \text{bulk}}$ PS as a function of silica content. Vertical errors bars are standard deviations from measurements (± 1 °C).

PS–silica composites prepared in different conditions,²⁹ but in further investigations of the same group, leading to better dispersion, this negative shift vanished.³⁰

IV. Discussion

The precise description of the key parameter that governs the reinforcement mechanisms of nanocomposites depends on a thorough knowledge of the filler dispersion on the local scale. This is not always accessible due to difficulties of sample processing (reproducibility, complexity) and suitability of the samples to characterization methods. Here, a reliable and reproducible processing technique allowed us to obtain well-defined nanocomposites, on which we were able to apply a combination of SANS and electronic microscopy to picture the nanomorphology of the silica particle inside the PS matrix. The dispersion can be summarized as follows: the system presents a silica volume fraction threshold (located around 7% v/v)

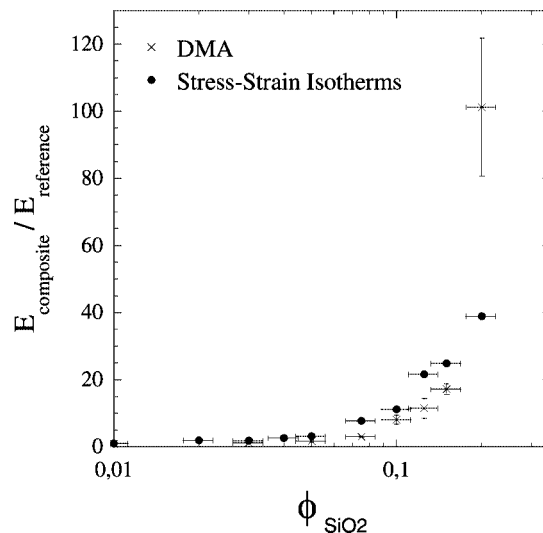


Figure 9. Reinforcement factor as a function of silica volume fraction for two different mechanical techniques: cross from DMA and full circle from stress–strain isotherms.

between two main domains of the silica organization in the matrix. For silica volume fractions lower than this critical value, the silica particles gather in finite-sized fractal clusters called “primary aggregates”, of a small mean radius ~ 30 nm, which are homogeneously dispersed on a larger scale inside the matrix; they have no direct connectivity since they are separated from each other by a mean typical rim-to-rim distance of ~ 60 nm, which represents the minimal estimated value. For silica volume fractions larger than the critical silica volume fraction, similar primary aggregates still exist, and due to the increase of their number per volume unit, they percolate into a directly connected and continuous network. The next step is now possible: to identify the mechanical responses of the composite with the two different structural organizations, for various characteristic time ranges (at 143 °C) and rates of deformation depending on the technique: shorter times (0.5–60 s) for DMA (low deformation) and (2 s) for stretching (large deformation) and longer times (200 s) for small deformation for ARES.

For the shorter times, the results are summarized in Figure 9. The moduli $E_{\text{nanocomposite}}$ extracted from the initial slopes of the stretching curves (see section II) have been represented in the form of the reinforcement ratio $E_{\text{nanocomposite}}/E_{\text{matrix}}$, as a function of filler concentration. We see in this plot a first linear part and then a fast divergence around 7%.

This behavior is confirmed in the same Figure 9 with moduli extracted from DMA measurements at $T = 1.3T_{\alpha}$, which corresponds to instrumental times at 143 °C equivalent to stretching times. The two curves show parallel behavior. Assuming a fully elastic contribution, the crossover of the reinforcement factor, which corresponds to the critical volume fraction of the connected filler network’s formation, can be interpreted in terms of connectivity, more precisely of percolation between the primary aggregates. Several classical equations^{11–13} have attempted to describe such effects in the literature but are known to fail to reproduce the divergence. This behavior was formerly observed for the rubbery modulus obtained from DMA of polymers reinforced by fillers of higher aspect ratio (fibers, platelets^{9,10}) and also formulated by Heinrich et al.¹⁴ for fractal aggregates. We have attempted to fit data to such a formula,¹⁴ but the fit is very sensitive to the value of the different fractal dimensions and easily gives unphysical values. If we restrict ourselves to the crossing between the low Φ_{SiO_2} and high Φ_{SiO_2} asymptotes of the curve in Figure 9, we obtain an indicative value of $\Phi_{\text{SiO}_2}^* \sim 7\text{--}10\%$. There is thus a clear

direct correlation here between such mechanical behavior in nanocomposites and the local structure of the filler in the polymer matrix: the divergence of the reinforcement factor appears at the critical silica volume fraction at which the isolated primary aggregates are closer to each other and form a connected network.

For the longer times, a second and more surprising mechanical response of the composite appears in the silica volume fraction domain, in which the filler elements are not directly connected to each other, i.e., below the silica volume fraction threshold, for $\Phi_{\text{SiO}_2} < \Phi_{\text{SiO}_2}^*$. Although the rims of primary aggregates are separated by a mean minimal distance of 60 nm, the oscillatory shear experiments (Figure 5) and the DMA experiment at high temperature (Figure 6) show an additional process corresponding to a longer terminal time, greater than the terminal time of the matrix. This means that after a decay of most of the elasticity at the matrix terminal time, an elastic fraction stays. At $\Phi_{\text{SiO}_2} \geq 4\%$, the complete relaxation of this elastic fraction is beyond our accessible time range. The occurrence of such elasticity between aggregates not directly connected, but separated by very long paths through a polymer matrix of shorter terminal time, which should shortcut any additional elasticity, is, to our knowledge at least, an unexpected and original result.

The origin of this additional elastic contribution can first be discussed along the idea of the existence of a “glassy zone” around the particle filler. This has been proposed from earlier studies,^{7,15–18} up to more recent research³⁵ from ¹H NMR and rheological measurements. It is suggested that this zone increases the effective volume of the filler around each particle³⁵ and also that it shifts the threshold for percolation between the hard regions. The EHM model³⁶ developed for ionomers assumes the existence around the hard zones of intermediate mobility regions of a given thickness, which merge into low mobility regions when they percolate. The EHM model has been extended to nanofillers in polymer.⁷ It has also been suggested that the hard coronas act on the steric repulsion (“hard-sphere model”) between the filler particles and hence on the spatial correlations as observed using SANS characterization.²³ In these systems, the filler is mostly spherical particles, and volume fractions are often higher than 10%.^{7,35,36} A comparison with these studies addresses the problem of the value of the thickness ζ of the glassy region around the filler. It should be equal to 30 nm in our case, considering that the lowest distance between the closest rims of two primary aggregates is 60 nm. Several of the earlier studies on ¹H NMR proposed an estimate for ζ of a few nanometers (for temperatures usually above T_g by several tens of °C). Similar values were proposed from the volume fraction dependence of DMA measurements in ionomers.³⁶ More recently, Berriot et al.³⁵ obtained by NMR an increasing thickness with decreasing T a bit closer to T_g : ζ_{NMR} increasing from 2 nm at $T - T_g = 100$ °C to 3 nm for $T - T_g \sim 50$ °C. These values of ζ_{NMR} agreed with the values of effective volume with respect to nominal volume fraction extracted from mechanical reinforcement. Using a formula extracted from the thickness dependence of T_g in thin films,³⁷ the same authors could extrapolate this dependence down to lower T , in the range $T - T_g < 50$ °C, and this dependence agreed with the values of ζ_{mech} obtained from mechanical reinforcement. The latter passes 25 nm only for T very close to T_g only ($\zeta_{\text{mech}} \sim 30$ nm at $T - T_g \sim 3$ °C³⁵). This is much closer to T_g than the temperature of our different mechanical measurements, i.e., between T and $T_g = 20$ and 70 °C. Since ζ_{NMR} decreases fast with increasing $T - T_g$, it remains notably smaller than 25 nm and does not explain our results.

Moreover, we face another discrepancy with the measurements of Berriot et al.^{19,35} In their case, the dependence of ζ over $T - T_g$ results in the failure of the usual William–

Landel–Ferry–Vogel–Fulcher time–temperature superposition. As a consequence, the reinforcement factor $R(T, \omega)$ does not obey the same time temperature superposition as the matrix. In our case, conversely, the time–temperature superposition applies correctly for oscillatory shear measurements, with the same coefficients as for the pure PS matrix. If a value of 25 nm is required for ζ to explain our $\Phi_{\text{SiO}_2} = 6.6\%$ data, this value must be kept at 120 °C for stretching and above for shear. This is also imposed by the DMA measurements at 5 Hz which display high reinforcements for $\Phi_{\text{SiO}_2} = 6.6\%$, up to $T - T_g = 70$ °C. So far from T_g , ζ_{NMR} has in most studies been estimated to a few nanometers. Keeping much larger values would mean a particularly strong interaction between the filler and the polystyrene. Though it is in principle possible, since the filler and the polymer are different from the ones in ref 35 and other NMR investigations, the existence of such an interaction is in contradiction with the DSC measurements: even at = 20%, DSC gives a shift of the average T_g of 6 °C only. In summary, attributing through-polymer connectivity between our aggregates to glassy zones around the nanofillers implies thicknesses larger by more than a factor 10 to commonly accepted values and without visible temperature dependence.

Along the same lines, the origin of the additional elastic contribution could be the result of the existence of continuous glassy paths between aggregates. This has been proposed as a theory to explain shifts in T_g and other dynamics in ultrathin films³⁸ for which some shift in T_g appears, for typical film thickness of 50 nm.³⁹ This analogy with thin film has also been proposed by Kumar et al.^{29,30} to explain the shift in T_g in some nanocomposites (which is abated in ref 29 but not in ref 30 as it can depend on the matrix polymer interaction and the processing). Note that if the orders of magnitude of the characteristic distance are the same in our system and in thin films, a marked difference appears in the sign of the shifts in T_g which are negative in thin film for cases corresponding to no or weak polymer–surface interaction, while it is slightly positive in our case (Figure 8). This observation implies the need to reconsider the polymer–filler interaction in our case which appears to be possibly stronger than expected. Apart from specific surface chemistry considerations, which we are not in a position to study in our system, the origin of a stronger polymer–filler interaction could be attributed to the shape of our primary aggregates; at scale between the size of the individual particles (5 nm) and the size of the aggregate (30 nm) the surface is contorted. This can be associated with earlier proposals that the interaction potential between polymer and a fractal filler surface is much enhanced by its roughness.^{14,20} This assumption of stronger polymer–filler interaction opens the way to an additional conformational contribution, via the bridging of the primary aggregates by some matrix chains. Saverstani et al.⁴⁰ have proposed a model and some simulations based on the formation of a mixed polymer–filler network by adsorption of the chain on the filler objects. They have showed that an additional elastic contribution appears in the modulus when the mixed network is formed for a typical rim-to-rim distance equal to twice the gyration radius of the polymer chains. For our PS chains ($M_w = 280\,000$ g/mol, $I_p = 2$) the average R_g should be ~ 15 nm; thus, a distance of 30 nm is expected, still lower than our minimal rim-to-rim distance of 60 nm, but molecular weight polydispersity could play a role in this phenomenon.

To end this discussion, we would like to recall that secondary relaxation times were formerly observed in filled systems of well-dispersed particles;²³ in this case, a model assuming no specific lower mobility regions, but only spatial correlations at large distances, was used.⁴¹ However, the plateau moduli obtained in this case are much lower than in the present study.

V. Summary and Conclusion

In summary, we have been able to synthesize, over a wide range of volume fraction, polymer systems filled with very small particles (5 nm in size), aggregated at nanometer size only, and well dispersed at all larger sizes. We were then able to characterize the structure precisely over the full relevant size range, from nanometer to sample size, owing to a combination of small-angle neutron scattering and transmission electronic microscopy. The fillers form small primary aggregates of tens of particles, of elongated, slightly ramified shape, with a radius around 30 nm, distributed homogeneously in the matrix and separated by a mean rim-to-rim distance of 60 nm. When the silica volume fraction is increased, a threshold $\Phi_{\text{SiO}_2}^*$ appears, at which the primary aggregates percolate in a directly connected filler network. Two very different nanocomposite structures can thus be tuned with the simple silica volume fraction parameter. The resulting mechanical response of the material was then analyzed through different mechanical tests. Initially, with short time spans, both stretching and DMA experiment were a simple illustration of the influence of the filler network connectivity on reinforcement properties. A direct correlation between the divergence of the reinforcement factor and the formation of the primary aggregates' connected filler network was seen. Second, with longer time spans (than the matrix terminal time) and small deformation (1%), a more surprising mechanical signature appeared below the silica volume fraction threshold for connectivity: the material exhibited an additional elastic contribution, with very long terminal times (not accessible). Comparing this effect with the dynamic effect attributed to a glassy layer model around the filler, the discrepancy is that the typical extension layer was around 2 nm, much lower than our rim-to-rim distance of ~ 60 nm. Similar values were however seen in T_g shifts of thin polymer films (the typical thickness threshold being around 50 nm). We must also reconsider the polymer–filler interaction, which can be stronger due to the higher adsorption capacity of fractal filler compared to single spheres. In this case, the mechanical behavior could be the result of an additional conformational effect through the formation, for a typical distance of $2R_g \sim 30$ nm, of a mixed polymer–filler network by a bridging effect on the part of the polymer chains.

Acknowledgment. We thank the Région Bretagne and the CEA for N. Jouault's PhD Grant. The Laboratoire Léon Brillouin is a common facility of the CEA (IRAMIS) and CNRS.

References and Notes

- Leblanc, J. L. *Prog. Polym. Sci.* **2002**, *27*, 627–687.
- Jing, X.; Zhao, W.; Lan, L. *J. Mater. Sci., Lett.* **2000**, *19*, 377–379.
- Flandin, L.; Prasse, T.; Schueler, R.; Bauhoffer, W.; Schulfe, K.; Cavallé, J.-Y. *Phys. Rev. B* **1999**, *59*, 14349–14355.
- Kluppel, M.; Heinrich, G. *Rubber Chem. Technol.* **1995**, *68*, 623–651.
- Botti, A.; Pyckout-Hintzen, W.; Richter, D.; Urban, V.; Straube, E. *J. Chem. Phys.* **2006**, *124*.
- Melé, P.; Marceau, S.; Brown, D.; de Puydt, Y.; Albérola, N. D. *Polymer* **2002**, *43*, 5577–5586.
- Tsagaropoulos, G.; Eisenberg, A. *Macromolecules* **1995**, *28*, 6067–6077.
- Cassagnau, P. *Polymer* **2003**, *44*, 2455–2462.
- Chabert, E.; Bornert, M.; Bourgeat-Lami, E.; Cavaille, J.-Y.; Dendievel, R.; Gauthier, C.; Putaux, J.-L.; Zaoui, A. *Mater. Sci. Eng. A* **2004**, *381*, 320–330.
- Dalmas, F.; Cavallé, J.-Y.; Gauthier, C.; Chazeau, L.; Dendievel, R. *Compos. Sci. Technol.* **2007**, *67*, 829–839.
- Einstein, A. *Ann. Phys.* **1906**, *17*, 549.
- (a) Smallwood, H. M. *J. Appl. Phys.* **1944**, *15*, 758. (b) Guth, E. *J. Appl. Phys.* **1945**, *16*, 20.
- Batchelor, G. K.; Green, J. T. *J. Fluid Mech.* **1972**, *56*, 401–427.
- Heinrich, G.; Kluppel, M.; Vilgis, T. A. *Curr. Opin. Solid State Mater. Sci.* **2002**, *6*, 195–203.
- Kaufman, D.; Slichter, W. P.; Davis, D. D. *J. Polym. Sci., Polym. Phys. Ed.* **1971**, *9*, 829.
- O'Brien, J.; Cashell, E.; Wardell, G. E.; McBrierty, V. J. *Macromolecules* **1976**, *9*, 653.
- Ito, M.; Nakamura, Tanaka, T. *J. Appl. Polym. Sci.* **1985**, *30*, 3493–3504.
- Dutta, N. K.; Choudhury, N. R.; Haidar, B.; Vidal, A.; Donnet, J. B.; Delmotte, L.; Chazeau, J. M. *Polymer* **1994**, *35*, 4293–4299.
- Berriot, J.; Montes, H.; Lequeux, F.; Long, D.; Sotta, P. *Macromolecules* **2002**, *35*, 9756–9762.
- Vilgis, T. A. *Polymer* **2005**, *46*, 4223–4229.
- Berriot, J.; Montes, H.; Martin, F.; Mauger, M.; Pyckout-Hintzen, W.; Meier, G.; Frielinghaus, H. *Polymer* **2003**, *44*, 4909–4919.
- Carrot, G.; El Harrak, A.; Oberdisse, J.; Jestin, J.; Boué, F. *Soft Matter* **2006**, *2*, 1043.
- Inoubli, R.; Dagréou, S.; Lapp, A.; Billon, L.; Peyrelasse, J. *Langmuir* **2006**, *22*, 6683–6689.
- Oberdisse, J.; El Harrak, A.; Carrot, G.; Jestin, J.; Boué, F. *Polymer* **2005**, *46*, 6695–6705.
- Jestin, J.; Cousin, F.; Dubois, I.; Ménager, C.; Schweins, R.; Oberdisse, J.; Boué, F. *Adv. Mater.* **2008**, *20*, 2533–2540.
- Calmettes, P. *J. Phys. IV* **1999**, *9*, 83.
- Williams, M. L.; Landel, R. F.; Ferry, J. D. *J. Am. Chem. Soc.* **1955**, *77*, 3701.
- Ferry, J. D. *Viscoelastic Properties of Polymers*, 3rd ed.; Wiley: New York, 1980; p 641.
- Bansal, A.; Yang, H.; Li, C.; Cho, K.; Benicewicz, B. C.; Kumar, S. K.; Schadler, L. S. *Nat. Mater.* **2005**, *4*, 693.
- Sen, S.; Xie, Y.; Bansal, A.; Yang, H.; Cho, K.; Schadler, L. S.; Kumar, S. K. *Eur. Phys. J. Spec. Top.* **2007**, *141*, 161–165.
- Rivière, C.; Wilhelm, F.; Cousin, F.; Dupuis, V.; Gazeau, F.; Perzynski, R. *Eur. Phys. J. E* **2007**, *22*, 1–10.
- Percus, J. K.; Yevick, G. J. *Phys. Rev.* **1958**, *110*, 1.
- Benoit, H.; Decker, D.; Duplessix, R.; Picot, C.; Rempp, P.; Cotton, J.-P.; Farnoux, B.; Jannink, G.; Ober, R. *J. Polym. Sci.* **1976**, *14*, 2119–2128.
- Stauffer, D. Taylor and Francis: London, 1985.
- Berriot, J.; Montes, H.; Lequeux, F.; Long, D.; Sotta, P. *Eur. Phys. Lett.* **2003**, *644*, 50–56.
- Eisenberg, A.; Kim, J. S. *Introduction to Ionomers*; Wiley-Interscience: New York, 1998.
- Forrest, J. A.; Mattson, J. *Phys. Rev. E* **2000**, *61*, R53.
- Long, D.; Lequeux, F. *Eur. Phys. J. E* **2001**, *4*, 371.
- Alcoutlabi, M.; McKenna, G. J. *Phys.: Condens. Matter* **2005**, *17*, R461–R524.
- (a) Sarvestani, A. S. *Eur. Polym. J.* **2008**, *44*, 263–269. (b) Yezek, L.; Schaefer, W.; Yongming, C.; Gohr, K.; Schmidt, M. *Macromolecules* **2003**, *36*, 4226.
- Dagréou, S.; Mendiboure, B.; Allal, A.; Marin, G.; Lachaise, J.; Marchal, P.; Choplin, L. *J. Colloid Interface Sci.* **2005**, *282*, 202–211.

MA801908U

Direct small-angle-neutron-scattering observation of stretched chain conformation in nanocomposites: More insight on polymer contributions in mechanical reinforcement

Nicolas Jouault,¹ Florent Dalmas,² Sylvère Said,³ Emanuela Di Cola,⁴ Ralf Schweins,⁵ Jacques Jestin,^{1,*} and François Boué¹

¹Laboratoire Léon Brillouin, CEA Saclay, 91191 Gif-Sur-Yvette, France

²Institut de Chimie et des Matériaux Paris-Est, UMR 7182, CNRS, 2-8 rue Henri Dunant, 94320 Thiais, France

³LIMATB, UBS, rue Saint Maudé, BP 92116, 56321 Lorient Cedex, France

⁴ESRF, BP 220, F-38043 Grenoble Cedex, France

⁵Institut Laue-Langevin, DS/LSS, 6 rue Jules Horowitz, BP 156, 38042 Grenoble Cedex 9, France

(Received 30 March 2010; published 1 September 2010)

In this paper we present a direct measurement of stretched chain conformation in polymer nanocomposites in a large range of deformation using a specific contrast-matched small angle neutron scattering (SANS) method. Whatever are the filler structure and the chain length the results show a clear identity of chain deformation in pure and reinforced polymer and offer more insight on the polymer chain contribution in the mechanical reinforcement. It suggests that glassy layer or glassy paths, recently proposed, should involve only a small fraction of chains. As a result, the remaining filler contribution appears strikingly constant with deformation as explained by continuous locking-unlocking rearrangement process of the particles.

DOI: [10.1103/PhysRevE.82.031801](https://doi.org/10.1103/PhysRevE.82.031801)

PACS number(s): 82.35.Lr, 81.05.Qk, 61.05.fm

Polymers filled with nanoparticles (PNCs) exhibit improved mechanical properties compared to the pure matrix making them interesting materials for many applications [1]. Reinforcement mechanisms can be described according to two main contributions: one associated to the filler and the other to the chains. We focus here on chains, more specifically on their deformation, how it is affected by fillers, and the impact of this deformation on the elastic modulus. One increasingly recognized point is filler dispersion. It acts on geometrical confinement of chains, as measured [2–4] and modeled [5,6] in the isotropic state, and on their interfacial dynamics: authors detected glassy polymer layers around fillers that increase the volume of the rigid phase [7,8], for sufficient dispersion. Liquid layers have also been proposed, by analogy with thin films, for systems showing a decrease in the average glass transition temperature T_g [9]. This suggested a different filler-polymer interaction, but the difference in dispersion appeared also determining [10]. Our system, well representative in the field of PNCs, associates polystyrene (PS) and silica, as extensively studied [4,9,10], in two filler structures, dispersed fractal aggregates, and connected filler network. Its mechanical tests approach the most active type of nowadays industrial effort along the line of, e.g., composites with carbon black.

Up to date, the evolution of chain conformation under stretching in nanocomposites has been investigated mostly by indirect measurements. Deuterium NMR experiments [7,8,11,12] on elastomers provide an average of local strain within the matrix, and deformation inhomogeneities have been observed, increasing with filler fraction, directly correlated with the increasing of mechanical reinforcement. Recent simulations yield a similar picture [13]. Getting the single chain form factor by small angle neutron scattering (SANS) [14,15], homogeneous overstrain has been established in triblock copolymer micelles of PI-PS-PI in cross

linked polyisoprene (PI) matrix, nicely dispersed but different from classical PNCs, where a direct measurement of polymer chain deformation is not available. Hence, it remains difficult to separate the chain from the filler contributions to the final macroscopic reinforcement. The present paper addresses such direct measurement.

The zero average contrast (ZAC) method, based on a mixture of nondeuterated (H) and deuterated (D) PS chains, is the only technique which enables a direct measurement inside a composite without further approximations. Then stress measurements will allow us to correlate the local chain deformation effects with influence of strain on the macroscopic material modulus and discriminate the contribution of the chain deformation from the one of the filler structure.

We have generated our model system by dispersing nanosilica ($R \approx 6$ nm) in a PS matrix. The nanocomposites were prepared by mixing a silica solution with a PS solution and drying to get three final silica volume fractions: 0%, 5% and 15% v/v, characterized by a combination of x rays and transmission electronic microscopy [16]. Nanosilica arranges at low silica volume fraction in small aggregates, not visibly connected, with an essentially narrow size distribution, and forms a clearly connected network with mesh size of 125 nm for 15% v/v. Differential scanning calorimetry gives $T_g = 94$ °C for 0%, 95 °C for 5%, and 98 °C for 15% v/v [16], suggesting glassy layers in the 15% v/v connected structure. To correct for T_g shift effect on stress, nanocomposites of length L were stretched at constant temperature $T - T_g = 20$ °C with a constant rate of deformation $\dot{\epsilon} = 5 \times 10^{-3}$ s⁻¹ up to the maximum elongation ratio $\lambda = L(t)/L(0) = 1 - 6$, and subsequently quenched for SANS recording. The effect of filler dispersion on mechanical properties of these samples has been already detailed [16] for low and large deformations. We focus first on SANS measurements at large elongation ratios λ .

We have adapted the ZAC method to our system. It consists of making the sample by mixing H and D PS chains of close molecular weights in specific proportions with a third

*jacques.jestin@cea.fr

continuous medium, which is usually a solvent replaced with the silica in our case. The total scattering function of the resulting three-component system can be expressed by the relation

$$I(q) = (\rho_D - \rho_H)^2 x(1-x) \nu \Phi NP(q) + [x\rho_D + (1-x)\rho_H - \rho_0]^2 [\nu \Phi NP(q) + V\Phi^2 S(q)], \quad (1)$$

where ρ_H , ρ_D , and ρ_0 are, respectively, the scattering length densities of the H chains, of D chains, and of the continuous medium (here, silica); x is the molar fraction of deuterated chains; ν is the molar volume of the chain segment H as well as D, V is the total volume; and Φ is the total volume fraction of polymer in the system. $P(Q)$ and $S(Q)$ are, respectively, the form factor and the structure factor of the interchain H or D. When the average scattering length density of an H chain/D chain mixture (60.9% v/v/39.1% v/v) is equal to the one of the silica, i.e., when $[x\rho_D + (1-x)\rho_H - \rho_0] = 0$, all correlations involving silica are cancelled out, as well as interchain correlations if the H and D chains have the same weight distribution (with polydispersity index lower than 1.2). Then only the intrachain signal, proportional to the average form factor of a single chain $P(q)$, is measured [first term of Eq. (1)]. The scattering intensity $I(q)$ described by Eq. (2) is then reduced to

$$I(q) = (\rho_D - \rho_H)^2 x(1-x) \nu \Phi NP(q). \quad (2)$$

However, imperfect matching of the silica filler by the H/D matrix might perturb the scattering signal. To ensure perfect matching, we used conditions different from the ZAC ones: we have synthesized some statistical H/D PS chains from a mixture of H and D styrene, whose scattering length density is equal to the one of the silica and used it with a mixture of H chains/D chains of mass 138 k in ZAC proportions.

Figure 1 shows the SANS results for $M_w = 315$ k in directions parallel and perpendicular to the stretching for direct comparison of unfilled and filled polymer matrix at 5% silica, in log-log representation for $\lambda = 2, 4$, and 6, or for $\lambda = 1.28$ for comparison with a sample filled with 15% of silica. Intensity maps of the two-dimensional (2D) detector (inset) show strong anisotropy, evidencing the deformation of the chains.

At first sight, particularly striking is the unanimous identity of chain conformation with and without fillers, in both directions, for each elongation ratio. This is true at 5% silica from $\lambda = 2$ to $\lambda = 6$, as shown in Figs. 1(a)–1(c). It is also true for 15% silica: the samples were much more difficult to stretch, reaching only an elongation ratio $\lambda = 1.28$ [Fig. 1(d), showing a difference at the lowest q 's due to crazes]. The chain deformation is unperturbed by the presence of silica contrary to previous study [14], with different characteristic sizes and filler structures in a cross linked matrix. It is not sensitive to any confinement due to filler reorganizations resulting from the deformation either for low filler content (below the percolation threshold) or for large filler content (above the percolation threshold). This effect is clearly con-

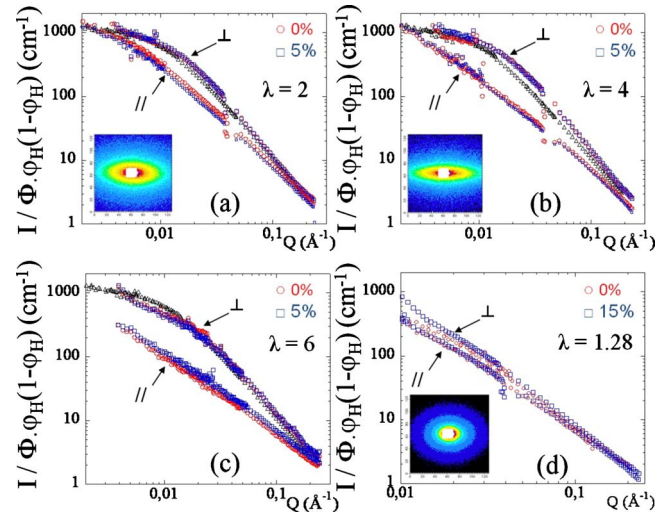


FIG. 1. (Color online) SANS results (absolute intensity) normalized by $\phi_H(1-\phi_H)$ from chains in stretched unfilled polymer (red circle symbols) and nanocomposites filled with 5% v/v of silica particles (blue square symbols) for a molecular weight of 315 k ($M_w = 315$ kg/mol) in directions parallel (\parallel , lower symbols) and perpendicular (\perp , upper symbols) to the stretching, and for elongation ratios (a) $\lambda = 2$, (b) $\lambda = 4$, and (c) $\lambda = 6$ and (d) for higher filler content of 15% v/v at $\lambda = 1.28$. Inset: intensity maps of the 2D detector. Black triangle symbols: isotropic scattering (identical in filled and unfilled unstretched samples).

firmed at 5% in Fig. 2 for three other molecular weights: lower [138 k, Fig. 2(a)], comparable [430 k, Fig. 2(b)], and higher [1777 k, Fig. 2(c)].

Again the scattering from filled (5%) and unfilled samples superimposes perfectly in the probed Q range. The 430 and 1777 k cases correspond to an H chain/D chain mixture with silica, while the 138 k case corresponds to an H chain/D chain mixture in a statistical H/D matrix which matches the silica. The conclusion is the same in all cases, confirming very good matching. For the pure PS matrix, the curve is classical for stretched chains, and it has been well described in the literature. At low Q (Guinier regime), the radius of gyration R_g of the deformed chain is determined using the classical Debye function in parallel and perpendicular directions. Its experimental variation with λ is compared (Fig. 3) with predictions for a chain inside a tube [extending the phantom network model by replacing cross links with entanglements (sliplinks)]; R_g is calculated [17] for a chain passing by a number k of sliplinks, $k = M_w/M_e$, where the mass M_e between entanglements is 18 000 for PS. For both molecular weights, the radius is less deformed, as due to chain reptation [18,19] during stretching, which is faster for the lower M_w , as expected. When increasing q , i.e., decreasing the distance, the form factor reflects also this relaxation by a loss of anisotropy. It is known that this can be accounted by implying relaxation between the sliplinks, i.e., inside the tube, followed by reptation out of the tube [20,21]. The presence of the filler is expected to modify this behavior for all chains or at least a fraction of them, by creating specific polymer/filler interaction which could apply at short or long range, as a function of the filler structure. This should affect

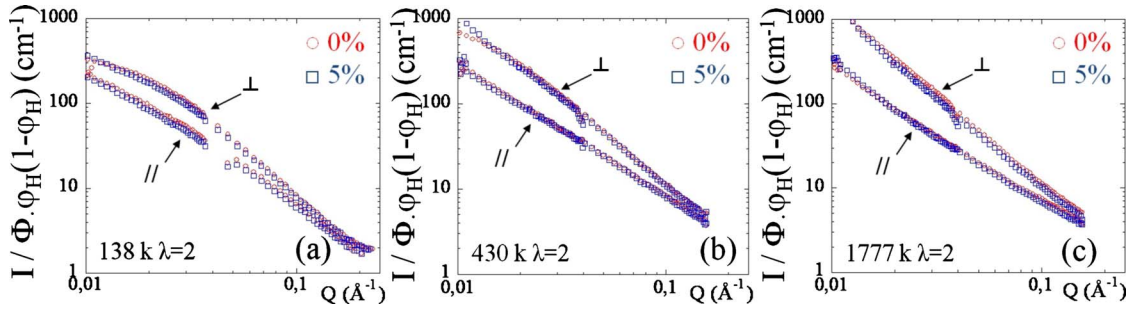


FIG. 2. (Color online) Normalized scattering of stretched unfilled polymer (red circle symbols) and 5% v/v filled nanocomposites (blue square symbols) $\lambda=2$ for molecular weights (a) $M_w=138$, (b) 430, and (c) 1777 k.

the relaxation processes (including reptation) of the chains under stretching, but such modification is clearly not observed here.

The second important result concerns the mechanical response: at variance with chain conformation, the mechanical response of the nanocomposites is very different in the pure matrix and in the reinforced polymer. For instance, for $\Phi_{silica}=15\%$ at $\lambda=1.28$ only, the stress is larger than the matrix one by an order of magnitude [16]. For the samples observed here (5% v/v), the difference in stress survives at high elongation ratio as highlighted in Fig. 4(a). At this stage, it is worth noting that the curves look as shifted, with respect to the pure polymer curve, by a constant value, increasing with silica fraction. This prompts us to subtract the pure polymer curve from the composite one, in agreement also with the independence of average chain deformation on filler concentration. The remaining stress after such subtraction is presented for 315 k in Fig. 4(a) (black triangle symbols) and for all molecular weights in Fig. 4(b). We obtain a second striking behavior: the remaining contribution to stress is quasiconstant with λ ; this is seen for all polymer sizes and has also been observed for two other deformation gradients 0.001 and 0.01 s^{-1} (not shown).

Thanks to a well-defined model nanocomposite, we have shown that the deformation of the chains is not affected by the presence of the structured silica filler inside the nanocomposite (Figs. 1 and 2). This result suggests that the chain deformation does not contribute more than for the intrinsic

matrix to the elastic modulus of the material, whatever are the silica content, the filler structure, and the polymer molecular weight. This has two important consequences with respect to the different reinforcement models. Models [22,23] implying that some chains would connect elastically the fillers predict a stronger deformation of these chains: the absence of such effects suggests a very small fraction of them. A more recent approach [8,9,24] proposes the existence of a fraction of glassy chains (glassy layer or glassy paths) to explain reinforcement depending on $T-T_g$ [25]. In a simplistic picture, glassy chains then would not be largely deformed, with the other chains undergoing most of the deformation: this should also result in a difference in average chain deformation. To enhance this difference, since glassy effects increase closer to T_g , we decreased the stretching temperature down to $T_g+10^\circ C$. We see in Figs. 4(c) and 4(d) that again the scattering signal of the filled sample su-

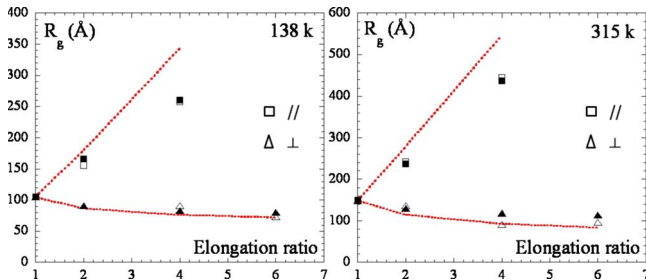


FIG. 3. (Color online) Radius of gyration of chains of molecular weights 138 k (left) and 315 k (right), in direction parallel (\parallel , squares) and perpendicular (\perp , triangles) to stretching: experimental result using Debye function for filled (5% v/v, full symbols) and unfilled (0% v/v, empty symbols) polymers, and phantom network predictions (dashed red line) assuming one sliplink, each with 180 segments.

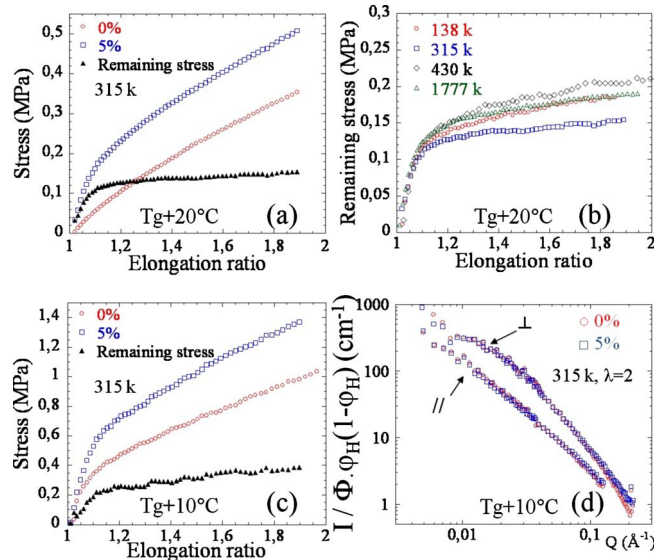


FIG. 4. (Color online) (a) Stress-strain for unfilled polymer (red circles) and 5% filled nanocomposite (blue squares) for $M_w=315$ k. The remaining stress after subtraction of unfilled polymer stress (black triangles) reaches a plateau above $\lambda=1.1$. (b) Remaining stress versus elongation ratio for four molecular weights (from 138 to 1777 k) at the same silica volume fraction of 5% v/v. (c) and (d) Stretching closer to T_g ($T_g+10^\circ C$): (c) stress-strain curves and (d) scattering intensities filled (blue squares) and unfilled (red circles) at $\lambda=2$ for $M_w=315$ k.

perimposes perfectly with the unfilled one, and the remaining stress is still quasiconstant with λ . To summarize, glassy effect is not excluded but clearly concerns in our case a very small fraction of chains, although our system displays a positive T_g shift for 15%v/v of silica. As a result, the constant value of the remaining modulus when increasing deformation could be attributed mostly to the contribution of the filler structure. This surprising and rarely reported effect [26] could be explained by a combination of filler displacement

[27] and filler orientation [28] along the stretching direction inducing a continuous locking-unlocking process of filler associations. These observations offer more insight on the physics of chain confinement, including the actively discussed case of glass transition in ultrathin films [29], in the basic mechanisms of reinforcement, and can enable the design of new hybrid materials with improved mechanical properties in a large range of deformation.

-
- [1] S. Tjong, *Mater. Sci. Eng. R.* **53**, 73 (2006).
- [2] A. I. Nakatani, W. Chen, R. G. Schmidt, G. V. Gordon, and C. C. Han, *Polymer* **42**, 3713 (2001).
- [3] A. Tuteja, P. M. Duxbury, and M. E. Mackay, *Phys. Rev. Lett.* **100**, 077801 (2008).
- [4] S. Sen, Y. Xie, S. K. Kumar, H. Yang, A. Bansal, D. L. Ho, L. Hall, J. B. Hooper, and K. S. Schweizer, *Phys. Rev. Lett.* **98**, 128302 (2007).
- [5] J. E. Mark, R. Abou-Hussein, T. Z. Sen, and A. Kloczkowski, *Polymer* **46**, 8894 (2005).
- [6] G. Allegra, G. Raos, and M. Vacatello, *Prog. Polym. Sci.* **33**, 683 (2008).
- [7] N. K. Dutta, N. R. Choudhury, B. Haidar, A. Vidal, J. B. Donnet, L. Delmotte, and J. M. Chazeau, *Polymer* **35**, 4293 (1994).
- [8] J. Berriot, H. Montes, F. Lequeux, D. Long, and P. Sotta, *Macromolecules* **35**, 9756 (2002).
- [9] A. Bansal, H. Yang, C. Li, K. Cho, B. C. Benicewicz, S. K. Kumar, and L. S. Schadler, *Nature Mater.* **4**, 693 (2005).
- [10] S. Sen, Y. Xie, A. Bansal, H. Yang, K. Cho, L. S. Schadler, and S. K. Kumar, *Eur. Phys. J. Spec. Top.* **141**, 161 (2007).
- [11] P. Ekanayake, H. Menge, H. Schneider, M. E. Ries, M. G. Brereton, and P. G. Klein, *Macromolecules* **33**, 1807 (2000).
- [12] S. Dupres, D. Long, P. A. Albouy, and P. Sotta, *Macromolecules* **42**, 2634 (2009).
- [13] D. Long and P. Sotta, *Macromolecules* **39**, 6282 (2006).
- [14] S. Westermann, M. Kreitschmann, W. Pyckhout-Hintzen, D. Richter, E. Straube, B. Farago, and G. Goerigk, *Macromolecules* **32**, 5793 (1999).
- [15] E. Straube, V. Urban, W. Pyckhout-Hintzen, D. Richter, and C. J. Glinka, *Phys. Rev. Lett.* **74**, 4464 (1995).
- [16] N. Jouault, P. Vallat, F. Dalmas, S. Said, J. Jestin, and F. Boué, *Macromolecules* **42**, 2031 (2009).
- [17] R. Ullman, *Macromolecules* **15**, 1395 (1982).
- [18] P. G. de Gennes, *Scaling concepts in polymer physics* (Cornell University Press, Ithaca, NY, 1999).
- [19] M. Doi and S. F. Edwards, *The theory of polymer dynamics* (Clarendon Press, Oxford, 1986).
- [20] F. Boué, *Adv. Polym. Sci.* **82**, 47 (1997).
- [21] F. Boué, J. Bastide, M. Buzier, A. Lapp, J. Herz, and T. Vilgis, *Colloid Polym. Sci.* **269**, 195 (1991).
- [22] P. G. Maier and D. Goritz, *Kautsch. Gummi Kunstst.* **49**, 18 (1996).
- [23] A. S. Sarvestani, *Eur. Polym. J.* **44**, 263 (2008).
- [24] D. Long and F. Lequeux, *Eur. Phys. J. E* **4**, 371 (2001).
- [25] J. Berriot, H. Montes, F. Lequeux, D. Long, and P. Sotta, *EPL* **64**, 50 (2003).
- [26] A. J. Meuler, G. Fleury, M. A. Hillmyer, and F. S. Bates, *Macromolecules* **41**, 5809 (2008).
- [27] J. Oberdisse, Y. Rharbi, and F. Boué, *Comput. Theor. Polym. Sci.* **10**, 207 (2000).
- [28] J. Jestin, F. Cousin, I. Dubois, C. Ménager, R. Schweins, J. Oberdisse, and F. Boué, *Adv. Mater.* **20**, 2533 (2008).
- [29] M. Alcoutlabi and G. B. McKenna, *J. Phys.: Condens. Matter* **17**, R461 (2005).

Polymer-Grafted-Nanoparticles Nanocomposites: Dispersion, Grafted Chain Conformation, and Rheological Behavior

Chloé Chevigny,[†] Florent Dalmas,[‡] Emanuela Di Cola,[§] Didier Gigmes,[⊥] Denis Bertin,[⊥] François Boué,[†] and Jacques Jestin^{*†}

[†]Laboratoire Léon Brillouin, CEA Saclay 91191 Gif-sur-Yvette Cedex, France, [‡]Institut de Chimie et des Matériaux Paris-Est, UMR 7182 CNRS/Université Paris-Est, 2-8 rue Henri Dunant 94320 Thiais, France, [§]ESRF 6 rue Jules Horowitz B.P. 220, 38043 Grenoble Cedex 9, France, and [⊥]Laboratoire Chimie Provence, UMR 6264, CNRS et Universités d'Aix-Marseille 1, 2 et 3, Site de St Jérôme, Av. Esc. Normandie-Niemen case 542, 13393 Marseille Cedex 20, France

Received June 15, 2010; Revised Manuscript Received December 3, 2010

ABSTRACT: We investigate the dispersion mechanisms of nanocomposites made of well-defined polymer (polystyrene, PS) grafted-nanoparticles (silica) mixed with free chains of the same polymer using a combination of scattering (SAXS/USAXS) and imaging (TEM) techniques. We show that the relevant parameter of the dispersion, the grafted/free chains mass ratio R tuned with specific synthesis process, enables to manage the arrangement of the grafted nanoparticles inside the matrix either as large and compact aggregates ($R < 0.24$) or as individual nanoparticles dispersion ($R > 0.24$). From the analysis of the interparticles structure factor, we can extract the thickness of the spherical corona of grafted brushes and correlate it with the dispersion: aggregation of the particles is associated with a significant collapse of the grafted chains, in agreement with the theoretical models describing the free energy as a combination of a mixing entropy term between the free and the grafted chains and an elastic term of deformation of the grafted brushes. At fixed grafting density, the individual dispersion of particles below the theoretical limit of $R = 1$ can be observed, due to interdiffusion between the grafted and the free chains but also to processing kinetics effects, surface curvature and chains polydispersity. Mechanical analysis of nanocomposites show the appearance of a longer relaxation time at low frequencies, more pronounced in the aggregated case even without direct connectivity between the aggregates. Correlation between the local structure and the rheological behavior suggests that the macroscopic elastic modulus of the nanocomposite could be described mainly by a short-range contribution, at the scale of the interactions between grafted particles, without significant effect of larger scale organizations.

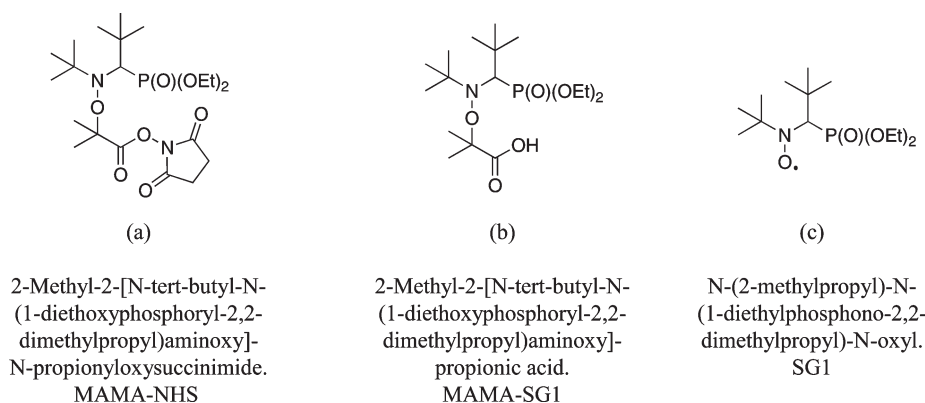
I. Introduction

The properties of a polymer, an elastomeric matrix, can be amazingly enhanced by inclusion of hard inorganic particles. The resulting material, which makes use of both the softness of the polymer matrix and the specificities of the particles, constitutes an innovative way of designing new products for applications in mechanical, optical, fuel cells, or gas barrier engineering. Recently, more attention was focused on the size reduction of the particles down to the nanometer range, to increase the specific surface available and thus obtain improved macroscopic properties. At this scale, these properties are directly related to the local organization of the nanoparticles inside the matrix, which can present a large variety of structures: directly connected or not, from the well-dispersed case to the formation of large and compact aggregates, with intermediate structures like ramified or elongated objects. Different strategies were developed to tune and control the hierarchical structure of the particles distribution in order to tune and control the expected final properties: one can play on the initial shape using anisotropic fillers like carbon nanotubes¹ or fractal fillers,² or one can use an external trigger by simple control of the processing conditions,^{3,4} such as for instance controlling the electrostatic repulsion⁵ or a magnetic field.⁶ An alternative route of tuning is to use an internal trigger: grafting chemistry to cover the particles with a corona of grafted polymer of the same nature as the matrix. Many recent studies⁷ present

various refined synthesis processes of well-defined grafted nanoparticles using radical-controlled polymerization (RCP), particles which can then be used as fillers by mixing with free chains of the same polymer. The resulting interactions between grafted chains and free chains from the matrix were described from a theoretical point of view for planar surfaces^{8,9} as a function of two main parameters: the chain length ratio between the free and the grafted chains (expressed using the polymerization indexes N for the grafted chains and P for the free chains) and the chains grafting density. For $P \leq N$, the phase diagram exhibits a complete wetting region bound by two grafting density limits, a lower σ^* and an upper σ^{**} (defined as $P^{-1/2}$). These two limits coincide for $P = N$, namely when the free chains length is identical to that of the grafted ones, and incomplete wetting takes place. These theoretical concepts have been transferred to colloidal systems^{10,11} for $P \leq N$: in this case, interparticles interactions and surface curvature have to be taken into account. For high grafting density, attractive interactions between grafted chains dominate and induce aggregation of particles.¹² For low grafting density, interparticles interactions dominate due to incomplete surface coverage and the particles can aggregate, or percolate into a continuous network. In the intermediate grafting density situation ($\sigma^* < \sigma < \sigma^{**}$), the dispersion is mainly dominated by the interactions between the grafted and the free chains, and thus by the grafted to free chain length ratio: the surface coverage is large enough to suppress the percolation but lower enough to reduce the attractions between grafted chains. The total free energy can be expressed as the sum

*Corresponding author. E-mail: jacques.jestin@cea.fr.

Scheme 1



of a mixing entropy term between the grafted and the free chains, and an elastic term of deformation (stretching or compression) of the grafted chains. The key parameter is then the ratio between the length of grafted chains (N) and of free chains (P), $R = N/P$. When an identical polymer is used for the free and for the grafted chains, which is our case all along this article, the ratio can then directly be expressed as $R = M_{n \text{ grafted}}/M_{n \text{ matrix}}$. When $R > 1$, the free chains, which are shorter, can penetrate into the grafted corona according to a favorable entropic potential and consequently swell it: the grafted chains are stretched and the brush is “wet”. When $R < 1$, the mixing entropy is much lower, swelling elastic dominates, which expels free chains from the brush and changes its conformation: the grafted chains are compressed, and the brush becomes “dry”. From an experimental point of view, these concepts have been studied mainly in the case of microgel systems^{13–16} or for large particles¹⁷ (micrometric scale) but less in the case of nanocomposites.¹⁸

The present paper first addresses the experimental validation of this theory, through the effect of R (expected to be the key parameter) on the dispersion of grafted nanoparticles inside a polymer matrix. We focus here on the specific case of $N < P$, i.e. $M_{n \text{ grafted}} < M_{n \text{ matrix}}$ or $R < 1$, while working at fixed intermediate grafting density. Our previous works^{19,20} allowed us to develop a controlled synthesis process of well-defined polystyrene-grafted silica nanoparticles, with grafting densities around 0.2 molecules/nm² and varying grafted chains molecular masses between 5000 and 50 000 g/mol. We thus obtained the materials required to formulate nanocomposites filled with grafted nanoparticles, nanocomposites in which we are able to change the R parameter according to two different strategies: either by varying the mass of the free chains at constant mass of the grafted chains, or by varying the mass of the grafted chains at constant matrix mass. The second important purpose of this article is to link the dispersion of the particles with the conformation of the grafted brushes. We recently showed through a refined combination of X-rays and neutron scattering that we could directly observe the conformation of the grafted brushes inside the nanocomposite.²¹ By comparison with the conformation of the grafted corona in solution, we showed a compression in the composite, a “wet” to “dry” conformational transition, which illustrates the competition between the mixing entropy of grafted and free chains and the elastic deformation of the grafted chains.

In this contribution, two main questions will then be addressed: first, the relation between the conformation of the grafted brush and the dispersion state, second the correlation between the dispersion and the macroscopic mechanical response of the material.

II. Material and Methods

1. Synthesis of the Grafted Nanoparticles. We developed our own versatile polymer-grafted nanoparticles synthesis

method.¹⁹ This method, based on nitroxide-mediated polymerization (NMP), consists of binding covalently the alkoxyamine (which acts as an initiator and controlling agent) to the silica nanoparticles surface in two steps, and then polymerize from the alkoxyamine-functionalized surface of the particles (“grafting from” method). For the grafting of the initiator, the first step is a reaction between aminopropylsilane and the silica particles in order to functionalize the particle surface with an amino group, and in a second step, the initiation-controlling alkoxyamine moiety is introduced via an overgrafting reaction between the amino group and the *N*-hydroxysuccinimide-based MAMA-SG1 activated ester (MAMA-NHS Scheme 1a). The initiator-grafted particles are then ready for the polymerization, which is performed at 120 °C, in the presence of free alkoxyamine MAMA-SG1 (Scheme 1b) (for a better control of the polymerization). To simplify both their chemical transformation and the polymerization step, the native silica particles, initially dispersed in water, are transferred to an organic solvent, dimethylacetamide (DMAc), which is also a good solvent of the polystyrene. The synthesis parameters were optimized to maximize grafting density, conversion rates, and enhance synthesis reproducibility, while keeping the colloidal stability and avoiding any aggregation of silica particles (which could be induced by the change in interparticles interaction during the synthesis). After synthesis, the final grafted objects are purified and the non-grafted polymer chains formed in the solvent washed out by ultrafiltration. The grafted particles were studied using small angle neutron scattering (SANS) coupled with a neutron contrast variation method from which we can extract a complete description of the grafted objects: number and mass of the grafted chains, number of particles. Using this first synthesis method, we synthesized two batches of particles grafted with deuterated PS chains: $M_{n \text{ grafted}} = 24\,000$ g/mol, PDI = 1.3 and $M_{n \text{ grafted}} = 24\,400$ g/mol, PDI = 1.27, similar chain length, polydispersity and grafting density (0.19 chains/nm²). Alternatively to this first route, we also developed a new route²⁰ to obtain grafted nanoparticles with tunable grafted chain length, by replacing the free initiator in solution by the controller agent (SG1) (Scheme 1c) at the beginning of the polymerization process. This allowed us to obtain four batches of grafted nanoparticles with hydrogenated PS chains of $M_{n \text{ grafted}} = 5300$ g/mol, $M_{n \text{ grafted}} = 19\,000$ g/mol, $M_{n \text{ grafted}} = 32\,000$ g/mol, and $M_{n \text{ grafted}} = 50\,000$ g/mol. Grafting densities are comprised between 0.15 and 0.20 chains/nm².

2. Preparation of Nanocomposites. The preparation of nanocomposites follows the process developed in the laboratory as described by Jouault et al.³ The grafted nanoparticles, dispersed in the DMAc are mixed with a concentrated solution of atactic PS (10% v/v, also in DMAc), of $M_n = 140\,000$ g/mol

(Aldrich, PDI = 2, used as received) or $M_n = 98\,000$ g/mol (PDI = 1.7, synthesized by classical radical polymerization), at various fractions of particles ranging from 0 to 15% v/v. The mixtures are stirred (using a magnetic rod) for 2 h. They are then poured into Teflon molds (5 cm \times 5 cm \times 2.5 cm) and let cast in an oven at constant temperature $T_{\text{cast}} = 130$ °C during 1 week. This method of preparation enables us to obtain stable films whose local structure does not evolve with time. This yields dry not crystallized films of dimensions 5 cm \times 5 cm \times 0.1 cm (i.e., a volume of 2.5 cm³). Disks are then cut out of the films (diameter 1 cm, thickness 1 mm) for the plate–plate oscillatory shear cell.

3. SAXS/USAXS Experiments. SAXS experiments were done at the ESRF at the high brilliance small-angle X-ray scattering beamline (ID2) using the pinhole configuration at single energy (12.46 keV) and two sample–detector distances 1.5 and 10 m covering a scattering vector Q range from 0.5 down to 0.001 Å⁻¹. Complementary ultrasmall X-ray (USAXS) measurements were done using the available Bonse-Hart camera allowing exploring a Q range from 0.0001 to 0.01 Å⁻¹.

4. Transmission Electronic Microscopy. In order to complete at larger scale the SAXS analysis of the nanocomposites structure, conventional TEM observations were also performed on the composite materials. The samples were cut at room temperature by ultramicrotomy using a Leica Ultracut UCT microtome with a diamond knife. The cutting speed was set to 0.2 mm \cdot s⁻¹. The thin sections of about 40 nm thick were floated on deionized water and collected on a 400-mesh copper grid. Transmission electron microscopy was performed on a FEI Tecnai F20 ST microscope (field-emission gun operated at 3.8 kV extraction voltage) operating at 200 kV. Precise scans of various regions of the sample were systematically done first at small magnification, then at increasing magnification. The slabs observed were stable under the electron beam. The sample aspect was the same in every spot of every piece, and typically, 10 different slabs were observed. The pictures presented in the following are completely representative of the single aspect of the sample, which appears on average to be homogeneous.

5. Oscillatory Shear Small Deformation Tests. Shear tests, corresponding to low deformation levels (0.5%), were carried out in the dynamic mode in strain-controlled conditions with a plate–plate cell of an ARES rheometer (Rheometric-TA) equipped with an air-pulsed oven. This thermal environment ensures a temperature control within 0.1 °C. The samples are placed between the two plates (diameter 10 mm) fixtures at high temperature (180 °C), far above the glass transition, put under slight normal stress (around 0.5 N), and temperature is decreased progressively, while gently reducing the gap to maintain a constant low normal stress under thermal retraction. The zero gap is set by contact, and the error on sample thicknesses is thus minimal and estimated to ± 0.010 mm with respect to the indicated value. Slipping artifacts are noticeably reduced by this procedure, as checked by its reproducibility, and also by a sweeping in amplitude, at constant pulsation, which also makes it possible to determine the limit of the range of linear deformation. To stay below this limit, the shear amplitude is fixed to 0.5%. Samples are stabilized at the temperature for 30 min before starting measurements. The reproducibility was first tested on pure PS samples with an average of five repeated measurements, permitting an estimation of variations which is found to be of about 10%. In dynamic mode, the frequency range is from 0.5 to 100 rad/s for different temperatures (from 160 to 120 °C), and time–temperature superposition is applied. The obtained multiplicative factor can be adjusted to WLF law²² as follows: $\log(a_T) = C_1(T_{\text{ref}} - T)/C_2 + (T - T_{\text{ref}})$, where a_T is the multiplicative factor, T_{ref} is the reference

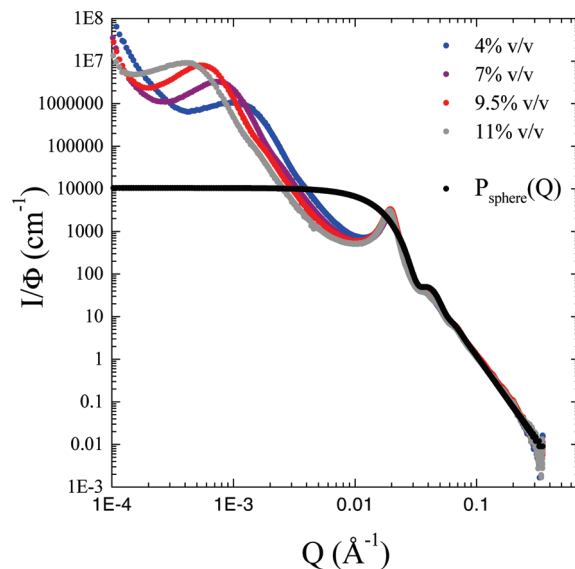


Figure 1. USAXS and SAXS scattering curves of PS nanocomposites ($M_{n \text{ matrix}} = 140\,000$ g/mol) filled with PS grafted silica nanoparticles ($M_{n \text{ grafted}} = 24\,000$ g/mol) corresponding to a grafted-free chain length ratio $R = 0.17$ as a function of the particles concentration (4, 7, 9.5 and 11% v/v). The pure matrix contribution has been subtracted and the curves have been normalized by the silica concentration. The full black line is the calculated form factor of a single particle (see text).

temperature of the master curve (in our case 143 °C), T is the temperature of the measurement, and C_1 and C_2 are the WLF parameters. We found $C_1 = 6.19$ and $C_2 = 97.23$ °C, which are commonly obtained values for PS.

III. Results

1. Dispersion of the Grafted Nanoparticles in the Nanocomposite.

1.1. Varying the Mass of the Matrix Chains. The first system we analyzed is a set of nanocomposites made of nanoparticles grafted with short chains ($M_{n \text{ grafted}} = 24\,000$ g/mol) introduced in a matrix of longer chains ($M_{n \text{ matrix}} = 140\,000$ g/mol), corresponding to a grafted/free chains length ratio R of 0.17. Four films containing silica volume fraction of $\Phi_{\text{SiO}_2} = 4, 7, 9.5,$ and 11% v/v were formed. The X-rays scattering, dominated by the strong contrast between the silica particles and the polymer, reveals the dispersion of the particles inside the melt without discrimination between the grafted and the free polymer chains. The corresponding scattered intensities are reported on the Figure 1a as a function of the wave vector Q . The scattering coming from the pure matrix was subtracted according to the following equation $I = I_{\text{nanocomposite}} - (1 - \Phi_{\text{SiO}_2}) \times I_{\text{matrix}}$. In the low Q region close to 10^{-4} Å⁻¹, we can observe a strong increase of the intensity (decreasing as a function of Q^{-3}) due to the formation of voids domains inside the composite during the film processing.²³ In the large Q region, all curves superimpose nicely indicating the good corrections by the sample thicknesses and the silica volume fractions. In this region, the intensity decreases as a function of Q^{-4} , which is a classical scattering behavior of flat surfaces in a continuous medium characteristic of silica particles. At glimpse, the scattering patterns present several features: at 4×10^{-2} Å⁻¹, we observe a first oscillation which is related to the form factor of the silica particles. This form factor, determined from the scattering of an aqueous dilute solution of particles,¹⁹ can be easily modeled with the well-known sphere form factor convoluted with a log-normal dispersion of 0.14 (slight polydispersity of the silica particles) around a mean sphere radius of 134 Å (see the full black line in Figure 1a).

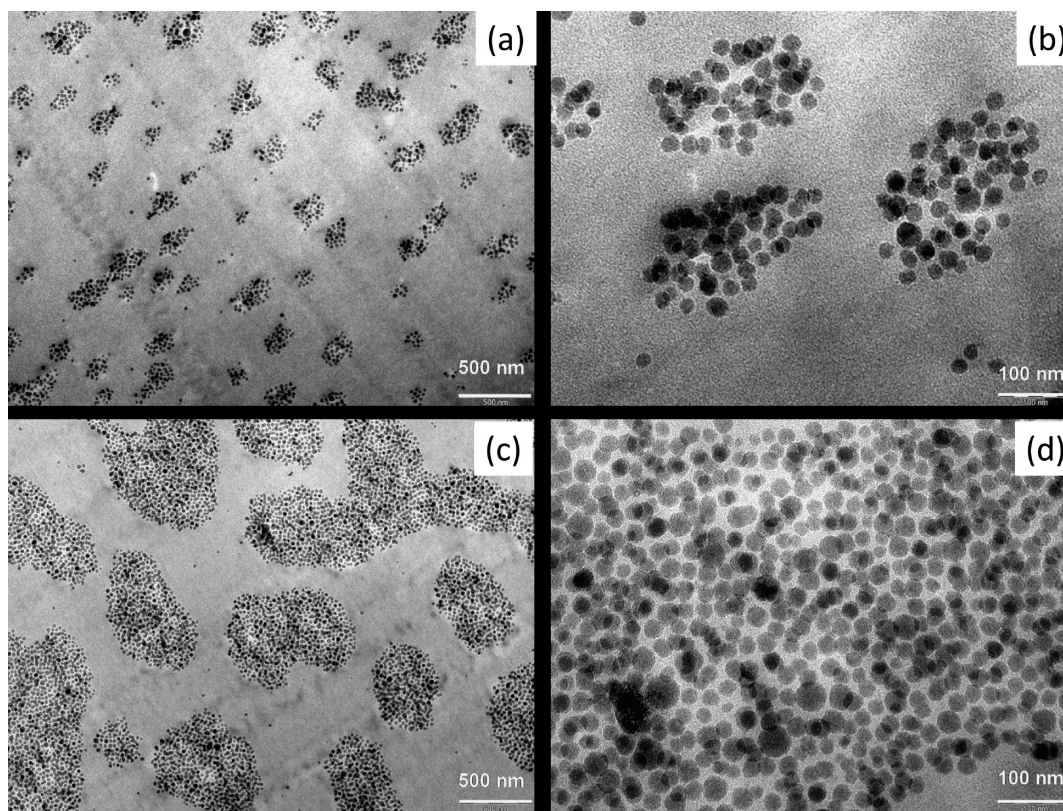


Figure 2. Transmission electronic microscopy on the nanocomposites ($M_{n \text{ matrix}} = 140\,000$ g/mol) filled with 4% v/v of grafted silica particles ($M_{n \text{ grafted}} = 24\,000$ g/mol) (the grafted-free chain length ratio $R = 0.17$) at low (a) and medium (b) magnification and filled with 11% v/v of grafted particles at low (c) and medium (d) magnification.

At $2 \times 10^{-2} \text{ \AA}^{-1}$, we observe a strong peak whose position, noted Q^* , does not vary with the silica volume fraction. The presence of this peak and its behavior with the particle concentration is a first indication of particles aggregation inside the polymer matrix. Indeed, from the peak position, we can deduce the mean distance D between the center of masses of the particles in the real space using the relation $Q^* = 2\pi/D$. The resulting calculated distance $D = 314 \text{ \AA}$ is close to the one for particles in close contact. Between $Q = 10^{-2}$ and 10^{-3} \AA^{-1} , we observe a strong increase of the intensity, which indicates that we observe now objects bigger than the single particle: this confirms the aggregation of the grafted particles inside the film. Again in this range, the scattered intensity varies as Q^{-4} , meaning that at the corresponding scale, the aggregates behave as compact. Finally, between 10^{-3} and $2 \times 10^{-4} \text{ \AA}^{-1}$, we see a second maximum, noted here as Q^{**} , whose position and intensity change with the particles concentration: the position is shifting toward the small Q values and the intensity increases when the silica content increases. From the position of the peak, we can extract the mean distance between the center of masses of the aggregates, $D = 2\pi/Q^{**}$ equal respectively to 0.65, 0.85, 1.15, and $1.60 \mu\text{m}$ for $\Phi_{\text{SiO}_2} = 4, 7.5, 9,$ and 11% v/v. We can also estimate the number of silica particles per aggregates by assuming a cubic network: $N_{\text{agg}} = D^3 \Phi_{\text{SiO}_2} / (4/3\pi R_{\text{particles}}^3)$, which gives 1000, 4200, 13100, and 40900 particles per aggregate for $\Phi_{\text{SiO}_2} = 4, 7.5, 9,$ and 11% v/v. To summarize, inside the matrix, the grafted particles of form factor $P_{\text{particles}}$ arrange in close contact according to an interparticle structure factor $S_{\text{inter-particle}}$, to form compact aggregates of form factor $P_{\text{aggregates}}$. The size of the aggregates and the distance between them, illustrated with a repulsive inter-aggregates structure factor $S_{\text{inter-aggregate}}$, increases with the particles content. This picture, extracted from the behavior in

Q space, is nicely confirmed by direct observation in real space with the microscopy experiments (TEM) presented in Figure 2 for two particles concentrations: 4 and 11% v/v, at low (parts a and c) and high magnification (parts b and d). At low magnification and low particles content, we can observe the well-dispersed organization of small-sized aggregates of grafted particles, an organization which is preserved up to the micrometer scale. The typical sizes and interparticle distances deduced from SAXS and USAXS analysis are confirmed here and increase with Φ_{SiO_2} . The largest magnification picture confirms the evolution of the number of grafted particles per aggregates as a function of the particle content.

In a second step, we obtained and observed a different situation: we still used the same molecular mass of grafted chains ($M_{n \text{ grafted}} = 24\,400$ g/mol), but reduced the mass of the free matrix chains ($M_{n \text{ matrix}} = 98\,000$ g/mol), which gives a chain mass ratio $R = 0.25$. Four films at four particles content ($\Phi_{\text{SiO}_2} = 5, 9, 12$ and 14% v/v), still using the same film processing conditions, are again characterized by X-rays scattering experiments (Figure 3). In the large Q domain, the intensities normalized by the particles content show the same behavior than for the previous films: the scattering is dominated by the signal of the single silica particles illustrated with the poly disperse sphere form factor calculation in full black line ($R = 134 \text{ \AA}$, $\sigma_{\log\text{-normal}} = 0.14$). On the reverse, the lower Q behavior is different: around 0.01 and 0.02 \AA^{-1} , we see a correlation peak, whose intensity and position, Q^* , now varies with Φ_{SiO_2} : the intensity increases and the position is shifted toward higher Q values while increasing the particles content. However, the main difference with the previous set of data is the vanishing of the strong increase of the intensity in the low Q region (previously varying as Q^{-4}) and of the correlation peak Q^{**} between aggregates around $5 \times 10^{-4} \text{ \AA}^{-1}$. There is

only a slow increase of the intensity left in the low Q range, which comes from the scattering of crazes, the voids domains which form during the film processing. This is a strong indication that the particles are now individually dispersed inside the polymer matrix for this chain length ratio. This also matches

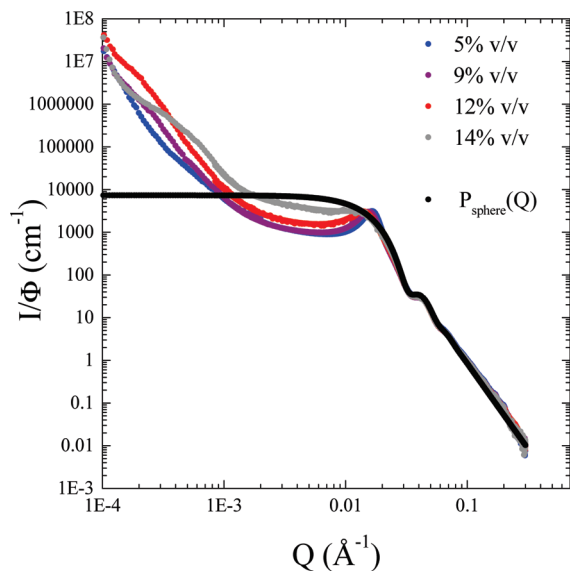


Figure 3. USAXS and SAXS scattering curves of PS nanocomposites ($M_{n \text{ matrix}} = 98\,000$ g/mol) filled with PS grafted silica nanoparticles ($M_{n \text{ grafted}} = 24\,400$ g/mol) corresponding to a grafted-free chain length ratio $R = 0.25$ as a function of the particles concentration (4, 9, 12, and 15% v/v). The pure matrix contribution has been subtracted and the curves have been normalized by the silica concentration. The full black line is the calculated form factor of a single particle (see text).

with the variation of Q^* around 0.01 and 0.02 \AA^{-1} with Φ_{SiO_2} , which thus corresponds to particles coming closer when more concentrated. This Q space evidence of the grafted particles perfect dispersion inside the polymer matrix is one again nicely confirmed in the real space by TEM, in Figure 4 for two particles volume fractions, 5% and 14% v/v. From high magnification (Figure 4, parts b and d) up to lower magnification (Figure 4, parts a and c), one can see that the dispersion is homogeneous until the micrometer scale. The reduction of the interparticle distance with increase of concentration is also clearly highlighted.

1.2. Varying the Mass of the Grafted Chains. The dispersion of the grafted nanoparticles inside a polymer matrix can then be probed as a function of the grafted/free chain mass ratio with fixed free chains mass ($M_{n \text{ matrix}} = 140\,000$ g/mol) and variable grafted chains mass. Four nanocomposite films were prepared and measured by SAXS as previously (Figure 5). The silica content is fixed at 5% v/v and the grafted/free chain length ratio is varied from $R = 0.04, 0.14, 0.23$, to 0.36 by the use of particles with grafted chains masses of respectively $M_{n \text{ grafted}} = 5\,200, 19\,000, 32\,000$, and 50 000 g/mol. In the large Q domain, all the normalized curves superimpose perfectly and the scattering is, as in both the previous cases, proportional to the form factor of single silica particles. In the intermediate Q range, we can observe a correlation peak of abscissa Q^* moving toward the small Q values while increasing the mass ratio R , indicating that the interparticle distance increases along with the grafted chains mass. Two different behaviors appear then, especially in the low Q domain: for the three lower values of $R = 0.04, 0.14$, and 0.23, we observe a strong increase of the scattered intensity, similar to the case of $R = 0.17$ in Figure 1 and characteristic of dense aggregates. Conversely, for the highest

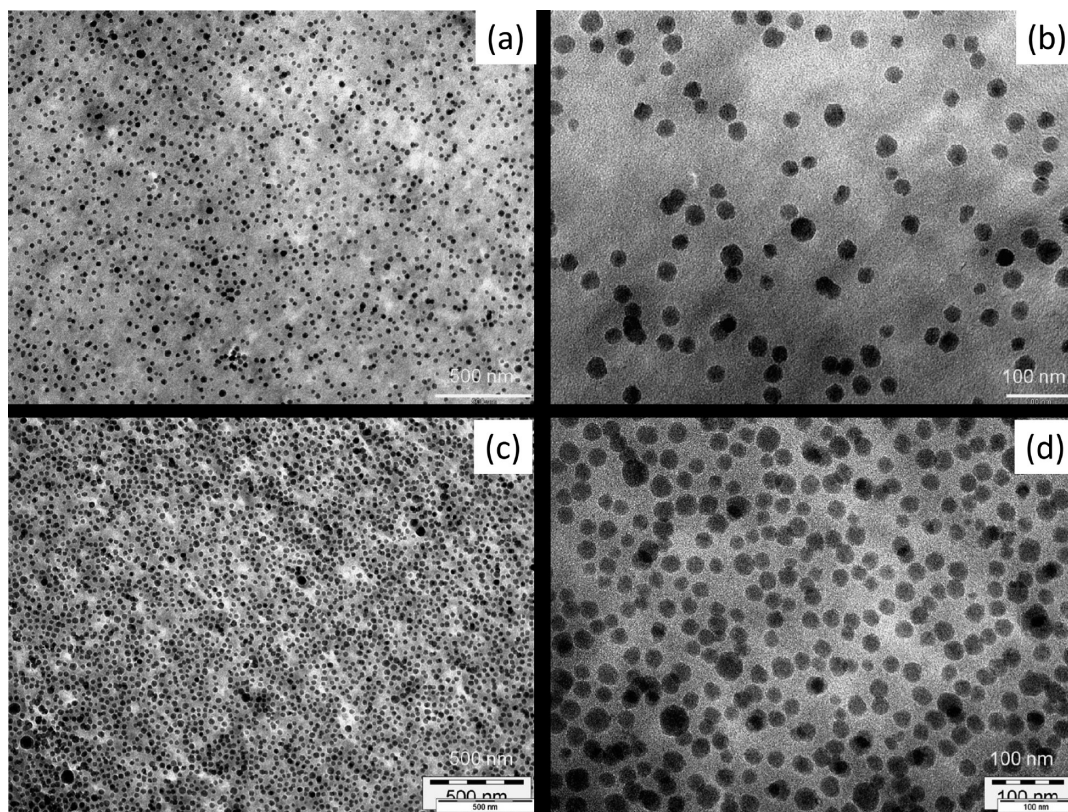


Figure 4. Transmission electronic microscopy on the nanocomposites ($M_{n \text{ matrix}} = 98\,000$ g/mol) filled with 5% v/v of grafted silica particles ($M_{n \text{ grafted}} = 24\,400$ g/mol) (the grafted-free chain length ratio $R = 0.25$) at low (a) and medium (b) magnification and filled with 14% v/v of grafted particles at low (c) and medium (d) magnification.

value of $R = 0.36$, the intensity at small Q is close to a plateau, as for the case $R = 0.25$ in Figure 3, corresponding to a complete dispersion of the particles. So by varying the grafted chains mass, and thus varying the chains length ratio from $R = 0.04$ to $R = 0.36$, we are able to observe a transition:

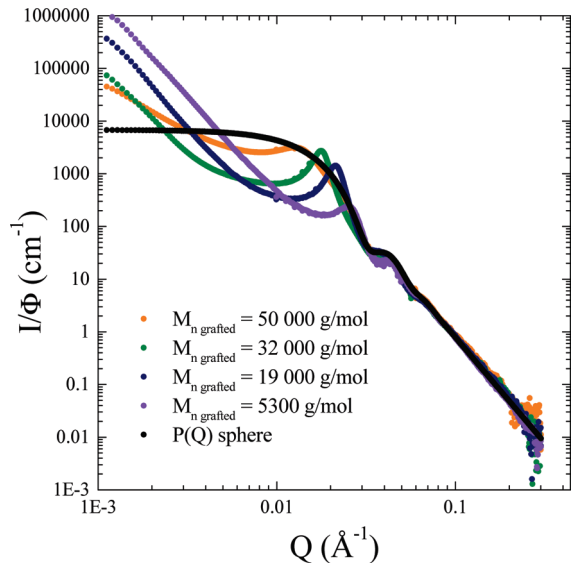


Figure 5. SAXS scattering curves of PS nanocomposites ($M_{n \text{ matrix}} = 140\,000$ g/mol) filled with 5% v/v of PS grafted silica nanoparticles with variable grafted chain length $M_{n \text{ grafted}} = 5300, 19\,000, 32\,000,$ and $50\,000$ g/mol corresponding to grafted-free chain length ratios $R = 0.04, 0.14, 0.23,$ and 0.36 . The pure matrix contribution has been subtracted and the curves have been normalized by the silica concentration. The full black line is the calculated form factor of a single particle (see text).

between the formation of dense aggregates of grafted nanoparticles for $R < 0.24$, and the complete dispersion of the grafted nanoparticles for $R > 0.24$. This transition is confirmed by TEM pictures shown in Figure 6, where we see directly the formation of aggregates for $R = 0.04$ (Figure 6a), $R = 0.14$ (Figure 6b), and $R = 0.23$ (Figure 6c) and a complete dispersion for $R = 0.36$ in Figure 6d. We also see distinctly that the interparticles distance increases along with the grafted chains mass.

2. Interparticles Structure Factor $S_{\text{inter-particle}}$. The combination of scattering and imaging methods showed that, whatever the way of varying the grafted over free chains mass ratio R (at constant grafted chain mass or at constant matrix mass), we observe a transition between the formation of compact aggregates of grafted nanoparticles, for $R < 0.24$, and a complete dispersion of the grafted nanoparticles inside the matrix for $R > 0.24$. We will now analyze more in details the interparticles structure factor, which can provide an indirect determination of the thickness of the polymer corona grafted around the nanoparticles. We first analyze the case described in Figure 3 and 4, i.e., $R = 0.25$, corresponding to a complete dispersion of the nanoparticles. Following the general behavior of the scattering intensity from particles:

$$I \sim \Delta\rho^2 \Phi v_{\text{particle}} P_{\text{particles}}(Q) S_{\text{inter-particle}}(Q) \quad (1)$$

(with $\Delta\rho^2$ as the contrast term), the interparticles structure factor can be extracted by dividing the total scattering intensity with the particle form factor:

$$S_{\text{inter-particle}}(Q) \sim I/P_{\text{particles}}(Q) \quad (2)$$

Since we measured the form factor of our silica particles, such operation can be easily done by dividing the total

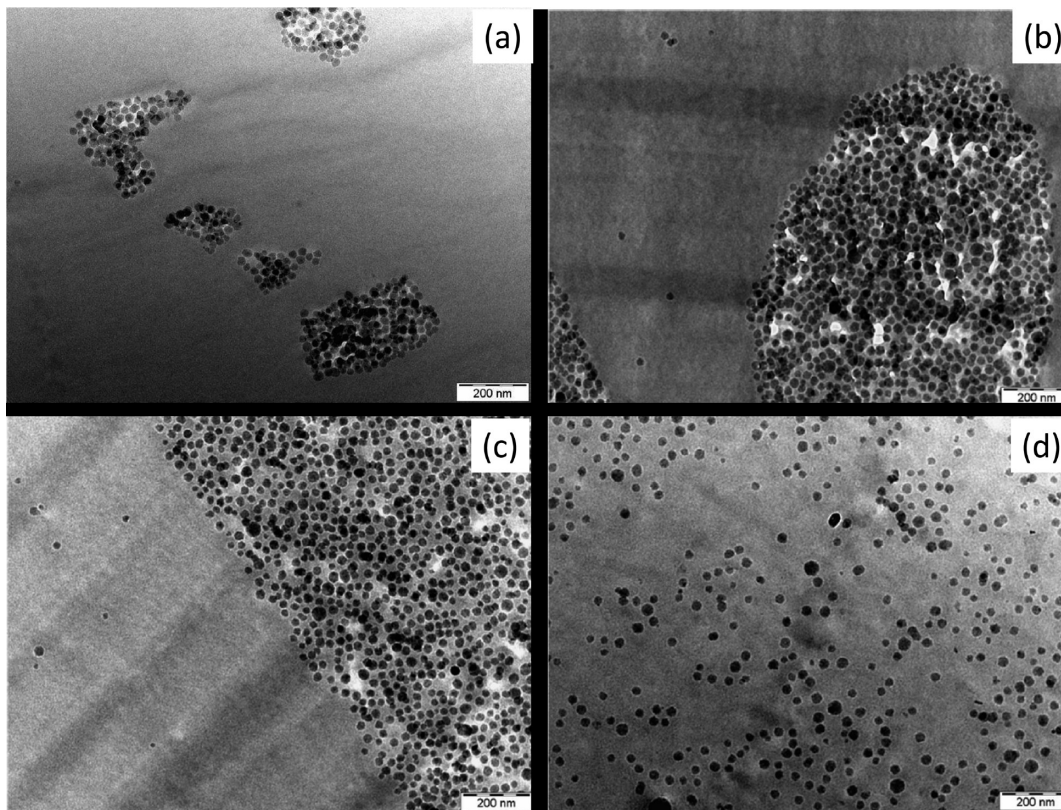


Figure 6. Transmission electronic microscopy on the nanocomposites ($M_{n \text{ matrix}} = 140\,000$ g/mol) filled with 5% v/v of PS grafted silica nanoparticles with variable chain length $M_{n \text{ grafted}} = 5300$ g/mol, $R = 0.04$ (a), $M_{n \text{ grafted}} = 19\,000$ g/mol, $R = 0.14$ (b), $M_{n \text{ grafted}} = 32\,000$ g/mol, $R = 0.23$ (c), and $M_{n \text{ grafted}} = 50\,000$ g/mol, $R = 0.36$ (d).

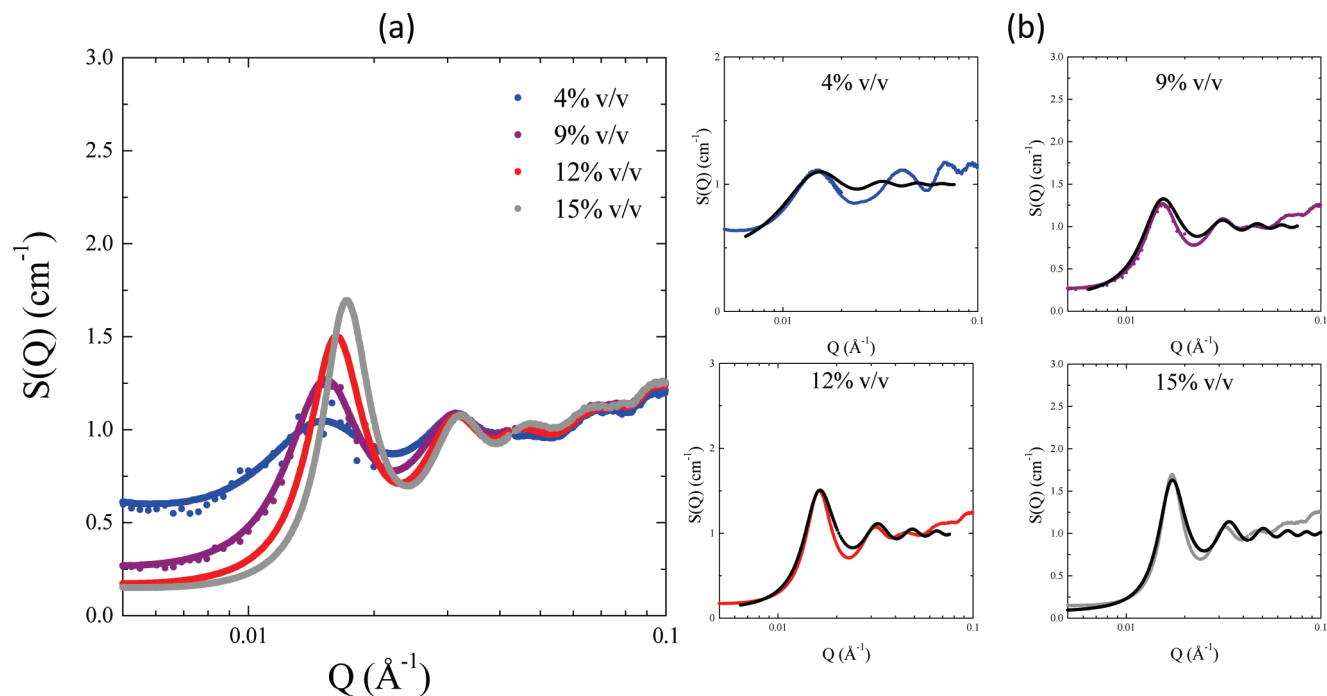


Figure 7. (a) Interparticle structure factor $S(Q)$ deduced from the division of the total scattering intensity (Figure 3) by the silica form factor (full black line in Figure 3) for dispersed grafted nanoparticles ($M_{n, \text{grafted}} = 24\,400$ g/mol) in a 98 000 g/mol matrix ($R = 0.25$) at the four particle contents. (b) Fits with the Percus–Yevick model (full black line) for each particle content.

intensity with the full black line from Figure 4 (representing the single silica particle form factor). The result is presented in Figure 7a (for silica content $\Phi_{\text{SiO}_2} = 4, 9, 12,$ and 14% v/v). While increasing Φ_{SiO_2} , the peak position moves toward higher Q values and its intensity increases, indicating a decrease of the interparticles distance and (increase of the interparticles interactions). The interparticles structure factor can be modeled by the Percus–Yevick model,²⁴ for which an analytical solution was calculated by Wertheim, for a hard spheres system:²⁵ it models the interactions between noncharged hard spheres. This model mainly depends on two parameters: the volume fraction Φ_{eff} and the radius R_{eff} of the interacting particles. The best adjustments are presented in Figure 7b for all silica volume fractions. A rather good agreement is found between the experimental data and the model, even if the calculation does not take into account the polydispersity of the particles.

Knowing R_{SiO_2} from our previous solution measurements ($R_{\text{SiO}_2} = 134$ Å), we can extract the thickness of the grafted layer on particles, assuming the parameters of the Percus–Yevick to be related to the whole particles: polymer corona plus silica sphere. Then the R_{eff} represents the radius of a grafted particle $R_{\text{grafted particle}}$, and the thickness e of the corona is easily obtained by:

$$e = R_{\text{eff}} - R_{\text{SiO}_2} \quad (3)$$

The volume fraction of the grafted particles can be expressed as:

$$\Phi_{\text{grafted particles}} = N\nu_{\text{grafted particles}}/V \quad (4)$$

with N the number of particles and V the total volume. The silica volume fraction can be expressed as well:

$$\Phi_{\text{SiO}_2} = N\nu_{\text{SiO}_2}/V \quad (5)$$

Combining 4 and 5 allows expressing a *modeled* grafted particle volume fraction as a function of the silica volume fraction, the radius R_{SiO_2} of the silica particles, and the thickness e

of the grafted polymer layer:

$$\Phi_{\text{grafted particles}}^{\text{mod}} = \Phi_{\text{SiO}_2} [1 + e/R_{\text{SiO}_2}]^3 \quad (6)$$

Besides, from thermo-gravimetric analysis (TGA) on the dry grafted particles, we know the mass ratio between silica and polymer and are then able to estimate an *experimental* volume fraction of grafted particles, $\Phi_{\text{grafted particles}}^{\text{exp}}$. If the approximation $R_{\text{eff}} = R_{\text{grafted particles}}$ is appropriate, both these $\Phi_{\text{grafted particles}}$ should be similar to Φ_{eff} . All the parameters useful for the fitting procedure (Φ_{SiO_2} , $\Phi_{\text{grafted particles}}^{\text{exp}}$) or deduced from it (R_{eff} , Φ_{eff} , e , $\Phi_{\text{grafted particles}}^{\text{mod}}$) are reported in Table 1. We find a good agreement between Φ_{eff} and $\Phi_{\text{grafted particles}}^{\text{exp}}$, which justifies the assimilation of the “interacting particles” from the Percus–Yevick model with the grafted particles. $\Phi_{\text{grafted particles}}^{\text{mod}}$ is also pretty close to both these parameters, which is one more justification of this assimilation. Besides, the effective radius of particles, and therefore the thickness of the polymer coronas as well, appear to be quite independent of the silica content

The interparticle structure factor was also derived for the chain length ratio $R = 0.17$ ($M_{n, \text{grafted}} = 24\,000$ g/mol and $M_{n, \text{Matrix}} = 140\,000$ g/mol). Here too, it is obtained by dividing the total intensities (Figure 1) by the form factor of the silica particle (full black line). The result is presented in Figure 8a for different silica contents (4, 7, 9.5, and 11% v/v). The modeling is shown in Figure 8b for each silica concentration and the fitting parameters reported in Table 2. Once more there is a good agreement between model and experiment. In this case where the grafted particles form compact aggregates inside the polymer matrix, the effective volume fraction of particle corresponds to a number of particles per aggregate and is thus very high, around 40% v/v. This value then cannot be directly expressed as a function of the number of grafted particles and compared with the volume fraction of grafted particles as for the previous well-dispersed case. However, the indirect evaluation of the thickness of the grafted corona e from the radius of particles deduced from the Percus–Yevick

Table 1. Fitting Parameters of the Inter-Particle Structure Factor by the Percus–Yevick Model for the Chain Length Ratio $R = 0.25$ as a Function of the Silica Volume Fraction (Particles Dispersed Inside the Polymer Matrix)

silica volume fraction $\Phi_{\text{SiO}_2}^a$	experimental grafted particles volume fraction $\Phi_{\text{grafted particles}}^{\text{exp}a}$	effective volume fraction Φ_{eff}^b	effective radius of particles R_{eff}^b	thickness of the grafted corona e^d	modeled grafted particles volume fraction $\Phi_{\text{grafted particles}}^{\text{mod}c}$
5	14	11	189	55	14
9	26	24	198	64	29
12	36	31	195	61	37
14	42	34	187	53	38

^a Experimental values. ^b Deduced from the fit with the Percus–Yevick model. ^c $e = R_{\text{eff}} - R_{\text{SiO}_2}$ with $R_{\text{SiO}_2} = 134 \text{ \AA}$. ^d Deduced from eq 6 (see text). Volume fractions are in % [v/v], lengths in \AA .

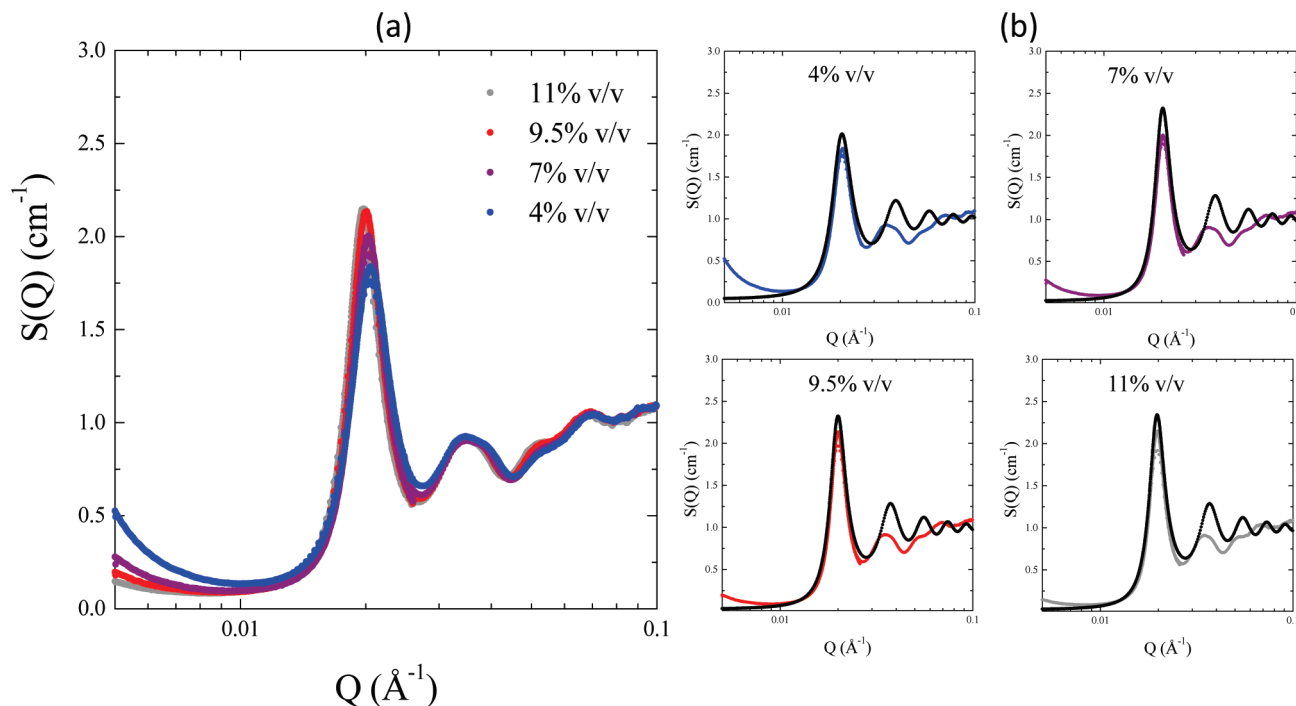


Figure 8. (a) Interparticle structure factor $S(Q)$ deduced from the division of the total scattering intensity (Figure 1) by the silica form factor (full black line in Figure 1) for aggregated grafted nanoparticles ($M_{\text{n, grafted}} = 24000 \text{ g/mol}$) in a 140000 g/mol matrix ($R = 0.17$) at the four particle contents. (b) Fits with the Percus–Yevick model (full black line) for each particle content.

fits is still valid inside an aggregate. We observe that the thickness e , still independent of the silica content, is smaller of about a factor two compared to the layer thicknesses corresponding to well-dispersed particles (Table 1): average value was then around 60 \AA , and is now around 30 \AA .

Finally, we analyzed the evolution of the interparticle structure factor when varying the grafted chains mass ratio R at constant matrix mass. It is again calculated by dividing the total intensities (Figure 5) with the form factor of the silica particles. The interparticles structure factors are presented in Figure 9a for $R = 0.04, 0.14, 0.23$, and 0.36 . The Percus–Yevick modeling is shown in Figure 9(b) and the corresponding fitting parameters are reported in Table 3. The results correspond to the transition between the aggregation and the good dispersion of the particles previously observed when increasing the chain length ratio R . For the first three values ($R = 0.04, 0.14$, and 0.23), the high value ($\sim 40\%$) of the effective volume fraction of the particles deduced from the fit, reflects the particles aggregation: this Φ_{eff} is then about four times higher than the $\Phi_{\text{grafted particles}}^{\text{exp}}$ deduced from TGA. For the last value ($R = 0.36$), we find a good agreement between Φ_{eff} and $\Phi_{\text{grafted particles}}^{\text{exp}}$ (both $\Phi_{\text{grafted particles}}^{\text{exp}}$ and $\Phi_{\text{grafted particles}}^{\text{mod}}$), illustrating the good dispersion of the particles. Yet independently of the dispersion state of the particles, we can still extract the thickness e of the grafted polymer layer from the radius of the particles deduced

Table 2. Fitting Parameters of the Inter-Particle Structure Factor by the Percus–Yevick Model for the Chain Length Ratio $R = 0.17$ as a Function of the Silica Volume Fraction (Particles Aggregated Inside the Polymer Matrix)

silica volume fraction $\Phi_{\text{SiO}_2}^a$	experimental grafted particles volume fraction $\Phi_{\text{grafted particles}}^{\text{exp}a}$	effective volume fraction Φ_{eff}^b	effective radius of particles R_{eff}^b	thickness of the grafted corona e^c
4	12	40.5	162	28
7.5	21	44	167	33
9	28	44	169	35
11	32	44.5	171	37

^a Experimental values. ^b Deduced from the fit with the Percus–Yevick model. ^c $e = R_{\text{eff}} - R_{\text{SiO}_2}$ with $R_{\text{SiO}_2} = 134 \text{ \AA}$. Volume fractions are in % [v/v], lengths in \AA .

from the fit, except for the $R = 0.04$ (for which the effective radius is very close to the one of the naked silica meaning that the layer thickness is below the limit of detection of the method, which is estimated to be of the order of 10 \AA).

3. Mechanical Behavior. We investigated the mechanical response of the composites for both the dispersion states described previously: complete dispersion, and large and compact aggregates. We used oscillatory shear measurements at small deformation (amplitude 0.5%) with a plate–plate rheometer ARES. The evolution of the elastic modulus G' and G'' was determined as a function of the filler content (% v/v) for the

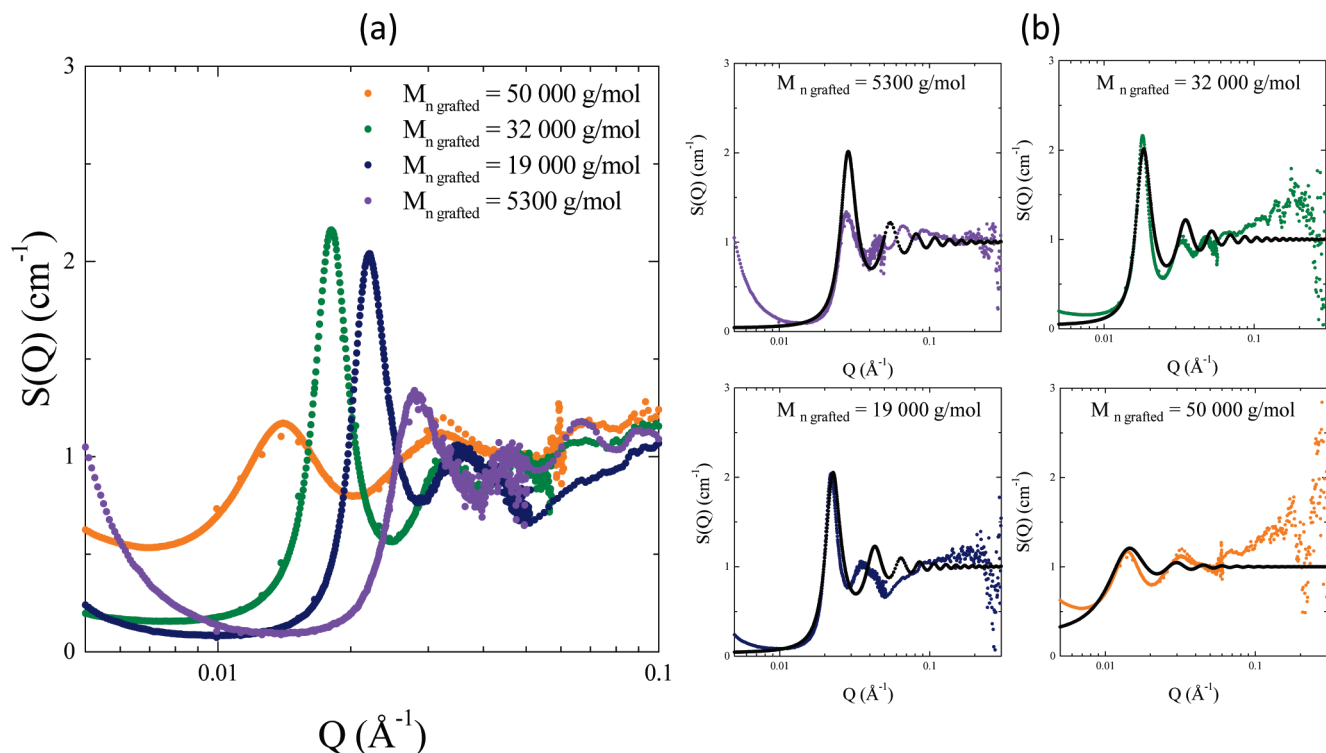


Figure 9. (a) Interparticle structure factor $S(Q)$ deduced from the division of the total scattering intensity (Figure 5) by the silica form factor (full black line in Figure 5) as a function of the chain mass ratio R : matrix of mass $M_{n \text{ matrix}} = 140\,000$ g/mol filled with 5% v/v of silica nanoparticles with grafted chain mass $M_{n \text{ grafted}} = 5300, 19\,000$ and $50\,000$ g/mol corresponding to $R = 0.04, 0.14, 0.23$ and 0.36 . (b) Fits with the Percus–Yevick model (full black line) for each chain length ratio R .

Table 3. Fitting Parameters of the Inter-Particle Structure Factor by the Percus–Yevick Model at Fixed Silica Volume Fraction of 4.5% v/v for Various Chain Length Ratios R

chain length ratio R^a	experimental grafted particles volume fraction $\Phi_{\text{grafted particles}}^{exp}$ ^a	effective volume fraction Φ_{eff}^b	effective radius of particles R_{eff}^b	thickness of the grafted corona e^c	modeled grafted particles volume fraction $\Phi_{\text{grafted particles}}^{mod}$ ^d
0.04	9	40	115		
0.14	9	41	146	12	
0.23	12	40	180	46	
0.36	17	18	207	73	17

^a Experimental values. ^b Deduced from the fit with the Percus–Yevick model. ^c $e = R_{\text{eff}} - R_{\text{SiO}_2}$ with $R_{\text{SiO}_2} = 134$ Å. ^d Deduced from eq 6 (see text). Volume fractions are in % [v/v], lengths in Å.

complete dispersion, obtained with a grafted/free chain length ratio $R = 0.25$ ($M_{n \text{ grafted}} = 24\,400$ g/mol, $M_{n \text{ matrix}} = 98\,000$ g/mol) (Figure 10 (a), G' and 10 (b), G''), and for the case of dense aggregates of grafted particles, for $R = 0.17$ ($M_{n \text{ grafted}} = 24\,000$ g/mol, $M_{n \text{ matrix}} = 140\,000$ g/mol) (Figure 10 (c), G' and 10 (d), G''). The two matrices (98 000 and of 140 000 g/mol) used as references do not show significant differences as a function of the frequency, indicating that their contribution are similar for the two kinds of dispersion and will not influence the comparison of the nanocomposites. Whatever the silica content and the dispersion state, the curves (G' and G'') superimpose perfectly in the whole high frequencies range (above $0.1 \text{ rad} \cdot \text{s}^{-1}$). This means that the short characteristic times (the Rouse modes) of the polymer matrix are not affected by the fillers. Conversely, in the lower frequencies domain (between 10^{-3} and $0.1 \text{ rad} \cdot \text{s}^{-1}$), we observe, especially on the G' , an increase of the modulus. This can be associated with the apparition of a longer time in the relaxation modes of the polymer chains, becoming longer with increasing filler content. In addition, the effect seems to be more pronounced for the aggregated case than for the dispersed one. Such a long-time effect at low frequencies can be seen as a process analogous to a liquid–solid transition inside the materials, whose origin can be interpreted in different ways. One of the main view postulates that the transition is associated with the

formation of a connected network of the filler. This can be a direct connection^{3,26} or a specific interaction between the particles^{15,27,28} but also an indirect connection through the polymer chains. In addition, some interfacial effects can also contribute: mobility of the polymer chains at the interface with the fillers is modified because of confinement.^{29,30}

IV. Discussion

We address the dispersion mechanisms of a model nanocomposite, formed by silica nanoparticles grafted with PS chains and spread inside a PS matrix, as a function of the key parameter R . Dispersion can be tuned either by coupling fixed grafted chains length ($M_{n \text{ grafted}} = 24\,000$ g/mol) with variable free matrix chain length ($M_{n \text{ matrix}} = 98\,000$ or $M_{n \text{ matrix}} = 140\,000$ g/mol), or by coupling variable grafted chain length ($M_{n \text{ grafted}} = 5300, 19\,000, 32\,000$ and $50\,000$ g/mol) with fixed free chains length ($M_{n \text{ matrix}} = 140\,000$ g/mol): we cover then a wide range of values from $R = 0.04$ up to 0.36 . This specific approach allowed us to obtain a clear and unambiguous result:

When $R < 0.24$, the grafted nanoparticles organize inside the polymer matrix as dense and large aggregates, which size and distance between each other increase along with the silica content.

When $R > 0.24$, the grafted nanoparticles form a repulsive well-dispersed organization inside the polymer matrix: while

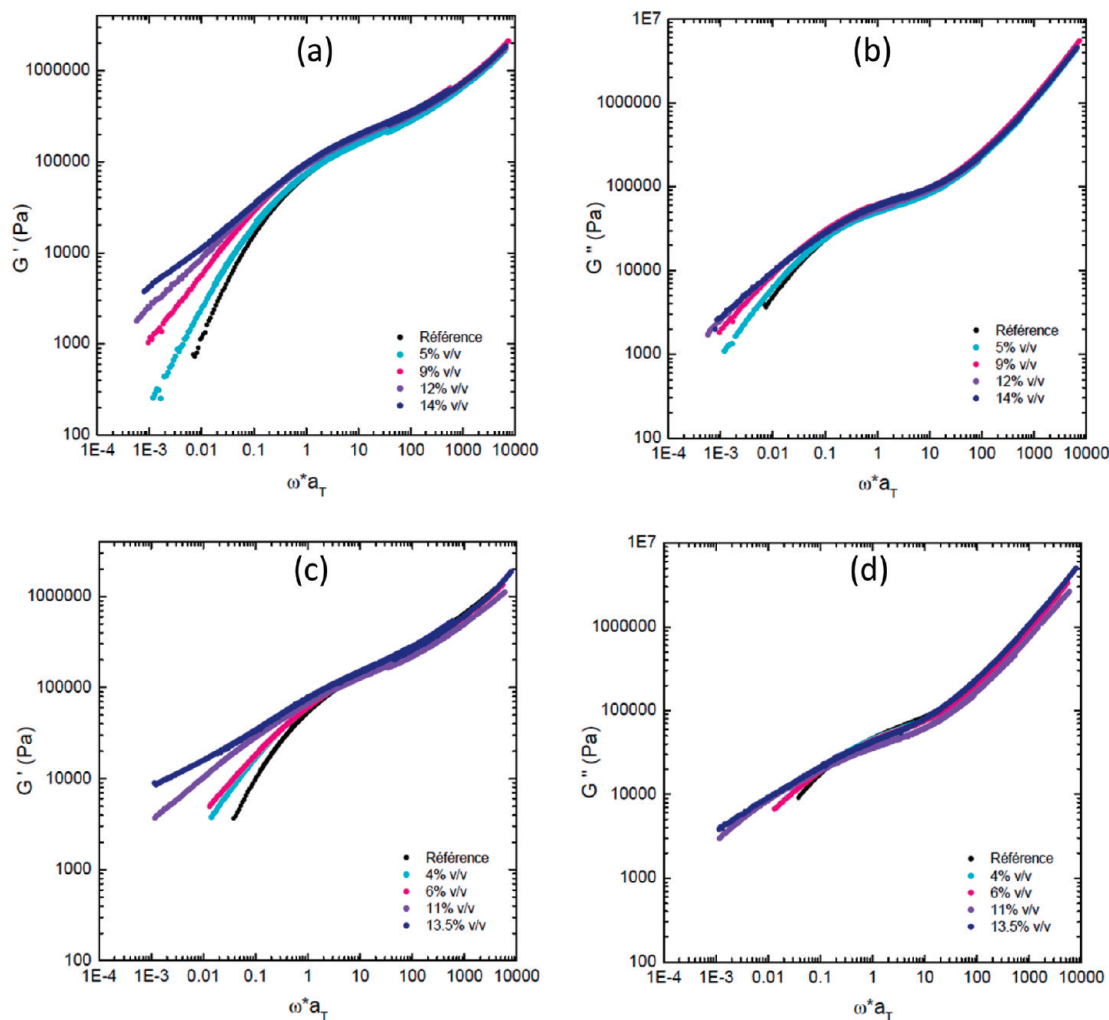


Figure 10. Elastic shear modulus as a function of pulsation ω , using time–temperature superposition ($T_0 = 143\text{ }^\circ\text{C}$) coefficient a_T defined in the text, for different volume fractions (% v/v) of grafted particles in the composite for two dispersion state of the particles inside the polymer matrix: (a) G' , (b) G'' complete dispersion of the particles inside the matrix corresponding to the grafted/free chain length ratio $R = 0.25$ and (c) G' , (d) G'' , aggregation of grafted particles inside the matrix corresponding the grafted/free chain length ratio $R = 0.17$.

increasing the silica content, the mean interparticles distance decreases, according to a classical volume compression process. Using the Percus–Yevick hard-sphere model to fit our interparticles structure factor, we extracted the thickness e of the polymer layer grafted around the particles. In the case of complete dispersion, the values ($53\text{ \AA} < e < 64\text{ \AA}$ for $R = 0.25$ and $e = 73\text{ \AA}$ for $R = 0.36$) obtained with this indirect method are to compare with the ones calculated in our previous work ($e = 62\text{ \AA}$ for $R = 0.25, 0.43$, and 0.71), in which the thickness was determined in a direct way using a specific neutron contrast technique.²¹ As the thickness of the grafted layer depends intrinsically on the length of the grafted chains, we normalized the thicknesses e of the grafted layers by the radius of gyration R_g for Gaussian conformation ($R_g = 0.275M^{1/2}$ for polystyrene). The results deduced from both the ways of determination are reported as a function of R in Figure 11. We see an excellent agreement between the two methods. Besides, we observe that the transition between complete dispersion and formation of aggregates is accompanied by a significant reduction of the normalized thickness of the grafted polymer layer: by about a factor of 2. These results show that the dispersion can be tuned by a refined control of the grafted/free chains wetting properties.

These observations can be qualitatively described considering the total free energy as a combination of a mixing entropy term between the grafted and the free chain and an elastic term of

compression or stretching of the grafted brushes. For $R < 0.24$, according to a depletion process, entropic expulsion of the free chains from the grafted corona is observed, and the corona eventually collapses. The resulting short-ranged interparticles potential induces therefore aggregation. For $R > 0.24$, the free chains can partly swell the grafted corona which is then more extended and creates a repulsive long-ranged interparticles potential, favoring the complete dispersion of the particles. If these observations are qualitatively in agreement with theoretical considerations,^{8,10,11,31} open questions remain to be clarified, especially concerning the parameter fixing the R value separating dispersed from aggregated state. Indeed, we obtained a complete dispersion for value below $R = 1$, which is the theoretical limit below which no complete wetting is possible. Similar observations are reported in the literature^{32–34} and are usually explained by kinetic effects, related to the processing conditions of the systems: the observed dispersed state is indeed a metastable state, in which particles should aggregate but cannot move anymore because of solvent evaporation. The depletion effects being stronger for larger differences in chain lengths, and stronger depletion then inducing quicker aggregation, it explains why we see aggregates for larger chains. Another explanation could be the presence of an interpenetration domain³⁵ between the grafted and the free chains, even when the free chains are longer than the grafted chains, which would then allow dispersion. This idea is supported by the fact that the

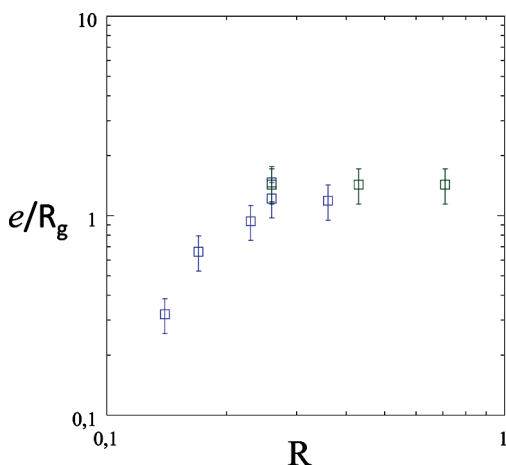


Figure 11. Evolution of the thickness e of the spherical grafted polymer layer normalized by the Gaussian radius of gyration R_g as a function of the grafted/free chain length ratio R determined indirectly from the analysis of the interparticle structure factor (open blue squares) and measured directly with SANS (open green squares) as reported by us in ref 21. The error bars are determined by taking into account for the cumulative experimental errors and the calculation approximations.

dispersed state corresponds to a collapse of the grafted chains which is only partial ($e = 50\text{--}70\text{ \AA}$), in comparison with the complete collapse observed for the aggregated state ($e = 30\text{--}40\text{ \AA}$) and the totally expanded conformation observed in solution ($e = 120\text{ \AA}$), corresponding to wet brushes ($R \gg 1$). In addition, the surface curvature,³⁶ which can come in play for spherical particles, and the polydispersity of the grafted and of the matrix chains, constitute two other relevant contributions which could also have an influence on the transition between aggregated and individual particles. To progress in the understanding of the experimental limiting R parameter, varying the grafting density would certainly be an interesting method of investigation.

The direct correlation between the local structure and the macroscopic rheological response of a material is in many cases difficult to establish. At first order, the mechanical response of our nanocomposites as a function of the two dispersion states, aggregated particles or dispersed ones, shows in both cases the apparition of a much longer relaxation time in the low-frequencies range, which appears to be more pronounced in the case of aggregates. Because of grafting and as revealed by the entire dispersion study, the observed rise in time, which has some features of a liquid–solid transition, cannot be interpreted as a direct percolation^{3,26} of the silica fillers or of the compact aggregates. However, it could be the signature of the formation of an indirect network by means of the grafted layer. For the individual dispersion, the particles come in brush-to-brush contact at $\Phi_{\text{SiO}_2} = 12\%$ v/v, illustrating that the observed liquid–solid like transition could be related to the direct contact between grafted brushes. It was already observed in other well dispersed and diluted systems.^{15,27,28} In the case of aggregated particles, the aggregates are not connected, but dispersed in a matrix which is liquid at the considered frequencies ($\omega^*a_T = 10^{-2}\text{ rad}\cdot\text{s}^{-1}$). Moreover, the large distances between aggregates increase with silica content, while the modulus also increases: this is contradictory with a confinement effect between aggregates. Such behavior is indicative that at this given frequency, the elastic modulus of the filled nanocomposite should only be depending on short-ranged phenomena, governed by the interparticle interactions. No additional long-range contribution, as already shown in nanocomposites showing fractal dispersion,³ seems to be observed. The short-range interparticle effects could be related to the interpenetration between the grafted brushes, which becomes then dominant compared to the interaction between grafted and free chains. Besides, confinement can also alter the dynamics of chains

grafted to particles, especially by slowing-down effects. Finally, this new relaxation could also be related to the intrinsic relaxation of the polymer-silica aggregates, depending on the aggregates sizes. However, such interpretations remain to be experimentally validated, for instance by probing directly the dynamics of the chains with inelastic neutron scattering experiments.

V. Summary and Conclusion

Using a combination of refined synthesis of polymer-grafted nanoparticles with a controlled formation process of nanocomposites films, we investigated the complex problem of the dispersion of polymer grafted particles inside a matrix of the same polymer (PS). For a given intermediate density of grafted chains, the dispersion of the particles inside the films was analyzed with complementary scattering (SAXS/USAXS) and imaging (TEM) techniques as a function of the particle content. The relevant parameter in this case is the grafted/free chains length ratio R , which can be tuned either at fixed grafted chains length, by varying the molecular mass of the free chains, or at fixed molecular mass for the chains of the matrix, by varying the length of the grafted chains. In the probed range of the R parameter always below 1 in our case, between 0.04 and 0.36, we demonstrate the possibility of two dispersion states of the grafted particles inside the polymer matrix: for R below 0.24, the particles arrange in compact and large aggregates whose size and interaggregate distance increase when increasing the particle content. For R above 0.24, the particles form a complete well-defined repulsive organization inside the matrix, where interparticle distance decreases while increasing the silica content, without any aggregation. From the analysis of the interparticle structure factor, we indirectly extract the thickness of the spherical grafted brushes and correlate it with the dispersion state: aggregation of the particles is clearly associated with a significant collapse of the spherical grafted brushes. These results, showing the tuning of the dispersion by a refined control of the grafted/free chains wetting properties, are in qualitative agreement with the theoretical description of the dispersion mechanisms but also lead to questionings about the numerical value of R separating the two dispersion states. The mismatch with the expected theoretical frontier of $R = 1$ can be linked to the possible existence of an interdiffusion zone between the grafted and free chains, along with processing kinetics, surface curvature and chains polydispersity effects. Finally, mechanical analysis shows the appearance of a longer relaxation time at low frequencies more pronounced for the aggregates. The observed liquid–solid like transition can be attributed to the contact between the grafted brushes for the individual dispersion, while modulus increase for the aggregates seems to be also dominated by a short-ranged contribution, with no significant effect of larger scale organizations. This suggests a substantial influence of the interpenetration between grafted brushes or of grafted chains confinement, but this remains to establish with complementary techniques to clarify the contributions of the different effects described above. Such control on the design and the characterization of well-defined nanocomposites and the understanding of correlations between local dispersion, chain conformations and rheological behavior can have a significant impact on the progresses and design of new applicative materials.

Acknowledgment. We thank CEA for the PhD Grant of C. Chevigny and ESRF for beam-time allocation. The Laboratoire Léon Brillouin is a joined facility of CEA and CNRS.

References and Notes

- (1) Dalmás, F.; Cavallé, J.-Y.; Gauthier, C.; Chazeau, L.; Dendievel, R. *Compos. Sci. Technol.* **2007**, *67*, 829–839.

- (2) Heinrich, G.; Klüppel, M.; Vilgis, T. A. *Curr. Opin. Solid State Mater. Sci.* **2002**, *6*, 195–203.
- (3) Jouault, N.; Vallat, P.; Dalmas, F.; Said, S.; Jestin, J.; Boué, F. *Macromolecules* **2009**, *42*, 2031–2040.
- (4) Sen, S.; Xie, Y.; Bansal, A.; Yang, H.; Cho, K.; Schadler, L. S.; Kumar, S. K. *Eur. Phys. J. Spec. Top* **2007**, *141*, 161–165.
- (5) Oberdisse, J.; El Harrak, A.; Carrot, G.; Jestin, J.; Boué, F. *Polymer* **2005**, *46*, 6695–6705.
- (6) Jestin, J.; Cousin, F.; Dubois, I.; Ménager, C.; Schweins, R.; Oberdisse, J.; Boué, F. *Adv. Mater.* **2008**, *20*, 2533–2540.
- (7) Radhakrishnan, B.; Ranjan, R.; Brittain, W. J. *Soft Matter* **2006**, *2*, 386–396.
- (8) de Gennes, P. G. *Macromolecules* **1980**, *13*, 1069–1075.
- (9) Maas, J. H.; Fleer, G. J.; Leemakers, F. A. M.; Cohen Stuart, M. A. *Langmuir* **2002**, *18*, 8871–8880.
- (10) Gast, A.; Leibler, L. *Macromolecules* **1986**, *19*, 686–691.
- (11) Leibler, L.; Pincus, P. A. *Macromolecules* **1984**, *17*, 2922–2924.
- (12) Hasegawa, R.; Aoki, Y.; Doi, M. *Macromolecules* **1996**, *29*, 6656–6662.
- (13) Lindenblatt, G.; Schärfl, W.; Pakula, T.; Schmidt, M. *Macromolecules* **2001**, *34*, 1730–1736.
- (14) Klos, J.; Pakula, T. *Macromolecules* **2004**, *37*, 8145–8151.
- (15) Yezek, L.; Schärfl, W.; Chen, Y.; Gohr, K.; Schmidt, M. *Macromolecules* **2003**, *36*, 4226–4235.
- (16) Lindenblatt, G.; Schärfl, W.; Pakula, T.; Schmidt, M. *Macromolecules* **2000**, *33*, 9340–9347.
- (17) Green, D. L.; Mewis, J. *Langmuir* **2006**, *22*, 9546–9553.
- (18) Akcora, P.; Liu, H.; Kumar, S. K.; Moll, J.; Li, Y.; Benicewicz, B. C.; Schadler, L. S.; Acehan, D.; Panagiotopoulos, A. Z.; Pryamitsyn, V.; Ganesan, V.; Ilavsky, J.; Thiyagarajan, P.; Colby, R. H.; Douglas, J. *Nat. Mater.* **2009**, *8*, 354–359.
- (19) Chevigny, C.; Gignes, D.; Bertin, D.; Jestin, J.; Boué, F. *Soft Matter* **2009**, *5* (19), 3741–3753.
- (20) Chevigny, C.; Jestin, J.; Gignes, D.; Bertin, D.; Boué, F., *Polym. Chem.* **2010**, DOI: 10.1039/C0PY00271B.
- (21) Chevigny, C.; Jestin, J.; Gignes, D.; Schweins, R.; Di Cola, E.; Dalmas, F.; Bertin, D.; Boué, F. *Macromolecules* **2010**, *43*, 4833–4837.
- (22) Williams, M. L.; Landel, R. F.; Ferry, J. D. *J. Am. Chem. Soc.* **1955**, *77*, 3701.
- (23) Rottler, J.; Robbins, M. O. *Phys. Rev. E* **2003**, *68*, 011801.
- (24) Percus, J. K.; Yevick, G. J. *Phys. Rev. Second Ser.* **1958**, *110* (1), 1–13.
- (25) Wertheim, M. S. *Phys. Rev. Lett.* **1963**, *10* (8), 321–323.
- (26) Akcora, P.; Kumar, S. K.; Moll, J.; Lewis, S.; Schadler, L. S.; Li, Y.; Benicewicz, B. C.; Sandy, A.; Narayanan, S.; Ilavsky, J.; Thiyagarajan, P.; Colby, R. H.; Douglas, J. F. *Macromolecules* **2010**, *43*, 1003–1010.
- (27) Inoubli, R.; Dagréou, S.; Lapp, A.; Billon, L.; Peyrelasse, J. *Langmuir* **2006**, *22*, 6683–6689.
- (28) McEwan, M.; Green, D. *Soft Matter* **2009**, *5*, 1705–1716.
- (29) Berriot, J.; Montes, H.; Lequeux, F.; Long, D.; Sotta, P. *Europhys. Lett.* **2003**, *64* (1), 50–56.
- (30) Kropka, J. M.; Putz, K. W.; Pryamitsyn, V.; Ganesan, V.; Green, P. F. *Macromolecules* **2007**, *40*, 5424–5432.
- (31) Gohr, K.; Schärfl, W. *Macromolecules* **2000**, *33*, 2129–2135.
- (32) Corbierre, M. K.; Cameron, N. S.; Sutton, M.; Laaziri, K.; Lennox, R. B. *Langmuir* **2005**, *21*, 6063–6072.
- (33) Xu, C.; Ohno, K.; Admiral, V.; Composto, R. J. *Polymer* **2008**, *49*, 3568–3577.
- (34) Lan, Q.; Francis, L. F.; Bates, F. S. *J. Polym. Sci., Part B: Polym. Phys.* **2007**, *45* (16), 2284–2299.
- (35) Geoghegan, M.; Boue, F.; Bacri, G.; Menelle, A.; Bucknall, D. G. *Eur. Phys. J. B* **1998**, *3* (1), 83–96.
- (36) Xu, J. J.; Qiu, F.; Zhang, H. D.; Yang, Y. L. *J. Polym. Sci., Part B: Polym. Phys.* **2006**, *44*, 2811–2820.

Cite this: *Soft Matter*, 2012, **8**, 3407

www.rsc.org/softmatter

PAPER

Controlled grafted brushes of polystyrene on magnetic γ -Fe₂O₃ nanoparticles via nitroxide-mediated polymerization†

Anne-Sophie Robbes,^{ab} Fabrice Cousin,^{*a} Florian Meneau,^b Chloé Chevigny,^a Didier Gignes,^c Jérôme Fresnais,^d Ralf Schweins^e and Jacques Jestin^{*a}

Received 27th July 2011, Accepted 5th January 2012

DOI: 10.1039/c2sm06438c

We present a new multi-step efficient “grafting from” method to obtain well defined magnetic γ -Fe₂O₃ nanoparticles grafted by polystyrene (PS) chains, from the synthesis of the native nanoparticles up to the refined characterization of the final grafted objects in different organic solvents, using a combination of small angle scattering (SAXS and SANS) and deuteration methods. The polymerization technique, based on a two-step Nitroxide-Mediated Polymerization (NMP), has been adapted for maghemite particles from a protocol previously established for negatively charged silica nanoparticles in dimethylacetamide (DMAc), a polar organic solvent. Such a method requires an initial inversion of the charge surface of the maghemite particles after their synthesis in an aqueous solvent. The colloidal stability of the system has been kept and controlled at every stage of the process to avoid aggregation of the particles to optimize the synthesis parameters in terms of grafting density, conversion rates, and reproducibility. The grafted objects, redispersed in different solvents, have been studied by SAXS (to characterize their γ -Fe₂O₃ core) and SANS (to characterize their grafted PS corona, either hydrogenated or deuterated) at different concentrations to extract both the form factor of the object and the structure factor of the suspension. The experimental scattered curves were modelled by a Pedersen model. The parameters extracted from the model can be directly compared with the masses of the degrafted chains. The grafted objects, better dispersed in DMAc than in toluene, are organized as linear fractal aggregates of 3–4 native particles grafted with PS chains whose behavior is in agreement with scaling laws derived for brushes in a theta solvent.

Introduction

Magnetic nanoparticles have numerous applications. In stable suspensions, they form ferrofluids, *i.e.* dipolar magnetic fluids which have both a fundamental interest as dipolar liquids¹ or for industrial applications such as liquid seals. Associated with other systems, their magnetic properties are used for dedicated industrial use,² for example in magnetic storage, in ink jet printing or in many biomedical applications (MRI contrast enhancement, hyperthermia, targeted drug delivery, ...). This has led in the past

few decades to intense research towards two directions: (i) the synthesis of new types of magnetic nanoparticles, with various chemical compositions, sizes and shapes, and (ii) the surface modification of existing nanoparticles for their incorporation in dedicated solvents while keeping their colloidal stability, or in dedicated systems such as nanocomposites. For the latter, various strategies have been used for the surface modification of nanoparticles, including the adsorption or grafting of organic ligands, silica, surfactants or polymers, as nicely reviewed by Laurent *et al.*² Concerning the grafting of polymers, most of the works have concerned biopolymers (alginate) or biocompatible polymers (Dextran, PEG) soluble in aqueous media, as requested for biomedical applications. By contrast, there are fewer works concerning the functionalization of magnetic nanoparticles by controlled grafted dense brushes of polymers soluble in organic solvents. However, such nanoparticles would be perfectly suited to be incorporated in polymeric systems. It motivated the work described in this paper that presents the synthesis of single magnetic nanoparticles of maghemite (γ -Fe₂O₃) of around \sim 10 nm of diameter, which are grafted by a dense brush of polystyrene (PS). A specificity of this system is the possibility to re-disperse the powders of dried nanoparticles into stable

^aLaboratoire Léon Brillouin, CEA Saclay, 91191 Gif/Yvette, France. E-mail: jacques.jestin@cea.fr; fabrice.cousin@cea.fr

^bSynchrotron SOLEIL, L'Orme des Merisiers, PO Box 48, Saint-Aubin, 91192 Gif/Yvette, France

^cInstitut de Chimie Radicalaire, UMR 7273, Aix-Marseille Université - CNRS, Av. Esc. Normandie Niemen Service 542, 13397 Marseille Cedex 20, France

^dLaboratoire PECSA Université Pierre et Marie Curie, Case Courrier 51 4 place Jussieu, 75252 Paris Cedex 5, France

^eInstitut Laue Langevin (ILL) DSI/LSS 6 rue Jules Horowitz, 38042 Grenoble Cedex 9, France

† Electronic supplementary information (ESI) available: Additional results. See DOI: 10.1039/c2sm06438c

solutions. We believe that such single PS-grafted magnetic nanoparticles will have special interest for the design of ferrofluids based on good solvents of PS, in the field of polymeric nanocomposites, *i.e.* polymeric matrixes reinforced by inorganic nanoparticles, and also in the domain of lyotropic self-associating diblock copolymer-based systems. There is indeed an ongoing research for designing magneto-responsive polymeric ferromagnetics or ferrosmetics by incorporation of magnetic nanoparticles in such systems either in bulk,³ in thin layers or in lamellar bilayers.⁴

In polymeric nanocomposites, a key point to tune the macroscopic properties of materials is the control of the final dispersion of the nanoparticles within the polymer matrix.⁵ Among the different ways used to play on polymer/particle interactions to control such dispersions during nanocomposite processing,^{6–10} two routes are very promising. The first one consists of using an external magnetic field during casting with magnetic nanoparticles, in order to obtain different dispersion states, ranging from isotropic aggregates to chains of particles. The dispersion depends on the applied magnetic field intensity and/or on the particle size that monitors the dipolar interactions.^{11–13} The second one is to graft at the nanoparticles surface the same polymer chains as used in the polymer matrix. It enabled us to obtain a large panel of particles dispersion from individual particles to large compact aggregates by playing on the grafting parameters (grafting density and grafted to free chains mass ratios).^{14,15} Thus our system, for which these two strategies can be associated, should enable the design of nanocomposites with an unprecedented control of the dispersion.

For the grafting of polymer chains on surfaces, two main strategies are used. The grafting “onto” technique,¹⁶ where functionalized tethered chains are covalently grafted on the surface, or the grafting “from” technique, where the polymeric chains grow directly from the nanoparticles surface. Usually, the grafting “from” technique leads to denser brushes than the “onto” technique (typically by a factor of 10), which prompted us to choose it. The grafting “from” technique can be performed with various controlled polymerization techniques as ATRP (Atom Transfer Radical Polymerization),¹⁷ NMP (Nitroxide-Mediated Polymerization)¹⁸ or RAFT (Reversible Addition Fragmentation Chain Transfer)¹⁹ which are efficient in terms of conversion rates and reproducibility. However, when performed on nanoparticles in solution, such techniques could be difficult to implement as the colloidal stability of the system could be lost at any step of the polymerization process. Previous studies have demonstrated the potentiality to graft various kinds of monomers like styrene,^{4,20–22} methacrylate,^{20,21} MEMA,²³ and P3VP²² on magnetic nanoparticles, magnetite or maghemite using either ATRP or NMP. The authors obtained both a good grafting density (typically between 0.2 and 2 molecules per nm²) and a good control of the polydispersity index of the masses of the grafted chains (M_w/M_n below 1.3). But in all of those studies there remains some partial aggregation of nanoparticles, even if the grafting tends to limit it, by favoring the dispersion in a good solvent of the polymeric brush.

We have chosen here to adapt a grafting method based on NMP performed on silica nanoparticles, because it enabled a well defined control of the grafting process while preserving the colloidal stability at the local scale all along the polymerization,

as proven by small angle scattering.^{24,25} Moreover, NMP was preferred because it involves only one chemical species that acts both as an initiator and a controller, in comparison with ATRP or RAFT for which the multi-components initiating system can be a source of particles aggregation. To achieve such a method, first the silanization of the nanoparticles has to be performed in order to graft the initiator and then to carry out the polymerization. Since the γ -Fe₂O₃ nanoparticles we used are synthesized in acidic aqueous media (positive charge surface), a controlled transfer to a basic medium (negative charge surface) in a polar solvent has to be performed prior to the silanization, in order to guarantee a covalent bonding between the silane molecules and the nanoparticles. Indeed, an attempt to conduct maghemite silanization in acidic media has led to a simple polycondensation of the silane, forming a shell around the maghemite nanoparticle.²⁶ In this article, we report the synthesis of well defined grafted magnetic nanoparticles and their detailed structural characterization by SAXS/SANS combination.

Experimental

Materials

FeCl₂, FeCl₃ and ammonia solutions were purchased from VWR Prolabo without further purification. The different solvents, dimethylacetamide (DMAc), toluene, acetone, diethyloxide, nitric acid and chloridric acid, were used as received from Aldrich. Tetrabutylammonium (TBA) was purchased from Fluka. Aminopropyltriethoxysilane (APTES), *N*-hydroxy-succinimide, dicyclohexylcarbodiimide and styrene were purchased from Aldrich and used as received. *N*-(2-Methylpropyl)-*N*-(1-diethylphosphono-2,2-dimethylpropyl)-*O*-(2-carboxyprop-2-yl)hydroxylamine (MAMA-SG1, BlocBuilder MA®) was kindly provided by Arkema and used as received. Deuterated DMAc (D-DMAc), deuterated toluene (D-tol) and deuterated styrene were purchased from Eurisotop and used without further purification. Dialysis bags (MWCO = 12 000–14 000 Da) are from Roth-Sochiel.

Synthesis of γ -Fe₂O₃ nanoparticles

The γ -Fe₂O₃ nanoparticles were synthesized according to the Massart method,²⁷ by coprecipitation of FeCl₂ and FeCl₃ salts in an aqueous ammonia solution. The obtained maghemite nanoparticles were then fully oxidized by nitric acid. The resulting positively charged nanoparticles of maghemite are electrostatically stabilized by NO₃⁻ counterions in acidic media. We performed a size-sorting process based on colloidal gas-liquid transitions²⁸ to obtain rather monodisperse solution of γ -Fe₂O₃ nanoparticles. We chose to work with nanoparticles of 8.1 nm diameter with a polydispersity of 0.29, following a poly-disperse log-normal distribution. The size was determined by magnetization measurements with a home-made vibrating magnetometer apparatus and by SAXS/SANS experiments.

Charge surface modification in aqueous media

A solution of tetrabutylammonium was added dropwise at constant stirring up to pH = 13. During the pH increase, the nanoparticles passed through a reversible aggregation state

characterized by a brown turbid solution, due to their PZC (Point of Zero Charge) located at $\text{pH} = 7.4$. In order to ensure that a state of perfect re-dispersion of the nanoparticles is achieved, the final basic solution was stirred at room temperature for 12 h under nitrogen to avoid carbonation of the basic aqueous solution, TBA. The ions in excess (H^+ , NO_3^- , TBA, OH^-) are then removed by dialysis in an alkaline aqueous reservoir at $\text{pH} = 12.25$. The basic solution of maghemite nanoparticles is placed in a dialysis bag made of regenerated cellulose with a MWCO of 12 000–14 000 Da.

Solvent transfer

The magnetic nanoparticles are transferred into the DMAc by dialysis (MWCO = 12 000–14 000 Da). The procedure is repeated two times in order to remove all the water molecules and the ions in excess.

Silanization of the nanoparticles

APTES was added to $\gamma\text{-Fe}_2\text{O}_3$ nanoparticles negatively charged in DMAc. In a typical run, 2.35 g of APTES is added to 155 g of $\gamma\text{-Fe}_2\text{O}_3$ nanoparticles solution at $\Phi_{\text{mag}} = 1.9\%$ v/v, corresponding to about 2 molecules per nm^2 . The reaction mixture was mixed for 12 h with a magnetic stirrer under nitrogen at room temperature. The solution was then filtered under nitrogen pressure using a Millipore Ultra-filtration apparatus with a regenerated cellulose 30 000 Da pore diameter filter (Millipore) in order to remove the unreacted APTES molecules. The solution was filtered 4 times. Each time, 100 mL of the solution is diluted with 200 mL of DMAc. Finally, the solution is filtered with a filtration paper.

Over-grafting of the polymerization initiator

2-Methyl-2-[*N-tert*-butyl-*N*-(1-diethoxyphosphoryl)-2,2-dimethylpropyl]aminoxy]-*N*-propionylsuccinimide (MAMA-NHS), previously prepared according to ref. 29, was added to the silanized $\gamma\text{-Fe}_2\text{O}_3$ nanoparticles solution (105.6 mg of MAMA-NHS in 116 g of 5.1 wt% $\gamma\text{-Fe}_2\text{O}_3$ nanoparticles). The reaction was carried out under nitrogen bubbling at 0 °C, in order to avoid the decomposition of the alkoxyamine, for 2 h.

Polymerization from the nanoparticles surface

A first model polymerization in solution without particles has been made before under the same conditions to check the feasibility of the reaction in terms of control and efficiency. The following procedure was used (with and without particles): styrene (44.8 g) was added dropwise to the solution of MAMA-NHS grafted $\gamma\text{-Fe}_2\text{O}_3$ nanoparticles (118 g at 1 wt%) placed in a three-necked flask under stirring. Free initiator MAMA-SG1 (261 mg) was then added to the solution. The reaction mixture was deoxygenated during 30 min under nitrogen. The three-necked flask was put in an oil bath at 120 °C at the beginning of the polymerization reaction for 6 hours. At the end of the polymerization, the solution was placed in an ice cup in order to stop the reaction. The PS-grafted $\gamma\text{-Fe}_2\text{O}_3$ nanoparticles were separated from the PS chains in solution coming from the addition of the free initiator MAMA-SG1 by seven successive

centrifugations (the first one for 4 h at 16 000 tr min^{-1} and the others for 2 h at the same speed). In a typical run, 20 mL of the solution at 0.5 v/v% is placed in a 50 mL centrifugation tube in which 15 mL of pure DMAc is added. After each run, the upper part of the tube containing only a solution of free PS chains in DMAc is removed and replaced by pure DMAc. The quantity of free PS chains is measured by gravimetry at the end of each run (see Fig. 1 in the ESI†). When the processing was finished, DMAc was added to recover the initial volume of the solution. The final solution was ultra-sonicated for 12 h to redisperse the PS-grafted nanoparticles. Scheme 1 resumes the whole grafting process.

Cleavage of the PS chains

In order to measure the molecular weight of the grafted PS chains, a concentrated HCl solution (1 mL at 37 wt%) was added to the PS-grafted $\gamma\text{-Fe}_2\text{O}_3$ nanoparticles (2.5 mL at 0.055 v/v%) to dissolve the nanoparticles. This procedure leaves the PS chains intact. When the procedure was over, the solution was yellow, which showed the total dissolution of the red magnetic nanoparticles. The solution was then diluted by a factor of 5 in tetrahydrofuran and precipitated in an excess of cold ethanol. The PS chains are finally recovered by filtration and dried at room temperature.

Grafting densities

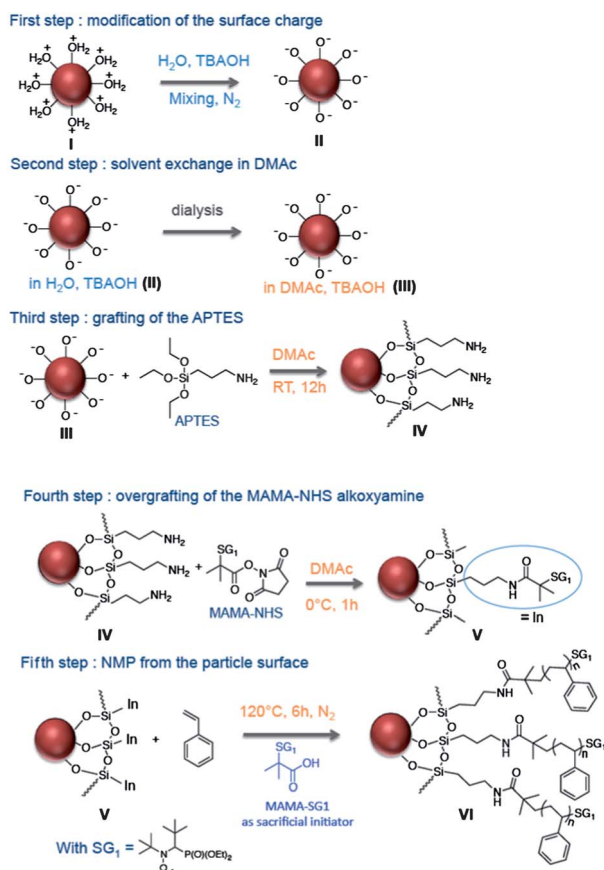
The grafting densities of grafted species (APTES, initiator and PS) were determined by thermogravimetric analysis (TGA). We used a TA instrument Q50 with the following analysis program: 10 min at 100 °C to remove all the solvent traces and then a scan at a rate of 10 °C min^{-1} up to 800 °C under nitrogen flow (40 mL min^{-1}). The grafting densities were determined using the equation below:

$$D_g = \frac{S_{\text{spe}}}{M_{\text{gr}} N_a} \frac{W_{\text{tot}} - W_{\text{ref}}}{100 - (W_{\text{tot}} - W_{\text{ref}})} \quad (1)$$

where S_{spe} is the specific surface ($\text{nm}^2 \text{g}^{-1}$) of the $\gamma\text{-Fe}_2\text{O}_3$ nanoparticles, M_{gr} the molar mass of the grafted molecules (APTES, initiator, PS), N_a the Avogadro number, W_{tot} the weight loss of the grafted sample and W_{ref} the weight loss of the reference sample (respectively the $\gamma\text{-Fe}_2\text{O}_3$ nanoparticles, the APTES-grafted $\gamma\text{-Fe}_2\text{O}_3$ nanoparticles or initiator-grafted $\gamma\text{-Fe}_2\text{O}_3$ nanoparticles).

Analytical techniques

Polymer molecular weights and polydispersities were determined by gel permeation chromatography (GPC) on a system comprising a Waters 515 HPLC pump equipped with a pre-column (Nucleogel, Macherey-Nagel) and two columns thermostatted at 40 °C (PSS SDV, linear M, 8 mm \times 300 mm, bead diameter: 5 μm). Detection was made with two detectors: UV/visible (Waters 486) and RI (Waters 2414). THF was the mobile phase, with a flow rate of 1 mL min^{-1} . Calibration was based on polystyrene standards.



Scheme 1 Scheme of the steps of nanoparticles synthesis and grafting: the charge surface modification [I], solvent transfer [II], silanization [III], the over-grafting of the initiator [IV] and the polymerization from the particles surface [V].

Small angle scattering (SANS and SAXS)

SAXS measurements were performed on the beam-line SWING at Soleil. Two configurations were used in order to cover a large q -range. The beamline energy was set to 7 keV and the sample to detector distance to 6.5 m and 1.8 m. Using a 3 mm beamstop (vertical size) with a photodiode inserted in its centre (to measure the transmitted intensity), the resulting q -range spans from 1.8×10^{-3} to 0.15 \AA^{-1} , where $q = 2\pi \sin \theta / \lambda$. The detector non-linearities were corrected, and the resulting 2D SAXS images were then radially averaged and normalised by the transmitted intensity. The parasitic scattering from the air and mica windows was subtracted from the total scattering intensity. Finally, both the scattering of the solvent I_{solvent} and the scattering of the capillary $I_{\text{capillary}}$ were removed by the subtraction of $(1 - \Phi)[I_{\text{solvent}} - I_{\text{capillary}}]$ from all the solutions.

SANS measurements were performed at the Institut Laue Langevin on the spectrometer D11. Three configurations were used with a wavelength of 8 Å and sample-to-detector distances of 34 m, 8 m and 1.5 m, corresponding to a total q -range of 0.001 \AA^{-1} to 0.2 \AA^{-1} , and at the Laboratoire Léon Brillouin on the spectrometers PAXE and PACE, using three configurations: 4.7 m—12 Å, 4.7 m—5 Å and 1.2 m—5 Å, covering a q -range from 0.0034 \AA^{-1} to 0.36 \AA^{-1} . All measurements were done under atmospheric pressure and room temperature. Standard corrections for sample volume, neutron beam transmission, empty cell

signal subtraction, detector efficiency, subtraction of incoherent scattering and solvent were applied to get the scattered intensities in the absolute scale.³⁰ The data reduction has been done with the Pasinet software³¹ for both SANS and SAXS. The different models used to analyze the scattering data are described in the Appendix.

Contrast variation

We use the contrast complementarity between the X-rays and neutrons (see the values of Scattering Length Densities (SLDs) in Table 1) to characterize our particles at each step of the grafting process. Due to the high electronic density of maghemite, SAXS permits to characterize finely the $\gamma\text{-Fe}_2\text{O}_3$ core of the particles, whatever the solvent and whatever the grafted species (silane, PS chains), taking advantage from the high flux and resolution given by synchrotron radiation. The grafted PS chains can be characterized by SANS, either under the “empty” core condition or under the “full” core condition. The “empty” condition is realized when the neutron SLD of the core is very close to the one of the solvent and is achieved by substituting hydrogenated solvents by deuterated ones. The “full” condition corresponds to the case for which the contrast of the core is very close to the one of the grafted chains. This is the specificity of our system and is obtained by grafting deuterated PS chains. The maghemite core of the particle can however never be perfectly matched because their SLD is always slightly higher than the ones of the solvents or PS chains. In addition, the complete redispersion of the grafted particles in DMAC requires the presence of a few percentage of hydrogenated species, accentuating more the difference between the respective SLDs of the core and of the solvents. Eqn (A7) of the Appendix cannot thus be simplified to the perfect matching conditions.

Results and discussion

In order to adapt the polymerization process successfully applied for silica particles²⁴ to the maghemite nanoparticles, two conditions are required. The particles must be neutral or negatively charged to react with the aminosilane and they must be stable in DMAC, the optimized organic polar solvent of the polymerization. The reaction of magnetic particles with amino-silane under basic conditions has been previously described for magnetite.³² We present here a protocol enabling the transfer of the $\gamma\text{-Fe}_2\text{O}_3$ maghemite nanoparticles in an alkaline organic solvent which allows the covalent bonding of silane molecules at their surfaces.

Modification of the charge surface of the nanoparticles

At the end of the synthesis and after the size-sorting process, the $\gamma\text{-Fe}_2\text{O}_3$ nanoparticles are positively charged (Fe-OH_2^+) in an acidic solution at pH = 2. These conditions do not allow a proper bonding of the aminosilane because: (i) the reaction of hydrolysis between the silane molecules and the nanoparticle surface is only possible when the alcohol groups present at the nanoparticles surface are neutral or fully deprotonated to have access to the nucleophilic character of the oxygen atom and (ii) under acidic conditions, the silane molecules are not reactive with respect to the polymerization initiator, due to the protonation of the amine function.

Table 1 Scattering Length Densities (SLDs) (X-rays/Neutrons) of the components of the systems and of the solvents

SLD (10^{10} cm^{-2})	$\gamma\text{-Fe}_2\text{O}_3$	H-PS	D-PS	H-DMAc	D-DMAc	H-tol	D-tol
Neutrons	6.86	1.43	6.56	0.53	6.60	0.94	5.61
X-Rays	40.20	9.68	9.68	8.80	8.80	7.99	7.99

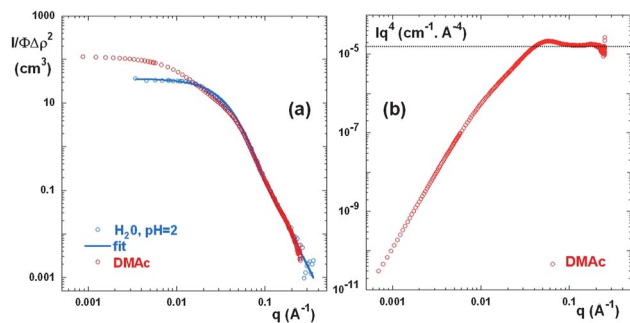


Fig. 1 (a) Scattering of a dilute solution (0.5% v/v) of magnetic nanoparticles dispersed in an acidic aqueous solution (blue curve, SANS) and in an organic (DMAc) alkaline medium (red curve, SAXS). The blue line is a fit with a polydisperse sphere form factor (see text). (b) Scattering signal of the particles in DMAc in the Porod representation Iq^4 vs. q .

An efficient way to set the good conditions for silanization is to increase the pH of the aqueous solution up to be in basic conditions. This enables to inverse the surface charge of the nanoparticles to make them anionic (Fe-O^-) since their PZC is around 7.4. In order to ensure a good colloidal stability of the nanoparticles suspension, the pH has to be higher than 12. Such a colloidal stability is indeed provided by electrostatic repulsions between nanoparticles. Below pH 10, suspensions are not stable because the surface charge of the nanoparticles is too weak. The electrostatic repulsions thus cannot overcome van der Waals attractions. Between pH = 10 and pH = 11, there are gel phases^{33,34} which probably result from the aggregation of some clusters of nanoparticles present in solution. It is thus likely that some small clusters of nanoparticles remain in solution between pH = 11 and pH = 12.³³ Above pH 12, stable suspensions of individual particles are obtained. The choice of the counterion of the strong base is important. One commonly uses a big counterion, tetramethylammonium (TMA^+), to stabilize the $\gamma\text{-Fe}_2\text{O}_3$ nanoparticles at high pH. However, TMA^+ is not soluble in DMAc. We have thus decided to use TetraButylAmmonium (TBA^+) counterions which are a strong base of important size permitting the stabilization of the nanoparticles and are soluble in DMAc. At the end of the procedure, the solution was limpid at pH 13 and red because nanoparticles optically absorb in red, as for the initial solution in an acidic medium. During the addition of TBAOH, the solution passed by a brownish turbid stage due to the reversible aggregation state close to the PZC (pH = 7.4). The recovering of limpidity shows that the PZC of the $\gamma\text{-Fe}_2\text{O}_3$ nanoparticles has been crossed and thus that the surface charge has been inverted.

Solvent transfer and optimization of the experimental conditions for silanization in DMAc

The nanoparticles in the aqueous solution are then transferred into the DMAc by dialysis. The dialysis also enables us to decrease the concentration of ions in solution which is important after the addition of TBA-OH up to pH = 13 (TBA^+ , OH^- and the NO_3^- remaining from the original solution in the nitric acid medium). Such ionic concentrations have indeed to be decreased in order to avoid undesired reactions of APTES with TBA. The dialysis has to be performed in two steps, as explained in the ESI†. The key point for the whole silanization process is the pH of the TBA-OH alkaline aqueous reservoir of the first dialysis. This optimal pH is 12.25, as determined by the measurement of the effective surface density of the grafted silane molecules on the nanoparticles surface as a function of $\text{pH}_{\text{reservoir_bath}}$ in a pH range lying from 11.8 to 13 (see ESI†). Such a study enabled us to find the best conditions in terms of colloidal stability for the covalent bonding of silane molecules at the maghemite nanoparticles surface. After the silanization of the nanoparticles in DMAc, the solution was purified to remove all the APTES molecules that did not react with the nanoparticles (see the Experimental section). After purification and removing all non-covalently bonded APTES molecules adsorbed on the nanoparticles surface, the surface density of grafted silane molecules on the nanoparticles surface was measured by TGA at 0.23 mol nm^{-2} (see Table 2).

SAXS characterization of the stability of the solution of particles

All along the procedure, the stability of the particles was checked by SAXS/SANS. Fig. 1(a) compares the stability of the nanoparticles in an acidic aqueous solution (at $\Phi_{\text{mag}} = 0.5\%$ v/v) and in an alkaline medium in DMAc. In water (blue curve), at large q , the curve exhibits a slope in q^{-4} preceded by an oscillation at intermediate q . It is typical from the scattering of the sharp interface between compact nanoparticles and water. At low q , the curve exhibits a plateau, indicating that the objects present in solution have a finite size. The scattering intensity is perfectly modelled by a sphere form factor with a log-normal polydispersity (eqn (A4) of the Appendix) with a mean radius $R_0 = 3.8 \text{ nm}$ and $\sigma = 0.32$, indicating the perfect initial dispersion of the nanoparticles in water. In DMAc, after the charge modification surface, the scattering intensity of the suspension at the same particles concentration exhibits in the lower q range a higher intensity than the form factor of the single particle (red curve), indicating that some aggregation occurred. The ratio of the intensities at $q \rightarrow 0$ gives an aggregation number of around 3 particles. This aggregation is not related to the solvent transfer because the DMAc enhances the stability of the nanoparticles.¹² It appeared then during the alkalization of the initial aqueous suspension. It is likely due to the possible formation of small “living” aggregates in an alkaline medium below pH 12. As recalled before, nanoparticles are perfectly dispersed in TMA-based ferrofluids and form clusters between pH 11 and pH 12.³³ The transition is maybe slightly shifted towards higher pH with TBA, which could explain the formation of these small aggregates of 3 particles. We can determine the specific surface of the aggregates by analysis of the so-called “Porod” domain which

Table 2 Chemical analysis deduced from thermogravimetric measurements for the different polymerizations

Polymerization number	Silane ^a /nm ²	Initiator ^a /nm ²	Chain ^a /nm ²	Chain/part ^a	M_n /g mol ⁻¹ , sol ^b	M_n /g mol ⁻¹ , grafted ^c	PDI ^c	Conversion rate ^b (%)
H1	0.23	0.23	0.16	95	26 000	26 600	1.7	51
D1	0.23	0.23	0.15	89	17 600	15 700	1.8	48
Model	—	—	—	—	25 900	—	1.27	42

^a Determined by TGA. ^b Determined by weight. ^c Determined by SEC after cleaving.

gives, in a Iq^4 versus q representation (Fig. 1(b)), a plateau at high q proportional to the specific surface of the particles:

$$\lim Iq^4 \approx 2\pi\Phi_{\text{mag}}(1 - \Phi_{\text{mag}})\Delta\rho^2 S/V \quad (2)$$

In water, the specific surface of individual particles is equal to 150 m² g⁻¹ for nanoparticles with 8 nm in diameter while it is reduced to 99 m² g⁻¹ in DMAc due to aggregation. This precise knowledge of the specific surface of the clusters is a very important parameter to determine correctly the grafting densities using eqn (2).

The stability of the particles after the silanization process was then checked by SAXS (Fig. 2). Again, the intensity at low q is higher than the single particle form factor indicating a slight aggregation of silanized particles. However, the level of aggregation remains constant ($N_{\text{agg}} \approx 3$).

Thus, the modification of the nanoparticles surface after the silanization step did not influence strongly the interactions between the particles. In particular, it did not induce the formation of larger aggregates. We succeeded in bonding covalently the silane molecules onto the surface of the nanoparticles in an organic alkaline polar medium while controlling the colloidal stability of the system. We then dispose of well-defined silanized small clusters of 3–4 primary particles on which we can apply the following step of the polymerization process.

Polymerization of the $\gamma\text{-Fe}_2\text{O}_3$ nanoparticles

Before starting the polymerization on the MAMA–NHS grafted nanoparticles, a model polymerization (without any particles) was realized in order to optimize the synthesis conditions for good conversion rates of polymerization. These conditions

were defined according to the ones determined previously for silica particles.²⁴ The result of this model polymerization (120 °C, 30% v/v styrene, $M_{n \text{ theo}} = 50\,000$ g mol⁻¹, DMAc) is reported in Fig. 3.

The conversion of the polymerization was measured by gravimetric analysis by weighing after solvent evaporation of samples taken along the whole reaction *via* sterile syringes. We obtained a conversion rate of 40% after 6 hours. The chain molecular weight distribution of the free chain displays a low polydispersity index (PDI) of 1.27 with a molecular weight $M_n = 30\,000$ g mol⁻¹ which varies linearly with the conversion as expected for a controlled polymerization with an efficient initiation. The polymerization initiator, MAMA–NHS (previously prepared according to ref. 29), is added to the silanized $\gamma\text{-Fe}_2\text{O}_3$ nanoparticles solution. After purification by ultra-filtration, the content of the organic grafted organic material was determined by TGA (see Table 2). The polymerization from the nanoparticles surface is realized under the same conditions as for the model polymerization described before: 30% v/v styrene, 120 °C, $M_{n \text{ theo}} = 50\,000$ g mol⁻¹ in DMAc at 1% v/v of $\gamma\text{-Fe}_2\text{O}_3$ nanoparticles during 6 hours. At this stage, we were not interested in changing the molecular weight of the chains by changing the synthesis conditions. Indeed, an increase of the initial quantity of styrene may induce aggregation of the particles resulting in a destabilization of the medium and an increase of the ratio $n_{\text{initiator}}/n_{\text{styrene}}$ will decrease both the efficiency and the control of the polymerization.

Two different polymerizations were realized on the same over-grafted nanoparticles: one with hydrogenated monomers and the other with deuterated monomers. In both cases, it is necessary to add a sacrificial initiator (MAMA–SG1) to reach the persistent radical effect and ensure a good control of the reaction.²⁴ The results of the evolution of the conversion as a function of time are

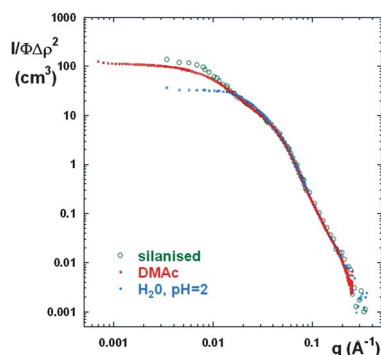


Fig. 2 Scattering curves of the particles after the silanization process (green circles, SANS), compared with the scattering of the particles in DMAc before the silanization (red dots, SAXS) and in water (blue dots, SANS).

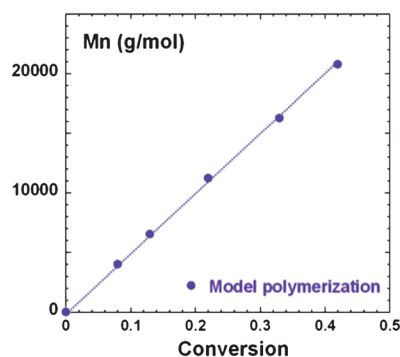


Fig. 3 Evolution of the molecular mass M_n as a function of conversion for the model polymerization. The dashed line is a guide for the eye illustrating the control of the polymerization.

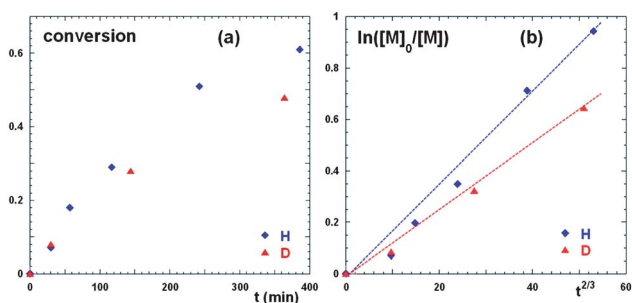


Fig. 4 (a) Conversion rates with time and (b) semi-logarithmic evolution of the conversion as a function of $t^{2/3}$ for the hydrogenated monomer (blue) and the deuterated monomer (red).

presented in Fig. 4 for the two polymerizations H-1 and D-1. The chosen representation, $\ln([M]_0/[M])$ as a function of $t^{2/3}$, exhibits a quasi-linear variation indicating a good control and efficiency of the reaction. It shows that the chain growth (propagation) is as fast as the initiation. The conversion rates are reported in Table 2. It is worth noting that one recovers the high conversion rate (around 50%) formerly observed for silica particles²⁴ in spite of the initial state of the surface of naked maghemite particles (Fe-OH_2^+) and of the subsequent modifications of their surface. There is a difference in efficiency reactivity between hydrogenated monomers and deuterated monomers which can be explained by the presence of additive species inside the deuterated styrene used for stabilization and storage. The grafting densities deduced from TGA are also given in Table 2. They are comparable for both polymerizations at around 0.15 chains per nm^2 .

The PS-grafted $\gamma\text{-Fe}_2\text{O}_3$ nanoparticles were then separated from the free PS in solution coming from the introduction of MAMA-SG1 in the medium by centrifugation. The removed quantity of free PS chains was measured by gravimetry at the end of each run (see ESI†). One of the most interesting advantages of our system is the possibility of easy dissolution of the maghemite nanoparticles for a direct characterization of the PS-grafted chains.

Contrary to silica where fluorhydric acid (highly corrosive and contact poison) is required to dissolve the particles, the dissolution is simply achieved by the addition of a concentrated solution of HCl. The molecular weights of the cleaved hydrogenated and deuterated chains are measured by SEC and compared to the PS chains in solution. They are found to be of the same order of magnitude (Table 2), as previously demonstrated in ref. 35–37 showing that the mass of the grafted chains is usually close to the untethered chains.

SAXS/SANS characterizations of the grafted nanoparticles in solution

After purification, the different batches of grafted $\gamma\text{-Fe}_2\text{O}_3$ particles were measured by SAXS and SANS under different contrast matching conditions. We studied both dilute solutions (typically $\sim 0.1\%$ v/v of maghemite) to determine the form factors of the grafted objects, and more concentrated solutions to extract the structure factors in order to probe the interactions between the grafted objects. For most of the experiments, the grafted $\gamma\text{-Fe}_2\text{O}_3$ particles have been dried by evaporation of the

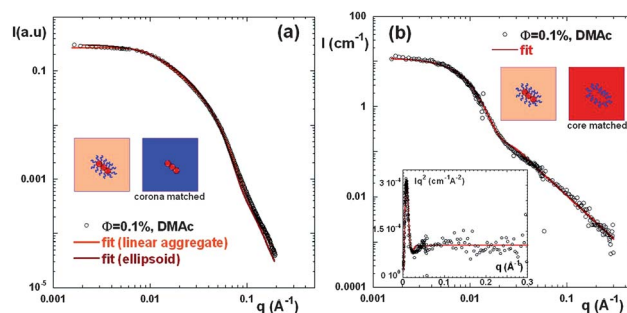


Fig. 5 (a) SAXS scattering curve of a dilute solution (0.1% v/v) in maghemite of the grafted maghemite nanoparticles with hydrogenated PS chains in a mixture of 95% v/v of D-DMAc and 5% v/v of H-DMAc. The X-ray scattering signal arises from the maghemite core. (b) SANS scattering of the same solution, the neutron scattering comes from the grafted PS chains. The red lines are the best fitted results of modeling (see text for details). Sketches are representations of the grafted objects in the real space.

H-DMAc to form powders and then re-dispersed by ultra-sonication at the desired volume fraction in the chosen solvent.

Dispersion in DMAc: form and structure factors of grafted particles

According to the neutron scattering length densities (see Table 1), the most effective matching of the core would occur in a 100% D-DMAc solvent. However, it has not been possible to achieve here the redispersion of dried nanoparticles by ultrasonication in pure D-DMAc. A macroscopic irreversible aggregation of the nanoparticles occurred, probably due to some additives present in the D-DMAc for stabilisation and storage. An alternative possibility for the exchange of D-DMAc with the initial H-DMAc solvent would have been dialysis, but it requires a huge quantity of D-DMAc which is too costly. We thus decided to dilute by a factor of 20 the solution of nanoparticles in H-DMAc by D-DMAc corresponding to a final H/D ratio of 5/95% v/v of the solvent. The resulting solution at 0.1% v/v in maghemite was measured by SAXS to characterize the maghemite core and then by SANS, to obtain information about the PS corona. The resulting scattering curves are shown in Fig. 5. Both SAXS and SANS curves exhibit a flat plateau at low q indicating that, at low concentration, the interactions between the objects can be neglected. This shows that the objects are well dispersed in the solvent. At intermediate and large q , both curves show a different behavior: a rapid decay like q^{-4} for SAXS, characteristic of the maghemite core form factor and a q^{-2} decay for SANS, arising from the scattering of the PS chains. As the silanization was performed on small aggregates of nanoparticles, we assume that the polymerization occurs on the same aggregates and not on individual particles. This is confirmed by SAXS data which can be perfectly modelled using a form factor of a fractal aggregate made of a finite number of individual maghemite particles (eqn (A5) and (A6) of the Appendix). The best fit is obtained for a linear aggregate ($D_f = 1$) of 4 primary particles. For a further simplification of the modelling of the corona, we also chose to analyze the SAXS curve with the form factor of an ellipsoid (eqn (A11) of the Appendix). The adjustable parameters are: Φ , the

Table 3 Best-fitted results parameters of the fitting procedure applied on the hydrogenated grafted particles in DMAc and in toluene

Solvent	Maghemite particle concentration ($\Phi\%$ v/v)	$R_{\text{core}}/\text{\AA}$	Polydispersity σ	Ellipticity ν	Volume of the grafted chain V/nm^3	Grafting density/ mol nm^{-2}	R_g of grafted chains/ \AA
DMAc	0.1	40	0.22	0.22	54.7	0.13	92
Toluene	0.1	40	0.23	0.22	62.6	0.13	97

$\gamma\text{-Fe}_2\text{O}_3$ nanoparticles volume fraction, R_0 , the mean radius of the $\gamma\text{-Fe}_2\text{O}_3$ nanoparticles corresponding to the small side of the ellipse, σ , the particle polydispersity and ν , the ellipticity ratio. The scattering length density between the particles and the solvent is fixed. The best fit calculation shows a nice agreement with the experimental data. In particular, the value of ν (0.22) is consistent with the aggregation number of the linear aggregate. The parameters deduced from the fit are reported in Table 3.

The SANS curve has been analyzed by the Pedersen model described with eqn (A7) of the Appendix. The parameters of the core have been fixed at the values determined previously from the SAXS analysis using the ellipsoid model. The respective SLDs of the core, of the solvent and of the chains have been fixed at their calculated values (Table 1).

Finally, the fitting variable parameters are reduced to only three: the grafting density of chains N , the volume of the polymer chain and the radius of gyration of the grafted chains. The best fit result shows a good agreement with the experimental data (Fig. 5(b)). The grafting density deduced from such a fit is consistent with the one calculated from TGA (see Table 2). The extension of the grafted layer $h = 2R_{\text{g-corona}} = 18.4$ nm is found to be 1.5 times larger than the corresponding Gaussian chain in solution ($2R_{\text{g-bulk}} = 12.0$ nm with $R_{\text{g-bulk}} = 0.275M_w^{0.5}$) determined by SEC after the cleaving process (Table 1). This points out the stretching of the chain at the surface of the particle. Such a stretching, which can be explained by excluded volume interactions with lateral neighboring chains, has been described by scaling laws of the grafting density σ by Alexander.³⁸ For a layer grafted on a planar surface, the extension of the grafted layer is expected to be $h \approx aN\sigma^{1/3}$ for a good solvent and $h \approx aN\sigma^{1/2}$ for a theta solvent, where a is the monomer length and N the number of monomers.³⁹ The calculations from such scaling laws give respectively 55 nm and 40 nm, showing that we are closer to

the theta solvent regime. In addition, the effect of surface curvature $r_0^{2/5}$ has also to be taken into account. It will reduce the extension of the grafted layer down to $h \approx N^{3/5}\sigma^{1/3}r_0^{2/5}$.⁴⁰ The surface curvature here is difficult to estimate in the case of our linear aggregate. As a comparison, the extension for the corresponding grafted brush on a single maghemite particle would give $h \approx 11$ nm.

The value of the extension of the grafted layer deduced from the fit for our objects is in agreement with the scaling laws of grafted brushes in a theta solvent, taken for the surface an intermediate geometry between a spherical surface and a planar one. It is consistent with the modelization of the core with linear aggregates made of primary spheres. Fig. 6(a) shows the SAXS scattering curve of grafted particles at higher concentration in DMAc (0.5% v/v of maghemite). The curve exhibits a correlation peak in the low q domain at 0.008 \AA^{-1} and a weak compressibility ($I(q)_{q \rightarrow 0}$ is decreasing), which arise from repulsive interactions between the objects. The structure factor $S(q)$ can be extracted by dividing the total scattering intensity $I(q)$ by the form factor of the core made of linear aggregates of 4 native particles. The resulting $S(q)$ can be compared (Fig. 6(b)) with an approximation of Percus–Yevick (P–Y)⁴¹ that describes the interactions in a system of hard spheres.⁴² The P–Y calculation necessitates the knowledge of the total volume fraction of objects and of the diameter of the hard spheres. Taking into account the grafted polymer layer, the volume fraction of objects is equal to 0.15. The diameter taken for the spheres is 52 nm, corresponding to the length of grafted linear aggregates, obtained by summing the 4 maghemite cores and the thickness of the polymer layer. The P–Y model reproduces very well the position of the correlation peak. This confirms the well dispersed organization of the grafted objects in DMAc. The experimental correlation peak has a much

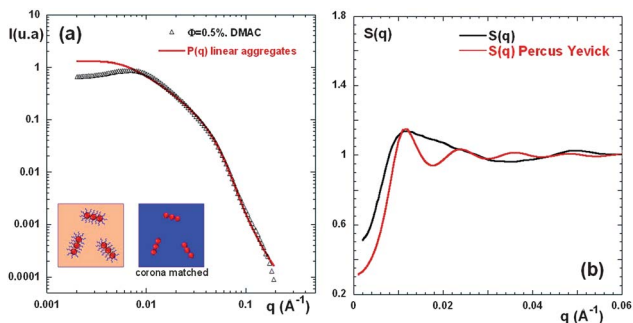


Fig. 6 (a) SAXS of grafted particles in H-DMAc at 0.5% v/v in maghemite. The red line corresponds to the modeling of linear fractal aggregates. (b) Structure factor $S(q)$ deduced from the division of the total scattering intensity by the form factor of the linear aggregates (black line) and P–Y modelization (red line) see text for details. Sketches are representations of the grafted objects in the real space.

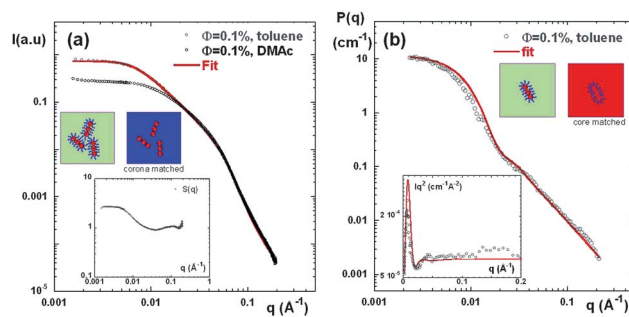


Fig. 7 (a) SAXS scattering curve of a dilute solution (0.1% v/v) in maghemite of the grafted maghemite nanoparticles with hydrogenated PS chains re-dispersed in D-toluene. The X-rays scattering signal arises from the maghemite core. (b) SANS scattering of the same solution, the neutron scattering comes mainly from the grafted PS chains. The red lines are the best fitted results of modelling (see text for details). Sketches are representations of the grafted objects in the real space.

softer shape than the calculated P–Y one because the grafted particles are not hard and the aggregates are not spherical.

Dispersion in toluene

We did the same experiments in toluene as in DMAc in order to test the influence of the nature of the solvent on the conformation of the grafted brush, while keeping the core of the grafted objects unchanged. In toluene, the dried grafted nanoparticles can be directly dispersed in D-toluene by ultrasonication without macroscopic irreversible aggregation. As the SLD of the D-toluene is lower than the SLD of maghemite, the core cannot be perfectly matched in this solvent. A dilute solution of grafted particles (0.1% v/v of maghemite) with hydrogenated chains in D-toluene has been measured by SAXS to extract the parameters of the core and by SANS to extract the parameters of the grafted corona (Fig. 7). At low q , the SAXS scattering curve in toluene is higher than the one in DMAc, indicating an aggregation process of the grafted objects. This aggregation may come from a partial re-dispersion of the dried objects in toluene. In order to simplify the further modelling of the corona, we calculated the effective structure factor $S_{\text{eff}}(q)$ describing the structure of the aggregates arising from such an aggregation process.

It is done by dividing the SAXS signal by the form factor of the core of the grafted particles determined previously in DMAc, in the absence of aggregation. The result is presented in the inset of Fig. 7(a). The shape of $S_{\text{eff}}(q)$ is typical of the formation of finite aggregates of 2–3 grafted objects, which are linear aggregates of 3–4 particles themselves. The SAXS curve can indeed be perfectly fitted with a model of a branched fractal aggregate ($D_f = 1.6$) of finite size, made of primary maghemite particles ($N_{\text{agg}} = 10$). Such a $S_{\text{eff}}(q)$ is crucial for the refined analysis of the grafted corona in toluene, as it enables to obtain the form factor $P(q)$ of the grafted corona by dividing the total SANS scattering intensity $I(q)$ by $S_{\text{eff}}(q)$, as presented in Fig. 7(b). The resulting form factor can then be analyzed by the Pedersen model according to the same fitting procedure than for DMAc. In this case, only the radius of gyration of the grafted chains and the volume of the chains were fitted. All the other parameters were kept fixed with the values obtained in the DMAc case. The agreement between the calculation and experimental data appears less accurate than for DMAc probably because of the aggregation process in toluene. However, it remains acceptable. The values of the radius of gyration and of the chain volume extracted from the fit are very close to the ones in DMAc (Table 3). Thus there is no significant effect due to the solvent quality on the conformation of the grafted layer, which also scales as a brush in the theta solvent in toluene.

Again, we probed the dispersion of the grafted objects in toluene with SAXS on a concentrated solution at 0.5% v/v in maghemite (Fig. 8). There is still a repulsive correlation peak, but with a higher intensity and at a smaller q position than in DMAc. This is consistent with the slight aggregation observed for the dilute case in toluene: (i) as the whole aggregates involve more particles in toluene than in DMAc, the mean distance between objects is increased and the peak is shifted towards low q (see sketches of Fig. 8), and (ii) the overall intensity at low q is weighted by the mass of aggregates and is thus higher in toluene. We did not extract here the structure factor because its

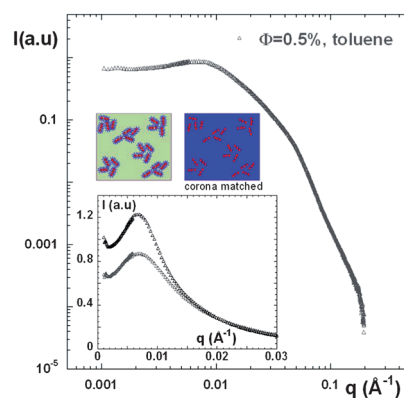


Fig. 8 SAXS of grafted particles in H-toluene at 0.5% v/v in maghemite. The inset compares the SAXS curve of the grafted objects dispersed in DMAc and in toluene in linear representation. Sketches are representations of the grafted objects in the real space.

calculation would require the exact knowledge of the form factor of the aggregates of grafted object, which may evolve with the concentration of objects. This measurement proves that there are repulsions between grafted objects in toluene. The dispersion of the grafted objects appears less good in toluene than in DMAc. As it is clearly not an isotopic effect (the dispersions are similar in H and D solvents), we guess that this difference is more governed by the kinetic of dissolution of dried grafted objects for a given solvent. We believe that a full dispersion of individual grafted objects would thus be possible in toluene with longer re-dissolution time under ultrasonic conditions.

Deuterated grafted particles

We finally characterized the particles grafted with deuterated PS chains (polymerization D1) by combination of SAXS and SANS (Fig. 9). The particles have been dissolved in fully hydrogenated DMAc at 0.5% v/v in maghemite. We describe here the results only from a qualitative point of view. The SAXS curve, which gives only the structure of the core, shows

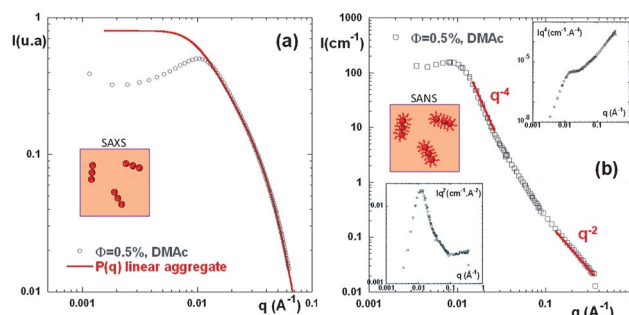


Fig. 9 (a) SAXS scattering curve of a solution (0.5% v/v) in maghemite of the grafted maghemite nanoparticles with deuterated PS chains re-dispersed in D-DMAc. The red line is the linear aggregate modeling. The X-ray scattering signal arises from the maghemite core. (b) SANS scattering of the same solution, the neutron scattering comes mainly from the grafted D-PS chains. The insets permit to illustrate the two respective q^{-4} and q^{-2} regimes. Sketches are representations of the grafted objects in the real space.

a strong correlation peak at $\sim 0.008 \text{ \AA}^{-1}$ indicating repulsive interactions between the grafted objects. The position of the correlation peak is similar to the one of the H-PS grafted chains in H-DMAc at the same volume fraction of maghemite. In the SANS experiment, there is almost no contrast between the core and the corona shell because the SLD of the grafted D-PS chains is very close to the one of the maghemite particles (Table 1). From a neutron point of view, the grafted particles correspond thus to the case of homogeneous hairy spherical particles dispersed in a solvent. The q^{-4} behavior observed at intermediate q comes then from the form factor of the spheres. At large q , where the neutrons probe the interface between the object and the solvent, the intensity decays nicely like q^{-2} , illustrating the Gaussian behavior of the grafted chain in a theta solvent. The correlation peak highlighted in the SAXS measurement at $\sim 0.008 \text{ \AA}^{-1}$ is also present in the low q region.

Conclusions

We demonstrate here the possibility to modulate the charge surface of maghemite nanoparticles, from positive to negative, while transferring them in an organic solvent without any aggregation in order to apply a PS controlled grafting from method based on NMP to finally obtain well defined PS-grafted- $\gamma\text{-Fe}_2\text{O}_3$ particles. The colloidal stability has been kept at every stage of the grafting process and high conversion rates with low PDI and controlled grafted molecular masses using either deuterated and hydrogenated monomers were successfully synthesized. The final grafted objects have been purified and re-dispersed in two solvents, DMAc and toluene, at low and high concentrations to analyze, by a combination of SAXS/SANS methods, the form factor and the interaction of the core-polymer-grafted particles. The core is organized as a linear fractal assembly of 3–4 native particles and the polymer-grafted corona can be nicely fitted with a Gaussian chain Pedersen model and directly compared with masses of de-grafting chains. The grafted chain conformations are in accordance with scaling laws for brushes in a theta solvent for the intermediate spherical/plane surface curvature geometry.

We believe that these PS-grafted magnetic nanoparticles are of great interest for many applications owing to their versatile properties: the size of their core or/and of their shell can be tuned through the synthesis parameters, a single synthesis provides a huge quantity of nanoparticles (typically 200 mL at 1% v/v in maghemite) and the nanoparticles can be perfectly re-dispersed in different solvents from dried powders. In particular, they can be used as fillers in nanocomposites, for the design of self-assembled hybrid systems based on copolymers or as a support of active species for drug delivery.

Appendix: fitting models

The total intensity $I(q)$ scattered by a colloidal suspension of centrosymmetrical particles with a volume fraction Φ can be written as follows:

$$I(q) = \Phi \Delta\rho^2 V_{\text{part}} F(q) S(q) \quad (\text{A1})$$

V_{part} is the volume of the particle, $\Delta\rho^2$ is the difference between the scattering length density of the particle and the scattering length density of the solvent, $F(q)$ is the form factor of the particles and $S(q)$ is the structure factor of the system. For diluted colloidal solutions, the interactions between the particles are negligible and $S(q) \approx 1$ on the whole q -range. The form factor of a $\gamma\text{-Fe}_2\text{O}_3$ nanoparticle which we assume to be a compact sphere is written as:

$$F(q) = [3f(qR)]^2 \quad \text{with} \quad f(x) = \frac{\sin(x) - x \cos(x)}{x^3} \quad (\text{A2})$$

R is the radius of the sphere. The polydispersity in size of the $\gamma\text{-Fe}_2\text{O}_3$ nanoparticles is described as a log-normal distribution with the mean diameter R_0 and the polydispersity σ .

$$P(R, R_0, \sigma) = \frac{1}{\sqrt{2\pi}\sigma} \exp\left(\frac{-1}{2\sigma^2} \ln^2 \frac{R}{R_0}\right) \quad (\text{A3})$$

The form factor with polydispersity is calculated by integration:

$$F(q) = \int P(R, R_0, \sigma) F(q, R) dR \quad (\text{A4})$$

This form factor can be used to analyze the scattering signal of the perfectly dispersed nanoparticles in solution. During the different steps of surface modifications, a slight aggregation can lead these particles to form small fractal objects of a finite number of primary particles. The scattering intensity of such aggregates presents three distinct behaviors as a function of q separated by two cut-offs qc_1 and qc_2 .⁴³

(i) at very large q (for $q > qc_2$), the scattering can be identified with the form factor $P(q, R)$ of the primary particles as given by eqn (A4).

(ii) at intermediate q (for $qc_1 > q > qc_2$), the scattering intensity scales as

$$I(q) \approx q^{-D_f} \quad (\text{A5})$$

(iii) at low q (for $q > qc_1$), the scattering intensity is equal to:

$$I(q) = \Phi \Delta\rho^2 N_{\text{agg}} P(q \rightarrow 0, R) \quad (\text{A6})$$

where N_{agg} is the number of single particles inside an aggregate, D_f is the fractal dimension of the aggregates. This expression is valid when the particles are diluted enough to consider that the interactions between aggregates are negligible, *i.e.* with a structure factor between aggregates equal to 1.

The model we use to model the grafted particles has been developed by Pedersen⁴⁴ for block copolymer micelles and is representative of the form factor for non-interacting Gaussian chains. The general expression can be written as follows:

$$F_{\text{pedersen}}^2(q, R) = V_{\text{core}}^2 \Delta\rho_{\text{core}}^2 F_{\text{core}}(q) + N \Delta\rho_{\text{chain}}^2 V_{\text{chain}}^2 F_{\text{chain}}(q) + 2N V_{\text{core}} V_{\text{chain}} \Delta\rho_{\text{core}} \Delta\rho_{\text{chain}} S_{\text{core-chain}}(q) + N(N-1) \Delta\rho_{\text{chain}}^2 V_{\text{chain}}^2 S_{\text{chain-chain}}(q) \quad (\text{A7})$$

where V_{core} and V_{chain} are respectively the volume of the core and of the chain, F_{core} and F_{chain} are the form factors of the core and of the chain, $\Delta\rho_{\text{core}}^2$ and $\Delta\rho_{\text{chain}}^2$, are the contrast between the core and the solvent and between the chain and the solvent, $S_{\text{core-chain}}$ and $S_{\text{chain-chain}}$ are the structure factors between the core and the

chain and the interchain structure factor, N is the number of grafted chains by particle. The form factor of the Gaussian chain F_{chain} can be written according to the classical Debye expression:

$$F_{\text{chain}}(q) = \frac{2(e^{-X} - 1 + X)}{X^2}, \quad \text{with} \quad X = q^2 R_g^2 \quad (\text{A8})$$

where R_g is the radius of gyration of the Gaussian chain. The crossing term related to the interaction between the core and the chain can be expressed as:

$$S_{\text{core-chain}}(q) = \frac{3}{q^3} \left[\frac{\sin(qR) - (qR)\cos(qR)}{R^3} \right] \times \frac{[1 - \exp(-q^2 R_g^2)] \sin[q(R_g + R)]}{(q^2 R_g^2) [q(R_g + R)]} \quad (\text{A9})$$

The intrachain form factor can be expressed as:

$$S_{\text{chain-chain}}(q) = \frac{[1 - \exp(-q^2 R_g^2)] \left(\frac{\sin[q(R_g + R)]}{[q(R_g + R)]} \right)^2}{(q^2 R_g^2)^2} \quad (\text{A10})$$

The form factor of the core F_{core} , composed of small fractal aggregates of a finite number of primary particles, can be written as an ellipsoid form. For the semi-axes, $R, R, \varepsilon R$:

$$P(q, R, \varepsilon) = \int_0^{2\pi} \int F[q, r(R, \varepsilon, \alpha)]^2 \sin \alpha d\alpha \quad (\text{A11})$$

where $r(R, \varepsilon, \alpha) = R(\sin^2 \alpha + \varepsilon^2 \cos^2 \alpha)^{1/2}$.

The total measured intensity $I(q)$ is expressed as:

$$I(q) = \frac{\Phi}{V_{\text{part}}} [F_{\text{Pedersen}}(q, R)] \quad (\text{A12})$$

The polydispersity can be included by integration of the expression of eqn (A12) according to eqn (A4). In the case of block copolymers, the model must contain an additional parameter modeling the inter-diffusion zone between the two polymers. An appropriate radial profile for the corona is chosen to account for the possibility for the chain to penetrate into the polymer core.⁴⁵ Such a refinement is not necessary in our case because it is impossible for the grafted chains to penetrate within the maghemite core, which simplifies the analytical formulation of the model. In the range of our experimental grafting densities, the interactions between the chains in the corona can be neglected. This prompted us to use the form factor of Gaussian chains, and not the one of interacting self-avoiding chains, which has been derived by Svaneborg and Pedersen on the basis of Monte Carlo simulations.⁴⁶ To analyze the experimental data, we use the SASFIT software developed by J. Kolbrecher.⁴⁷ The number of fitting parameters is model dependent. We reduced it by fixing some values from calculations (contrast term) or experiments (particle volume fraction) when it was possible. The routine is running by minimization of χ^2 on various combinations of the adjustable fitting parameters. All parameters are restricted within a range of values of physical meaning.

Acknowledgements

The authors thank Denis Bertin for fruitful discussions about polymerization with NMP and CEA and Synchrotron Soleil for PhD grant of A.S. Robbes.

References

- R. Rosensweig, *Ferrohydrodynamics*, Cambridge University Press, Cambridge, 1985.
- S. Laurent, D. Forge, M. Port, A. Roch, C. Robic, L. V. Elst and R. N. Muller, *Chem. Rev.*, 2008, **108**(6), 2064–2110.
- (a) S. Lecommandoux, O. Sandre, F. Checot, J. Rodriguez-Hernandez and R. Perzynski, *Adv. Mater.*, 2005, **17**(6), 712; (b) S. Lecommandoux, O. Sandre, F. Checot, J. Rodriguez-Hernandez and R. Perzynski, *J. Magn. Magn. Mater.*, 2006, **300**(1), 71–74; (c) S. Lecommandoux, O. Sandre, F. Checot and R. Perzynski, *Prog. Solid State Chem.*, 2006, **34**(2–4), 171–179.
- S. Douadi-Masrouki, B. Frka-Petesic, M. Save, B. Charleux, V. Cabuil and O. Sandre, *Polymer*, 2010, **51**, 4673–4685.
- M. E. Mackay, A. Tuteja, P. M. Duxbury, C. J. Hawker, B. Van Horn, Z. Guan, G. Chen and R. S. Krishnan, *Science*, 2006, **311**, 1740–1743.
- J. Oberdisse and B. Demé, *Macromolecules*, 2002, **35**, 4397.
- Y. Rharbi, B. Cabane, A. Vacher, M. Joanicot and F. Boue, *Europhys. Lett.*, 1999, **46**, 472–478.
- P. Melé, S. Marceau, D. Brown, Y. de Puydt and N. Alberola, *Polymer*, 2002, **43**, 5577–5586.
- N. Jouault, P. Vallat, F. Dalmas, S. Said, J. Jestin and F. Boué, *Macromolecules*, 2009, **42**(6), 2031–2040.
- S. Sen, Y. Xie, A. Bansal, H. Yang, K. Cho, L. S. Schadler and S. Kumar, *Eur. Phys. J. Spec. Top.*, 2007, **141**, 161–165.
- J. Jestin, F. Cousin, I. Dubois, C. Ménager, R. Schweins, J. Oberdisse and F. Boué, *Adv. Mater.*, 2008, **20**(13), 2533–2540.
- (a) A.-S. Robbes, J. Jestin, F. Meneau, F. Dalmas, O. Sandre, J. Perez, F. Boué and F. Cousin, *Macromolecules*, 2010, **43**(13), 5785–5796; (b) A.-S. Robbes, F. Cousin, F. Meneau, F. Dalmas, F. Boué and J. Jestin, *Macromolecules*, 2011, **44**(22), 8858–8865.
- D. Fragouli, R. Buonsanti, G. Bertoni, C. Sangregorio, C. Innocenti, A. Falqui, D. Gatteschi, P. Davide Cozzoli, A. Athanassiou and R. Cingolani, *ACS Nano*, 2010, **4**(4), 1873–1878.
- P. Akcora, L. Hongjun, S. K. Kumar, J. Moll, Y. Li, B. C. Benicewicz, L. S. Schadler, D. Acehan, A. Z. Panagiotopoulos, V. Pryamitsyn, V. Ganesan, J. Ilavsky, P. Thiyagarajan, R. H. Colby and J. F. Douglas, *Nat. Mater.*, 2009, **8**, 354–359.
- (a) C. Chevigny, J. Jestin, D. Gimes, R. Schweins, E. Di Cola, F. Dalmas, D. Bertin and F. Boué, *Macromolecules*, 2010, **43**, 4833–4837; (b) C. Chevigny, F. Dalmas, E. Di Cola, D. Gimes, D. Bertin, F. Boué and J. Jestin, *Macromolecules*, 2011, **44**, 122–133.
- Y. P. Wang, Y. Q. Shen, X. W. Pei, S. C. Zhang, H. G. Liu and J. M. Ren, *React. Funct. Polym.*, 2008, **68**, 1225–1230.
- K. Matyjaszewski and J. H. Xia, *Chem. Rev.*, 2001, **101**, 2921–2990.
- C. J. Hawker, A. W. Bosman and E. Harth, *Chem. Rev.*, 2001, **101**, 3661–3688.
- C. Z. Li and B. C. Benicewicz, *Macromolecules*, 2005, **38**, 5929–5936.
- C. Xu, K. Ohno, V. Ladmiral and R. J. Composto, *Polymer*, 2008, **49**, 3568–3577.
- K. Babu and R. Dhamodharan, *Nanoscale Res. Lett.*, 2009, **4**, 1090–1102.
- R. Matsuno, K. Yamamoto, H. Otsuka and A. Takahara, *Macromolecules*, 2004, **37**, 2203–2209.
- T. Gelbrich, M. Feyen and A. M. Schmidt, *Macromolecules*, 2006, **39**, 3469–3472.
- C. Chevigny, D. Gimes, D. Bertin, J. Jestin and F. Boué, *Soft Matter*, 2009, **5**, 3741–3753.
- C. Chevigny, D. Gimes, D. Bertin, R. Schweins, J. Jestin and F. Boué, *Polym. Chem.*, 2011, **2**, 567–571.
- S. Mornet, J. Portier and E. Duguet, *J. Magn. Magn. Mater.*, 2005, **293**(1), 127–134.
- R. Massart, *IEEE Trans. Magn.*, 1981, **17**, 1247.
- B. Berkovski, *Magnetic Fluids and Applications Handbook*, Begell House Inc. Publ., New York, 1996.
- J. Vinas, N. Chagneux, D. Gimes, T. Trimaille, A. Favier and D. Bertin, *Polymer*, 2008, **49**, 3639–3647.
- A. Brület, D. Lairez, A. Lapp and J.-P. Cotton, *J. Appl. Crystallogr.*, 2007, **40**, 165–177.
- <http://didier.lairez.fr/dokuwiki/doku.php?id=pasinet>.
- M. Ma, Y. Zhang, W. Yu, H. Shen, H. Zhang and N. Gu, *Colloids Surf., A*, 2003, **212**, 219–226.

- 33 E. Hasmonay, A. Bee, J. C. Bacri and R. Pezzyński, *J. Phys. Chem. B*, 1999, **103**(31), 6421–6428.
- 34 A. Ponton, A. Bée, D. Talbot and R. Perzzyński, *J. Phys.: Condens. Matter*, 2005, **17**(6), 821–836.
- 35 K. Ohno, T. Morinaga, K. Koh, Y. Tsujii and T. Fukuda, *Macromolecules*, 2005, **38**, 2137–2142.
- 36 T. von Werne and T. E. Patten, *J. Am. Chem. Soc.*, 1999, **121**, 7409–7410.
- 37 C. Flood, T. Cosgrove, I. Howell and P. Revell, *Langmuir*, 2006, **22**, 6923–6930.
- 38 S. Alexander, *J. Phys.*, 1977, **38**, 983.
- 39 P. Auroy, L. Auvray and L. Leger, *Phys. Rev. Lett.*, 1991, **66**(6), 719.
- 40 M. Daoud and J.-P. Cotton, *J. Phys.*, 1982, **43**, 531–538.
- 41 J. K. Percus and G. J. Yevick, *Phys. Rev.*, 1958, **110**(1), 1–13.
- 42 M. S. Wertheim, *Phys. Rev. Lett.*, 1963, **10**(8), 321–323.
- 43 C. Rivière, F. Wilhelm, F. Cousin, V. Dupuis, F. Gazeau and R. Perzzyński, *Eur. Phys. J. E: Soft Matter Biol. Phys.*, 2007, **22**, 1–10.
- 44 J. S. Pedersen and M. C. Gerstenberg, *Macromolecules*, 1996, **29**, 1363.
- 45 J. S. Pedersen, C. Svanborg, K. Almdal, S. W. Hamley and R. N. Young, *Macromolecules*, 2003, **36**, 416–433.
- 46 C. Svaneborg and J. S. Pedersen, *Macromolecules*, 2002, **35**, 1028.
- 47 <http://kur.web.psi.ch/sans1/SANSSoft/sasfit.html>.